DOCTOR OF PHILOSOPHY

Turbulence control of floc size in suspended particulate matter in the river estuary transition zone

Jackson, Suzie

Award date:
2014

Awarding institution:
Bangor University

Turbulence Control of Floc Size in Suspended Particulate Matter in the River Estuary Transition Zone

Suzanna Elizabeth Jackson

School of Ocean Sciences

PRIFYSGOL
BANGOR
UNIVERSITY

Acknowledgements

Firstly I would like to acknowledge and thank NERC for funding this project, without their financial support field campaigns on such a large scale would not have been possible. Secondly I would like to thank my supervisor Prof Colin Jago for all his help, guidance and support throughout my PhD. I would also like to thank Prof Dave Bowers for the many helpful discussions we have had over the years and for making me feel no question is too stupid to ask!
Chris Old must be acknowledged for his assistance in calculating TKE dissipations and guidance on ADCP and ADV set ups. Ben Lincoln also sparked invaluable discussions on the JCR surrounded by sea ice, I would mostly like to thank him for his unwavering enthusiasm for oceanographic data which helped me see the wood for the trees. Kath Braithwaite must also be acknowledged for helping me get to grips with the LISST-100. Extensive field work campaigns were carried out for this project, there are many people who must be thanked for their hard work and determination to collect good data, especially when ice was coming up off profiling instruments. The amazing technical team consisted of Ben Powell, Gwynne Parry Jones and Pete Hughes, without them none of this would have been possible. Ian Pritchard and Joan also played a crucial role in teaching me how to organise and prepare for a field campaign. I would also like to thank the following people for their filtering contributions: Dave Todd, John Wright, Ralf Heubner, Josh Griffith, Phil Green and last but definitely not least Sharolyn Parnham.
I would like to dedicate a special thank you to Ian Nicholls for making my moorings, his life was a tragic loss to our department but mostly as we lost another good friend.
I would also like to thank my friends and family for supporting me throughout my PhD and not getting fed up with my moaning about writing a thesis!

Abstract

The majority of terrestrially derived suspended particulate matter (SPM) is transported to the open ocean by rivers, therefore the river estuary transition zone (RETZ) represents a globally significant boundary separating the riverine and coastal regimes. The RETZ is comprised of the Tidally-Influence River (TIR), found above the limit of salt intrusion and the upper part of the estuary including the Estuarine Turbidity Maximum (ETM). The fate of SPM in the RETZ depends on its physical properties which are likely to be extremely variable in the RETZ which is characterised by large temporal and spatial gradients in hydrodynamic properties. Therefore, quantifying SPM properties in relation to physical forcings is key to determining the transfer flux of SPM from the catchment to the coastal ocean. The aim of this study is to interrogate the relationship between floc properties and the turbulence regime in the RETZ of a tidally dominated estuary over tidal, lunar and seasonal temporal scales.

Flocs are fragile in nature and their properties fluctuate on short spatial and temporal scales; therefore *in situ* optical instruments (LISST-100 and transmissometer) were deployed in the RETZ to obtain volume and mass concentrations of SPM. Turbulence measurements were determined via acoustic methods; ADCP and ADVs were deployed near to the bed to estimate TKE dissipation rates relating to the floc measurements. Data have been collected over five field campaigns, each included; spatial surveys characterising vertical profiles of SPM properties from the mouth of the estuary to the TIR, anchor station surveys measuring the temporal variations in SPM properties, bed-mounted mooring deployments in the RETZ and river surveys of the five main tributaries.

Diurnal and semi-diurnal signals in floc properties in the RETZ were observed: resuspension occurred at peak tidal flows, usually on the flood tide; the maximum floc sizes corresponded with minimum effective densities and largely corresponded with high and low waters, as a result of particle flocculation during low turbulence conditions. Turbulence dissipation did not simply scale on tidal current velocities due to the additional contribution of wind stress and direction to the turbulence field. The Kolmogorov turbulence microscale correlated significantly with floc size during periods of marine conditions (i.e. the flood and early ebb tides) but showed a variable relationship during the late ebb when the RETZ was dominated by fluvial conditions and particles. This was most evident in the ETM where marine influence was greater compared to the TIR where it occurred only on larger tides. Thus floc size was related to the turbulence microscale but differences between flood and ebb relationships were probably due to different floc strengths of marine and terrestrial particles. During the lunar cycle, the variations observed on springs were repeated on neaps except that the flocculation signal occurred late in the flood rather than at high water. These tidal and lunar variations of particle properties in the RETZ were observed at all seasons.

There were seasonal variations in marine and terrestrial particle properties. Marine particles (at the estuary mouth) were smaller in March than at other times, while terrestrial particles (in the river and tributaries) were larger in April than at other times. In March, July and September, terrestrial particles were smaller than marine particles. But in April, terrestrial particles were larger than marine particles. In September, during a major river event, terrestrial particle size increased significantly and exceeded marine particle size. In the RETZ, the size of terrestrial particles (as measured at low water) was seasonally consistent except during the September river event when the size increased in response to the increased sizes measured upstream.

SPM flux in the RETZ showed net seaward transport of coarse and fine particles during all seasons. During the river flood event in September, the seaward flux of both coarse and fine particles was an order of magnitude greater than during normal river flow conditions.

Key words: *River-estuary tranistion zone, Tidally-influenced river, floc, flocculation, suspended particulate matter, turbulence, terrestrial, marine.*

Contents

List of Figures

List of Tables

List of Symbols

C = Beam attenuation (m^{-1})

C_D = Drag coefficient

C_f = Floc strength coefficient

C_m = Mass concentration (mgl^{-1})

C_v = Volume concentration (μll^{-1})

Chl_a = Chlorophyll a concentration (μgl^{-1})

D_p = Size of primary particle (μm)

D_{10} = Particle diameter for which 10% of the particles by volume is finer (μm)

D_{50} = Particle diameter for which 15% of the particles by volume is finer (μm)

D_{90} = Particle diameter for which 90% of the particles by volume is finer (μm)

D_{50} = Mass concentration (mgl^{-1})

D_{90} = Volume concentration (μll^{-1})

F_{bed} = Near-bed suspended sediment flux $(10^{-6}ms^{-1})$

$F_{T_{bed}}$ = Tidally averaged near-bed suspended sediment flux $(10^{-6}ms^{-1})$

g = Gravitational acceleration (ms^{-2})

G_{bed} = Near-bed turbulence parameter G (s^{-1})

G_h = Depth averaged turbulence parameter G (s^{-1})

G_{bed_T} = Near-bed tidally averaged turbulence parameter G (s^{-1})

h = Height above bed (m)

h_T = Tidal range (m)

nf = Fractal dimension

Q = River flow rate (m^3s^{-1})

R = Rainfall (mm)

W = Wind speed (ms^{-1})

W_s = Settling velocity (ms^{-1})

u, v, w = velocity components in Cartesian coordinate system (ms^{-1})

u_* = Shear velocity (ms^{-1})

u_{bed} = Near-bed axial current velocity (ms^{-1})

u_h = Depth averaged axial current velocity (ms^{-1})

U_T = Tidally averaged maximum current speed (ms^{-1})

z_0 = Bed roughness length scale

α_D = Advection coefficient (μm^{-1})

β_D = Flocculation/resuspension coefficient ($\mu m(m/s)^{-1}$)

ϵ = TKE dissipation rate (WKg^{-1})

ϵ_{bed} = Near-bed TKE dissipation rate (WKg^{-1})

ϵ_h = Depth averaged TKE dissipation rate (WKg^{-1})

θ_u = depth average axial current direction (°)

θ_{wind} = Direction wind is travelling to (°)

κ = von Karman constant

λ_D = Particle size coefficient (μm)

λ = Scaling coefficient of floc strength

μ_k = Kolmogorov microscale (μm)

$\mu_{k_{bed}}$ = Near-bed Kolmogorov microscale (μm)

$\mu_{k_{bed_T}}$ = Near-bed tidally averaged Kolmogorov microscale (μm)

μ_{k_h} = Depth averaged Kolmogorov microscale (μm)

μ_{k_T} = Depth and tidally averaged Kolmogorov microscale (μm)

μ_k = Ozmidov scale (μm)

ν = Kinematic viscosity (m^2s^{-1})

ρ = Fluid Density (kgm^{-3})

ρ_e = Effective Density (kgm^{-3})

τ_o = Shear stress (Nm^{-2})

τ_w = Wind stress (Nm^{-2})

Chapter 1

Introduction

1.1 Rationale

Estuaries represent a globally significant boundary separating riverine and coastal regimes and play a critical role in the hydrological cycle. Estuaries are known to trap, filter and recycle suspended particulate matter (SPM), composed of lithogenic and biogenic components. The majority of terrestrially derived SPM reaches the coastal ocean via estuaries, therefore the transfer flux of terrestrial organic matter (TOM) is largely determined by estuaries. In fact, 50% (0.1 $Pg\ C\ yr^{-1}$) of the total annual organic carbon export via rivers to the coastal ocean is accounted for by SPM (Ittekkot, 1988). It is therefore essential to understand and quantify the processing of SPM in the estuarine environment due to the implications for the transport of organic carbon from catchment to coast (Arndt et al, 2009). Throughout the transfer from catchment to coast the physical properties of SPM, such as size, density and settling velocity vary, on short temporal and spatial scales; these properties influence the transport of organic material. In particular, the steep gradients in hydrodynamic, chemical and biological characteristics common in the River-Estuary transition zone (RETZ) significantly influence terrestrially derived SPM properties.

The RETZ, described in Figure 1.1, is comprised of the Tidally-Influence River (TIR),

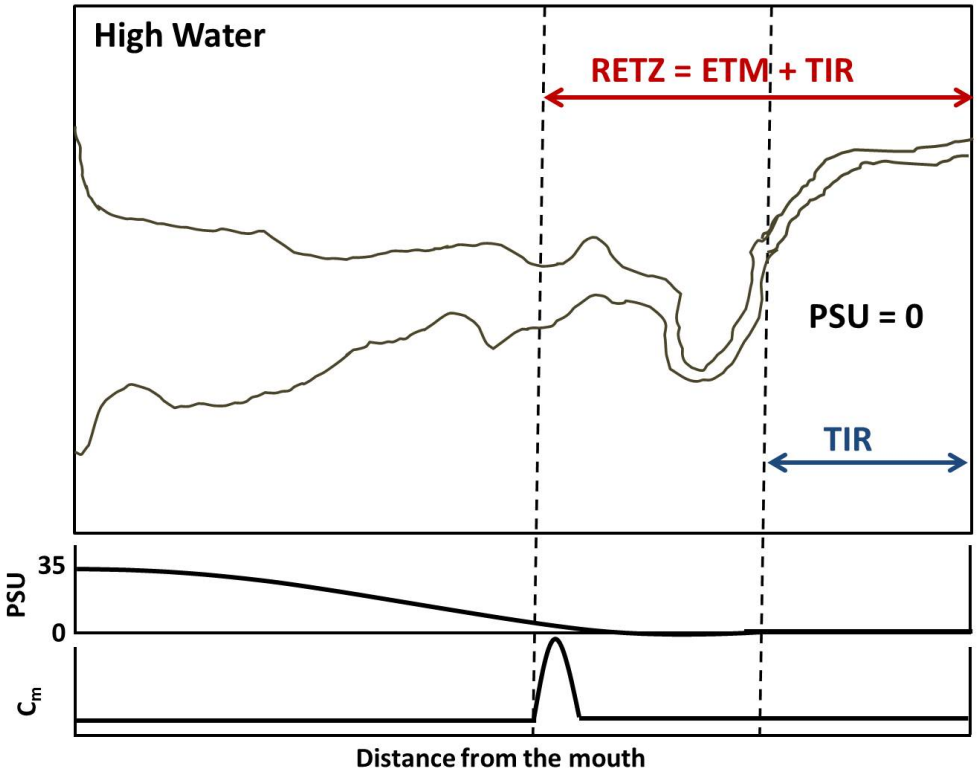

Figure 1.1: Schematic of an idealised case describing the river-estuary transition zone and tidally-influenced river at high water. C_m represents mass concentration of SPM.

found above the limit of salt intrusion although the surface height and velocity field are still tidally modulated; and the upper part of the estuary including the Estuarine Turbidity Maximum (ETM). The upper part of the estuary is characterised mainly by tidal currents which can be modified by low frequency, high magnitude river flood events. The ETM is an area of elevated turbidity, indicated by the rise in C_m found at the fresh-saline water interface (Figure 1.1). The ETM supports seasonal biological production, playing an influential role in estuarine biogeochemical processes, presenting a sink for SPM and associated biogeochemical components.

Presently our understanding of the key temporal and spatial scales which govern interactions in the RETZ between lunar and tidal variability with episodic river events is limited. This is important to address as these varying scales play a dominant role in

estuarine sediment dynamics and thus the export of SPM to the coastal ocean.

Further to this point, another major limitation of this research area has been measuring SPM, particularly in the estuarine environment. In the estuarine environment cohesive sediments are commonly found in suspension, which under certain conditions aggregate to form larger particles called flocs. Flocs consist of colloidal particles ($1 - 10\mu m$), microflocs ($50 - 125\mu m$) and macroflocs which can frequently exceed $500\mu m$ and up to a few millimetres in size (Hill et al, 1998; Traykovski et al, 2000; Fugate and Friedrichs, 2003; Uncles et al, 2006; Xu et al, 2008). A floc is a fragile, water-logged mixture of lithogenic and biogenic matter, held together by a combination of chemical charge and the cohesive properties of organic polymers such as Extracellular Polymeric Substances (EPS). Due to their fragile nature, the only accurate method for measuring size and concentration of SPM in the field is *in situ* sampling, which can now be obtained via optical methods (Agrawal and Pottsmith, 2000). Flocs are also known to act as the main carriers of clay minerals, organic matter, pollutants and pathogens (Fugate and Friedrichs, 2003). They do not act in the same manor as their primary particles; typically flocs have a low density relative to their size, with associated settling velocities (w_s) which vary over orders of magnitude depending on their composition, size and shape. It is therefore imperative to develop our understanding of fluctuations of floc properties in conjunction with the physical forcings occurring throughout the RETZ to ascertain an understanding of the biogeochemical transport pathways from catchment to coast.

With the current limits on our knowledge of estuarine sediment dynamics in mind, this study aims:

To develop understanding of interactions between floc size and physical processes occurring throughout the RETZ, including variations in transfer flux of SPM, on a tidal and lunar scale, along with low frequency seasonal modulations in climatic conditions such as river flood events.

In order to achieve this aim *in situ* high resolution observational data sets were collected

from the Dyfi estaury, a macrotidal estuary situated on the West coast of Mid-Wales. Five extensive field work campaigns have been carried out to ascertain how hydrodynamic forcings in the RETZ affect the size and concentration of SPM over seasonal, lunar and tidal temporal scales. In addition to this, the four main tributaries of the river Dyfi and the mouth of the estuary were sampled.

1.2 Thesis outline

Initially Chapter 2 discusses the past literature concerning estuarine sediment dynamics, concentrating specifically on the relationship between local turbulence and SPM and outlines the relevance of the current study in the context of physical estuarine research. Chapter 3 presents the study site, instrumentation and methods. Chapter 3 also addresses the observation strategy of the field work campaigns undertaken. Chapter 4 moves on to describe hydrodynamic and SPM characteristics throughout the Dyfi estuary. In addition SPM data from river tributary field sites and the mouth of the estuary are presented to provide a full spatial interpretation of the study site. Chapter 5 focuses on the relationship between floc size and the local turbulent kinetic energy dissipation on a tidal scale. For the final results chapter, chapter 6 addresses seasonal and lunar variation in SPM and hydrodynamic characteristics in the estuarine environment, in particular the implications of river events are discussed. The following Chapter 7 synthesizes the main conclusions of the study, discusses the hypotheses identified in Chapter 2 and suggests areas for future work.

Chapter 2

Scientific Background

2.1 Turbulence

2.1.1 Classifying turbulence

Turbulence plays a key role in the controlling and driving of a wide range of physical processes, from small scale mixing in the estuarine environment to large scale mixing driving global ocean circulation.

Classifying turbulence is difficult due to its random and highly non-linear characteristics, however a few specific characteristics are common among all turbulent flows. The first is the previously mentioned non-linear and random characteristics which arise from interactions of motions in a fluid or a gas occurring on different spatial scales. Secondly, turbulent flows display large scale diffusion of momentum and heat. Vorticity is also a characteristic of turbulent flows as they include a broad range of rotating eddy length scales.

2.1.2 Defining a turbulent flow

Reynolds (1883) first investigated the nature of turbulence through dye experiments of water flow through pipes in order to interrogate the transition between laminar flow

(smooth and linear) and a turbulent (random and non-linear) flow. This study gave rise to the non-dimensional Reynolds number:

$$Re = \frac{UL}{\nu} \quad Re_{crit} = 2000 \tag{2.1}$$

U represents velocity and L represents a length scale, the product of which describes the inertial force occurring in the flow. The inertial force is then constrained by the viscosity of the fluid (ν). Re_{crit} is the critical value at which a flow becomes turbulent; i.e. when the inertial forces are large compared to the viscous forces. In the event of low Reynolds numbers, the viscous forces are large compared to the inertial forces, thus indicating interactions on a molecular level are sufficient to resist the formation of turbulent eddies, also known as viscous dampening.

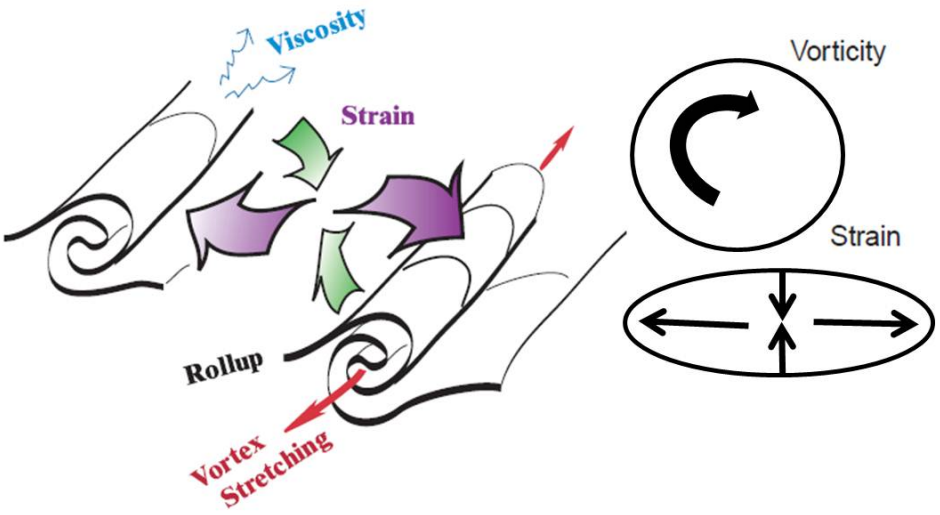

Figure 2.1: Schematic describing the mechanisms of vortex roll up, vortex stretching, strain and viscosity in a turbulence flow. Adapted from Smyth and Moum (2001).

2.1.3 Mechanisms of turbulence

The role turbulence can be separated into two categories; scalar mixing and momentum transport. Momentum transport refers to the transfer of energy or momentum across a gradient between two or more different flows. Therefore if one flow exhibits higher

velocities than another the slower flow reduces the velocity of the faster flow and vice versa. Scalar mixing describes mixing in a fluid through the random movements of molecules. On a small scale such as this, turbulence is driven by vorticity (rotation of a fluid parcel) and strain (the compression and stretching of a parcel of water in opposing directions).

The two main mechanisms using vorticity and strain to drive turbulence are **vortex roll up** and **vortex stretching** described in Figure 2.1. The roll up process occurs due to shear instabilities and creates line vortices which are then elongated further by vortex stretching (Figure 2.1). This causes the vortex rotation rate to increase in compensation for the stretching. At the same time molecular viscosity acts to oppose these mechanisms by dissipating energy from the vortices through the conversion to heat. It is important to note mixing due to turbulence is not prevalent inside the vortices, it is the areas acting under strain between vortices that give rise to mixing through the deformation of fluid parcels.

Figure 2.1 is a relatively simple schematic, however considering the potential for the mechanisms to occur simultaneously, varying on short temporal and spatial scales, the complexities of turbulent flows begin to unfold. For this reason at present statistical analysis is employed to estimate turbulence in terms of mixing rates, dissipation and production of turbulent kinetic energy.

2.1.4 Statistical approach to quantifying turbulence

Reynolds (1895) presented a statistical approach to quantifying turbulence through deconstructing the velocity terms, giving rise to a mean value ($\bar{u}$) which is averaged (over an appropriate temporal or spatial scale) and a measure of the turbulent fluctuation about the mean (u'). The horizontal and vertical velocity components can be presented as:

$$u = \bar{u} + u' \qquad v = \bar{v} + v \qquad w = \bar{w} + w' \tag{2.2}$$

The Navier-Stokes equations of motion, also known as the equations of conservation of

linear momentum, utilise Newton's second law of motion (Force = mass x acceleration) to describe fluid motion. The continuity equation below indicates both the average and turbulent flows are non-divergent, acting as neither a sink nor a source, neither producing nor destroying fluid. The equations of motion are presented in Cartesian coordinate system as reported by Pond and Pickard (1978):

$$\overbrace{\frac{\partial u}{\partial x}+\frac{\partial v}{\partial y}+\frac{\partial w}{\partial z}=0}^{\text{Continuity Equation}} \tag{2.3}$$

$$\frac{\partial u}{\partial t}+\overbrace{u\frac{\partial u}{\partial x}+v\frac{\partial u}{\partial y}+w\frac{\partial u}{\partial z}}^{\text{advection terms}}\overbrace{-fv}^{\text{Coriolis force}}=\overbrace{-\frac{1}{\rho_0}\frac{\partial p}{\partial x}}^{\text{pressure gradient}}+\overbrace{\nu\left(\frac{\partial^2 u}{\partial x^2}+\frac{\partial^2 u}{\partial y^2}+\frac{\partial^2 u}{\partial z^2}\right)}^{\text{viscous friction}}$$

$$\frac{\partial v}{\partial t}+u\frac{\partial v}{\partial x}+v\frac{\partial v}{\partial y}+w\frac{\partial v}{\partial z}+fu=-\frac{1}{\rho_0}\frac{\partial p}{\partial y}+\nu\left(\frac{\partial^2 v}{\partial x^2}+\frac{\partial^2 v}{\partial y^2}+\frac{\partial^2 v}{\partial z^2}\right)$$

$$\frac{\partial w}{\partial t}+u\frac{\partial w}{\partial x}+v\frac{\partial w}{\partial y}+w\frac{\partial w}{\partial z}=-g\,\frac{\rho}{\rho_0}-\frac{1}{\rho_0}\frac{\partial p}{\partial z}+\nu\left(\frac{\partial^2 u}{\partial x^2}+\frac{\partial^2 u}{\partial y^2}+\frac{\partial^2 u}{\partial z^2}\right) \tag{2.4}$$

t represents time, u, v and w are the velocity vectors moving in the x, y and z directions respectively. f represents the Coriolis force, calculated as $2\omega \sin\phi$, where ω is the angular frequency of the earth and ϕ denotes the latitude. ρ_0 is a constant reference density, whereas ρ is density of the fluid. ν represents the kinematic viscosity, g is gravitational acceleration and p is pressure. In the $x-$plane the first term denotes the change in u with respect to time which together with the advection terms for u in all three directions minus the product of the Coriolis force and v balances the terms on the left hand side; the pressure gradient and the viscous forces. In the $z-$plane the Coriolis force does not feature; however gravitational force and the density of the fluid are accounted for.

Reynolds' deconstructed velocity (Equation 2.2) terms can consequently be substituted in the equations of motion (Equations 2.4) whilst employing the continuity equation (Equation 2.3) to give the Reynolds averaged Navier Stokes equations below. D/Dt is

the total derivative $\partial/\partial t + \mathbf{u}.\nabla$.

$$\frac{D\bar{u}}{Dt} - f\bar{v} = -\frac{1}{\rho_0}\frac{\partial \bar{p}}{\partial x} + \nu\left(\frac{\partial^2 \bar{u}}{\partial x^2} + \frac{\partial^2 \bar{u}}{\partial y^2} + \frac{\partial^2 \bar{u}}{\partial z^2}\right) - \overbrace{\left(\frac{\partial \overline{u'u'}}{\partial x} + \frac{\partial \overline{u'w'}}{\partial y} + \frac{\partial \overline{u'w'}}{\partial z}\right)}^{\text{turbulent velocity fluctuations}}$$

$$\frac{D\bar{v}}{Dt} + f\bar{u} = -\frac{1}{\rho_0}\frac{\partial \bar{p}}{\partial y} + \nu\left(\frac{\partial^2 \bar{v}}{\partial x^2} + \frac{\partial^2 \bar{v}}{\partial y^2} + \frac{\partial^2 \bar{v}}{\partial z^2}\right) - \left(\frac{\partial \overline{v'u'}}{\partial x} + \frac{\partial \overline{v'v'}}{\partial y} + \frac{\partial \overline{v'w'}}{\partial z}\right)$$

$$\frac{D\bar{w}}{Dt} = -g\frac{\bar{\rho}}{\rho_0} - \frac{1}{\rho_0}\frac{\partial \bar{p}}{\partial z} + \nu\left(\frac{\partial^2 \bar{w}}{\partial x^2} + \frac{\partial^2 \bar{w}}{\partial y^2} + \frac{\partial^2 \bar{w}}{\partial z^2}\right) - \left(\frac{\partial \overline{w'u'}}{\partial x} + \frac{\partial \overline{w'v'}}{\partial y} + \frac{\partial \overline{w'w'}}{\partial z}\right) \quad (2.5)$$

The main difference to the original Navier-Stokes equations shown are the terms on the right hand side of Equations 2.5. The terms labelled turbulent velocity fluctuations describe the turbulent momentum fluxes in three dimensions commonly known as the **Reynolds stresses**. Reynold stresses describe the average rate of transfer of momentum to the turbulent fluctuations directly from the mean flow. Typically Reynolds stresses dominate the viscous forces (also on the right hand side of the equation) with the exception of close proximity to solid boundaries where turbulence fluctuations are forced to be small.

Richardson (1922) introduced the concept of an energy cascade, conveying the broad-band nature of turbulence. The energy cascade represents the transfer of turbulent kinetic energy (TKE) from the top end of the cascade; the large scale eddies (transferring momentum directly from the mean flow), which feed into smaller eddies and right down to the molecular level in which the dissipation of energy through viscous forces occurs. Kolmogorov (1941) developed this concept, identifying that the length scale of the largest eddies in a turbulent flow determines the length scale of the flow. Kolmogorov (1941) identified the relationship between viscous friction and TKE dissipation in determining the length scale of the smallest eddies in a turbulent fluid, often referred to as the **Kolmogorov microscale**.

$$\mu_k = \left(\frac{\nu^3}{\epsilon}\right)^{1/4} \quad (2.6)$$

Small scale eddies are associated with high wavenumber (k). Equation 2.6 described a

fluid in which turbulence production is dictated by both dissipation (ϵ) and viscous forces, ν represents viscosity. As k decreases, the eddy length scale increases and turbulence production becomes independent of viscous forces and solely dependent on dissipation, giving rise to the Kolmogorov $-5/3$ power law:

$$E(k) = C_k \epsilon^{2/3} k^{-5/3} \tag{2.7}$$

$E(k)$ represents the energy spectrum, C_k is a universal constant taken from atmospheric calculations of turbulence as ca. 0.55. This equation applies only to the **inertial subrange** which includes eddy length scales smaller than that of the eddies transferring energy directly from the mean flow but larger than the smallest eddy length scales that dissipate energy through viscous forces.

The Ozmidov scale presented below characterises the length scale of the largest eddies in the energy spectrum which encompass the ability to overturn a water column in stable and stratified conditions.

$$\mu_o = \left(\frac{\epsilon}{N^3}\right)^{1/2} \qquad N^2 = -\frac{g}{\rho_0}\left(\frac{\partial \rho}{\partial z}\right) \tag{2.8}$$

N^2 denotes the buoyancy frequency. The Ozmidov scale indicates the upper limit of the inertial subrange, the eddy length scales covered by this scale describe the eddies feeding directly from the mean flow, unaffected by viscous forces.

2.2 Estuarine environment

Due to the complex intertwined mix of physical and bio-geochemical processes occurring in the estuarine environment, the classification of an estuary is not a simple task. Many attempts have been made over the years to accurately define an estuary, one of the most widely accepted is by Dyer (1997) adapted from Cameron and Pritchard (1963): "An estuary is semi-enclosed coastal body of water which has free connection to the open sea, extending into the river as far as the limit of tidal influence and within which seawater is measurably diluted with freshwater derived from land drainage ".

This description highlights the main characteristics of an estuary with respect to the mixing of fresh and salt water, tidal influences and a connection to the coastal ocean.

2.2.1 Estuarine Classification

There are a multitude of ways to classify estuaries, this section will cover classification by; water balance, geomorphology, salinity structure, hydrodynamics and tidal forcing. Firstly estuaries can be classified as positive or negative with respect to water balance. A positive estuary experiences freshwater input that exceeds the rate of evaporation; typically the freshwater input in positive estuaries induces gravitational circulation. Conversely, evaporation rates exceed freshwater input via precipitation in negative estuaries and the freshwater input via rivers is negligible or non-existent.

The geomorphology of an estuary can be split into four categories; coastal plain, bar-built, fjords and tectonic. Coastal plain estuaries are essentially drowned river mouths caused by the latest post-glacial Pleistocene rise in sea level; they are typically wide and shallow. Bar-built estuaries were originally tidal embayments which became semi-closed due to littoral drift forming sand bars or splits restricting the mouth. Fjords are associated with high latitudes and glacial activity; they are characteristically elongated in shape and deep with a sill formed at the mouth due to the moraine of an inactive or active glacier. Finally, tectonic estuaries are formed through tectonic activity creating faults causing parts of the Earth's crust to sink and thus fill in with water.

The vertical salinity structure is a useful tool in classifying estuaries as the extent of vertical stratification can infer considerable information on the state of mixing and thus circulation patterns of an estuary. The extent of stratification is largely the competition between buoyancy forcing from freshwater inflow and the mixing forces from the tidal influence. The mixing from tidal forcing is directly proportional to the **tidal prism (P)** which is the product of the tidal range and the volume of the tidal basin. The two extremes of the vertical salinity classifications found in estuaries are the salt wedge and a well-mixed estuary. A salt wedge estuary has a large river discharge and low tidal forcing

which results in salinity profiles exhibiting sharp pycnoclines. As tidal forcing increases and river discharge weakens estuaries become well-mixed with respect to salinity, thus portraying vertically uniform profiles of salinity.

Davies (1964) suggested a form of classifying estuaries by tidal range as follows:

- Microtidal $< 2\,m$
- Mescotidal $< 4m > 2\,m$
- Macrotidal $< 6\,m > 4\,m$
- Hypertidal $> 6\,m$

Estuaries can be further classified with respect to acting as a sink or source for sediments. This depends on the cross-sectional area and the tidally active water volume of the estuary. The net sediment flux can be influenced by semi-diurnal forcing, wind magnitude, wave action, freshwater discharge and extreme weather such as storm surges. Quantifying suspended sediment fluxes in estuaries is difficult and usually involves assumptions of vertical homogeneity with respect to velocity and therefore in some cases significantly over or underestimating the net sediment flux. However, it is important to continue to develop our understanding of suspended sediment fluxes in estuaries to assess whether an estuary is acting as a sink or a source for sediment.

2.2.2 Boundary layer turbulence

In the estuarine environment the effects of a flow interacting with a boundary can influence SPM concentrations. Velocity shear is produced by the frictional drag caused by a flow over a solid boundary. For example a near bed flow is slower relative to the flow higher up in the water column due to the interaction with the bed, thus creating a bottom boundary layer (Figure 2.2). Turbulence can be produced by a flow over a bed due to the roughness and topographical features of the bed. For a vertically homogeneous

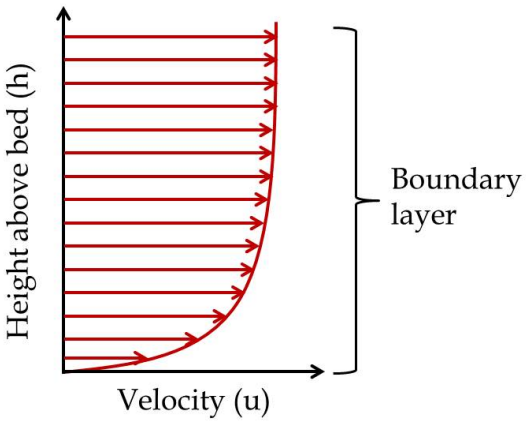

Figure 2.2: Schematic describing the velocity profile for a steady flow over a bed, exhibiting velocity shear in the bottom boundary layer. Adapted from Colling et al (1989).

flow close to the bed, the velocity profile can be described by the *von Karman-Prandtl equation*:

$$\frac{u}{u_*} = \frac{1}{\kappa} ln \frac{h}{z_0} \qquad u_* = \sqrt{\frac{\tau_0}{\rho}} \tag{2.9}$$

u_* is the shear velocity, τ_0 is the shear stress, κ is the von Karman constant (0.4) and z_0 represents a roughness length which is derived from the roughness of the bed. Moreover, experiments have shown shear stress (τ_0) is proportional to velocity squared at the bed, which is known as the quadratic friction law:

$$\tau_0 = \rho C_D \overline{u}^2 \tag{2.10}$$

$\overline{u}$ is the depth mean velocity. C_D is known as the drag coefficient which is related to z_0 this is explained in further detail by Dyer (1989).

2.2.3 Estuarine mixing

Mixing in estuaries is generally produced by a combination of internally and boundary generated turbulence, both of which are know to fluctuate on small spatial and temporal scales. The affects of mixing in estuaries can be easily portrayed through salinity profiles.

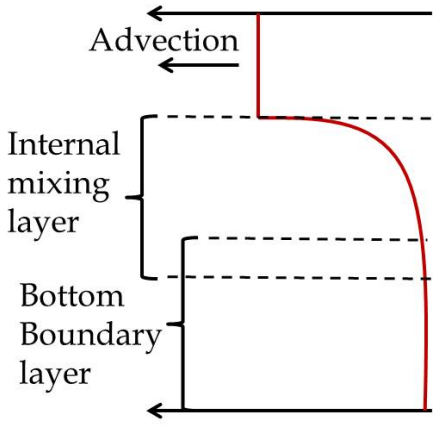

Figure 2.3: Schematic illustrating the salinity profile of a partially mixed estuary and the contributions of the internal mixing layer and the bottom boundary layer to the extent of vertical mixing . Adapted from Dyer (1997).

Figure 2.3 illustrates a salinity profile for a partially mixed estuary, indicating the interactions between different sections of the water column and the salinity gradient. The mixing is most effective in the region where the bottom boundary and internal mixing layers both occur. In well-mixed estuaries it is generally accepted that the bottom boundary layer dominates the production of mixing. Internally generated mixing presents a significant affect only during periods of low current speeds, such as slack water.

An external source of mixing or turbulence can occur due to the action of breaking waves or wind stress. Wave action has been identified in the literature not only as a source of turbulence but also as a control of the distribution of particles in the estuarine environment (Gabrielson and Lukatelich, 1985; Arfi et al, 1993). Weir and McManus (1987) commented on observations of wind strength and direction correlating with peaks in resuspension of material on a tidal flat. Sanford (1994) highlighted the neglect within the literature with regards to wind and wave action in estuarine environments. This is mainly due to tidal currents generally overwhelming other sources of mixing and turbulence. However in certain cases Sanford (1994) indicates wind generated currents and waves can form an integral part in mixing and even SPM transport processes (Bohlen, 1987; Wright et al, 1992), namely in estuaries exhibiting weaker tidal currents and some

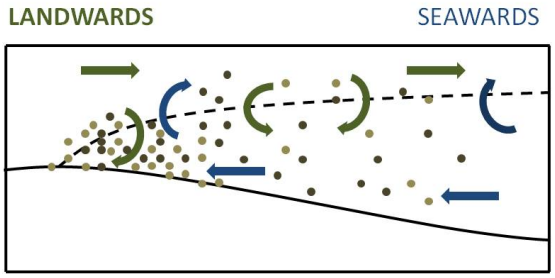

Figure 2.4: Schematic diagram describing the formation of an estuarine turbidity maximum in a partially mixed estuary, adapted from Colling et al (1989).

form of restriction at the mouth. Further to this point in a more recent study North et al (2004) suggested fluctuations on short temporal scales in wind direction and magnitude can significantly affect circulation patterns in the estuarine environment, including sediment transport. Furthermore, Simpson and Bowers (1981) also highlighted the potential for mixing fronts determined by h/u^3 to induce conditions conducive for flocculation, such as enhanced suspended sediment concentrations. With potential sources of mixing and turbulence in the estuarine environment in mind, this study plans to test the following:

Hypothesis 1: *TKE dissipation near to the bed is determined by the local velocity field which in a macrotidal estuary is governed by tidal forcing.*

2.2.4 Estuarine Turbidity Maximum

The Estuarine Turbidity Maximum (ETM) is a distinctive feature of partially and well mixed estuaries. As shown in Figure 2.4, the ETM is characterised by a region of high suspended sediment concentrations compared to the river or the coastal ocean localised around the salt water and fresh water interface (indicated by the black dashed line in Figure 2.4). The ETM acts to trap, mobilise and recycle suspended sediments. The ETM position is moderated by river discharge (Uncles and Stephens, 1989; Woodruff et al, 2001); furthermore the lunar spring to neap modulation affects the ETM as stronger tidal currents exhibited on spring tides immobilise more sediments from the bed via

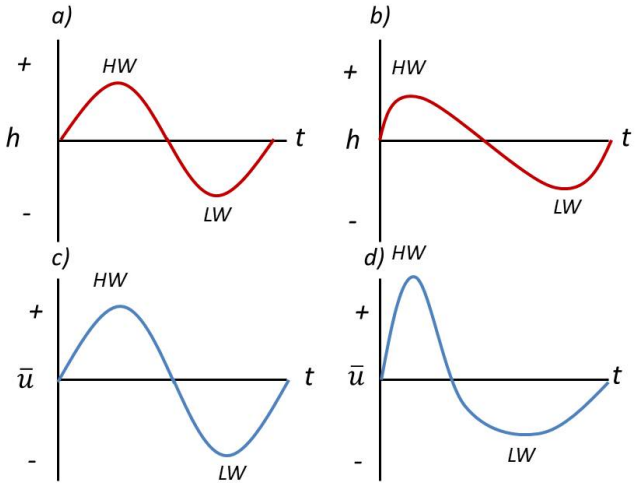

Figure 2.5: Illustration of tidal wave in shallow and deep water, portraying the affects of tidal asymmetry and the consequences to the flood and ebb phase of the tide.

resuspension. This study aims to test the following hypothesis concerning the ability of the ETM to act as a source or sink for SPM under fluctuating river discharge:

Hypothesis 2: *Under normal conditions the RETZ acts as a sediment trap due to the ETM, under conditions of elevated river flow the RETZ acts as a net exporter for SPM.*

2.2.5 Tidal asymmetry

Tidal asymmetry is an important feature in tidally dominated estuaries; it results from the combination of friction and the continuity of water volume (Bowers and Al-Barakati, 1997). Tidal wave asymmetry occurs in shallow water as the crest of the wave travels faster relative to the rest of the wave. This can be explained by consulting the equation for the speed of a wave (c) in shallow water:

$$c = (1 + \frac{3}{2}\frac{\eta}{\bar{h}})\sqrt{g\bar{h}} \tag{2.11}$$

η represents the local height of the tidal wave surface above the mean water level. $\bar{h}$ is the mean water depth. Equation 2.11 indicates that in shallow water, when h is small the ratio between η and $\bar{h}$ increases. This results in a rise in c, which is greatest at the crest

of the wave where η is at a maximum. Figure 2.5d portrays the affects of asymmetry of the tidal wave on the flood and ebb phase of the tide. This process is known as 'tidal pumping'. Moreover, asymmetry is thought to be one of the major factors in determining net suspended sediment transport in estuaries, which has a substantial consequence for the transport of biogeochemical pathways and the overall stability of the system. This study aims to investigate the affects of tidal asymmetry on SPM transport in an effort to identify whether asymmetry in tidal currents definitively results in asymmetry of SPM transport. Evidence of asymmetry in SPM transport is discussed in more detail later in the Chapter.

2.3 Suspended Particulate Matter dynamics

2.3.1 Suspended Particulate Matter

Suspended particulate matter (SPM) refers to particles in suspension, therefore by definition the particles spend long and irregular intervals in the water column without contact with the bed. SPM concentration and composition play a dominant role in vertical and cross-sectional fluxes of lithogenic and biogenic particulate material in coastal zones (Lane et al, 1997). The composition of SPM can vary considerably according to its origin which can be terrestrial or marine derived, including biogenic and lithogenic material (Bunt et al, 1999). The inherent chemical characteristics of SPM in the RETZ are paramount in dictating the reactivity, transportation and biological impact of substances from river catchments to the coastal zone (Burton et al, 1993). The current study aims to investigate the influence of terrestrial organic matter (TOM) under river flood conditions on the size of flocs in the RETZ and at the mouth of the estuary, by testing the following hypothesis:

Hypothesis 3 *The size of terrestrially derived SPM entering from the river dictates the size of flocs throughout the estuary during river floods.*

Further to this point Jones et al (1994) highlighted how integral SPM resuspension,

transportation and deposition can be vital in a variety of marine processes such as benthic fluxes, biological production, biogeochemical cycling and pollutant dispersal.

2.3.2 Flocs

Muddy sediments such as single clay and silt particles are cohesive and ubiquitous in estuarine environments. In contrast to non-cohesive sandy sediments, muddy sediments can flocculate to form larger particles in suspension called flocs or aggregates (Manning et al, 2007). There are two main types of flocs, microflocs ($< 125\mu m$) and macroflocs ($125\mu m > 3-4mm$) (Eisma, 1986). Macroflocs differ from microflocs in density; macroflocs are more fragile as they are more loosely bonded than microflocs which exhibit more tightly packed particles (Dyer and Manning, 1999), giving rise to more robust flocs (Eisma, 1986). Moreover microflocs can act as a constituent of macroflocs along with single mineral grains. The forces that hold these components together are van der Waal forces, intermolecular forces that can be broken down or formed in response to a complex mixture of physical forces (van der Lee et al, 2009). Concentrations of flocs range from $1mgl^{-1}$ in open waters to greater than several thousand mgl^{-1} in estuaries (Burban et al, 1990).

The term primary particle represents the smallest constituents of a floc which are compact in comparison to larger resultant aggregates. Flocs exhibit higher porosities compared to their primary particles due to the complex branch-like structures they form. This results in fragile collections of particles which can easily disaggregate under hydrodynamic conditions observed in estuaries (Kranenburg, 1994; Winterwerp, 1998; Maggi et al, 2006). As the size of a floc increases due to flocculation the respective effective density decreases due to the interstitial water pockets; however the associated settling velocity increases as described by Stokes Law (Dyer and Manning, 1999).

As mentioned above, flocculation is partly modulated by the interplay between forces of attraction via van der Waals forces (V_A) and forces of repulsion, electrostatic (V_R), as shown in Figure 2.6. For clay particles in suspension the overall V_R is negative,

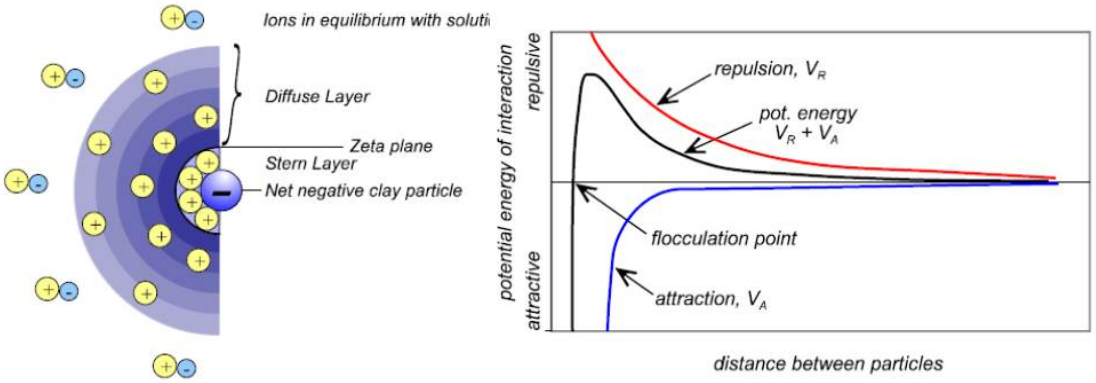

Figure 2.6: Schematic of flocculation (left); Negatively charged layers in the double layer attract positive ions. The concentration of these positive ions increases towards the negatively charged clay surface. Graphical representation of DLVO theory (right). The combined attractive and repulsive forces lead to aggregation at small inter-particle distances.

therefore in the RETZ when saline water is present cations such as sodium, potassium and magnesium are attracted to the face of clay particles, due to the opposite charges attracting. This reduces the negative charge of the particle allowing V_A to prevail and flocculation to occur. The relationship between salinity and flocculation is inversely exponential, the negative charge of clay particles declines with increasing salinity, and therefore flocculation occurs rapidly at low salinities. With this information in mind it is also important to note that not all clay sized particles are alike, for example kaolinite can begin flocculating at lower salinities than illite and montmorillonite. Moving focus to biological implications to flocculation; mucous films produced via bacterial activity possess positive charges thus decreasing V_R and enhancing flocculation through the same principle as salinity. There is evidence in the literature to suggest that biological activity is a crucial aggregating force which will be discussed in a later section. Freshwater clay particles remain negatively charged, therefore clay particles in fresh water repel each other. In the present study the composition of flocs such as the organic content or identification of clay minerals are not explored, this project was a separate part of a wider NERC project in which the chemical composition of flocs were further developed.

2.3.3 Controls on SPM variability

In this section the physical controls of SPM concentration are to be considered. Multiple physical controls govern the cohesive sediment cycle of; erosion, resuspension, advection, flocculation, settling, deposition and bed consolidation (Allen et al, 1980; Officer, 1981; Nikora et al, 2004). Moreover these physical processes occur on varying temporal scales including; tidal, lunar and seasonal.

Resuspension of SPM is characterised by an increase in mass concentration which is often but not necessarily associated with a change in particle size; the change in particle size is governed by the material available at the bed for resuspension. Resuspension events are most likely to occur during peak flows, in an estuarine environment that would produce a quarter-diurnal (M_4) signal in SPM concentrations, increasing at maximum ebb and flood current speeds. Changes in SPM concentration in an estuary can also be due to advection of SPM by tidal forcing; if SPM concentrations increase in accordance with the tidal phase (i.e. present maximum values at high water and minimum at low water) advection is occurring. Conversely, flocculation and de-flocculation of SPM does not result in a change in mass concentration, these processes are associated with a change particle properties such as size.

Tidal scale

The main controls of SPM highlighted from observational data in the literature are resuspension, advection and flocculation/ de-flocculation, these processes can be superimposed which present difficulties in deciphering the dominant processes (Jago and Jones, 1998). Early work in estuaries indicates the density circulation as the main control on the net movement of suspended sediment (Dyer, 1974; Officer, 1981). Further studies show that the transport of SPM in estuaries is also heavily influenced by tidal currents, waves, and bathymetry, in addition to the salinity gradient and river flow (Verney et al, 2009).

Tidal modulations have a significant effect on SPM concentrations; Allen et al (1980)

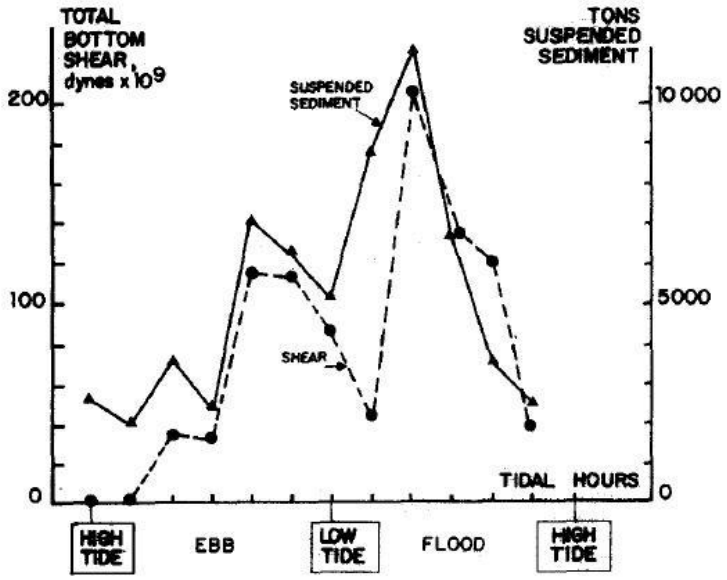

Figure 2.7: Asymmetry in shear production and SPM characteristics on a tidal scale; comparison of the variation in total bottom SPM in the Aulne estuary during a spring tide when bottom current shear was above the critical erosion value. Taken fromAllen et al (1980)

suggests an estuary exhibiting pronounced tidal asymmetry in shear stress will thus create asymmetry in suspended sediment characteristics (Figure 2.7). Figure 2.7 exhibits a clear disparity between the shear production on the ebb relative to the flood. During the flood phase of the tide, the higher levels of shear exerted on the bottom sediments causes increased erosion and therefore resuspension of sediments from the bed. Furthermore, flood dominance gives rise to a more intense ETM during the flood phase of the tide (Figure 2.7). The converse it also true as higher levels of sedimentation are observed during slack water. Figure 2.7 consolidates the argument that the flood-ebb cycle and thus tidal currents play a major role in governing the concentration of suspended sediments in the estuarine environment. Wolanski et al (1995) reported a 30% inequality in the magnitude of suspended sediment concentration in the Fly river estuary in response to only a 5% inequality in the diurnal tidal currents, portraying the significance of the diurnal time scale in influencing suspended sediment concentrations.

On a flood-ebb time scale Allen et al (1980) introduced the concept of variations in water volume driving residual movement of water into an estuary on the flooding tide and vice versa, ultimately driving a landward net transport of SPM. This hypothesis would be of interest to macrotidal estuaries where tidal amplitudes and thus tidal averaged water volumes fluctuate considerably throughout the flood-ebb cycle. Moreover, significant changes in the tidal prism also have knock on effects on the extent of mixing and thus periods of stratification within an estuary (Allen et al, 1980).

Weeks et al (1993) identified the occurrence of superimposed resuspension and advection events in the Irish Sea using beam attenuation measurements; tidal forcings were found to usurp previously existing horizonal gradients in SPM, giving rise to diurnal signals (M_2 frequency) in mass concentration. In addition to advection of SPM, modulations in SPM concentrations were reported at peak ebb and flood current speeds (M_4 frequency), due to resuspension. The superimposition of these processes gave rise to the 'twin peak' variation in SPM also identified in the North Sea (Jago et al, 1993). Fluctuations in SPM concentrations have also been observed in a response to the tidal phase in the estuarine environment. In the Winyah Bay estuary, Patchineelam and Kjerfve (2004) reported semidiurnal signals in SPM concentrations, linked to contrasting values of current speeds and shear observed on flood and ebb phases of the tide.

Returning to the Irish Sea, through the deployment of a LISST-100 which measured volume concentration of SPM in 32 size classes, Ellis et al (2004) was able to comment further on the 'twin peak' SPM phenomenon reported over a decade previously. Initially it was concluded that a combination of resuspension and advection were responsible for the 'twin peak' in concentration, however Ellis et al (2004) suggested the resuspension component was over estimated as 1/4 of the resuspension signal was described by flocculation and de-flocculation processes, occurring at slack water and maximum current speeds respectively. Continuing in the Irish Sea, Jago et al (2006) interrogated the relationship between SPM and turbulence; it was concluded that spatial and temporal gradients in turbulence were influential. The time-varying turbulence was related to variations in SPM occurring on an M_4 frequency, in the form of flocculation at slack water and a

combination of resuspension and de-flocculation during maximum levels of turbulence. The spatial variation in ambient turbulence conditions at the study site was linked to SPM through the horizontal gradient in particle size occurring on an M_2 frequency.

More recently Braithwaite et al (2012) investigated observational relationships between turbulence and particle properties in more detail, in an energetic tidal channel. The median size of particles was reported to change by a factor of three during a tidal cycle. Changes in size were attributed to flocculation during periods of low turbulence conditions and de-flocculation when turbulence was high. Furthermore, particle size was shown to scale with the Kolmogorov microscale when a $30 - 60$ minute phase lag was applied. This implies particle size was limited by the length scale of turbulent eddies when a period of adjustment was applied; allowing for particles to react to the changes in the local turbulence regime.

Lunar variations

In addition to modulations on a tidal scale, Smith et al (2003) presents evidence to suggest there is a strong relationship between the spring-neap tidal cycle and SPM concentrations (Smith et al, 2003). Jones et al (1998) commented on the significant variability of not only SPM concentrations over spring-neap time scales but also particle size, settling velocity and floc composition. The distinction between spring and neap tides is paramount in describing the potential consequences to particles in suspension. For example Wolanski et al (1995) infer that without the elevated current speeds characteristic of spring tides the majority of SPM would remain deposited at the bed during slack water.

Wolanski et al (1995) reported the significance of the spring neap cycle in the Fly river estuary, a combination of spring tides and elevated trade winds giving rise to significant peaks in SPM concentrations, attributed to resuspension of sediments from the bed. The highest suspended sediment concentrations were observed during spring tides and the minimum during neap tides, which infers the ability of the spring-neap cycle to control SPM concentrations.

Seasonal variation

In practice on a seasonal time scale the relationship between river discharge and sediment discharge can be highly variable, however Velegrakis et al (1997) did report that the fluctuation in particle supply (forced by the variation in fluvial and marine inputs) can act as a key control on SPM concentrations in an estuarine environment. Sanford et al (2001) indicated that seasonal variations govern the type of sediments delivered during major perturbations in the hydrological cycle. During winter periods the river flow can be significantly increased, affecting the longitudinal density gradients within the estuary, increasing stratification and potentially eroding different terrestrially derived sediments (Droppo, 2001; Sanford et al, 2001). More recently Patchineelam and Kjerfve (2004) presented a significant correlation between river flow and the resultant sediment load transport for the Pee Dee river; as river flow increased the sediment load transport also increased. This evidence highlights the importance of understanding SPM estuarine dynamics, as global climate change research (IPCC, 2013) predicts the frequency of river events are set to rise, thus emphasising the importance of the role SPM plays in the transport pathways of biogeochemical components, pollutants and pathogens.

Krivtsov et al (2008) highlighted the transition between summer and spring in SPM dynamics from observational data. In August advection over ruled all other processes, which was portrayed through a lower M_4 signal than the M_2, the converse was true for September when the M_4 resuspension signal became prevalent thus imposing on the advection signal (Krivtsov et al, 2008).

The effects of seasonal variation on shelf sea SPM dynamics have been well documented (van der Lee et al, 2009). Our knowledge of seasonal variation in estuarine environments with respect to SPM, particularly in the RETZ is an area in which further research is required, to better understand how a changing climate; such as enhanced sea level rise and increased storm frequencies, will affect the transport pathways of SPM and its associated biogeochemical components.

2.3.4 Physical mechanisms of flocculation

As discussed previously, the majority of SPM in estuaries and coastal regions exists as flocs. The extent of flocculation is governed by a multitude of physical factors in addition to the particle type, making the investigation of flocculation a multi-variant issue (Krivtsov et al, 2009).

The mechanisms controlling floc formation in the marine environment have received significant observational and modelling investigations over the past few decades. Kranck (1973) recognised flocculation as a factor in sediment transport that required a higher level of understanding. Our knowledge of this subject area is limited by the complex interplay of physical and biochemical processes controlling floc size. Moreover, floc size can vary on short spatial and temporal scales in a dynamic environment, characteristics of estuaries (Mehta and Partheniades, 1975; Van Leussen and Cornelisse, 1993; Winterwerp, 2002). Moreover, the previous studies such as Mehta and Partheniades (1975) investigated the physical affects on sediments of known chemical compositions which is a more straight forward case than unidentified estuarine sediments. The main physical processes governing flocculation reported in the literature are as follows:

- Brownian motions
- Differential settling
- Turbulent motions and shear (orthokinesis)
- Sediment concentrations and turbidity
- Density gradients
- Fractal dimension

The frequency of particle collisions are governed by three collision mechanisms; Brownian motions, fluid shear and differential settling (Camp and Stein, 1943; Lick et al, 1993),

which make up the collision frequency function ($B_{(i,j)}$). Collision frequency ($N_{(i,j)}$), the number of collisions occurring between flocs of two respective size classes (i and j) can be parametrised (Smoluchowski, 1917; Ives, 1978; Camp and Stein, 1943; Lick et al, 1993) when binary collisions are assumed as:

$$N_{(i,j)} = B_{(i,j)} n_i n_j \tag{2.12}$$

$B_{(i,j)}$ describes the collisions occurring between the two separate size classes. n_i and n_j represent the number of particles per unit volume of a particular size class with respect to indexing.

Brownian motions

Brownian motions simply describe the random movement of suspended particles in a fluid due to thermal energy (Lick et al, 1993). Winterwerp (2002) described Brownian motions as one of the three main agents governing the settling velocity of sediments in estuaries. Brownian motions typically affect particles $< 1\mu m$ and only at high particle densities (Crombie, 2000), which is not representative of the size classes of naturally occurring flocculated particles in estuaries. Therefore, despite the fact that Brownian motions have been labelled as a main force in causing particle collisions by Lick et al (1993), Van Leussen and Cornelisse (1993) found Brownian motions to be negligible with respect to flocculation in estuarine and coastal environments.

Fluid Shear

Fluid shear enhances particle collisions due to the relative particle motions which occur in a shear flow (Lick et al, 1993). The effect of fluid shear is proportional to the turbulence in any given body of water, therefore fluid shear becomes significant in regions of high energy such as coastal zones and estuarine environments. Fluid shear can be represented

as:

$$B_{(i,j)} = \frac{G}{6}(f_i + f_j)^3 \tag{2.13}$$

Here f denotes the diameter of colliding particles and G represents the mean velocity shear in the fluid. In a turbulent fluid G can be estimated as $(\epsilon/\nu)^{1/2}$, where ϵ is TKE energy dissipation and ν is kinematic viscosity.

Differential Settling

Differential settling describes a process through which larger flocs settle faster than smaller flocs and flocculate as they come into contact vertically in the water column. This process of floc growth is therefore heavily dependent on the hydrodynamic regime of the surrounding fluid and settling velocities of flocs. As fluid shear decreases, the effects of fluid shear on particle collisions also decreases, thus differential settling will become the prevalent driver of particle collision and thus flocculation. This is most likely to occur in low energy regimes such as the open ocean as oppose to an estuarine environment; however periods of low energy do occur in the estuarine environment at slack water and low water..

Turbulent kinetic energy (TKE) and turbulent shear (Orthokinesis)

Orthokinesis describes flocculation forced by velocity gradients. Significant evidence presented in the literature suggests turbulence is one of the most significant mechanisms governing flocculation and therefore floc size (Lick et al, 1993; Winterwerp, 1998; Manning and Dyer, 1999; Ellis et al, 2004).

The early conceptual work of Dyer (1989) formed a comprehensive description of floc response to different levels of turbulence (Figure 2.8). Starting with low levels of turbulence floc diameters remain small and concentrations low, as turbulence intensity increases a peak floc diameter and concentration is reached (critical turbulence value), most likely

due to increased probability of collisions increasing the likelihood of aggregation. After the peak floc diameter is reached, the turbulence becomes too intense for larger macroflocs to withstand therefore they break down into smaller flocs, thus inducing a decline in floc diameter (Figure 2.8).

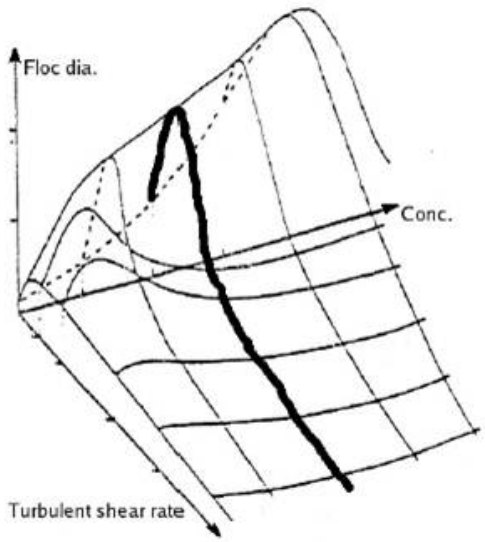

Figure 2.8: Conceptual diagram portraying the influence of turbulence on flocculation (Dyer, 1989), adapted from Thurston (2009).

Further study of turbulence and flocculation processes have concurred with Dyer's qualitative interpretation of the relationship between turbulence and flocculation (McCave, 1984; Eisma, 1986; Fugate and Friedrichs, 2002, 2003; Ellis et al, 2004; Jago et al, 2006). Turbulent motions have been shown to enhance flocculation through carrying particles within eddies which leads to collisions of particles and thus flocculation (van der Lee et al, 2009). Conversely, turbulent shear can cause flocculated particles or microflocs to be pulled apart thus causing de-flocculation (Winterwerp, 2002). In agreement with Dyer (1989), laboratory experiments reported by Dyer and Manning (1999) indicate high levels of shear can disrupt flocs at constant sediment concentrations whereas low levels enhance flocculation.

The literature appears to display a disparity in the effects of turbulent shear on macro and microflocs. Observations by Mikkelsen et al (2006) indicate that high stress leads to a marked decline in the volume of macroflocs whilst microfloc volumes increase. Conversely, when stress levels declined macrofloc volumes increased due to enhanced flocculation; however the settling velocity of macroflocs is higher than microflocs so they are deposited faster during less turbulent conditions. This study highlights the importance of floc size in the context of SPM dynamics as variations in diameter can alter the behaviour and fate of the floc.

Manning and Dyer (1999) reported that low shear coupled with increased turbidity encouraged flocculation, highlighting the possible significance of suspended sediment concentrations in the natural environment such as estuarine turbidity maxima and how variable levels of turbidity will affect floc diameters. Hill et al (2002) suggested that floc growth may actually be hindered by highly turbid waters indicating there may also be a critical sediment concentration. Furthermore, a critical level of turbulent shear ($0.35 Nm^{-2}$) coupled with high sediment concentrations was presented, identifying the level of shear required to disrupt flocculated particles (Manning and Dyer, 1999).

Maggi (2005) indicated that the turbulence regime a floc inhabits may dictate the shape as well as the size, for example near spherical flocs would be indicative of an environment undergoing high levels of turbulence shear such as an estuary. In the natural environment floc size is thought to ultimately limited by the Kolmogorov scale, as flocs larger than turbulent eddies are pulled apart in different directions (van der Lee et al, 2009; Braithwaite et al, 2012). Eisma (1986) also reported that turbulent shear dictates the maximum particle size in a body of water and that the size of the smallest turbulent eddie on the Kolmogorov scale is the same order of magnitude as the maximum floc size.

Taking the literature in to consideration this study aims to test the following hypothesis:

Hypothesis 4: *Floc size in the RETZ is governed by local turbulent conditions, the Kolomogorov microscale represents the upper limit for floc growth, modulated on a tidal*

temporal scale.

Further to this point, the relationship between Kolmogorov microscale and flocs size will be examined to test the concept of the eddy length scale calculated by the Kolmogorov microscale acting as an upper limit for floc growth.

2.3.5 Biogeochemical mechanisms of flocculation

Biogeochemical constituents that contribute to cohesive SPM in marine and freshwater environments can be defined by two major categories; living and non-living. Examples of live components are plankton microorganisms such as viruses, bacteria, fungi, phytoplankton and zooplankton species (Stramski et al, 2004). The non-living component consists of organic detritus, faecal pellets, polysaccharides, polymers and other waste products from aquatic organisms (Maggi, 2005).

The organic contribution to SPM in marine and freshwater environments and its role in SPM dynamics has been well documented within the literature. Kranck (1973) proposed that organic matter could be an 'important ingredient in the flocculation of inorganic sediment' due to observations of high organic composition of flocs sampled in the marine environment. These findings encouraged further studies into the influence of organic constituents on the behaviour of cohesive SPM.

Eisma (1986) inferred the importance of muco-polysaccharides (produced by bacteria, algae and plants of higher trophic levels) in the cohesion of suspended particles to form flocs. Dyer (1974) found that bacterial excreted mucus films and other organic components adsorbed from suspension in the water column promoted flocculation of suspended sediments. Manning and Dyer (1999) and Mikes et al (2004) both commented on the presence of organic components coating suspended particles with mucous filaments; observations showed that the 'physico-chemical bonds' binding the particles together were altered as a result. Furthermore, Dyer and Manning (1999) reported that in addition to electrostatic charges, mucal polysaccharides produced by bacteria contributed to the

flocculation of clay particles.

More recently Son and Hsu (2008) identified that flocculation is influenced by the biological and chemical properties of the water column as well as the hydrodynamic conditions. The effects of diatoms on flocculation behaviour of suspended sediments specifically have been investigated; for example Verney et al (2009) found increased concentrations of diatoms (caused by seasonal bloom) 'strongly' enhanced the rate of flocculation and potentially the efficiency due to their adhesive properties. This study consolidated previous hypothesises inferring the ability of diatoms to enhance floc growth. Alldrege et al (1995) presented evidence to suggest diatoms blooms increase the concentration of particulate organic carbon which in turn increased the number of macroflocs ($> 500\mu m$), through laboratory experiments simulating diatom blooms on a smaller scale than natural environments. Chen and Eisma (1995) also found higher concentrations of organic matter to accelerate floc growth through altering the structure and cohesiveness of suspended sediments. Further still Lunau et al (2006) provided evidence indicating that diatom blooms and bacterial concentrations promote floc growth. In addition to diatoms, dinoflagellates have also been linked to flocculation mechanisms (Jago and Jones, 2002; Jago et al, 2007).

Primarily as stated by (Weeks et al, 1993) the seasonal variation in SPM in coastal and estuarine environments is most likely to be influenced by the seasonal variation of organic concentrations in the water column. Phytoplankton blooms are modulated by the seasonal availability of nutrients, and increased concentrations of mucus produced by certain phytoplankton species enhance particle agglutination (Weeks et al., 1993). Ellis et al (2004) presented evidence to suggest that mean particle size and turbulence on the edge of a turbidity maximum in the Irish sea exhibit seasonal variation potentially in response to 'biological binding' occurring in summer, furthermore Jago et al (2007) identified the effects of biologically enhanced flocculation on size and settling velocity.

The biological impact on SPM does not end there as higher trophic organisms such as zooplankton can ingest SPM and excrete inorganic constituents in the form of faecal

pellets which has been found to increase post ingesting sedimentation (Krivtsov et al, 2001). Jones et al (1998) and Jago and Bull (2000) are in agreement with the concept of a positive biological influence on particle size during phytoplankton blooms in shelf seas; in addition the consequential modification of settling velocity is introduced. The settling flux of flocs with higher organic composition is smaller compared to inorganic flocs as the organic components contribute to a lower density (Jago and Bull, 2000).

2.4 Summary Points

- Turbulence is a random and highly non-linear phenomenon. Statistical analysis of fluctuations about the mean flow is the current method of estimating TKE dissipation. The Kolmogorov $-5/3$ power law identifies the inertial subrange including eddy length scale occurring under conditions in which turbulence is independent of viscous forces and solely dependent on dissipation.

- Velocity shear produced by frictional drag at the bed gives rise to the velocity profile shown in the bottom boundary layer. In macrotidal estuaries turbulence production is dominantly produced by strong tidal currents interacting with the bed. Under certain circumstances wind and wave action can also introduce mixing in estuaries from the surface.

- The ETM acts as a sediment trap. The position and concentration of the ETM is mainly influenced by river discharge and tidal currents. Thus the ETM plays a major role in determining SPM transport in estuaries. Tidal asymmetry occurs in estuaries due to the interplay of friction at the bed and the continuity of water mass. The asymmetry in tidal currents can present substantial consequence to SPM transport and associated bio-geochemical components.

- SPM is controlled by a cycle of physical processes including; erosion, resuspension, flocculation, transport, settling, deposition and bed consolidation. These processes are known to fluctuate on tidal, lunar and seasonal temporal scales.

- The majority of SPM in estuaries are found in the form of flocs. A multitude of physical and biogeochemical mechanisms control the behaviour of flocs (including flocculation, disaggregation, composition and settling velocity) which bears significant consequence to the transport of SPM, including substantial organic fractions from catchment to coast.

Chapter 3

Methodology

3.1 Introduction

This Chapter outlines the materials and methods employed; firstly the study area is considered, secondly the instrumentation deployed is introduced, along with analysis techniques. Finally the observational strategy is described.

3.2 Study site

The main study site is the Dyfi estuary, situated $10km$ north of Aberystwyth in Cardigan Bay on the west coast of mid-Wales, UK (Figure 3.1). Aberdyfi town, situated on the north bank of the estuary was built as a local trading port during the 19th century (Brown, 2007) and currently depends almost solely on tourism. For this reason improving the port facilities has been a top priority. Over the last 150 years significant changes to the estuary have been carried out; namely the use of flood banks to dampen the tidal influence and the drainage of low-lying areas.

The primary freshwater influence to this estuary is from Afon Dyfi, with a drainage area of $671km^2$. The Dyfi presents an annual average flow of $22.8m^3s^{-1}$, however this river also experiences a high frequency of flood events. River discharge data from the Dyfi Bridge

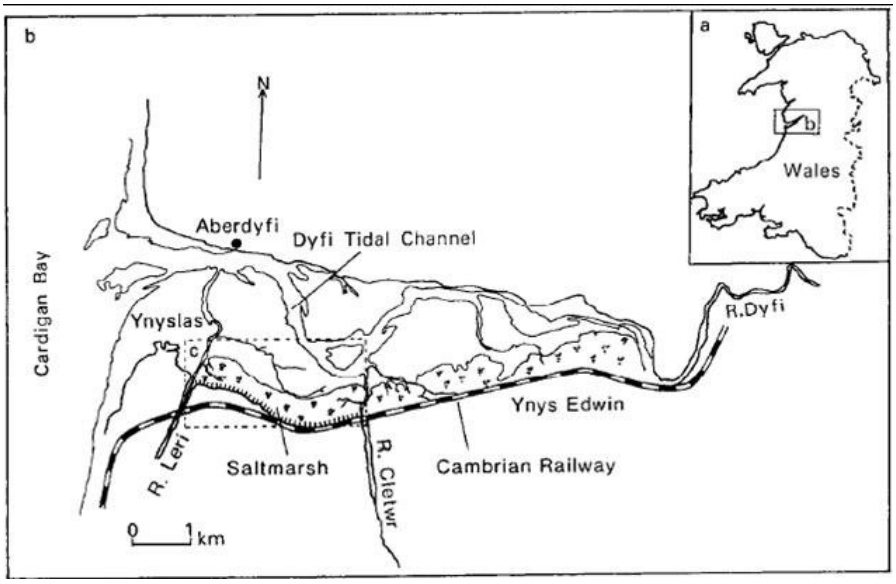

Figure 3.1: (a) The location of the study site in Wales; (b) Dyfi estuary including main geomorphological features. Taken from Shi et al (1995)

.

gauging station indicates bank full discharges have a recurrence interval of less than $1year$ and over bank floods of approximately $1year$. There are also two lesser contributors from the south of the estuary, the Afon Leri and the Afon Cletwr. The drainage area of the Dyfi is predominately underlain by Palaeozoic rocks (mainly including mudstones and shales) with Volcanic rocks outcropping in the north and west of the catchment area. The contemporary land use is dominated by sheep grazing on the valley sides and a mix of beef, diary and sheep farming on the valley floor. Furthermore, there is commercial forestry in the Dyfi forest towards the Northern extent of the catchment.

Figure 3.1 illustrates the triangular and converging shape of the estuary. At the southern extent of the mouth the Ynylas Spit extends where the Afon Leri joins the main channel and Aberdyfi town to the north. The RETZ extends to the Dyfi Junction (Figure 3.2) at which point the wide open sand flats bottle neck into a well defined meandering channel feeding into Afon Dyfi which is exposed at low tide and surrounded by low-lying grassy flood plains (Brown, 2007).

The Dyfi estuary covers an area of approximately $17.3km^2$ Shi (1991) and it is $8km$ in length. It is comprised mainly of open sand flats however, a significant muddy contribution to the estuary is seen along the southern extent, where low-lying saltmarshes can be found which lead onto the Borth Bog (Brown, 2007) seen in figure 3.2. The widest part of the estuary is at the mouth at $2.4km$ which then tapers to approximately $1.6km$ further upstream (Haynes and Dobson, 1969).

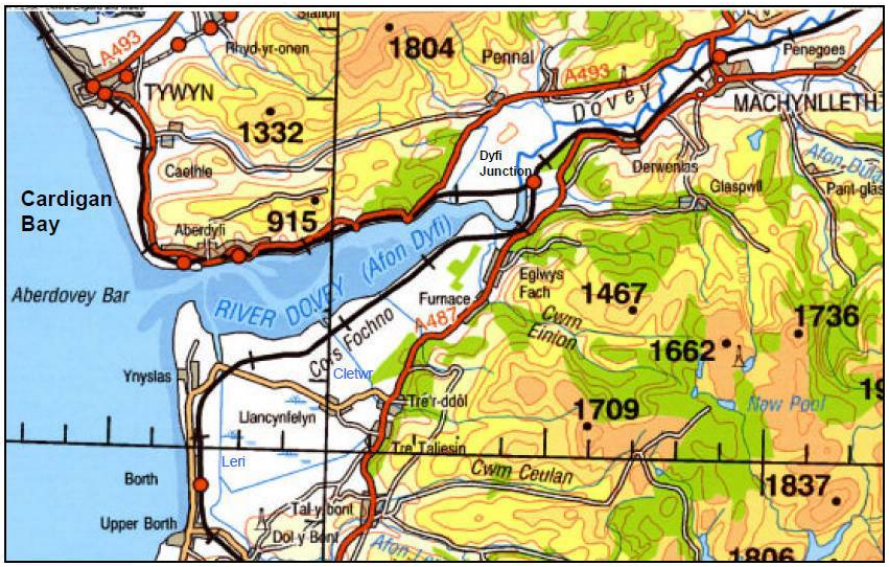

Figure 3.2: An OS map of the Dyfi Estuary.

The restriction at the mouth of the estuary results in an effective width at the mouth of the estuary as $0.8km$ (Haynes and Dobson, 1969). Due to this narrowing at the mouth the tidal flow is forced by the pressure gradient created by the difference in water height offshore and within the estuary (Brown, 2007), thus giving rise to the largest velocities in the estuary. As the estuary discharges directly onto the open coastline of Cardigan Bay long shore drift prohibits the formation of banks and channels; therefore the estuary mouth exhibits a restricted flood-ebb circulation (Haynes and Dobson, 1969).

The Dyfi is a macrotidal, tidally dominated estuary exhibiting a tidal range greater than $4m$ on spring tides (Haynes and Dobson, 1969), see Figure 3.3. Haynes and Dobson (1969) also reported the difference between extreme spring and neap tides as approximately

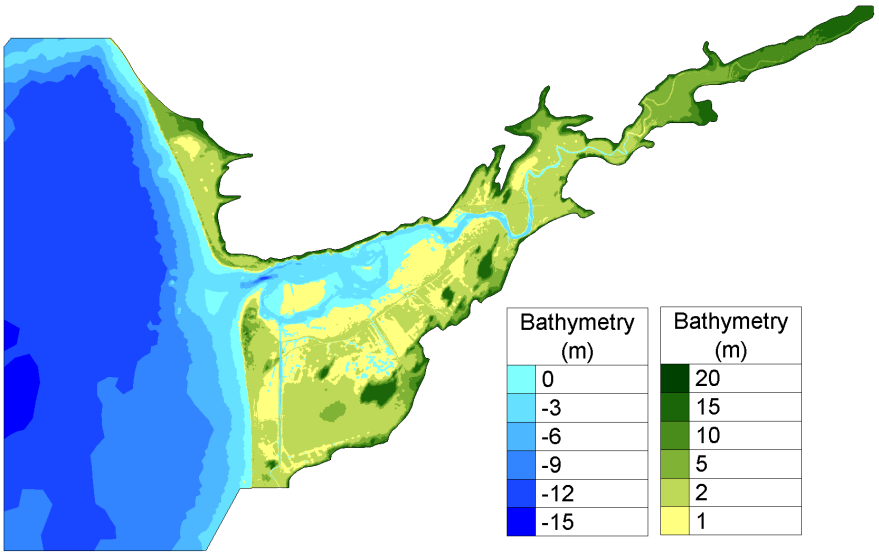

Figure 3.3: Bathymetry map of the Dyfi Estuary, adapted from (Robins, 2013).

2.13m. As mentioned previously, in addition to tidal domination the estuary exhibits a strong asymmetric tidal wave due to pronounced landward shallowing of Cardigan Bay, which leads to the occurrence of the mean spring high water in Aberdyfi in just 5$hours$ of the flood tide and the ebb duration is 7$hours$ (Brown and Davies, 2009). In many parts of the estuary peak tidal currents reach $50-61cms^{-1}$ (Brown, 2007). The combination of dominant tidal influence and the shallow nature of the Dyfi results in a well-mixed estuary where salinity stratification is not present (Jarvis, 1970). In addition to these factors, Prandle et al (2005) presents the main conditions required for a well-mixed temperate estuary in Table 3.1.

The Dyfi estuary fills the majority of the requirements in Table 3.1 therefore the development of gravitational circulation is inhibited. Moreover Prandle et al (2005) describes a criterion for determining the occurrence of a mixed estuary; $h/u^3 < 50s^3m^{-2}$ which is largely met in the Dyfi system. It is the local channel patterns that dictate the tidal movement (Jarvis, 1970). Due to a combination of the Coriolis force and northerly longshore current; an anticlockwise circulation occurs in the estuary (Brown and Davies, 2009). This has then led to a strong flow during the ebb phase of the tide past Aberdyfi

Table 3.1: Conditions for well-mixed estuaries at temperate latitudes. Taken from Prandle et al (2005)

	Range	Units
Tidal forcing, saline intrusion		
Tidal elevation	$1^{*} < \zeta < 4$	m
Tidal current amplitude	0.5<U<1.25	ms^{-1}
River flow	$0.25 < Q^{\dagger} < 3000^{\ddagger}$	m^3s^{-1}
Associated current	$0.001 < U_o^{\S} < 0.01$	ms^{-1}
Flushing time	$1 < t_F < 15$	days
Bathymetry		
Depth at the mouth	$1^{**} < D < 20^{\ddagger}$	m
Tidal intrusion length	$2.5^{**} < L < 100^{\ddagger}$	km
Age	100<Y<15000	years
Sediment regime		
Suspended Concentrations	$200 < C^{\dagger\dagger} < 750$	mgl^{-1}
Fall velocity	$0.5 < w_s^{\ddagger\ddagger} < 5$	mms^{-1}

* for 'mixed' estuaries
† implications for spacing between estuaries
‡ for mixing within the estuary
§ in the saline intrusion zone
** for continuous functioning over the tidal cycle
†† assuming 'unlimited supply'
‡‡ via flocs

town and encourages the flow during the flood in a southern channel along the south side of the mouth (Brown, 2007). Asymmetry in the maximum flow and duration can lead to significant variations in the net transport of suspended sediments.

The study site extends beyond the general estuarine domain and into the tidal river. The tidal river is modulated by the tide; however there is no salt water intrusion during the flood. The tidal river extends beyond the Dyfi junction and the maximum upstream extent is dependent on the lunar and seasonal variations in the amplitude of the tide.

The RETZ is a difficult environment to work in logistically due to its dynamic nature. Key parameters are changing on short spatial and temporal scales, resulting in large

temporal and spatial gradients. In order to combat this problem *in situ* measurements of both the hydrodynamic properties and particle properties have been made over varying temporal and spatial scales, appropriate to the changes expected in both floc size and local turbulent conditions. In addition to small scale changes the dynamic nature of the estuaries can also result in larger scale modulations such as changes to geometric shape, location and dimensions of approach channels, thus interfering with land run-off and the propagation of the tidal wave into the estuary. In the Dyfi estuary, the Ynylas Spit is an example for restriction of the tidal wave. It is therefore imperative to strive to develop our understanding of the transfer flux of suspended sediments from catchment to coast, as this is a dominant factor in the estuarine regime.

3.3 Optical Instrumentation

Optical instruments have been successfully implemented in studying sediment dynamics for multiple decades (Bale and Morris, 1987; Eisma and Kalf, 1996; Bunt et al, 1999). Since the earliest reported use of light transmission by Jones and Wills (1956), significant advances have been made in this field. Most notably the technological advances in optical instrumentation has involved *in situ* measurement of suspended sediments. *In situ* measurement is essential when sampling floc properties due to the fragility of flocs. In addition the inconsistency of flocculation and de-flocculation processes requires high resolution *in situ* measurements to quantify accurately the modulations in particle size and concentration over varying temporal scales.

This study utilises two types of optical instrumentation to describe estuarine SPM characteristics. Firstly, transmissometers were employed which use light attenuation to obtain SPM concentrations (Bartz et al, 1985). Secondly, the more sophisticated instrument is the Laser *In Situ* Scattering Transmissometry (LISST-100) particle sizer, which uses laser diffraction to obtain not only SPM concentrations but also particle size distributions (PSD) (Bale and Morris, 1987; Agrawal and Pottsmith, 2000).

3.3.1 Laser *in situ* Scattering Transmissometry particle sizer

The LISST-100 particle sizer was employed to measure volume concentration (C_v) in $\mu l l^{-1}$ of suspended sediments and particle size distributions in μm throughout the RETZ on varying temporal scales. It is able to resolve particles in suspension ranging from $2.5 - 500 \mu m$. Agrawal and Pottsmith (2000) introduced the LISST-100; this instrument has since been used extensively to study cohesive and non-cohesive SPM in estuarine and coastal environments (Agrawal and Pottsmith, 1994; Traykovski et al, 1999; Bolanos et al, 2009; Braithwaite et al, 2012).

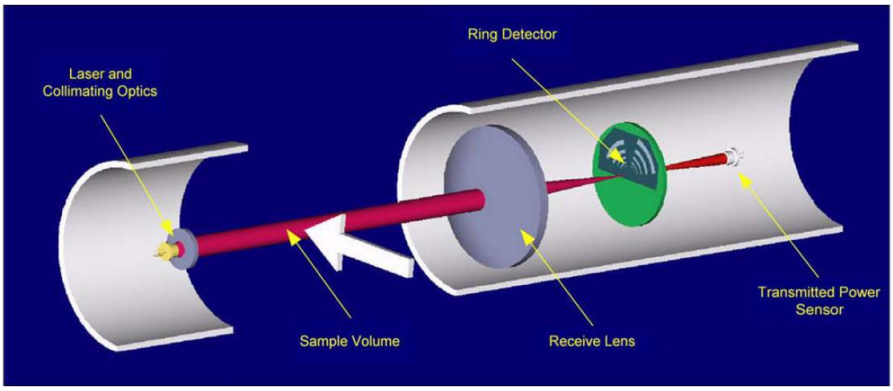

Figure 3.4: A schematic of LISST-100 optic formation. Taken from Sequoia Scientific (2012)

.

Laser diffraction, employed by the LISST-100, requires the measurement of the forward light scattering pattern from a particle in suspension. At small forward angles, the diffraction of light dominates the measured scattering signal, therefore the refractive index of a particle is insignificant. This means the LISST-100 can be used to measure a variety of compounds found in suspension. The instrument configuration involves a collimated laser beam with a width of $6mm$ which penetrates the sample volume and onto a receiving lens. The light scattering intensity measurement is acquired from a set of 32 concentric ring detectors as shown in Figure 3.4. The concentric rings are set to measure diffracted energy over a range of angles from $0.05 - 0.5°$. The dimensions of each ring detector are set logarithmically, each inner and outer ring radii increasing at a fixed

ratio. Each ring is associated with a scattering angle, which gives rise to a size class in the PSD. Smaller particles relate to larger forward scattering angles; they are detected by larger rings and vice versa. A positive linear correlation is assumed between the number of particles and the scattering intensity. This relationship allows the distribution of light intensity recorded by the LISST-100 to be related to both particle size and volume concentration (C_v) of particles in suspension. In addition, a hole at the centre of the ring detector allows a photo diode to measure the transmitted power of the laser and thus the beam attenuation.

Mie Theory is employed to determine the relationship between light intensity, scattering angles and particle size by predicting the light intensity expected to be recorded by each of the 32 ring detectors. The scattering measured over the predetermined angle range is inverted using the kernel matrix ($\mathbf{K}$) introduced by Agrawal et al (2008), to predict the size distribution of particles produced by the measured scattering. The kernel matrix provides information concerning the scattering signatures of a collection of randomly shaped particles.

The volume size distribution C_{vD} is obtained through matrix inversion as follows:

$$C_{vD} = \mathbf{K}^{-1}E \tag{3.1}$$

The sum of C_{vD} gives rise to the total volume concentration C_v and can be used to calculate parameters such as median particle size D_{50}.

Finally, the total scattering intensity measured by the LISST-100 encompasses scattering from both the water and the particles in suspension (*cscat*), therefore a correction to the total scattering must be applied to calculate the scattering due to particles in suspension alone (*scat*). In order to do so a background measurement of scattering in distilled water (*zscat*) and the attenuation (C) is carried out before the LISST-100 is deployed for experimental use. With this information a correction can be applied to the total scattering value taking into account the areas of each ring detector (*dcal*) previously

described by Davies (2013).

$$cscat = (\frac{scat}{C} - zscat)dcal \tag{3.2}$$

Limitations of LISST-100

The LISST-100, manufactured by Sequoia Scientific inc. is employed extensively throughout this study examining the relationship between particle size (including flocs from the estuarine environment) with local turbulent conditions therefore; it is important to consider the limitations of the LISST-100 described in peer-reviewed literature.

The main limitation associated with the LISST-100 converting small angle forward scattering measurements into volume concentrations of particle size distributions is the requirement to assume all particles are spherical. This is of particular importance when dealing with marine particles composed of complex structures such as flocs, phytoplankton and zooplankton. For example Baker and Lavelle (1984) reported a significant underestimation of observed attenuation through the calculation of attenuation from the scattering signature of spherical particles. This is mostly due to the optical diameter of particles found in the natural environment not coinciding with the volume of their associated volume equivalent spheres. Agrawal et al (2008) went some way to address this issue by incorporating the Kernal matrix into the inversion process which includes empirical measurements of the scattering properties of randomly shaped particles.

Multiple scattering has also been identified within the literature as a limitation when converting scattering signals into volume concentration and particle size (Baker and Lavelle, 1984; Moody et al, 1987). Multiple scattering occurs when a collection or cluster of particles create scattering signals that differ to the scattering signal that would be produced from the particles if they were not a component of the cluster. The LISST-100 relies on the linear relationship observed between the attenuation of light and particle concentration, however Moody et al (1987) presented observations indicating the linearity of the relationship is affected by multiple scattering and the temporal scale in which

particle size and concentration changes.

Karp-boss et al (2007) describes a specific case in which the composition of a particle does bear significant relevance when using the LISST-100, despite Agrawal and Pottsmith (2000) stating refractive index is not relevant for particles larger than a few microns. The sub-components of a copepod gave rise to three different peaks in concentration for three separate size classes. This is important to consider when using the LISST-100 during a period of high biological activity.

Finally, steep density gradients have presented a restriction on the accuracy of LISST-100 particle size analysis (Styles, 2006), due to fluctuations in density gradients interfering with the index of refraction, a process called schlieren. Mikkelsen et al (2008) presented LISST-100 beam attenuation and scattering measurements which exhibit the affects of schlieren, which ultimately result in an over-estimation of particle size. Schlieren could present as issue when using the LISST-100 in the estuarine environment, therefore spikes in particle size coinciding with steep density gradients should be treated with caution.

3.3.2 Transmissometer

The transmissometer used in this study is manufactured by Sea Tech inc. it is designed to acquire accurate *in situ* measurements of beam transmission and attenuation. Beam attenuation can be calibrated by gravimetric sampling to acquire mass concentration (C_m) of suspended particulate matter in the water column. Beam transmission is measured in a $25cm$ water path using a modulated Light Emitting Diode (LED) and a synchronous detector. The optical design includes a collimated LED transmitter with an associated beam divergence of greater than 3 millirads, the optical receiver acceptance angle is greater than 18 millirads in water, which acts to minimise errors incurred by scattered light in the water column.

Optical theory of Transmissometer

Absorption and scattering are the two fundamental processes which determine the distribution of light in the water column. Absorption has the capacity to transfer light into different forms of energy, whereas scattering conserves the light energy, but changes the direction in which it was travelling. In a body of water where only absorption occurs, the loss of light due to absorption in a collimated beam of monochromatic light is expressed as:

$$I(z) = I(o)e^{(-az)} \tag{3.3}$$

where $a(m^{-1})$ is the absorption coefficient. Moreover, in a body of water in which only scattering of light can occur, the light scattered from a collimated beam of monochromatic light is described as:

$$I(z) = I(o)e^{(-bz)} \tag{3.4}$$

where $b(m^{-1})$ is the volume scattering coefficient. The beam attenuation coefficient (c) is thus the sum of absorption and scattering. Therefore, the percentage light transmitted (T) over a vertical distance can be written as:

$$T(z) = e^{(-cz)} \tag{3.5}$$

The transmission distance can be calculated from the natural log of the percentage transmission over the path length of the instrument. It is important to note that this exponential relationship only stands if the light is monochromatic, therefore the transmissometer utilises an LED which is as close to monochromatic as possible that adopts a wavelength in the red section of the light spectrum of $670nm$. By adopting this wavelength the presence of dissolved materials in the water does not influence the results as they absorb strongly in the blue part of the spectrum. So at $670nm$ the attenuation of light is a result of SPM and seawater only.

The light scattering properties of an individual particle depend on its shape, size and internal index of refraction distribution, which typically vary spatially and temporally, therefore a calibration of SPM concentration is required for each location and time of

optical sampling. The beam attenuation acquired can be converted into SPM concentration as the relationship is linear. A calibration coefficient will be calculated for each field campaign in order to convert beam attenuation into SPM concentration using gravimetrically sampled SPM concentrations collected quasi-simultaneously with transmissometer profiles.

3.3.3 Fluorometer

The biological content of the water column is known to enhance the process of flocculation in the estuarine environment (Jones et al (1998) and Liss et al (2004)), therefore flurometers were adopted to determine chlorophyll *a* concentrations. When chlorophyll is irradiated with light of a specific wavelength it emits light of a higher wavelength. Using this principle fluorometers measure chlorophyll *a* concentrations by emitting a light beam in the blue wavelength spectrum and measures the light emitted back (at a higher wavelength in the red spectrum) from chlorophyll in the water column.

The fluorescence data acquired requires calibration by *in situ* water samples which were filtered (using Whatman GF/F filters). The chlorophyll was extracted in the laboratory using acetone and the fluorescence was measured (Holm-Hansen and Riemann, 1978; Jones et al, 1998).

3.4 Acoustic Instrumentation

During this study Acoustic Doppler Current Profilers (ADCPs) are used to estimate current velocities and TKE dissipation using the structure function method (Wiles et al, 2006). Acoustic Doppler velocimeters (ADVs) are used to measure point measurements of current velocity and TKE dissipation values near to the bed.

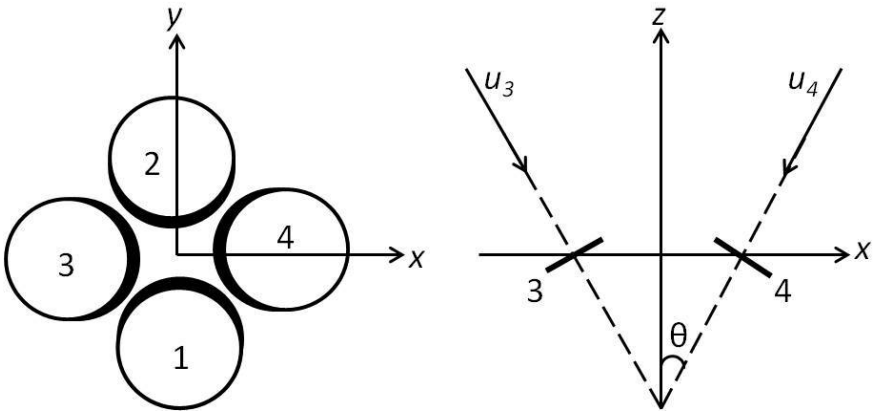

Figure 3.5: The Janus configuration of the ADCP transducer heads in plan and profile view. Adapted from Thurston (2009)

3.4.1 Acoustic Doppler Current Profiler

Typically an ADCP consists of three or four transducers at an angle of $20 - 30°$ from the vertical. The transducers emit sound pulses also known as pings. For each ping released into the water column, a certain portion of the scattered signal is reflected back to the transducer which receives the signal. The Doppler shift of the received signal frequency then determines the along beam velocity component of the water column. It is important to note that this method relies on the scattering agents (suspended sediments,phytoplankton and zooplankton) in suspension to be moving at the same rate on average as the surrounded fluid. In addition to this horizontally homogeneous flow is assumed, this is a fair assumption for an estuarine environment where a rectilinear flow is common.

In the Janus configuration (Figure 3.5) the along beam velocities are u_1, u_2, u_3, u_4 and the Cartesian velocities u, v, w. As shown in Figure 3.5 the two beam transducers three and four are in the xz-plane, therefore one and two are in the yz-plane (Thurston, 2009). The velocity measurements obtained from along the beam are simply the sum of the

horizontal and vertical velocities in that plane, they can be described as:

$$xz - plane: \quad u_3 = u\sin\theta + w\cos\theta \quad u_4 = -u\sin\theta + w\cos\theta \tag{3.6}$$

$$yz - plane: \quad u_1 = v\sin\theta + w\cos\theta \quad u_2 = -v\sin\theta + w\cos\theta \tag{3.7}$$

So it is possible to calculate the horizontal velocities by substracting along beam pair in the Equations 3.7 above, which gives rise to:

$$u = \frac{u_3 - u_4}{2\sin\theta} \quad v = \frac{u_1 - u_2}{2\sin\theta} \tag{3.8}$$

As shown in Figure 3.5 when four beams are used to measure three velocity components (x, y, z) an extra vertical velocity value is acquired from the sum of the along beam pairs:

$$w_x = \frac{u_3 + u_4}{2\cos\theta} \quad w_y = \frac{u_1 + u_2}{2\cos\theta} \tag{3.9}$$

Interestingly the difference between the two vertical velocity values acts as a type of error velocity; it can be used to indicate whether the assumption of horizontal homogeneity of the flow is in fact a fair assumption (Thurston, 2009).

The velocity profiles obtained by bed-mounted ADCPs were measured over bins or cells which were evenly spaced throughout the water column, with the distance intervals of $10cm$. A pulse is emitted from one of the transducers and the range of the scattered signal is then determined from the time taken for the pulse to return, the velocity calculated is then assigned to the cell it came from. The velocity measurements were then averaged over 12 *minutes*.

The structure function method allows the estimation of TKE dissipation rate from velocity data acquired from ADCP instruments. Wiles et al (2006) first presented this method which was adapted from radar meteorology. The method utilises the turbulent cascade theory of Kolmogorov to relate spatial correlations of velocity to TKE dissipation rate (Wiles et al, 2006). The second order structure function $D(z, r)$ can be defined at location z using the difference of the mean square of the velocity variance (v') between

two points at distance r.

$$D(z,r) = \overline{(v'(z) - v'(z+r))^2} \tag{3.10}$$

Wiles et al (2006) indicates the difference in variance velocities between two separate points shown in Equation 3.10 is mostly due to eddies with a length scale of a similar size to the distance between the two points (r) and an associated velocity scale (s') which is thereby a function of r and z:

$$D(r,z) \sim s' \tag{3.11}$$

Wiles et al (2006) state if an eddy is defined by a velocity scale s' and length scale r the kinetic energy of the eddy is proportional to s'^2. Moreover, if the eddy transfers the majority of its energy throughout a given number of overturns, r/s will then be proportional to that particular time scale. This indicates as per the Taylor cascade theory (Taylor, 1935) that the transfer rate of energy through the scale of eddies and thus into viscous dissipation is given by Equation 3.12, previously described by Gargett (1999).

$$\epsilon = \frac{s'^2}{r/s'} = \frac{s'^3}{r} \tag{3.12}$$

The structure function can then be presented as a combination of Equation 3.11 and Equation 3.12, which portrays the profile of velocity variances as a function of the dissipation rate and the spread of the beam.

$$D(z,r) = C_v^2 \epsilon^{2/3} r^{2/3} \tag{3.13}$$

C_v^2 is a constant taken from atmospheric studies as a value between 2.0 and 2.2 (Sauvageot, 1992). Wiles et al (2006) commented that Equation 3.13 will hold for values of r within the inertial sub-range, which means it is valid for eddy scales larger than the dissipation scale but smaller than the largest vertical eddies determined by the Ozmidov scale. The limit of the dissipation scale is not an issue due to the limitation of the ADCP instrument resolution; however the larger end of the scale must be acknowledged particularly at surface and bottom boundaries and in stratified flows where the Ozmidov scale presents the limitation.

3.4.2 Acoustic Doppler Velocimeter

The acoustic Doppler velocimeter (ADV) first introduced by Kraus et al (1994) provides a point measurement of the three dimensional velocity field. Figure 3.6 presents a schematic of a typical ADV configuration.

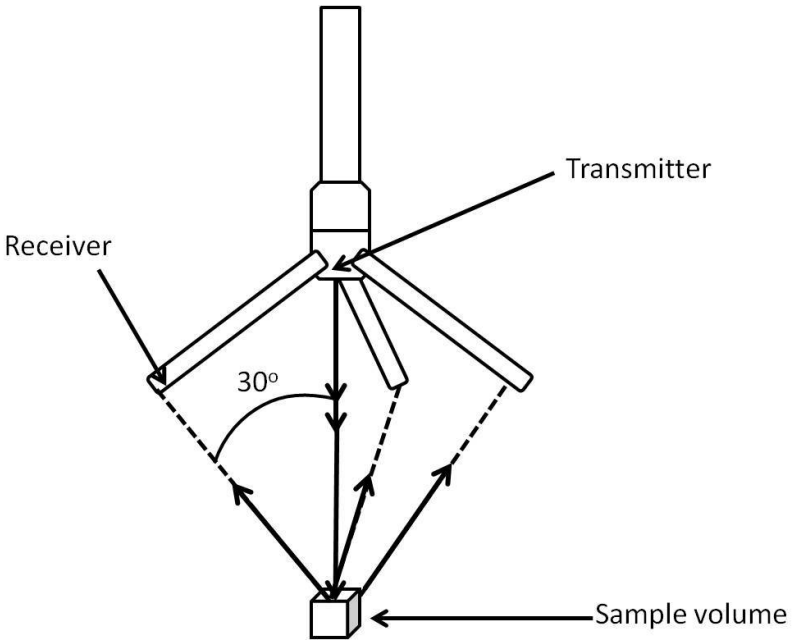

Figure 3.6: Schematic of ADV configuration. Adapted from Voulgaris and Trowbridge (1998)

Similar to the ADCP discussed previously, the operation of this instrument is based around the Doppler shift effect. It is implemented as a static instrument and consists of one transmitter and three receivers (Figure 3.6). The receivers are positioned in 120° increments around the transmitter and 30° from the axis of the transducer. All three receivers focus on one common sample volume, the dimensions of which are determined by the length of the transmitted pluses, width of the receiving window and the beam pattern of the received and transmitted pulses (Voulgaris and Trowbridge, 1998).

The system operates by transmitting short acoustic pulses along the transmit beam. As the pulses propagate through the water column a fraction of the acoustic energy is scat-

tered back to the receivers by suspended particles or zooplankon. The phase difference ($d\phi/dt$) between successive returning acoustic energy are converted into velocity estimates by using a pulse pair processing technique (Miller and Rochwarger, 1972). The phase data are then converted to speed values via the Doppler relation (Equation 3.14).

$$U = \frac{cd\phi/dt}{4\pi f} \tag{3.14}$$

Where f is the operating frequency of the ADV (10MHz), ϕ is the signal phase in radians, t is time and c is the speed of sound in water. Further details regarding phase data conversions can be found in Voulgaris and Trowbridge (1998).

ADV data is of sufficient resolution to calculate TKE dissipation rates via the inertial dissipation method. This method requires only one ADV above the bed at a specified height. The theory requires the existence of an inertial sub-range which requires a high local Reynolds number (Dewey et al, 1988).

The inertial dissipation method is based on the relationship between TKE dissipation and wave number in the inertial sub-range, where the flux of energy from low to high wave numbers is balanced by the dissipation rate (Xu et al, 1994), assuming there are no local energy sources or sinks. The TKE energy spectrum ($E(k)$) a function of wave number K and dissipation rate ϵ as show below:

$$E(k) = \alpha_k \epsilon^{2/3} k^{-5/3} \tag{3.15}$$

Equation 3.15 presents the Kolmogorov -5/3 power law, where α_k is the Kolmogorov constant (ca. 0.55). A three dimensional velocity spectrum is not often measured directly, however it can be obtained from the spectra of a single velocity component if isotrophy is assumed. This is a fair assumption to draw in an estuarine environment. Two further assumptions are made, firstly a local balance is assumed between production and dissipation of TKE and secondly that measurements are obtained in a section of the water column experiencing constant shear stress (Xu et al, 1994). From plotting the power

spectral density against wave number the inertial sub-range can be identified, the section of the plot which adheres to the -5/3 law and ϵ can be calculated.

3.5 Calibration Methods

3.5.1 Transmissometer calibration

Optical instruments such as transmissometers are routinely used to measure SPM concentrations. In order to accurately convert the raw output of total beam attenuation into engineering units of SPM, gravimetric analysis of *in situ* water samples is needed. $1l$ surface (less than $1m$) water samples were collected throughout the profiling period with the transmissometer and transported to be filtered on land. Before filtering the sample bottle was shaken thoroughly to obtain homogeneity. $500ml$ was filtered through a pretreated glass microfibre filter with a pore size of $0.7\mu m$ paper of a known weight (g).

(a) (b)

Figure 3.7: Examples of (a) water samples collected and (b) post-processed SPM filter papers

Depending on the turbidity of the water sampled the colouring of each filter paper varies, exemplified in Figure 3.7. Filter papers were pretreated by washing with $500ml$ distilled water and dried at $80°C$ for $12hours$. After the sample has filtered through the filter, the filter was rinsed with $200ml$ of distilled water to negate the influence of salt on the resultant weight of the filter paper. Each sample was then frozen before being transported

back to the lab. Frozen samples were thawed and dried in an oven at $80°C$ for a minimum of $12hours$. Once removed from the drying oven, filters were placed in a desiccator for a minimum of $2hours$ and re-weighed. The difference between recorded weights is the dry weight of sediment in suspension for each water sample. As a control every 10 samples a blank filter paper was processed though the same method outlined above. Processing blank filter papers quantifies the influence of the method on the weight of the filter paper, the changes in weight of these blank filter papers were subtracted from each sample dry weight, thus accounting for the error in the method.

The average beam attenuation at the surface layer of the water column (less than $1m$) was regressed against the gravimetrically determined mass concentrations for each field work campaign (Figure 3.8). The relationship between beam attenuation and mass concentration is shown in Equation 3.16:

$$C_m = mC + c \tag{3.16}$$

Where C_m is mass concentration, C is beam attenuation measured in (m^{-1}) and m and c are both constants.

Critical values of significant correlation coefficients (R^2 values) were determined using methods from Sokal and Rohlf (1995), in which degrees of freedom (number of data points minus 2) were used to assign 95% and 99% confidence intervals, thus relating the significance of a correlation to the number of data points employed in the statistical analysis. An indexing system implemented throughout results is as follows:

$$R^2(CI = 95\%) = R^{2*}$$
$$R^2(CI = 99\%) = R^{2**}$$

CI denotes the Confidence interval; therefore, an R^2 values associated with ** represent a correlation that has a 99% chance of reproducing the same result if the experiment was repeated, and * denotes a 95% chance of repeating the same result. Any correlations that do not satisfy either of these limits were deemed insignificant.

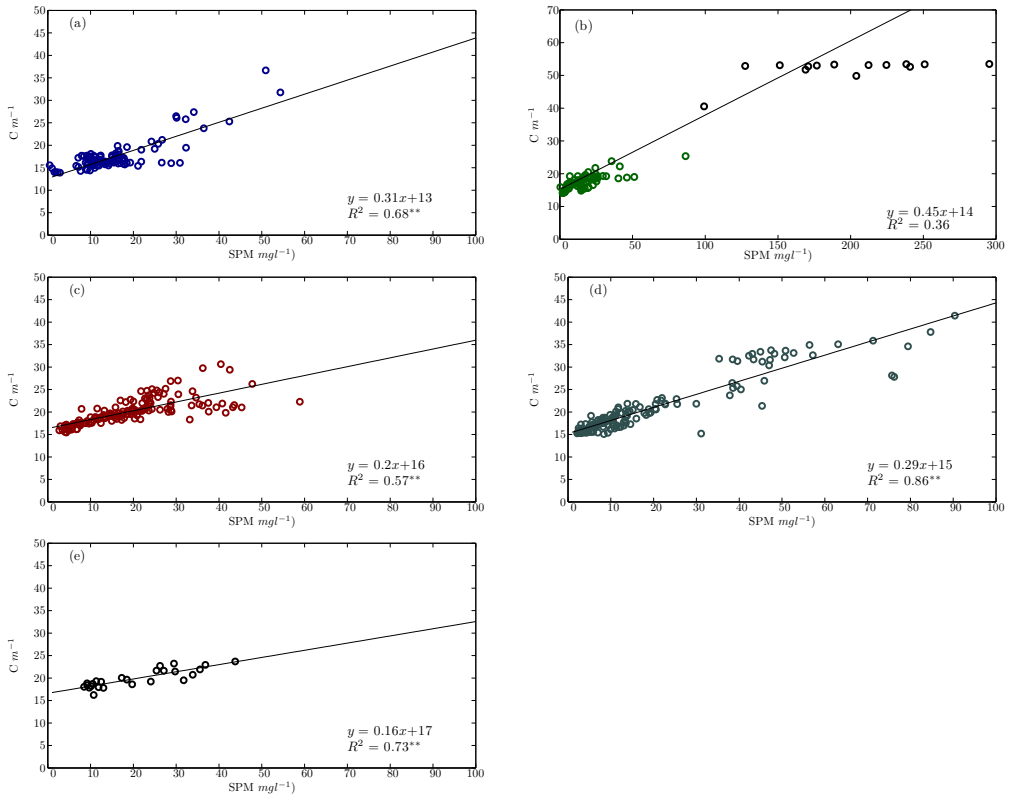

Figure 3.8: Calibration of beam attenuation (C) using gravimetric SPM samples (C_m). (a) April 2010 field campaign (b) September 2010 field campaign, black markers = samples in freshwater (PSU < 1) (c) March 2011 field campaign (d) July 2011 field campaign and (e) November 2011 field campaign.

The intercept and gradient of the calibration curves for each field campaign were similar and the correlation between beam attenuation and mass concentration was statistically significant in each case (Figure 3.8). The September calibration presents the weakest correlation due to significant variations in river flow rate (Q), during the sampling period a minor and major river flood event occurred significantly affecting SPM concentrations. The black markers on Figure 3.8b denote the samples made during the river events; the river flow increased over 10 fold and salinity values did not exceed 1. Furthermore Figure 3.8b also indicates the transmissometer reached saturation during the river events as the black markers remained around $50 - 60m^{-1}$ despite rising values of C_m. For this reason these points were not included in the calibration.

Calibrations across all field campaigns regressed together gives rise to a significant correlation as seen in Figure 3.9. Higher R^2 were observed when field campaigns were treated separately, thus individual calibrations were implemented.

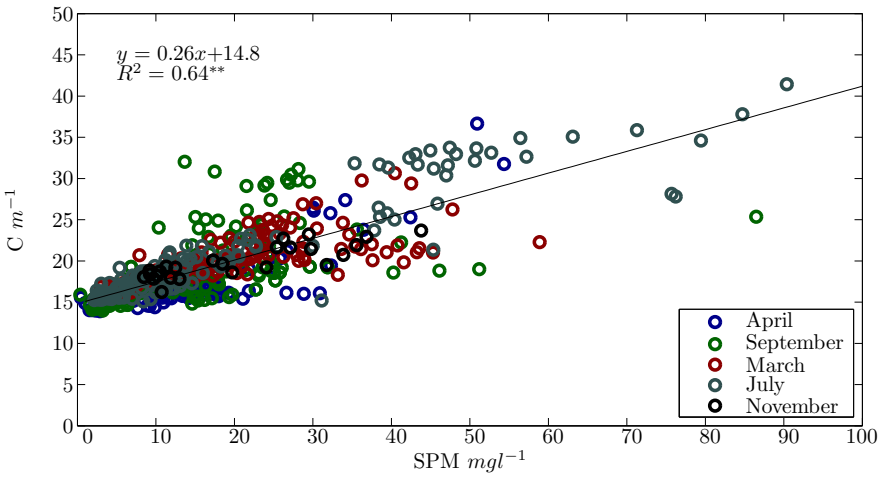

Figure 3.9: Calibration of beam attenuation (C) using gravimetric SPM samples (C_m) from all field campaigns.

In addition to linear regression analysis of beam attenuation and mass concentration determined from gravimetric analysis for instrument calibration, multiple regression analysis was explored. Due to the impact of biological composition of suspended particles on beam attenuation, chlorophyll measurements were also used to calibrate the transmissometer via multiple regression analysis shown in Equation 3.17 below:

$$C_m = aC + bChl_a + c \tag{3.17}$$

Where a, b and c are constants and Chl_a is chlorophyll concentration. Incorporating chlorophyll into the transmissometer calibration method did not significantly improve the calibration (Table 3.2), therefore mass concentration alone was used.

Table 3.2 presents a comparison of the R^2 values of a simple linear regression using mass concentration (SPM) and multiple regression incorporating mass concentration and chlorophyll respectively.

Table 3.2: Comparison of R^2 values for transmissometer calibration methods

Month	SPM	$SPM + Chl$
April	0.68	0.69
September	0.36	0.36
March	0.57	0.56
July	0.86	0.87
November	0.73	0.73

3.5.2 Fluorometer calibration

Chlorophyll a concentrations of surface water are measured in order to calibrate the self-contained underwater fluorescence apparatus (SCUFA) used along side the transmissometer in addition to contributing to the transmissometer calibration.

Water samples for chlorophyll analysis were collected in $1l$ bottles and stored in a cool dark environment before filtering. $250ml$ of water sample was filtered through a GF/F filter paper and rinsed with pre-filtered seawater after the sample filtered through. The filer paper was rolled into a tube covered in foil to avoid light contamination and frozen. Frozen samples were transported to the lab and thaw soaked in $10ml$ of 90% acetone for $16 - 18hours$. The liquid left in the tube was decanted into a fused quartz cuvette and processed in the table top 10-AU fluorometer to ascertain the chlorophyll a concentration in μgl^{-1}. Blank samples of acetone were processed and subtracted from each concentration.

3.6 Observational Strategy

Five field work campaigns were undertaken between April 2010 and November 2011, each two weeks in length. Field campaigns were carried out in April, September, March, July and November. Each campaign involved four sub-campaigns:

- Spatial surveys

- RETZ anchor station
- Estuary mouth anchor station
- Mooring deployment
- River survey

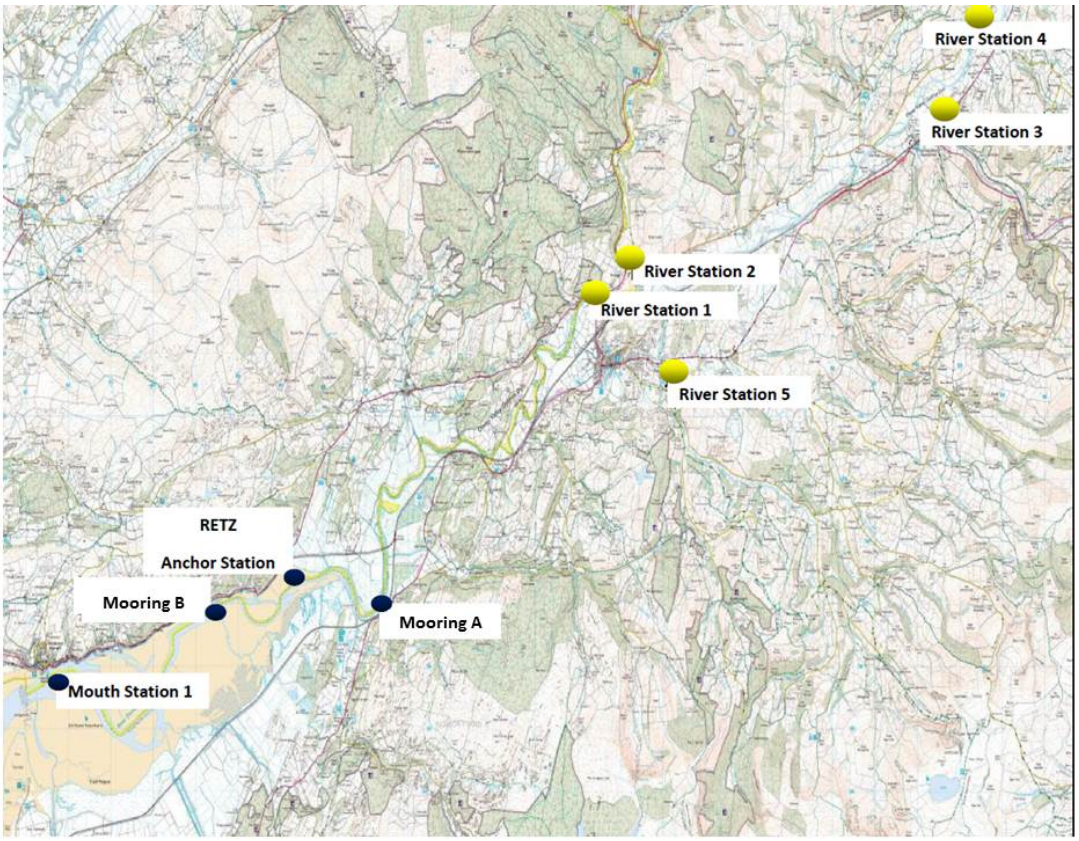

Figure 3.10: OS map of field work site showing the locations of river stations, RETZ anchor station, mooring deployments and the estuary mouth anchor station.

3.6.1 Spatial surveys

During high water longitudinal spatial surveys were undertaken from the mouth of the estuary to the landward limit of salt water intrusion. Spatial surveys were carried out on spring and neap tides. A quasi-simultaneous profile with the LISST-100 and CTD were

carried out at each station along with a $1l$ water sample to calibrate the transmissometer (Figure 3.11a). Figure 3.11a shows the instrumentation used for profiling the water column.

(a) (b)

Figure 3.11: (a)Picture of LISST-100 and CTD including transmissometer and fluorometer in profiling frameworks. (b) Picture of two boats used for surveying: Macoma (yellow catamaran) used for fixed station profiling and the aluminium rib used for spatial surveys.

3.6.2 River Estuary Transition Zone anchor station

The RETZ survey entailed profiling with the LISST-100 and CTD frame work at a fixed position within the RETZ every $15minutes$ over a $6hour$ period during spring and neap tidal cycles. A $1l$ water sample was also taken every $30minutes$ to calibrate the transmissometer and fluorometer. Due to the RETZ drying out during low water at this location it was not logistically possible to obtain profiling data throughout an entire tidal cycle. Figure 3.11b shows the boat moored in the RETZ and the instrument profiling configurations including the LISST-100, transmissometer, fluorometer and CTD.

3.6.3 Estuary mouth anchor station

At the end of each field work campaign the Macoma was relocated to the mouth of the estuary. The same $6hour$ survey as in the RETZ was undertaken including the quasi-simultaneous profiling of LISST-100 and CTD frame works and water sample collection.

3.6.4 Mooring deployment

At the beginning of each field work campaign two bed-mounted moorings were positioned within the RETZ, Mooring A (52.5527 N 3.9332 W) and Mooring B (52.5577 N 3.9661 W) . Moorings were retrieved approximately 14*days* later. The positions for the moorings are shown on Figure 3.10 by blue markers.

(a) Upstream

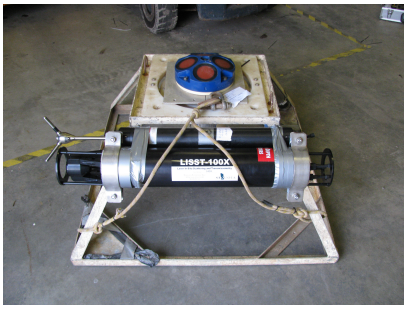

(b) Downstream

(c) Trial mooring

Figure 3.12: (a)Picture of Upstream (tidal river)mooring including ADCP, ADV, LISST-100 and CTD. (b) Picture of Downstream (RETZ) mooring with same instruments as above. (c) Mooring configuration used in March and July for the Upstream mooring including 3 x ADV and 1 x LISST-100

For the first two field work campaigns in April and September 2010 a simpler version of the mooring set up shown in Figure 3.12 without an ADV was employed. As the field work campaigns progressed the mooring set up was modified. For the deployments in March and July 2011, the upstream mooring was completely reconfigured as in Figure 3.12c with three ADVs situated in two horizontal planes and one in the vertical. This configuration permitted the measurement of the bottom boundary layer. However the

dimensions of this mooring made it unstable at high velocities during the flood so the original configuration was adopted for the last campaign in November 2011. Due to the blanking range of the ADCP exceeding the water surface height during low water an ADV was incorporated to the mooring configurations in November to obtain a point measurement of velocity and TKE dissipation where the LISST-100 was sampling.

3.6.5 River survey

Five tributaries were selected to encompass the drainage pattern of the Dyfi system. The river survey stations are indicated by the yellow markers in Figure 3.10. Each station was sampled once during each of the two week sampling periods. The LISST-100 and CTD frame work were deployed and an associated water sample collected.

3.6.6 Summary Points

- The Dyfi estuary is a relatively short, tidally dominated, shallow and well mixed estuary. The primary source of fresh water input is the Afon Dyfi, which exhibits frequent river events. The estuary is comprised of mudflats and extensive salt-marsh land fringing low-lying sand-flats.
- The main body of the field work was concentrated in the RETZ, however further data was acquired throughout the Dyfi system. This was achieved through the estuary mouth and RETZ anchor stations, spatial surveys and river surveys collecting high resolution data in order to describe variations in SPM and hydrodynamic characteristics over varying temporal scales.
- Optical instruments including a LISST-100, transmissometer and fluorometer were employed to characterise; SPM concentration (C_m), median particle size (D_{50}), volume concentration (C_v) and chlorophyll a concentration (Chl_a). Transmissometers and fluorometers require calibration from an *in situ* water samples to accurately calculate the concentration of SPM and chlorophyll a respectively.

- The LISST-100 presents specific limitations with regards to the inversion process from light scattering to volume concentration of particle size classes. It utilises Mie Theory, which assumes all particles in suspension are spherical. Agrawal et al (2008) have incorporated the Kernel matrix into the inversion process in an effort to represent the irregularly shaped particles typically encountered in the natural environment.

- Finally, acoustic methods have been adopted through the use of ADVs and ADCPs to estimate current velocities and TKE dissipations rates from the Kolmogorov $-5/3$ power law and the structure function method respectively.

Chapter 4

SPM and Hydrodynamic Characteristics of the Estuary

4.1 Introduction

This chapter explores the hydrodynamic and SPM characteristics of the Dyfi estuary over varying spatial and temporal scales. Data from bed-mounted moorings located in the RETZ are presented from four field campaigns; during March 2011, April 2010, September 2010 and November 2011. Longitudinal profiles of SPM and hydrodynamic data from spatial surveys are included for the four field campaigns. Additionally, SPM properties were measured at the estuary mouth and the five main tributaries of the river Dyfi river. The objective of this chapter is to describe variations of estuarine SPM and hydrodynamic characteristics on temporal and spatial scales appropriate to the variations observed in the estuary.

Observations presented in this chapter include bed-mounted mooring data collected on four separate field campaigns. In each campaign two moorings (Moorings A and B) were deployed in the RETZ. The location of Mooring A was designed to represent the TIR, however on spring tides observations showed the salt water extent reached this mooring.

Longitudinal profiles of the water column from the estuary mouth to the TIR were under-

taken during spatial surveys. The profiling data of temperature, salinity, chlorophyll a, SPM and particle size for the four field campaigns are presented in this Chapter. Particle size data are presented from the mouth of the estuary and the five main tributaries to the river Dyfi, comparing data obtained from the four separate field campaigns. Table 4.1 outlines the configurations of instruments deployed.

Table 4.1: A summary of the instrument configurations

Mooring deployments	**Anchor station**	**Spatial and River surveys**
LISST-100	LISST-100	LISST-100
CTD	CTD	CTD
ADCP	Transmissometer	
ADV	Fluorometer	

4.2 Results

4.2.1 Hydrological and meteorological conditions

Primarily the general conditions during mooring deployments are discussed including meteorological, river flow rate and surface elevation data. Wind direction, wind speed and rainfall data were acquired from the meteorological station in Cors Fochno, south of Aberdyfi, provided by the Environment Agency. Rainfall data for April 2010 was not available. The river flow rate data were measured at the Dyfi bridge in Machynllech and provided by the Environment Agency. The convention commonly used for describing wind direction is the direction the wind has travelled from. For the sake of continuity however, the wind direction is presented as the direction it is travelling to, in order to align with the convention in which current direction is described in oceanography.

March

Figure 4.1 displays the elevation and meteorological data for the observational period in March 2011. Elevation measurements were calculated from the pressure output from the

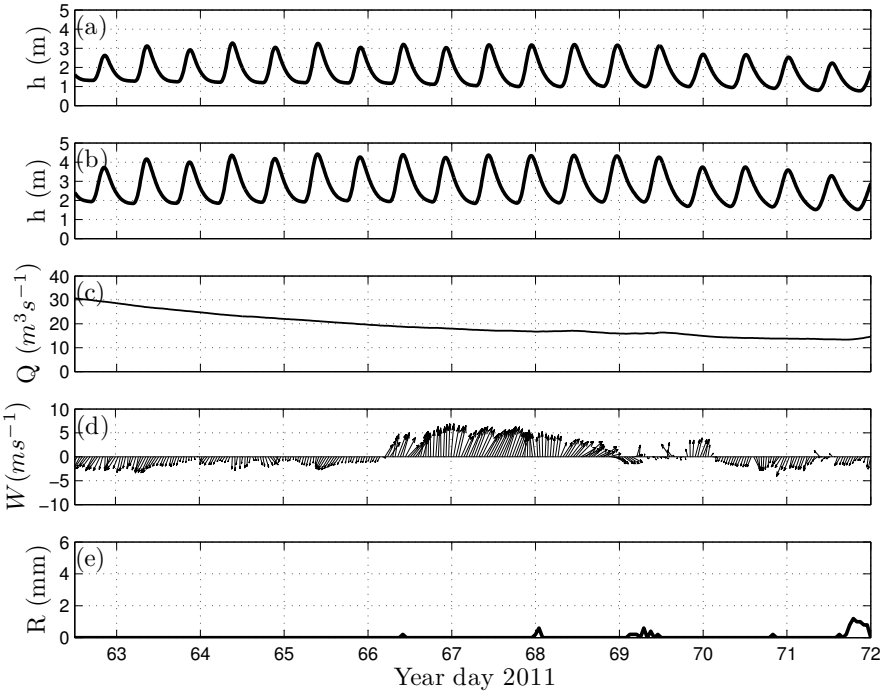

Figure 4.1: Time series of meteorological and elevation data for the observational period in March 2011. (a) h (m) at Mooring A. (b) h (m) at Mooring B.(c) River flow rate (Q) (m^3s^{-1}). (d) Wind direction (θ_{wind}) and speed (W) (ms^{-1}). (e) Rainfall $(R)(mm)$.

ADCP plus the hight of the instrument above the bed. The river flow rates presented typical baseline values from $20 - 30m^3s^{-1}$. Rainfall was low during this period, values rarely reached $1mm$. The wind speeds were comparatively low and predominantly moved to the south, with the exception of year days $65 - 66$, when strong winds dominated to the north east. The surface elevation data for the two moorings were similar, although the range of elevations was larger at Mooring B compared to Mooring A (Figures 4.1(a) and (b)).

April

Figure 4.2 portrays the surface elevation above the bed at both mooring sites, the magnitude of the wind direction and the river flow rate (Q) in April 2010. The surface elevation data denotes a strong tidal modulation and a progression from spring to neap tides. The

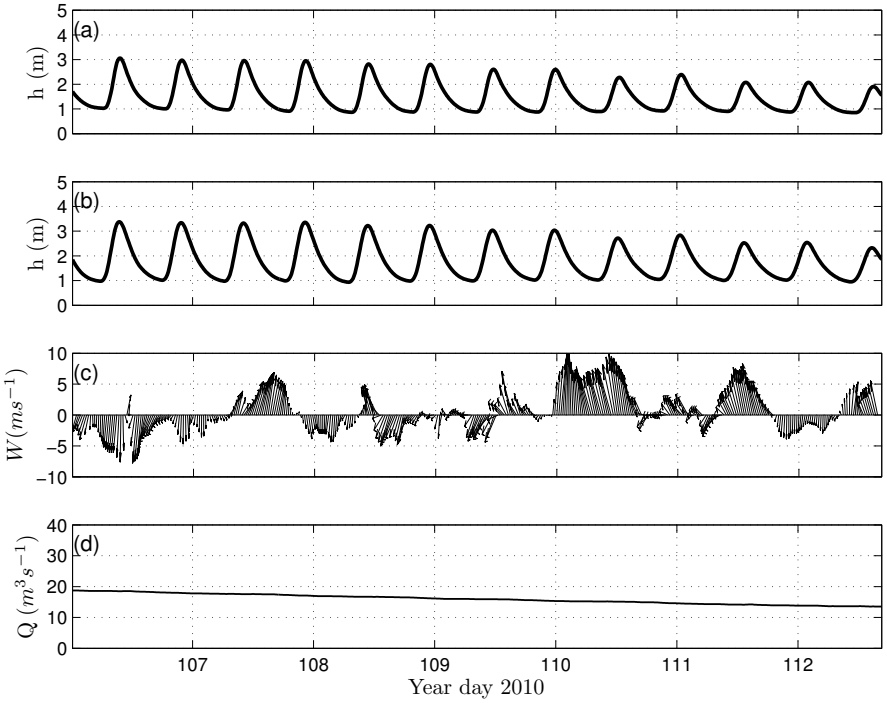

Figure 4.2: Time series of meteorological and elevation data for the observational period in April 2010. (a) h (m) at Mooring A. (b) h (m) at Mooring B. (c) Wind direction (θ_{wind}) and speed (W) (ms^{-1}). (d) River Dyfi flow rate (Q) (m^3s^{-1}).

asymmetric nature of the tidal curve is also evident at both Mooring A and Mooring B (Figure 4.2a and b). For the first four days of observations the wind direction was predominantly blowing to the south, on year day 110 the direction and strength of the wind changed to a faster northerly direction. Moreover, the flow rate of the river Dyfi was consistently at base level throughout the observational period of $\sim 20m^3s^{-1}$.

September

During the observational period in September 2010 two distinct river events occurred (Figure 4.3); during the second event river flow rates were in excess of $600m^3s^{-1}$. Figure 4.3c indicates the wind direction was dominated by north easterly winds, which are commonly associated with low pressure weather systems and increased precipitation. The strongest wind speeds were recorded between year day 256 and 258, which coincided

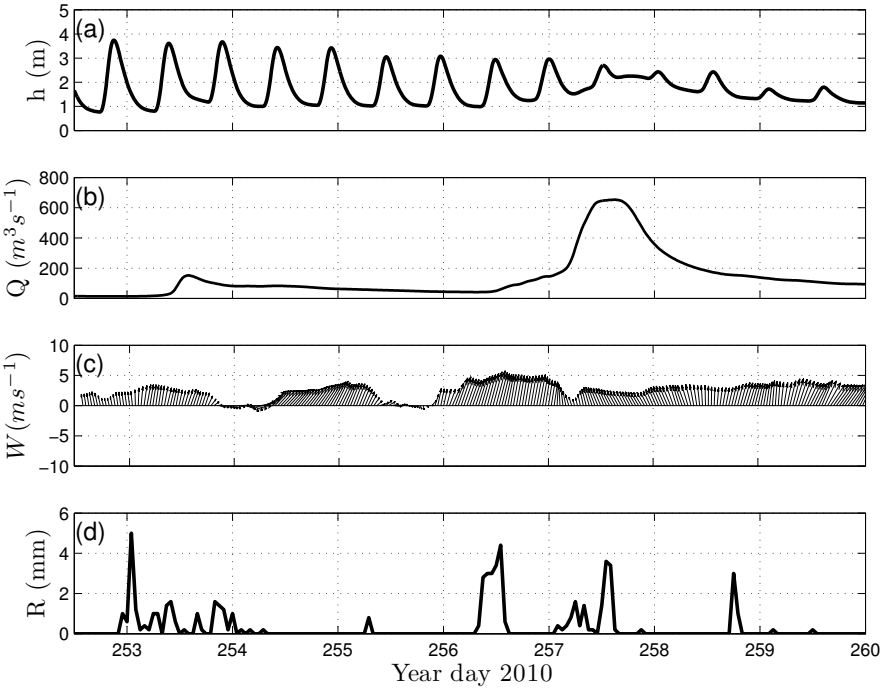

Figure 4.3: Time series of meteorological and elevation data for the observational period in September 2010. (a) h (m) at Mooring A. (b) River flow rate (Q) (m^3s^{-1}). (c) Wind direction (θ_{wind}) and speed (W) (ms^{-1}). (d) Rainfall $(R)(mm)$.

with the major river event. The surface elevation data shown in Figure 4.3 presents the evolution from spring to neap tides. Interestingly during the main river event on year day 257 the tidal signal in the surface elevation data was significantly dampened by the overall rise in river levels.

November

Figure 4.4 presents the time series of observational data collected in November 2011. Elevation data show spring progressing into neap tidal modulations. A lesser range of elevation values were presented at Mooring A compared to Mooring B (Figure 4.4). Overall the river flow rate was constant $(10m^3s^{-1})$ with the exception of a rise on year day 316. Rainfall was generally low, the wind was predominantly blowing in a southerly direction and does not exceed $10ms^{-1}$. A maximum of $2mm$ of rainfall was recorded on

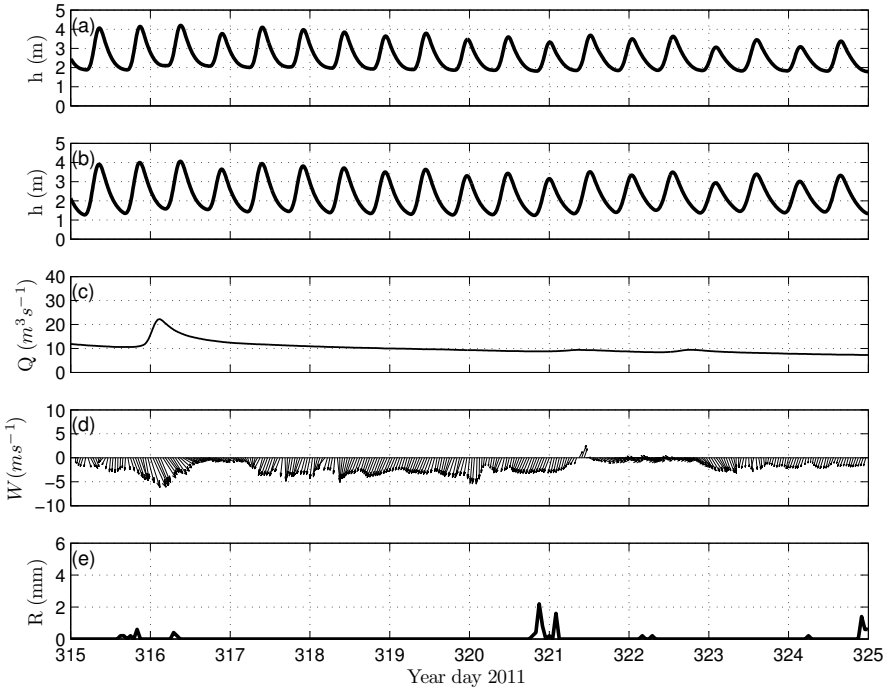

Figure 4.4: Time series of meteorological and elevation data for the observational period in November 2011. (a) h (m) at Mooring A. (b) h (m) at Mooring B.(c) River flow rate (Q) (m^3s^{-1}). (d) Wind direction (θ_{wind}) and speed (W) (ms^{-1}). (e) Rainfall (mm).

year day 321, rainfall was negligible for the remainder of the sampling period.

ADCP and ADV data

The Dyfi estuary is situated on the West coast of the UK, as a result prevailing winds blowing to the north east travel into the estuary and oppose the direction of the flow during the ebb phase of the tide. In the event of the wind direction opposing the tidal flow waves can be generated. It is well reported in the literature that increased levels of TKE dissipation (orders of magnitude higher than values produced solely by shear induced wind stress) can be found in the surface layer of the water column in the presence of breaking waves (Terray et al, 1995; Soloviev and Lukas, 2003; Jones and Monismith, 2008). Moreover, observational data in shallow water suggests large values of wind stress can result in elevations in ϵ, which can extend over large portions of the water column

(Young et al, 2005; Feddersen and Williams, 2007; Jones and Monismith, 2008).

$$\tau_w = \rho C_D W^2 (cos(\theta_u - \theta_{wind})) \tag{4.1}$$

Equation 4.1 describes the calculation of wind stress (τ_w) using the algorithm of Large and Pond (1981), where ρ is the density of air (taken as 1.2 kgm^{-3} at 20°C), C_D is a non-dimensional drag coefficient (10^{-3}) and W is the wind speed (ms^{-1}). τ_w is then multiplied by cos of the difference between θ_u and θ_{wind} to calculate the component of τ_w acting upon the estuary.

Profiles of axial current speed (u) and TKE dissipation rates (ϵ) are presented from both mooring locations for the field campaigns carried out in March, April and November. Data from September are considered in a later Chapter. These data permit investigation of estuarine hydrodynamic properties. The hydrodynamic characteristics of Mooring A and B will be compared over a seasonal scale in addition to the lunar scale. At each mooring location two spring and two neap tidal cycles are examined in this section. In addition to this the relationship between TKE dissipation and current velocities in conjunction with changes in wind stress and direction are investigated.

March

ADCP data are not available for Mooring A as the trial mooring described in Chapter 3 was deployed. Figure 4.5 describes the relationship between velocity and dissipation data for multiple tidal cycles from the ADV with τ_w. The ADV provides a point measurement of velocity (u_{bed}) and dissipation (ϵ_{bed}) $0.3m$ from the bed. u_{bed} did not exceed $0.25ms^{-1}$ during this period. Figure 4.5a indicates that the maximum value of ϵ_{bed} coincided with the maximum flood u_{bed}. During this period the wind was blowing in a north easterly direction, therefore θ_{wind} opposed θ_u during the ebb. This can be seen by blue markers dominating the ebb currents in Figure 4.5a and red dominating the flood. Figure 4.5c indicates the highest values of τ_w occurred around high water when Figure 4.5 indicates ϵ_{bed} was reaching a minimum. Overall, for the ADV data it appears ϵ_{bed} was more closely related to u_{bed} than τ_w.

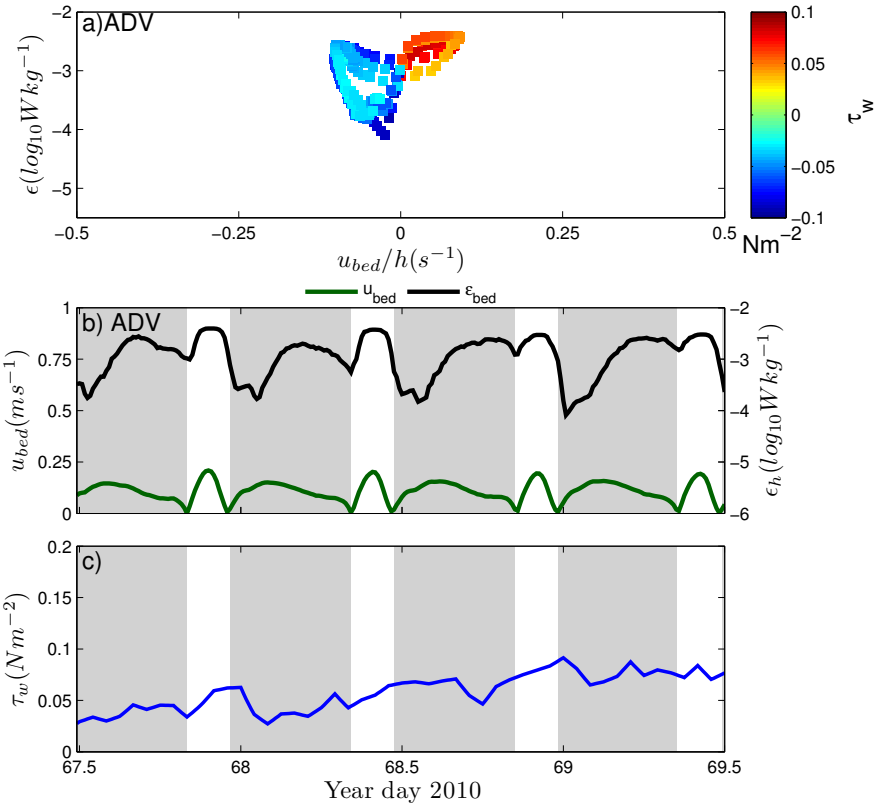

Figure 4.5: Relationship between hydrodynamic parameters; near bed axial current velocity u_{bed} and TKE dissipation rates ϵ_{bed} with wind shear stress (τ_w) in Mooring A in March 2011. a) Interactions between ϵ_{bed} and u_{bed} relative to (h) and τ_w. b) Time series of u_{bed} and ϵ_{bed}. c) Time series of τ_w.

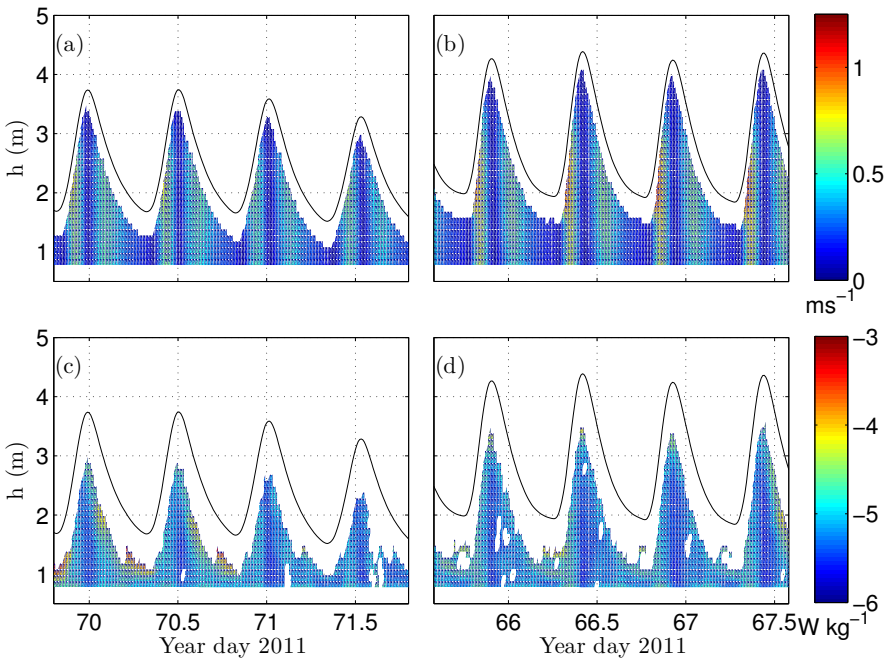

Figure 4.6: Time series of axial current speed u and TKE dissipation profiles ϵ for Mooring B in March 2011. (a) u (ms^{-1}) during neap tides. (b) u (ms^{-1}) during spring tides. (c) $log_{10}\epsilon$ (Wkg^{-1}) during neap tides. (d) $log_{10}\epsilon$ (Wkg^{-1}) during spring tides.

Figure 4.6 displays two tidal cycles of u and ϵ at Mooring B for spring and neap tides. During both spring and neap tides u was homogeneous with respect to h, with the exception of elevated values observed in the near surface during the flood on spring tides (Figure 4.6b). The highest values of u occurred on the flood tide reaching $1.25ms^{-1}$ on spring tides. ϵ reached a minimum at high water, which encompasses the vertical extent of the water column. Elevated values of ϵ were observed in the upper part of the water column during flood and ebb phases in both spring and neap cases (year days 70 and 68).

Figure 4.7 focuses on the interactions between ϵ_h, ϵ_{bed}, u_h, u_{bed} and τ_w for a section of the time series data from Mooring B in March. During this deployment both an ADCP and ADV were employed, giving rise to a comparison of hydrodynamic data from near the bed and throughout the water column. During this period as mentioned for Mooring A, the wind was blowing to the north east giving rise to opposing θ_{wind} and θ_u during the

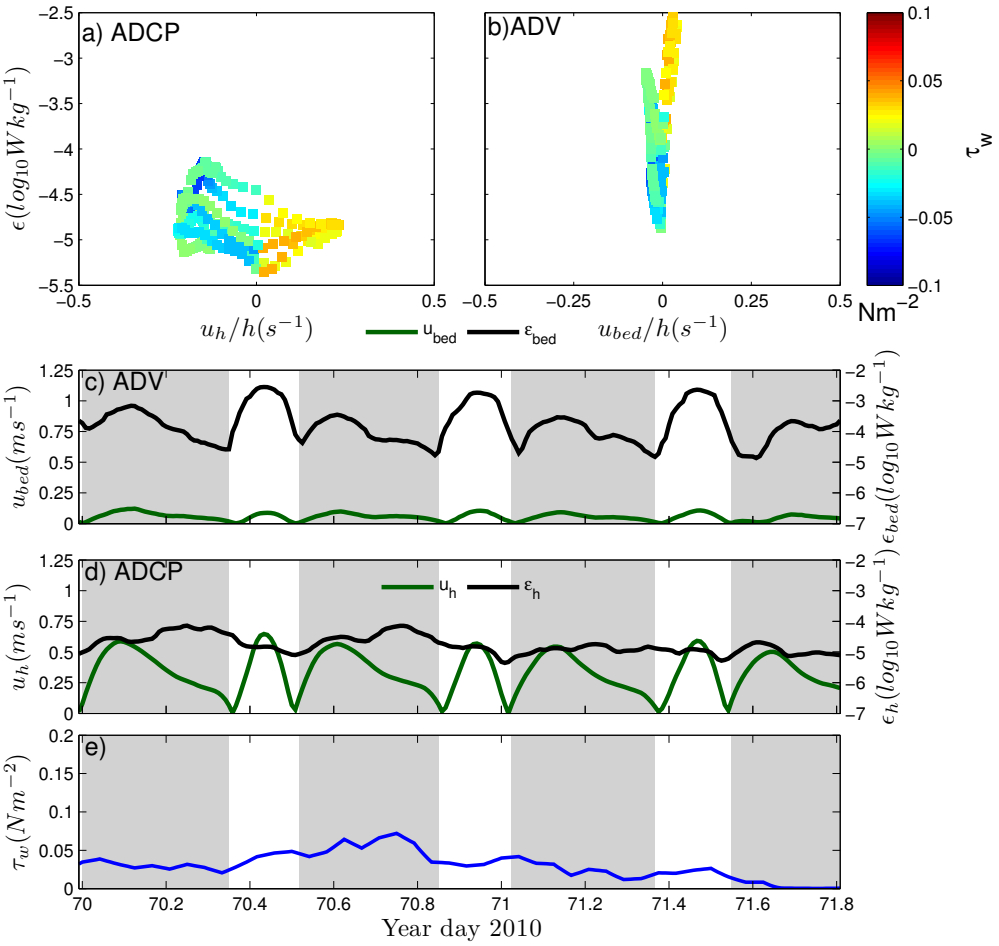

Figure 4.7: Relationship between hydrodynamic parameters; depth averaged axial current velocity u_h and TKE dissipation ϵ_h, axial velocity near the bed u_{bed} and TKE dissipation ϵ_{bed}, with wind direction θ_{wind}, tidal current direction θ_u and wind shear stress (τ_w) in Mooring B in March 2011. a) Interactions between ϵ_h and u_h relative to (h) and τ_w. b) Interactions between ϵ_{bed} and u_{bed} relative to (h) and τ_w. c) Time series of ϵ_{bed} and u_{bed}. d) Time series of ϵ_h and u_h. e) Time series of τ_w.

ebb. Figure 4.7a and b portray differing relationships between dissipation and current velocities near to the bed compared to depth averaged values. At the bed a strong relationship between u_{bed} and ϵ_{bed} was observed. Figure 4.7b and c indicate the highest values of ϵ_{bed} corresponded with the maximum values of u_{bed} regardless of the direction or magnitude of τ_w. Conversely, higher up in the water column the ADCP data reports the maximum values of ϵ_h coincided with the maximum u_h during the ebb when θ_{wind} was opposing θu at maximum values of τ_w.

April

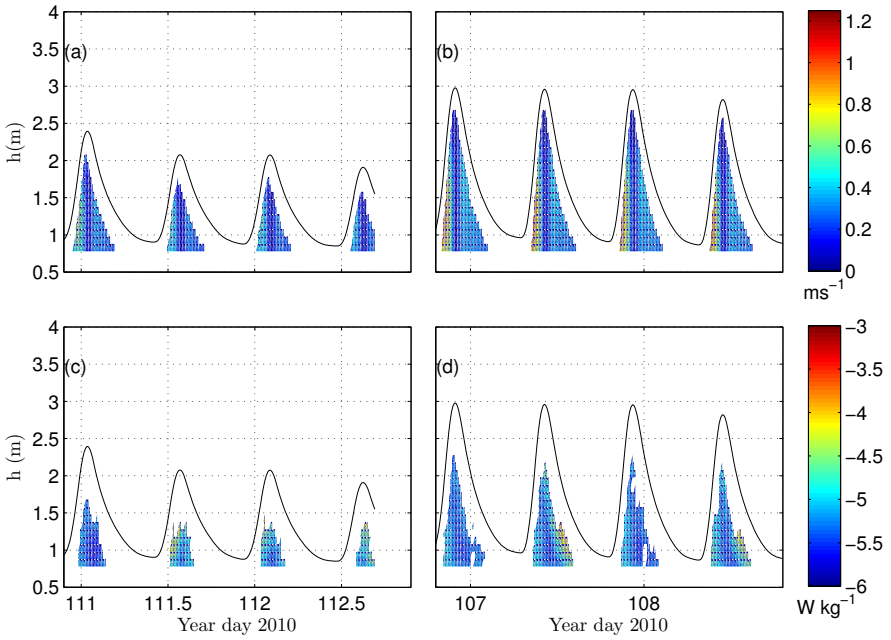

Figure 4.8: Time series of axial current speed u and TKE dissipation profiles ϵ for Mooring A in April 2010. (a) u (ms^{-1}) during neap tides. (b) u (ms^{-1}) during spring tides. (c) $log_{10}\epsilon$ (Wkg^{-1}) during neap tides. (d) $log_{10}\epsilon$ (Wkg^{-1}) during spring tides.

Firstly, Figure 4.8 indicates a notable difference in h between spring and neap tides at Mooring A. In both cases u was uniform with respect to h throughout the tidal cycle. The strongest values of u occurred during the flood phase in both spring and neap cases for both locations. The lowest values of u and ϵ for both spring and neap tides were

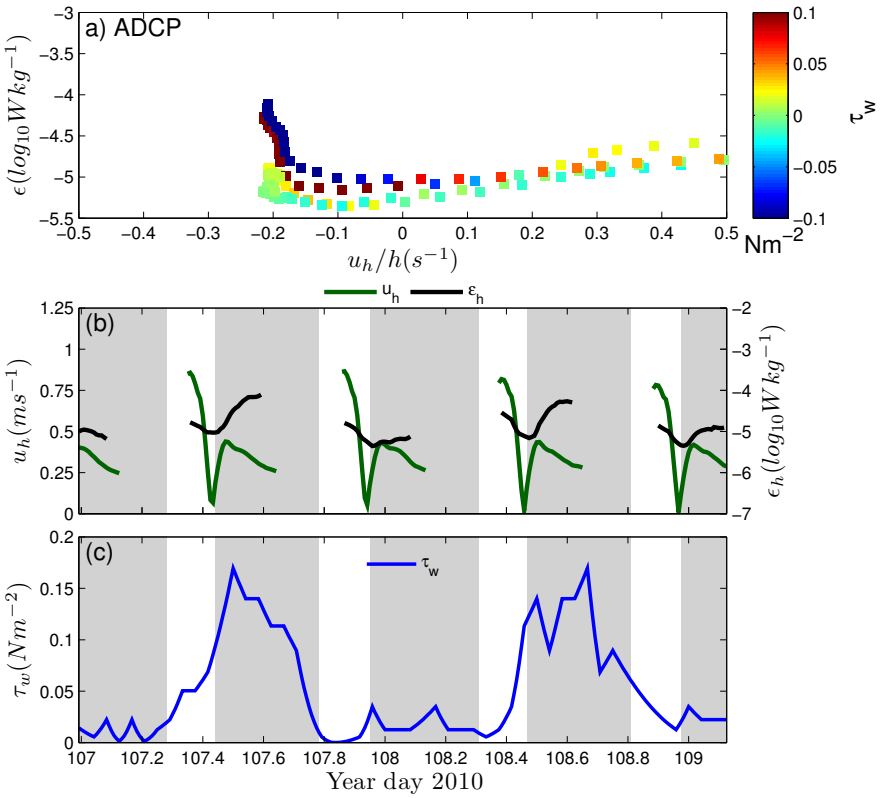

Figure 4.9: Relationship between hydrodynamic parameters; depth averaged axial current velocity u_h and depth averaged axial TKE dissipation rates ϵ_h with wind shear stress (τ_w) and direction at Mooring A in April 2010. a) Interactions between ϵ_h, u_h relative to (h) and (τ_w). b) Time series of ϵ_h and u_h. c) Time series of τ_w.

observed around high water, unfortunately data around low water was not available due to the blanking range of the ADCP previously discussed. Increased values of ϵ coincided with maximum u during the flood but the peak values of ϵ were observed at the surface of the water column during the second ebb of year days 107 and 108 (Figure 4.8). This indicates there could have been a diurnal variation occurring with enhanced ϵ observed during the ebb on alternate tides during daylight.

Figure 4.9 isolates a section of the time series to examine the effect of wind stress on ϵ_h. Figure 4.9a presents u_h as a function of ϵ_h, a weak relationship between u_h and ϵ_h is indicated; linear regression analysis of the two parameters results in an R^2 value of 0.03. Figure 4.9a suggests u_h and ϵ_h were positively correlated on the flood but not well

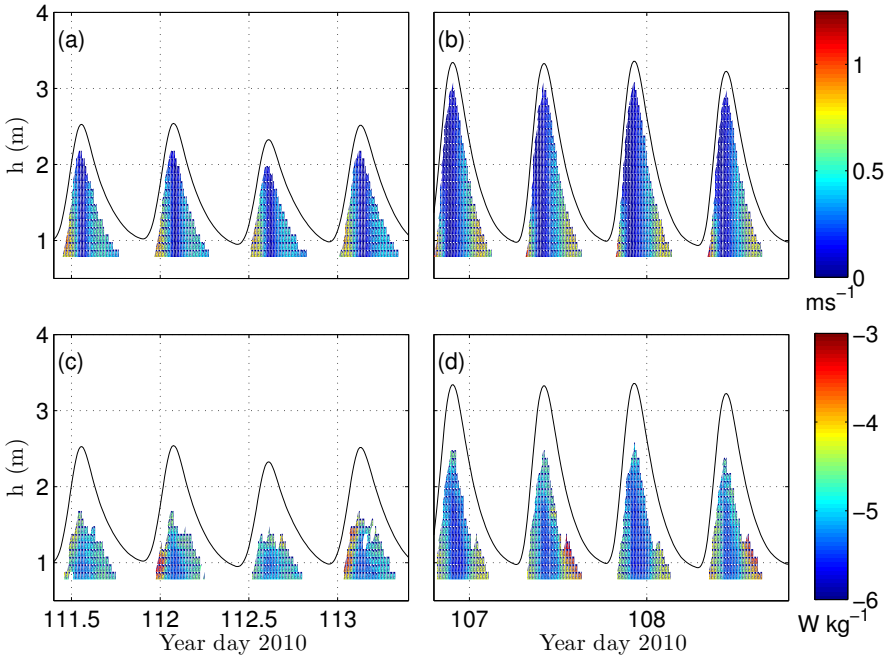

Figure 4.10: Time series of axial current speed u and TKE dissipation profiles ϵ for Mooring B in April 2010. (a) u (ms^{-1}) during neap tides. (b) u (ms^{-1}) during spring tides. (c) $log_{10}\epsilon$ (Wkg^{-1}) during neap tides. (d) $log_{10}\epsilon$ (Wkg^{-1}) during spring tides.

correlated on the ebb, for example ϵ_h increased independently of u_h during the ebb. τ_w, the third parameter shown in Figure 4.9a is plotted in colour. The sign of τ_w indicates the direction of θ_{wind} relative to θ_u. Negative values describe a situation in which θ_{wind} opposes θ_u, when values of τ_w were positive θ_{wind} and θ_u travelled in the same direction. In this instance the maximum values of ϵ_h coincided with the maximum u_h during the ebb and the largest values of τ_w regardless of direction. It is important to note ϵ_h was an order of magnitude higher on the ebb compared to the flood phase of the tide. The minimum values of ϵ_h occurred at a time of minimum values of u_h and τ_{wind}. Figure 4.9b shows the time series of u_h and ϵ_h which suggest ϵ_h was higher on the ebb (grey shaded areas on the Figure) during periods of high τ_w presented in Figure 4.9c.

At Mooring B u was also vertically uniform on a tidal scale (Figure 4.10). Overall u was higher at Mooring B compared to Mooring A, peak tidal currents were on average $0.24ms^{-1}$ faster at Mooring B over the sampling period. The dominance in u during

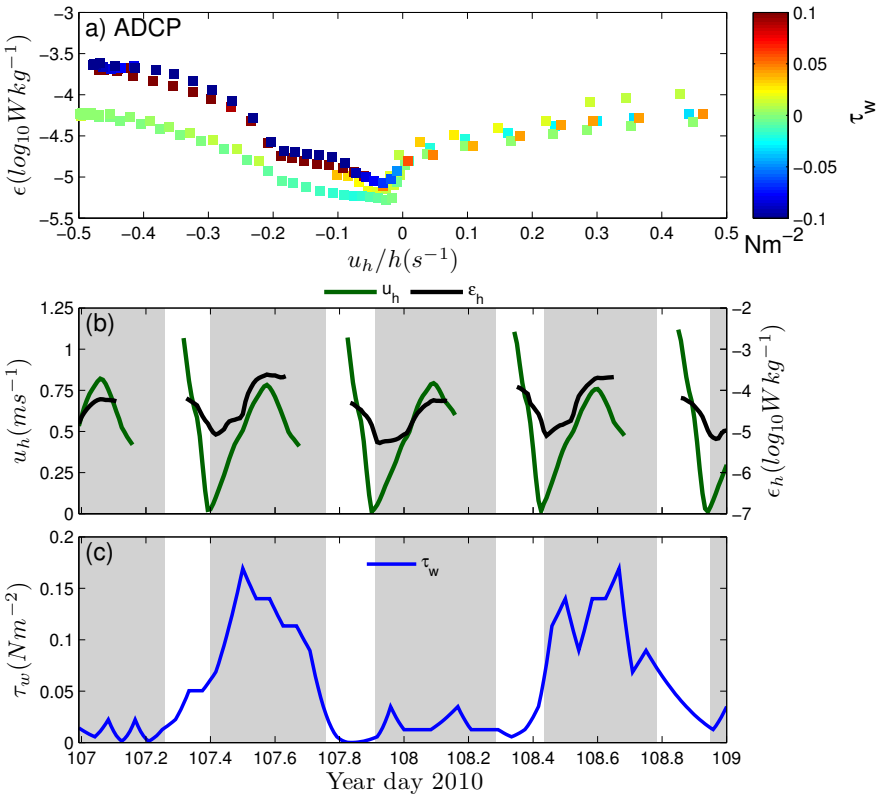

Figure 4.11: Relationship between hydrodynamic parameters; depth averaged axial current velocity u_h and depth averaged axial TKE dissipation rates ϵ_h with wind shear stress (τ_w) and direction at Mooring B in April 2010. a) Interactions between ϵ_h, u_h relative to (h) and (τ_w). b) Time series of ϵ_h and u_h. c) Time series of τ_w.

the flood phase of the tide remained in both spring and neap tides, however the ebb was on average 5 hours longer than the flood over the sampling period, this was also true at Mooring A. Elevated values of ϵ coincided with flood currents in both spring and neap cases. The highest values of ϵ were however again observed at the surface of the water column during the ebb phase of a spring tide (Figure 4.10d). The minimum values of u and ϵ both occurred around high water.

Figure 4.11 examines the effect of wind stress on TKE dissipation for Mooring B. Firstly ϵ_h was plotted against u_h/h, displaying a significant relationship ($R^2 = 0.6$), however as seen at Mooring A, values of ϵ_h up to two orders of magnitude higher were observed on the ebb compared to the flood for the same values of u_h. Figure 4.11a indicates the highest values of ϵ_h correlated with the maximum values of τ_w and the maximum u_h on the ebbing tide. During the flood lower levels of τ_w were reported in comparison to the ebb.

November

ADCP data collected at Mooring A in November displayed the overall lowest values of u, reaching a maximum of only $0.5ms^{-1}$ during the flood on neap tides, during the flood on spring tides u_h was greater than $1ms^{-1}$ close to the surface. Although, Figure 4.12a and b show elevated values of u occurring near to the surface reaching $0.75ms^{-1}$ on neap tides and $1ms^{-1}$ on spring tides. Figures 4.12c and d describe a strong asymmetry in ϵ, for both spring and neap tides ϵ was greater during the flood compared to the ebb. Figure 4.12c and d also describe a rise in ϵ towards the end of the ebb and the onset of low water.

Considering now the effects of τ_w and θ_{wind} for multiple tidal cycles, Figure 4.13 indicates a disparity between ADCP and ADV data regarding the relationship between ϵ_h and u_h as seen in the March data set. u_{bed} was again notably smaller than u_h and ϵ_{bed} was positively correlated with u_{bed} ($R^2 = 0.4$). θ_{wind} continuously blows to the south west during this sampling period, therefore θ_{wind} opposed θ_u during the flood and vice versa.

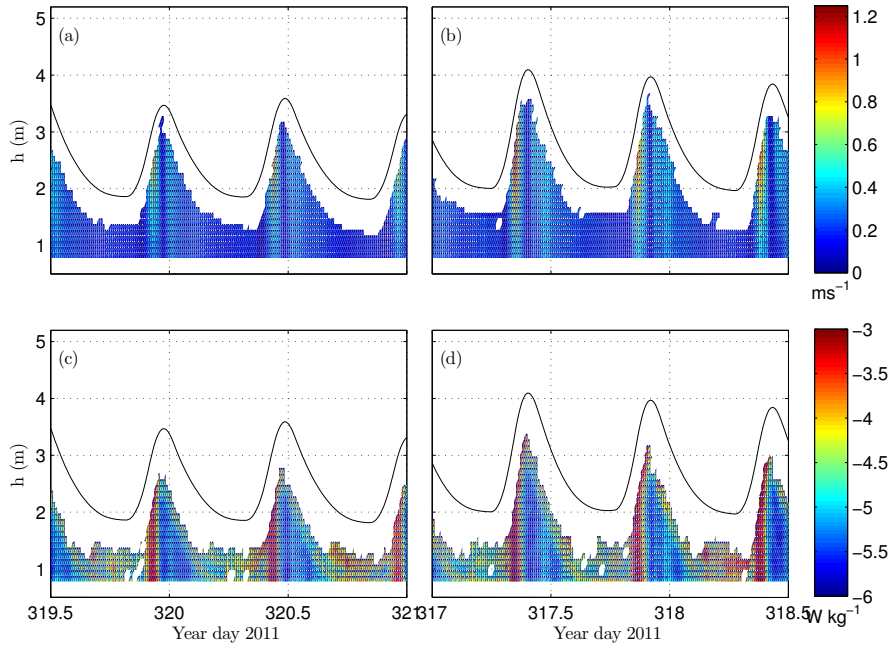

Figure 4.12: Time series of axial current speed u and TKE dissipation profiles ϵ for Mooring A in November 2011. (a) u (ms^{-1}) during neap tides. (b) u (ms^{-1}) during spring tides. (c) $log_{10}\epsilon$ (Wkg^{-1}) during neap tides. (d) $log_{10}\epsilon$ (Wkg^{-1}) during spring tides.

Highest values of ϵ_h were observed during the flood phase of the tide at a time when τ_w was strongest and opposing θ_u.

Larger values of u were reported at Mooring B compared to Mooring A in November, maximum values of u up to $1.25ms^{-1}$ and $1ms^{-1}$ during the flood and ebb respectively are shown in Figure 4.14b. Conversely during neap tides u did not exceed $0.8ms^{-1}$ on either the flood or the ebb. ϵ presents less of a definitive signal at Mooring B compared to Mooring A. Figures 4.14c and d indicate elevated values of ϵ at the beginning of the flood tide in both spring and neap cases. There is also evidence of increased ϵ in the upper part of the water column during the ebb again in both spring and neap tides.

As seen at Mooring A, u_{bed} and ϵ_{bed} were significantly positively correlated ($R^2 = 0.67$) and u_{bed} was smaller than u_h (Figure 4.15a and b). The tidal asymmetry of u_h was not

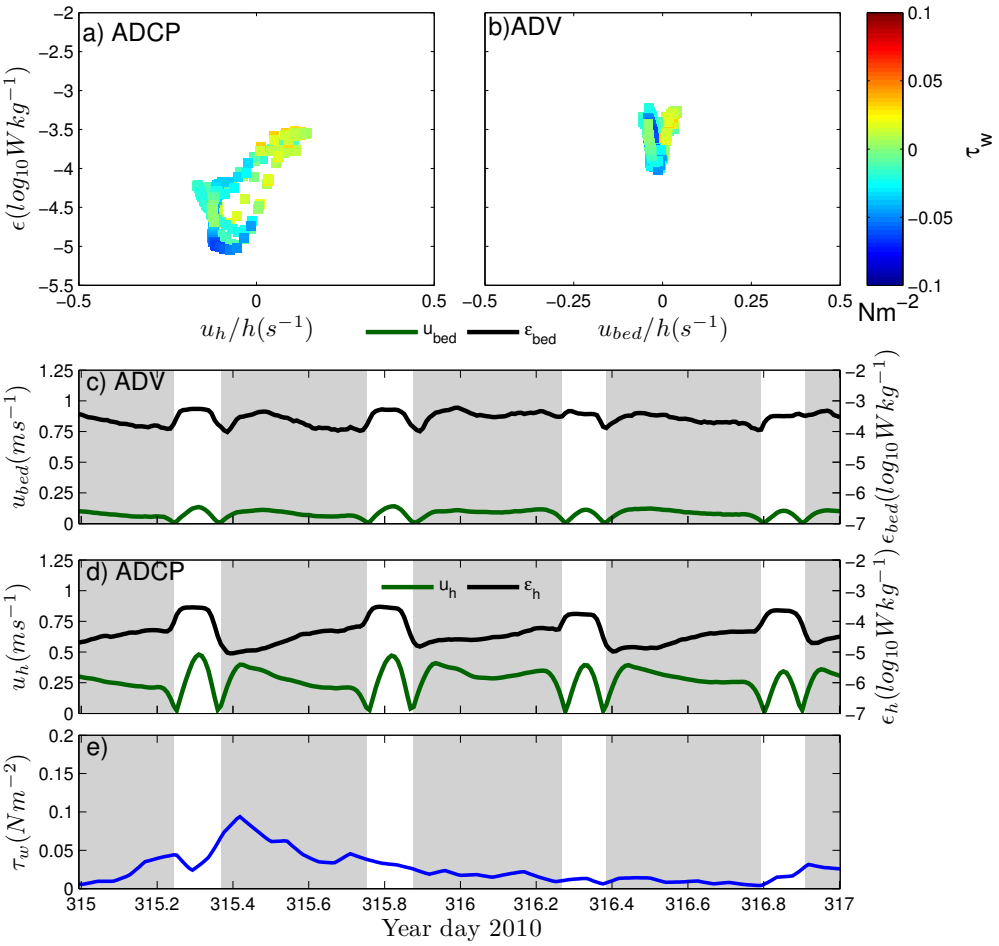

Figure 4.13: Relationship between hydrodynamic parameters; depth averaged axial current velocity u_h and TKE dissipation ϵ_h, near the bed axial velocity u_{bed} and TKE dissipation ϵ_{bed}, with wind shear stress (τ_w) and direction at Mooring A in November 2011. a) Interactions between ϵ_h and u_h relative to (h) and τ_w. b) Interactions between ϵ_{bed} and u_{bed} relative to (h) and τ_w. c) Time series of ϵ_{bed} and u_{bed}. d) Time series of ϵ_h and u_h. e) Time series of τ_w.

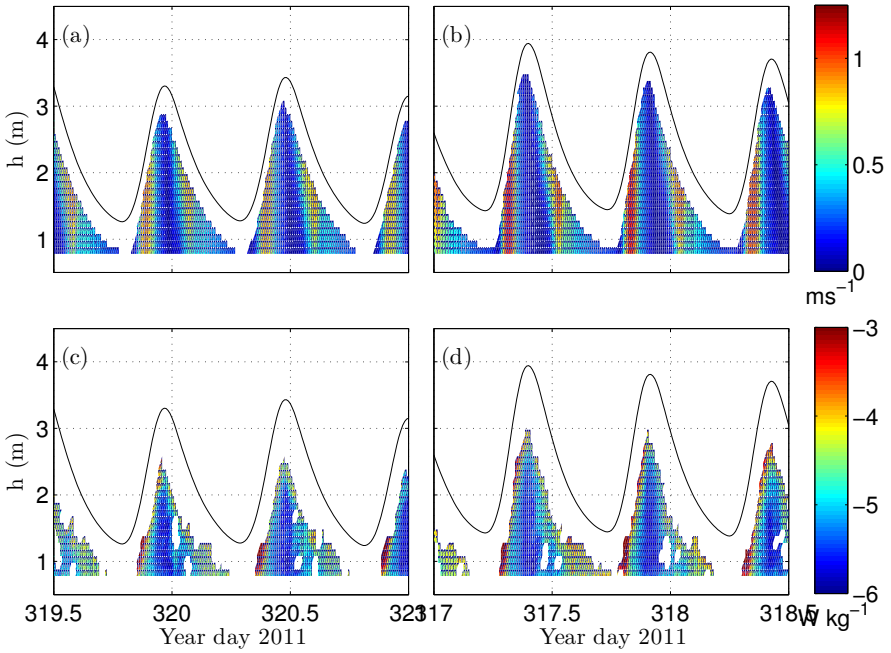

Figure 4.14: Time series of axial current speed u and TKE dissipation profiles ϵ for Mooring B in November 2011. (a) u (ms^{-1}) during neap tides. (b) u (ms^{-1}) during spring tides. (c) ϵ $log_{10}(Wkg^{-1})$ during neap tides. (d) ϵ $log_{10}(Wkg^{-1})$ during spring tides.

as pronounced as previously reported, maximum ϵ_h was an order of magnitude higher on the flood compared to the ebb (Figure 4.15a and d). Figure 4.15d also shows elevated ϵ_h values on the flood correspond with the maximum τ_{wind} at a time when θ_{wind} was opposing θ_u. However, Figure 4.15e shows the time series of τ_w which suggests τ_w was relatively small during this period.

Profiling CTD data

During each field campaign spatial surveys from the mouth of the estuary to the TIR were undertaken around high water. The field campaign undertaken in November did not include spatial surveys from the mouth to the TIR therefore only data from March, April, July and September are presented. Profiles of salinity and temperature from the

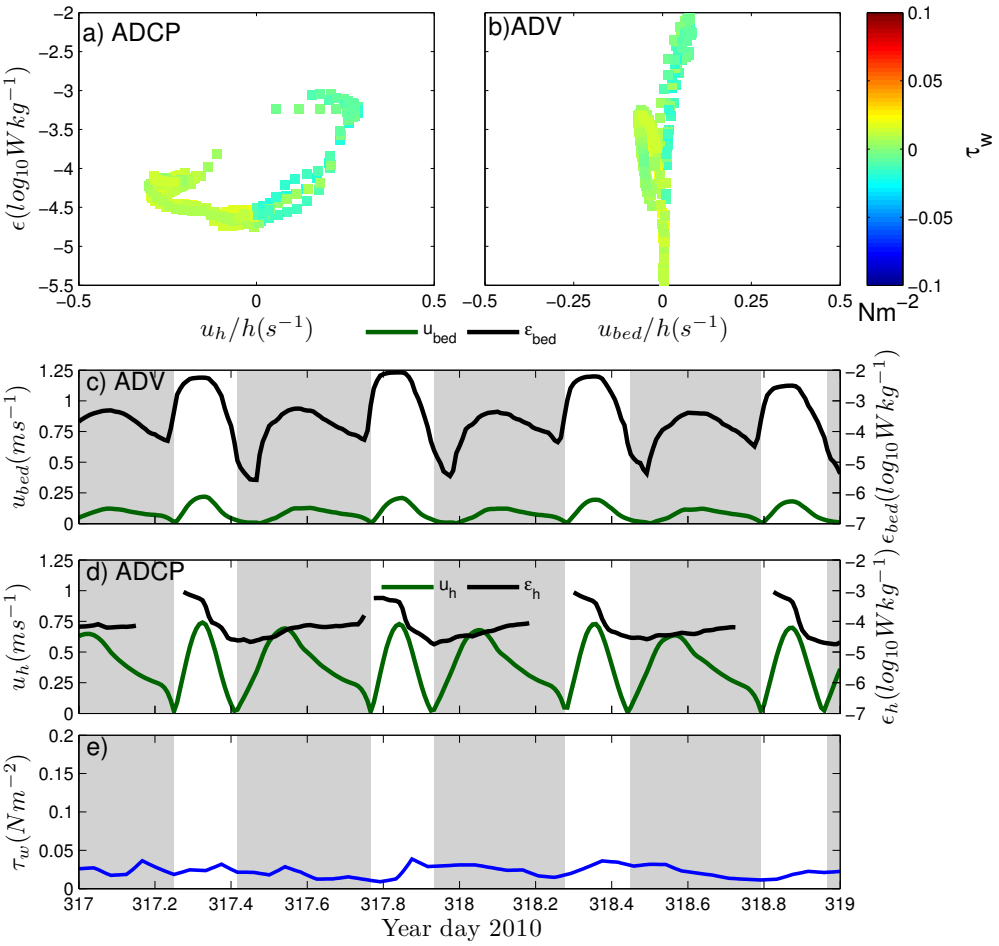

Figure 4.15: [Relationship between hydrodynamic parameters; depth averaged axial current velocity u_h and TKE dissipation ϵ_h, axial velocity near the bed u_{bed} and TKE dissipation ϵ_{bed}, with wind direction θ_{wind}, tidal current direction θ_u and wind shear stress (τ_w) in Mooring Bin November 2011. a) Interactions between ϵ_h and u_h relative to (h) and τ_w. b) Interactions between ϵ_{bed} and u_{bed} relative to (h) and τ_w. c) Time series of ϵ_{bed} and u_{bed}. d) Time series of ϵ_h and u_h. e) Time series of τ_w.

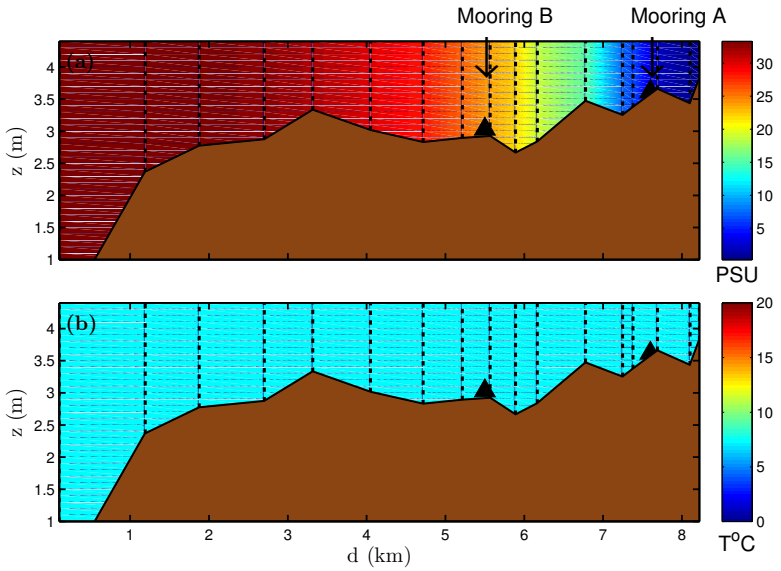

Figure 4.16: (a) Salinity and (b) Temperature ($°C$) profiles throughout estuary at high water on year day 70 March 2011.z is local depth relative to the surface and d is distance from the mouth of the estuary. Vertical black dashed lines indicate profiling locations.

spatial surveys are show in this section, black triangles denote locations of Moorings A and B.

March

Figure 4.16 describes the temperature and salinity structure of the water column throughout the estuary at high water in March 2011. Figure 4.16a indicates the salinity ranged from 33 at the mouth to 0 above Mooring A. Moreover, the salinity profiles show that Mooring B was not in the TIR as intended, however the position of Mooring A was not strictly in the TIR, there was some salt water intrusion at high water. In March the water column remained vertically uniform with respect to salinity and temperature (Figure 4.16). The temperature range was relatively small and did not exceed $6°C$, the river and the seawater temperatures were within a degree of each other.

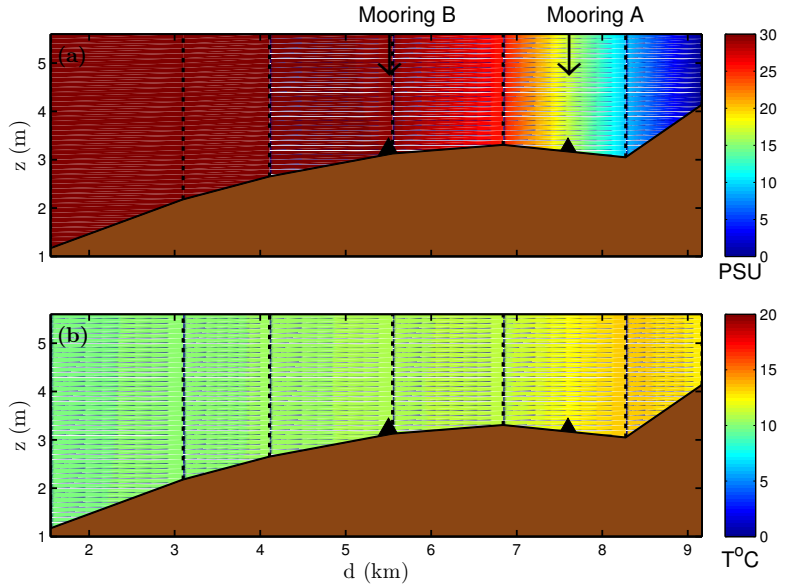

Figure 4.17: (a) Salinity and (b) Temperature ($°C$) profiles throughout estuary at high water year day 114 April 2010. z is local depth relative to the surface and d is distance from the mouth of the estuary. Vertical black dashed lines indicate profiling locations.

April

Figure 4.17 indicates Mooring A was further into the RETZ in April 2010, salinity values were above 15 at high water. The water column was still vertically uniform with respect to salinity and temperature throughout the estuary. The seawater was cooler than the river water at this time by $2.8°C$.

July

Figure 4.18 suggests the salt water intrusion extended notably less in July, salinity values began to fall $3km$ into the estuary and by $5km$ freshwater dominated. Furthermore, the temperature of the seawater was warmer than the river water by $3.4°C$.

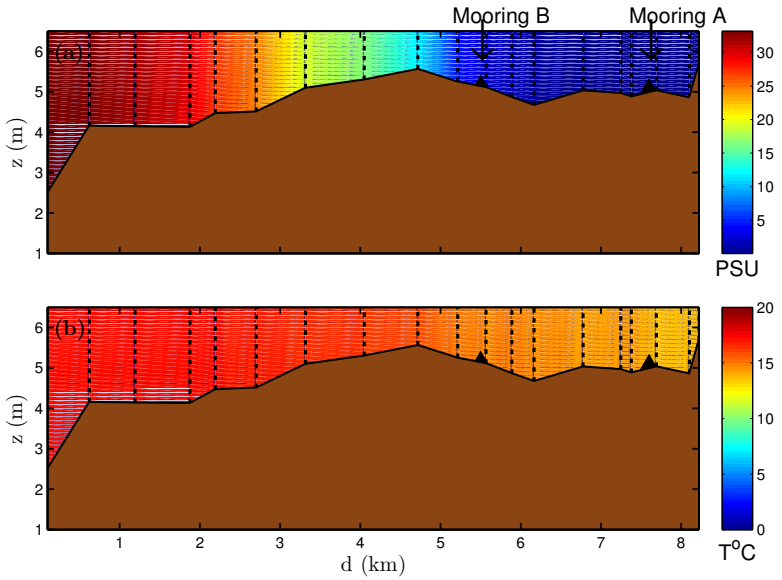

Figure 4.18: (a) Salinity and (b) Temperature ($°C$) profiles throughout estuary at high water on year day 202 July 2011. z is local depth relative to the surface and d is distance from the mouth of the estuary. Vertical black dashed lines indicate profiling locations.

September

In September, station locations were more concentrated around Mooring B compared to April. Salinities ranged from 33 at the mouth to less than 5 above Mooring A at the Dyfi bridge. The seawater temperature was now warmer than the river, the range in temperature was $3.2°C$. The water column was again vertically homogeneous with respect to salinity and temperature.

Table 4.2 summarises the key hydrodynamic characteristics for Mooring A and B for each sampling period. Tidal ranges are comparable across the sampling periods with the exception of July, however river flow varies notably. The strongest river flows occurred in September, the spatial survey was conducted between a minor and major river event shown in Section 4.2.1. April data indicates the smallest distance of salt water intrusion along with the smallest level of river flow. The lowest temperatures recorded were collected in March and the highest in September.

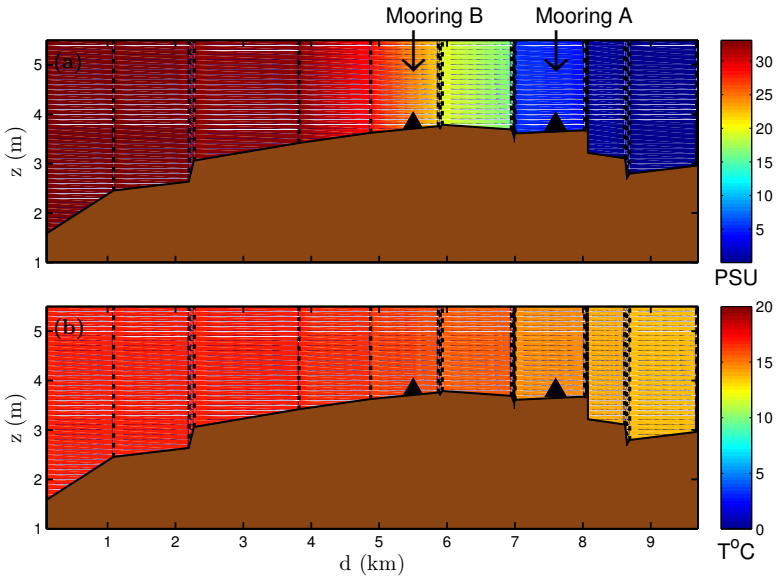

Figure 4.19: (a) Salinity and (b) Temperature ($°C$) profiles throughout estuary at high water on year day 255 September 2010. z is local depth relative to the surface and d is distance from the mouth of the estuary. Vertical black dashed lines indicate profiling locations.

With this summary Table 4.2 in mind, data collected in March will be used to represent seasonal conditions indicative of Winter and April data will be used to represent Spring conditions. July data is assumed to represent seasonal conditions typical of Summer and data collected in September is used to explore the affects of a significant river event on hydrodynamic and SPM characteristics throughout the estuary.

4.2.2 Observations of estuarine suspended sediment dynamics

Time series LISST-100X mooring data

The next component of this chapter involves the description of near-bed SPM characteristics at Moorings A and B for deployments in March, April and November. Both moorings deployed in July failed, therefore time series mooring data is unavailable. Time series data for September data is presented in a later Chapter in which the affects of the river events are considered in detail.

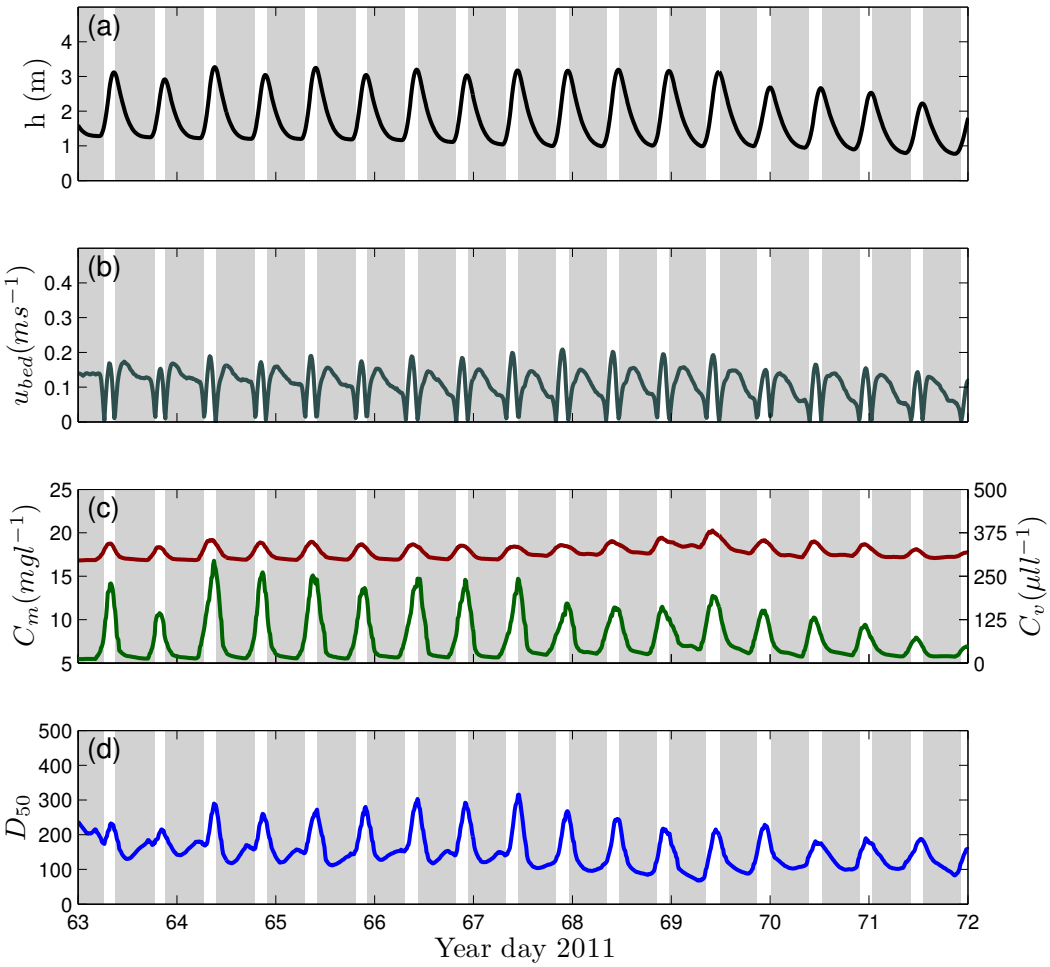

Figure 4.20: Time series of *in situ* SPM observations and hydrodynamic characteristics in Mooring A in March 2011.(a) $h(m)$. (b) u_{bed} (ms^{-1}) from ADV $0.3m$ above the bed. (c) Dark green line is C_v (μll^{-1}) $30cm$ above the bed. Dark red line is $C_m(mgl^{-1})$.(d) $D_{50}(\mu m)$.

Table 4.2: A summary and comparison of hydrodynamic characteristics at Mooring A and B throughout field campaigns in which spatial surveys were conducted.

	March	**April**	**July**	**September**
Tidal range	2.3 m	2.1 m	1.7 m	2.2 m
River flow	17.9 m^3s^{-1}	13.0 m^3s^{-1}	20.8 m^3s^{-1}	54.5 m^3s^{-1}
Salt water intrusion	7.6 km	9.1 km	5.4 km	7.2 km
Salinity Mooring A	7.0	16.5	4.0	7.5
Temperature Mooring A	6.0°C	13.0°C	14.6°C	14.3°C
Salinity Mooring B	24.9	27.2	6.5	25.3
Temperature Mooring B	6.0°C	10.1°C	15.1°C	16.0°C

Initially time series data are presented; light grey sections in each plot represents the ebb phase of the tide. In addition, depth averaged axial current speed (u_h) is presented to provide a hydrodynamic context for the SPM data.

March

The field campaign carried out in March 2011 span over 9 days, it began and ended during neap tides. At both Moorings A and B during neap tides the asymmetry in u_h over a tidal cycle was less obvious than during spring tidal flows (Figure 4.20 and 4.21). For both locations the flood was notably shorter in length than the ebb phase. At Mooring A the ebb was on average 4.4 times longer than the flood and 2.8 times longer at Mooring B over the sampling period.

As mentioned previously the instrument configuration at Mooring A in March did not involve an ADCP, therefore velocity measurements are solely from an ADV situated $0.3m$ from the bed (u_{bed}). Figure 4.20b indicates values of u_{bed} at Mooring A were notably smaller than u_h at Mooring B as the ADV was deployed close to the bed and this instrument provides a point measurement, whereas the ADCP obtains profiles of the water column above the instrument. The C_v and C_m at Mooring A were also modulated on a tidal scale. The signal was diurnal, during spring tides maximum C_v of sediment occurred at high water and at times of peak u_h during the flood for neap tides (Figure

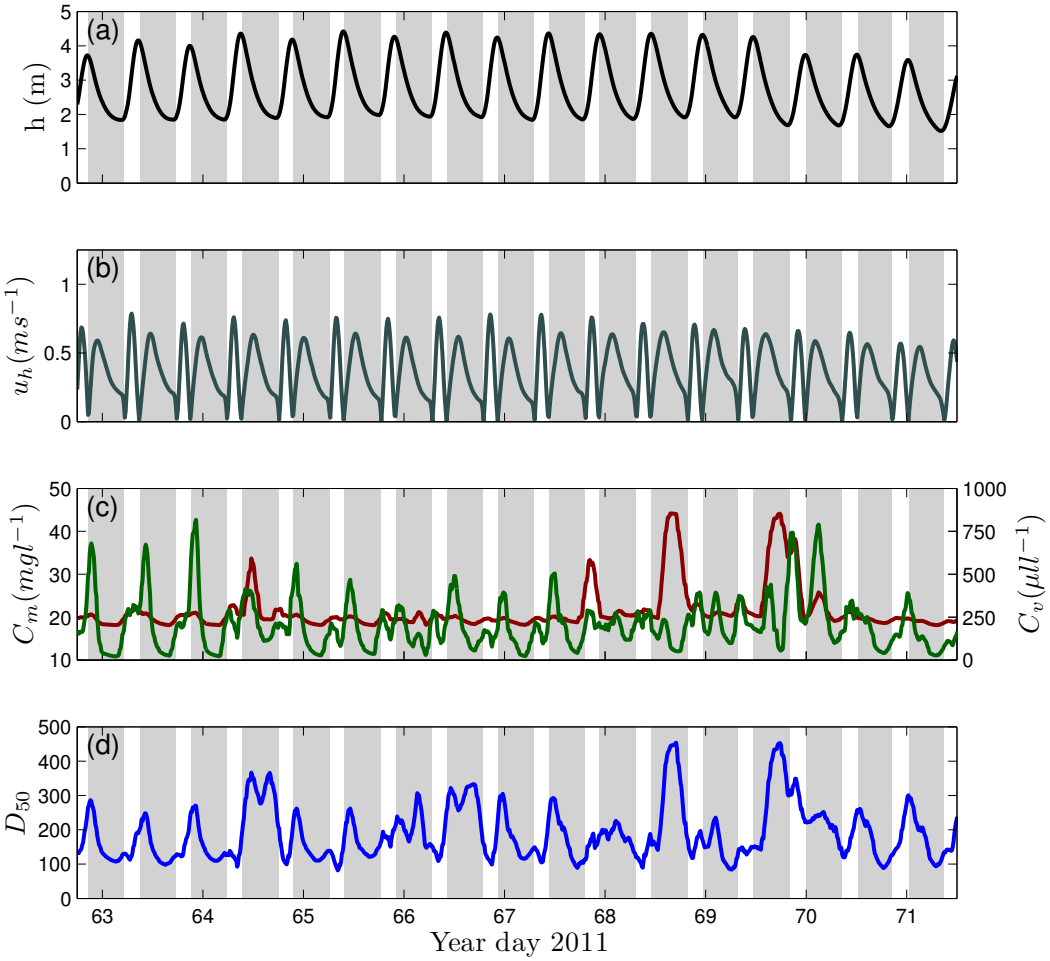

Figure 4.21: Time series of *in situ* SPM observations and hydrodynamic characteristics in Mooring B in March 2011.(a) $h(m)$. (b) u_h (ms^{-1}) from ADCP. (c) Dark green line is C_v (μll^{-1}) $30cm$ above the bed. Dark red line is $C_m(mgl^{-1})$.(d) $D_{50}(\mu m)$.

4.20c). Conversely, Figure 4.21c indicates a semi-diurnal signal of C_v at Mooring B, the main peak in C_v occurred at high water and a subsidiary peak corresponded with low water. C_m at Mooring B did not display the same pattern as C_v, the range of values were considerably smaller. Maximum values of C_m reached $40mgl^{-1}$ during the second ebb phase of year day 68 and 69. The major peaks in C_m corresponded with a major peak in D_{50} (greater than $400\mu m$) and a minima in C_v. Figure 4.20(d) conveyed a diurnal signal in the D_{50} time series for Mooring A, peaks corresponded with high water. The D_{50} at Mooring B presented a more complex signal, a baseline diurnal signal corresponding with high water was however apparent (Figure 4.21(d)). Superimposed on this signal were larger particles corresponding with an increase in C_m.

April

Mooring configurations in April did not include ADV instruments, therefore all velocity data were obtained via ADCP instruments. As discussed in Section 4.2.1 the time series data from Mooring A in April was in transition between spring and neap tides, which is demonstrated by the surface elevation (h) and depth averaged axial current speed (u_h) data (Figure 4.22(a) and (b)). Figure 4.22(b) also shows pronounced flood dominance in u_h occurred, while the ebb was 2.5 times longer than the flood on average for the sampling period. As the tides progressed into neap tides the maximum in C_v corresponded with the peak flood current speeds (4.22). But, during spring tides (C_v) presented a semi-diurnal signal with peaks occurring at both high water and low water. C_m followed the same trends however the range was significantly smaller ($10 - 20mgl^{-1}$). D_{50} in Figure 4.22(d) displays a clear diurnal signal, the maximum particle size occurred at high water during spring tides and at peak flood currents during neap tides.

The time series data from Mooring B displays stronger tidal currents than Mooring A, maximum u_h during the flood phase of the tide exceeded $1ms^{-1}$ during spring tides (Figure 4.23b). Figure 4.23 also indicates the asymmetry in u_h, as reported at Mooring A, the ebb was on average 2.5 times longer than the flood over the sampling period.

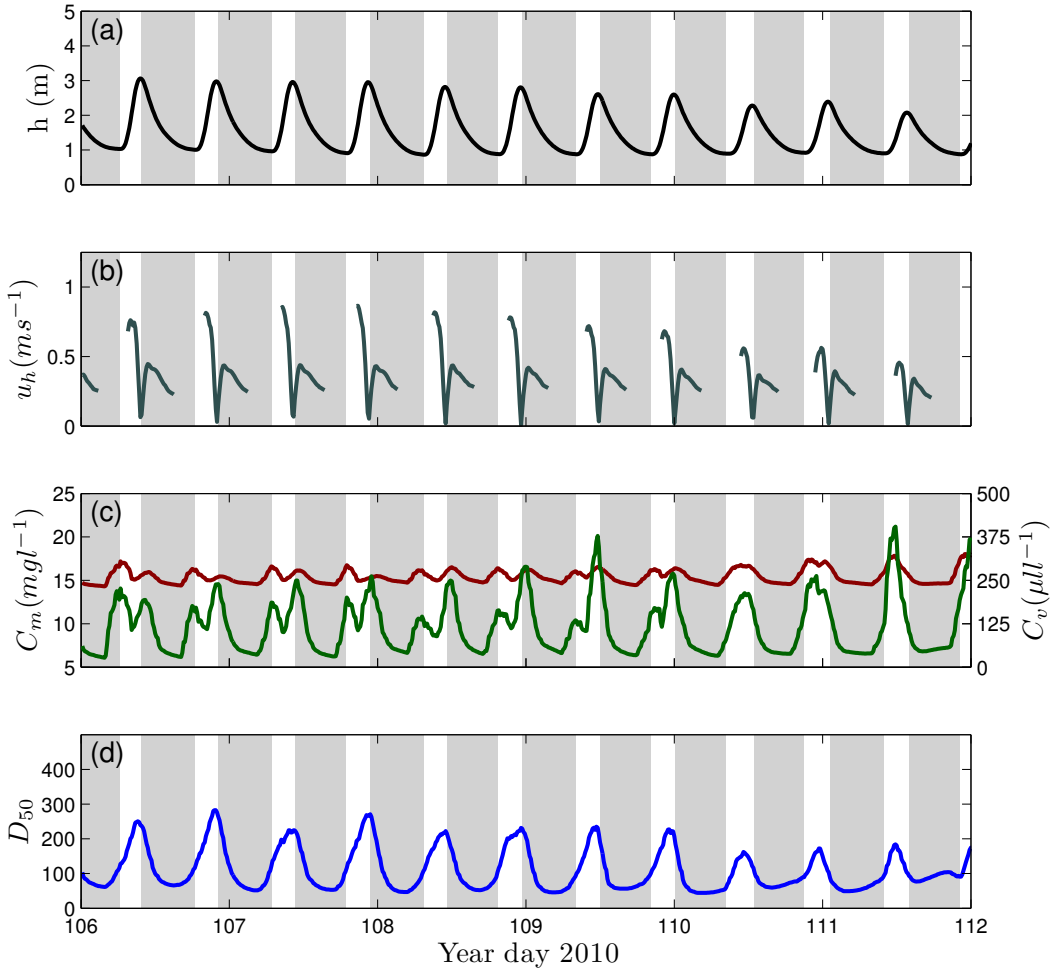

Figure 4.22: Time series of *in situ* SPM observations and hydrodynamic characteristics at Mooring A in April 2010.(a) $h(m)$. (b) u_h (ms^{-1}) from ADCP. (c) Dark green line is C_v (μll^{-1}) $30cm$ above the bed. Dark red line is $C_m(mgl^{-1})$.(d) $D_{50}(\mu m)$.

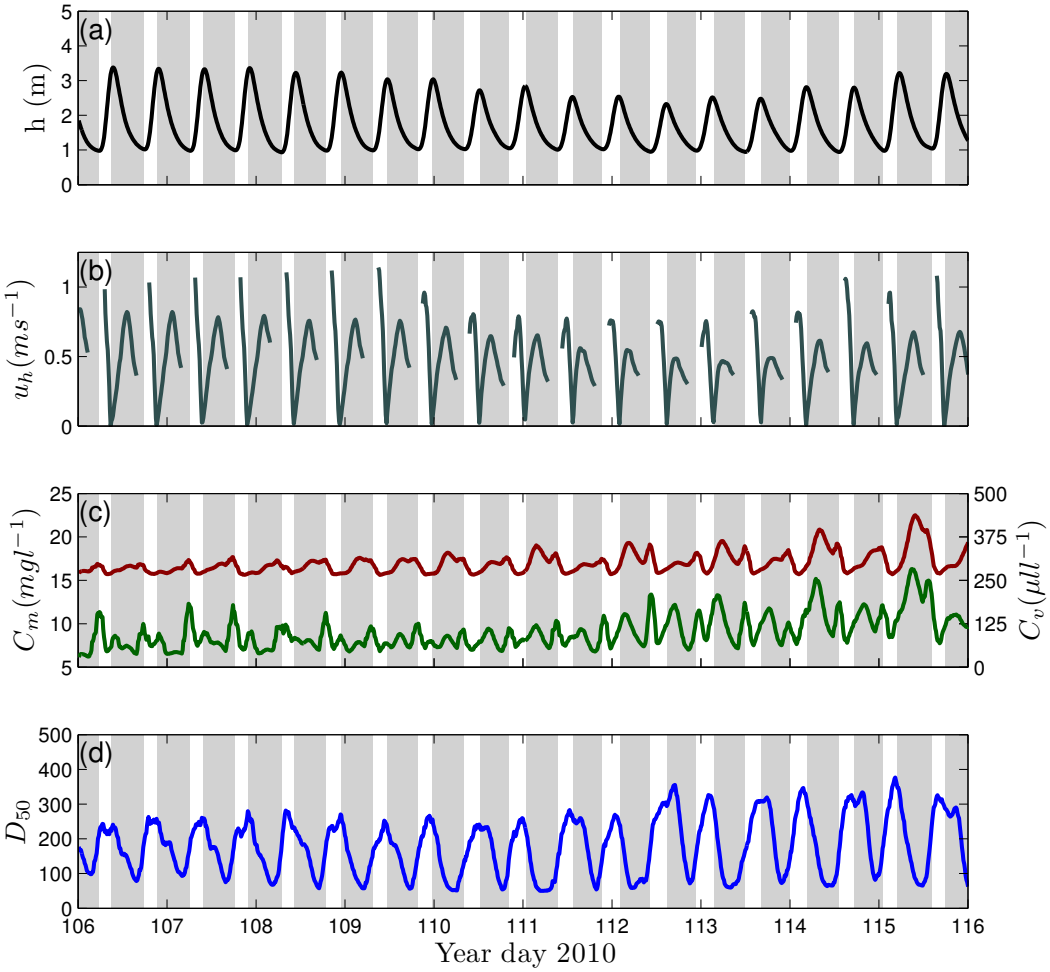

Figure 4.23: Time series of *in situ* SPM observations and hydrodynamic characteristics at Mooring B in April 2010.(a) $h(m)$. (b) u_h (ms^{-1}) from ADCP. (c) Dark green line is C_v (μll^{-1}) $30cm$ above the bed. Dark red line is $C_m(mgl^{-1})$.(d) $D_{50}(\mu m)$.

Peaks in C_v corresponded with high water and low water at Mooring B. C_m followed a similar pattern, however the range in concentration was small, as seen at Mooring A. D_{50} observations at Mooring B presented a largely diurnal signal, reaching a maximum at high water, during spring tides a subsidiary peak in D_{50} coincided with low water.

November

The final time series data sets to consider are the moorings deployed in November 2011. These moorings were deployed during spring tides and recovered during neap tides. Lower values of u_h obtained from an ADCP in Mooring A were observed (Figure 4.24(b)) compared to all other field campaigns. u_h did not exceed $0.5ms^{-1}$ throughout the sampling period, including spring tides. Less tidal asymmetry in u_h was displayed, for example at Mooring B the maximum average ebbing u_h was $0.63ms^{-1}$ compared to $0.66ms^{-1}$ for the flood over the sampling period. At Mooring A the maximum flooding u_h was on average $0.2ms^{-1}$ faster than the ebb over the mooring deployment. A disparity in time between the flood and ebb phase was also present at both mooring locations. At Mooring A the ebb was 4.3 times longer than the flood on average, whereas the ebb at Mooring B was 2.5 times longer than the flood. u_h was considerably stronger in Mooring B than Mooring A in November (Figure 4.25(b))and comparable to values observed in previous field campaigns at this location. The maximum flooding values of u_h were $0.3ms^{-1}$ faster on average. C_v in Mooring A presented a diurnal tidally modulated signal, observed in previous field campaigns at this location in the estuary (Figure 4.24(c)).

The maximum C_v did not correspond with high water in November however, it was observed during the ebb phase, after peak tidal flows occurred. At Mooring B C_v displayed a minor and a major peak per tidal cycle (Figure 4.25(c)). The minor peak corresponded with maximum u_h on the ebb, the major peak in C_v occurred during the ebb phase, after the maximum C_v value was observed at Mooring A. Both mooring locations presented a diurnal tidally modulated signal in D_{50} (Figure 4.24(d) and 4.25(d)). Maximum values of D_{50} at both Mooring A and Mooring B corresponded with the major peak in C_v.

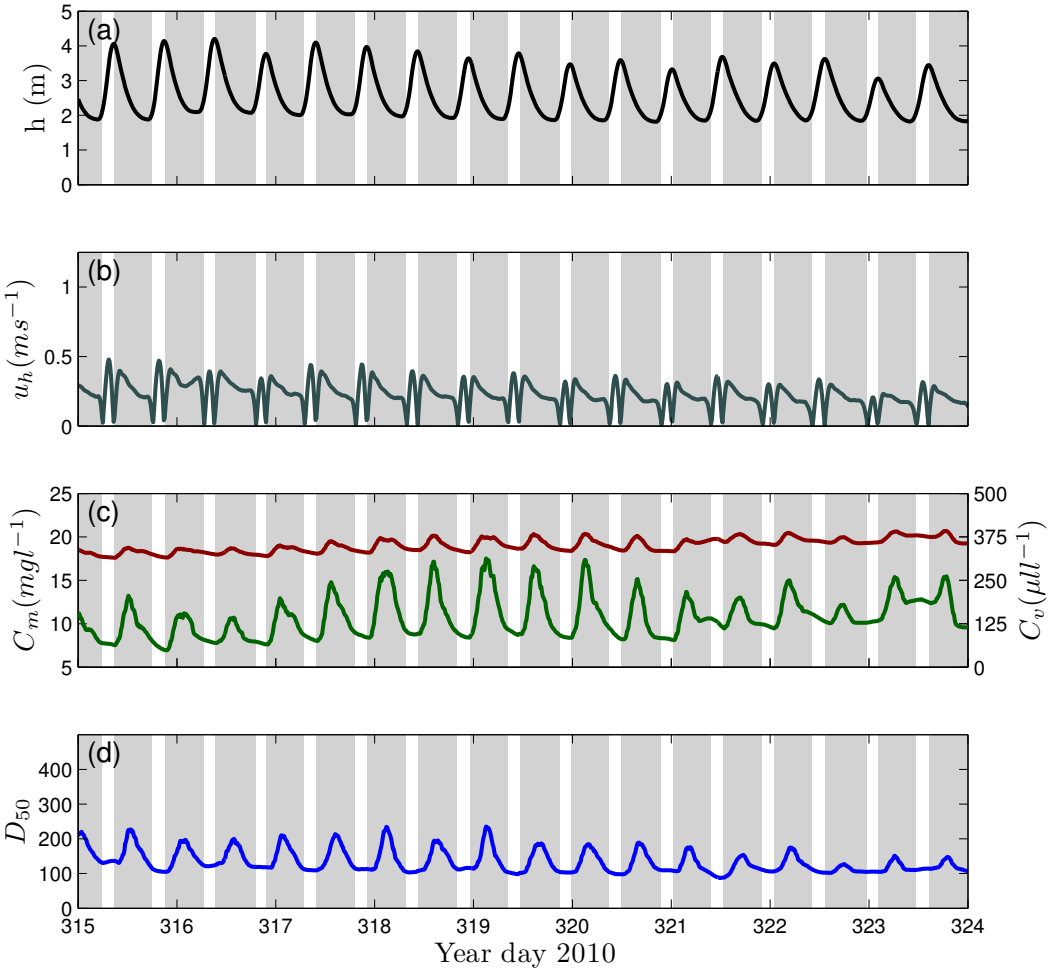

Figure 4.24: Time series of *in situ* SPM observations and hydrodynamic characteristics in Mooring A in November 2011.(a) $h(m)$. (b) u_h (ms^{-1}). (c) Dark green line is C_v (μll^{-1}) $30cm$ above the bed. Dark red line is $C_m(mgl^{-1})$.(d) $D_{50}(\mu m)$.

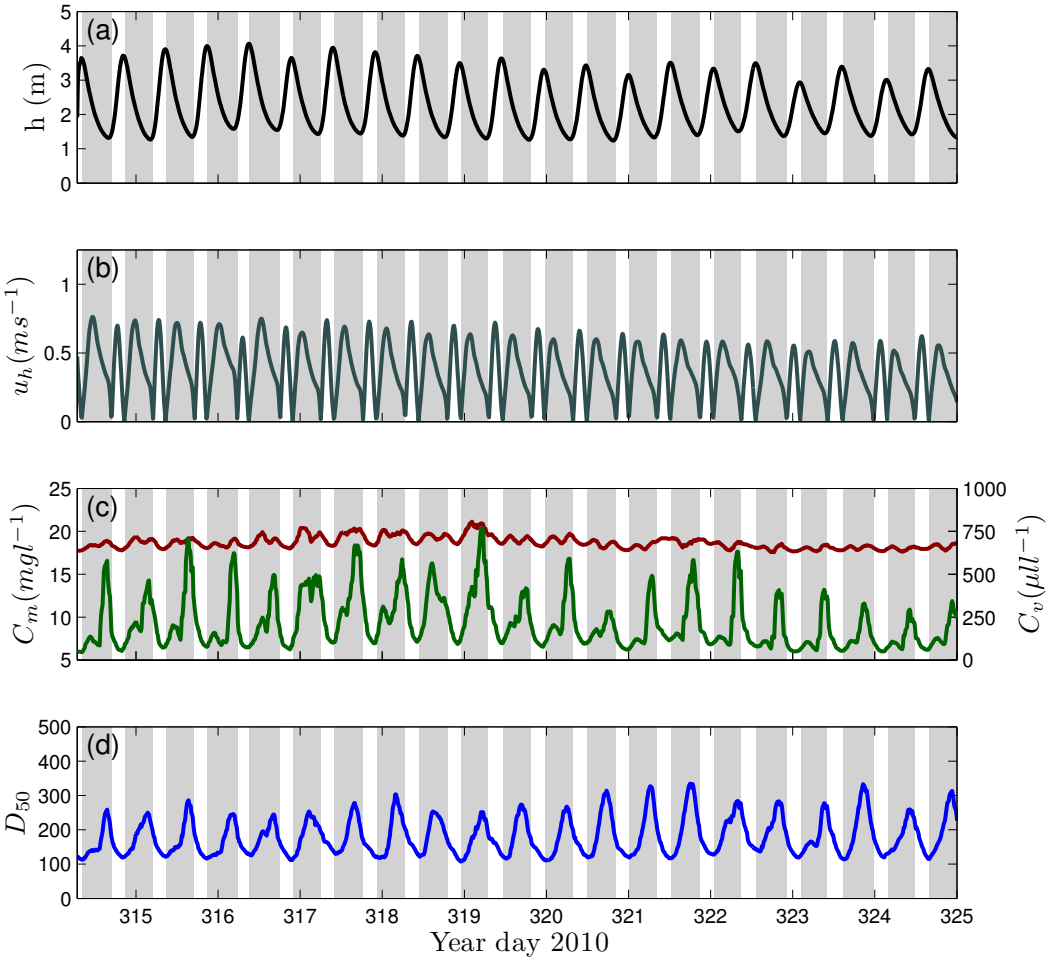

Figure 4.25: Time series of *in situ* SPM observations and hydrodynamic characteristics in Mooring B in November 2011.(a) $h(m)$. (b) u_h (ms^{-1}). (c) Dark green line is C_v (μll^{-1}) $30cm$ above the bed. Dark red line is $C_m(mgl^{-1})$.(d) $D_{50}(\mu m)$.

Table 4.3: A summary of mean D_{50} (μm) near to the bed for each sampling period. Numbers in brackets represent the standard deviation about the mean value.

	March	**April**	**September**	**September (River event)**	**November**
Mooring A	134.6(40.1)	109.7(18.1)	121.3(32.2)	198.0(30.4)	133.6(31.7)
Mooring B	186.7(42.7)	180.0(29.3)	-	-	180.0(54.8)

Table 4.3 summarises the mean values of D_{50} for each sampling period, allowing a broad comparison of particle size across the field campaigns. The associated error values are relatively large, however this is to be expected as particle size changes significantly on a tidal and lunar scale as shown by the LISST-100 time series data.

Overall Table 4.3 indicates D_{50} was larger at Mooring B compared to Mooring A, however the average size did not appear to vary significantly between field campaigns for each Mooring. But, in September the river event appears to have had an effect on the average particle size, the average D_{50} increased by 67% during the river event.

LISST-100X profiling data

Spatial surveys

In addition to time series data of SPM concentrations, vertical profiles of the water column are presented from the mouth of the estuary up into the TIR for data collected in March, April, September and July.

March

The spatial survey conducted in March indicates the vertical distribution of C_m remained uniform at high water (Figure 4.26(a)). Moreover, C_m did not present a large horizontal gradient either, depth averaged C_m at the mouth was $8.7 mgl^{-1}$ compared to $8.1 mgl^{-1}$ in the river. Chl_a remained within the same order of magnitude, concentrations were higher at the mouth of the estuary. Figure 4.26(c) describes elevated D_{50} throughout

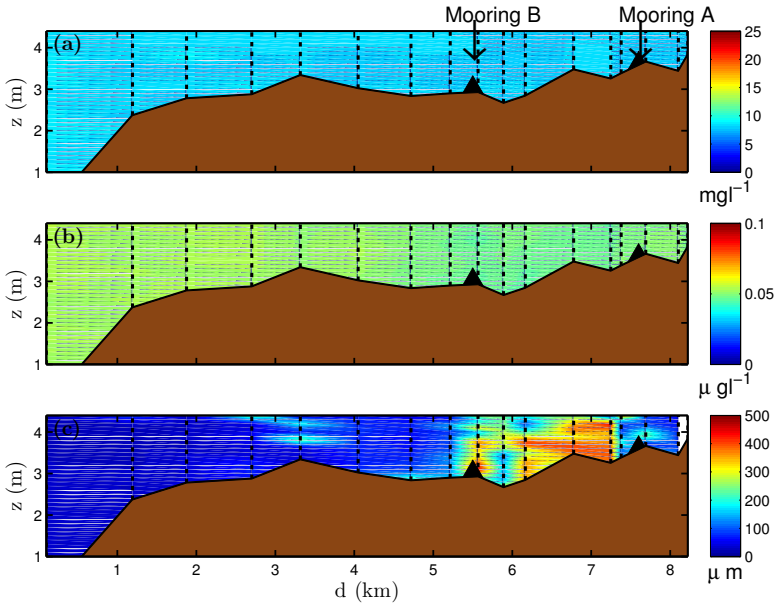

Figure 4.26: Spatial survey profiles of (a) mass concentration (mgl^{-1}), (b) chlorophyll concentration *a* $Chl_a(\mu gl^{-}1)$ and (c) median particle size $D_{50}(\mu m)$ in March 2011. z is local depth relative to the surface and d is distance from the mouth of the estuary. Vertical black dashed lines indicate profiling locations.

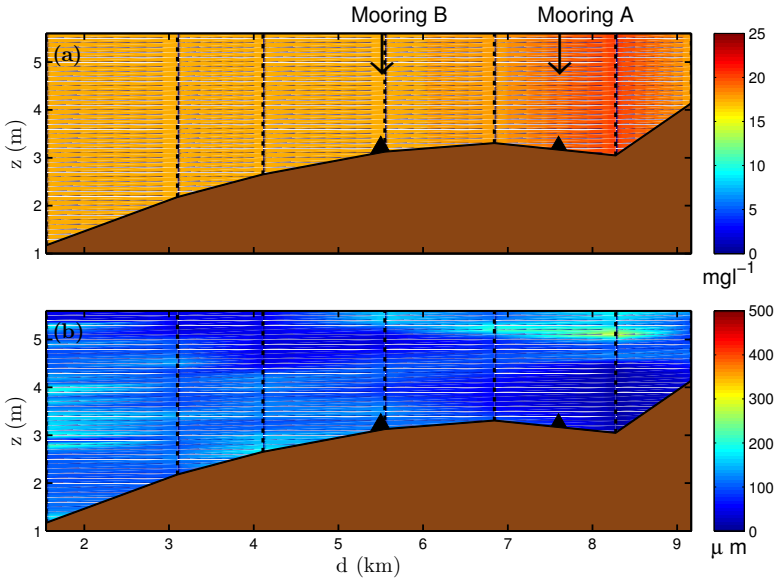

Figure 4.27: Spatial survey profiles of (a) mass concentration (mgl^{-1}) and (b) median particle size $D_{50}(\mu m)$ in April 2010.z is local depth relative to the surface and d is distance from the mouth of the estuary. Vertical black dashed lines indicate profiling locations.

the water column at Mooring B and in between the two moorings.

April

Figure 4.27 represents the vertical distribution of C_m and D_{50} in April. C_m was vertically and horizontally homogeneous in April with a depth averaged value of $17.3mgl^{-1}$ at the mouth and $17.6mgl^{-1}$ in the river. Larger particles were observed at the surface compared to the bed in April and the size of particles at the surface increased spatially towards Mooring A.

July

C_m profiles in July were uniformly distributed vertically and presented concentrations similar to previous field campaigns. Figure 4.28(b) describes the vertical structure of

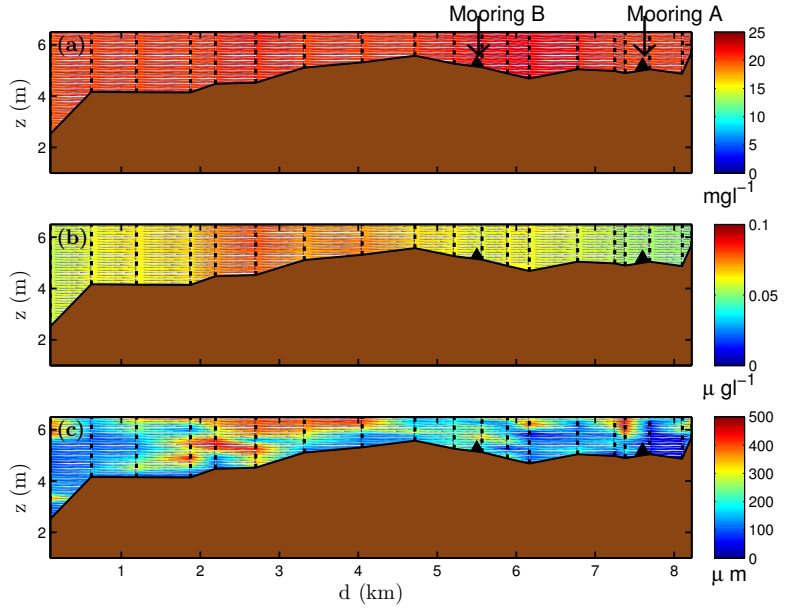

Figure 4.28: Spatial survey profiles of (a) mass concentration (mgl^{-1}), (b) chlorophyll concentration *a* $Chl_a(\mu gl^{-}1)$ and (c) median particle size $D_{50}(\mu m)$ in July 2011. z is local depth relative to the surface and d is distance from the mouth of the estuary. Vertical black dashed lines indicate profiling locations.

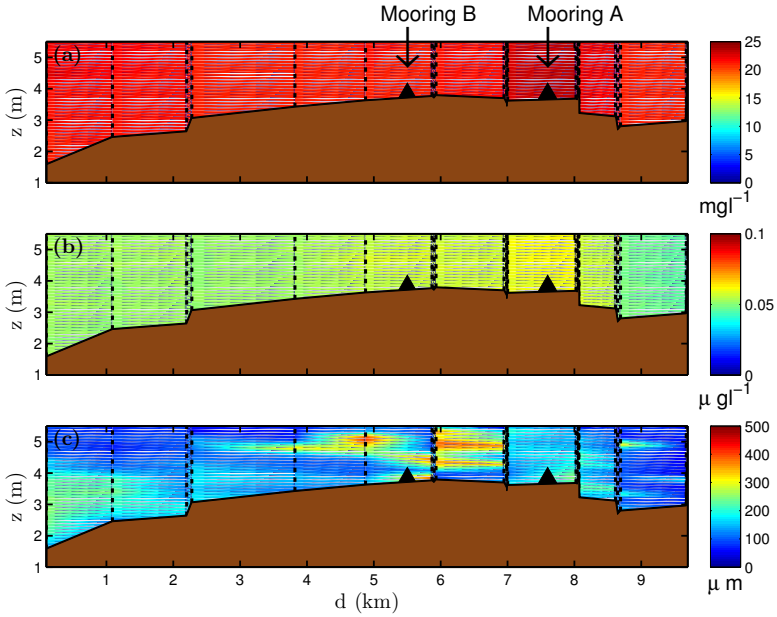

Figure 4.29: Spatial survey profiles of (a) mass concentration (mgl^{-1}), (b) chlorophyll concentration *a* $Chl_a(\mu gl^{-}1)$ and (c) median particle size $D_{50}(\mu m)$ in September 2010. z is local depth relative to the surface and d is distance from the mouth of the estuary. Vertical black dashed lines indicate profiling locations.

Chl_a throughout the estuary, highest concentrations were observed closest to the mouth of the estuary. It should be noted that Chl_a were higher in July than in the other observational periods. A rise in Chl_a between $2-4km$ from the mouth coincided with a rise in D_{50} throughout the water column (Figure 4.28b and c).

September

Figure 4.29(a) also infers vertical homogeneity in September with respect to C_m. The overall concentrations were higher in September than in April by an average of $4mgl^{-1}$. The spatial survey presented in Figure 4.29 was carried out on day 255, 2 days before the major flood event. Therefore this survey does not represent extreme river event conditions. Chl_a values were higher within Mooring B than at Mooring A or the mouth of the estuary (Figure 4.29(b)). D_{50} did not present an obvious spatial pattern. $5km$ from the mouth of the estuary a population of larger particles was observed near the bed

and between $6 - 7km$ from the mouth larger particles occurred throughout the water column (Figure 4.29(c)).

Anchor station surveys

Vertical profiles of the water column were undertaken with the LISST-100 and CTD at the Anchor station (shown in Chapter 3) for 6 hours during the flood and into the later half of the ebb. Anchor station surveys were carried out in April and September 2010, April data are presented in this section whilst data from September is examined in a later Chapter. The temporal scale of sampling at the Anchor station was governed by water levels, at low water it was not logistically possible to sample. The advantage of profile sampling at the Anchor station is that the data provides information of the whole water column between Mooring A and Mooring B, which can aid our understanding of the processes governing SPM characteristics occurring at the moorings.

April

Figure 4.30 shows the evolution of current velocity (u), salinity, mass concentration (C_m) and D_{50} from the early stages of the flood to the end of the ebb for a spring tide in April. At the onset of the flood when u was at maximum and the salinity gradient was high, an increase of C_m was observed corresponding with small particles (Figure 4.30). A rise in small particles coinciding with a rise in C_m can either be due to resuspension of smaller particles from the bed at a time of faster current velocities or simply an advection signal from the marine influence. At high water C_m decreased compared to the value during the flood, however D_{50} increased. This could be due to flocculation occurring at a more quiescent period of the tide, furthermore the decline in C_m may be due to deposition of SPM. Moving on to the period peak ebb current velocities, C_m remained relatively unchanged whilst D_{50} decreased, as there was no change in mass the change in size must be due to de-flocculation as a result of maximum u during the ebb. Finally towards the period of low water, Figure 4.30d shows D_{50} increased again as u and salinity decreased

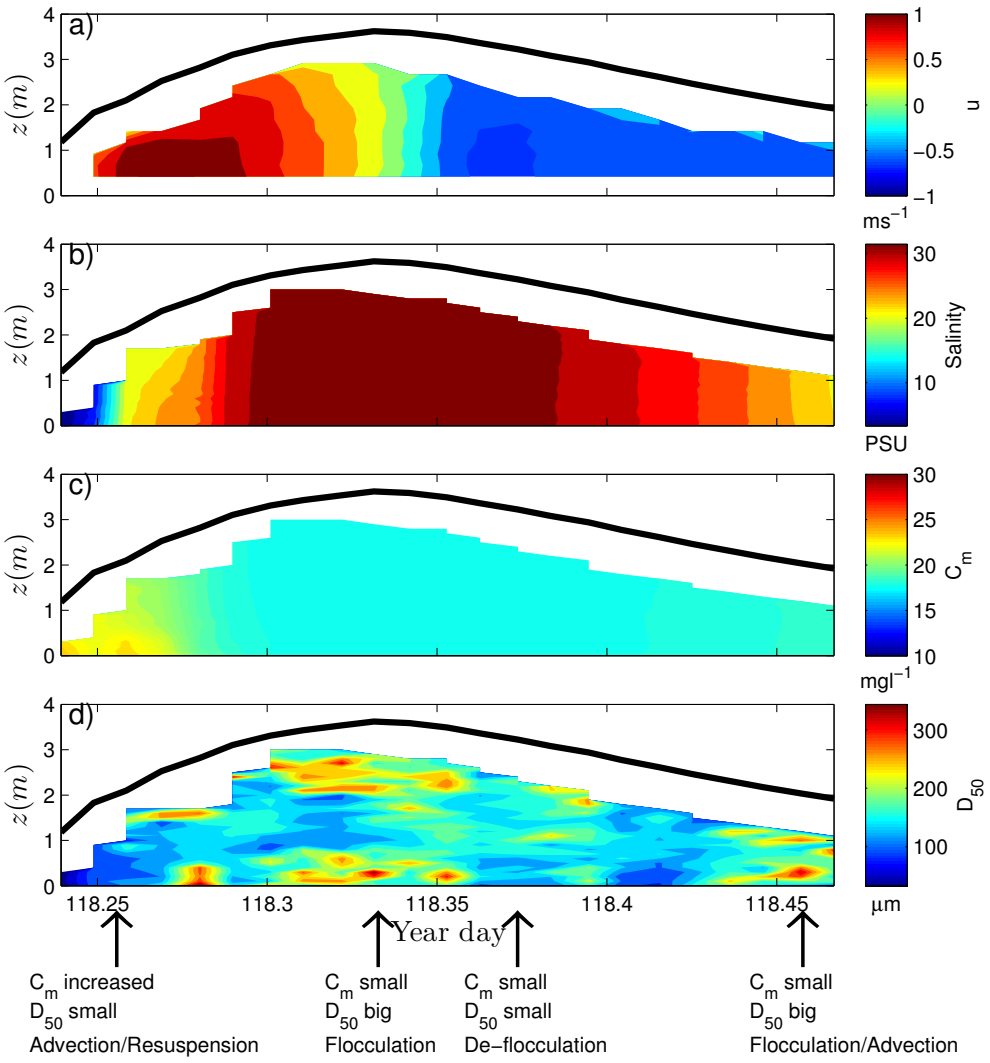

Figure 4.30: Temporal Anchor Station survey of hydrodynamic and SPM characteristics during a spring tide in April 2010. a) axial velocity profiles u. b) Salinity profiles. c) Profiles of mass concentration (C_m) (mgl^{-1}) and d) Profiles of D_{50} (μm).

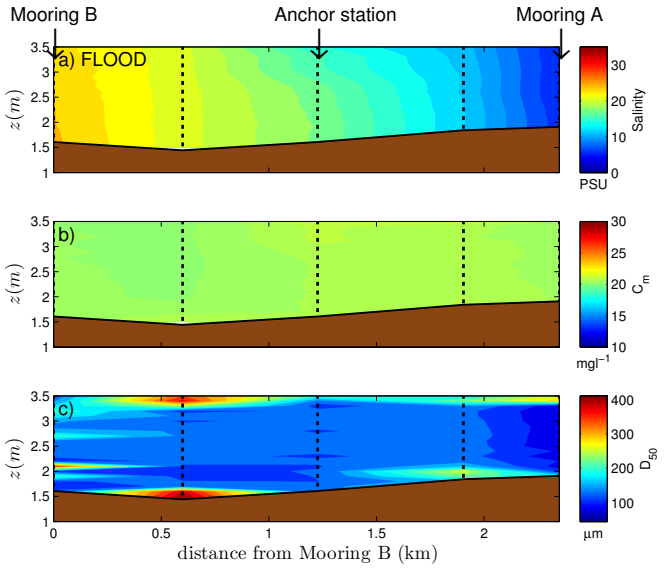

Figure 4.31: Spatial survey between Mooring A and B of Salinity and SPM characteristics during the flood of a spring tide in March 2011. a) Salinity profiles. b) Profiles of mass concentration (C_m) (mgl^{-1}) and c) Profiles of D_{50} (μm).

and C_m remained constant, again indicative of flocculation mechanisms.

It is also important to note the affects of the river, as the tidal phase moves towards low water terrestrially derived SPM can dominate the SPM characteristics through advection, however if that were the case in April a change in C_m would have been observed. The Anchor station data shown in Figure 4.30 complements the characteristics observed at Mooring A and B in April during spring tides, Figures 4.22 and 4.23 both present a semi diurnal signal in D_{50} and peaks were observed at high and low water as shown in Figure 4.30d.

Spatial surveys between Mooring A and B

March

Field campaigns carried out in March, July and November substituted the Anchor station survey for spatial surveys between Mooring A and B during the encompassing the

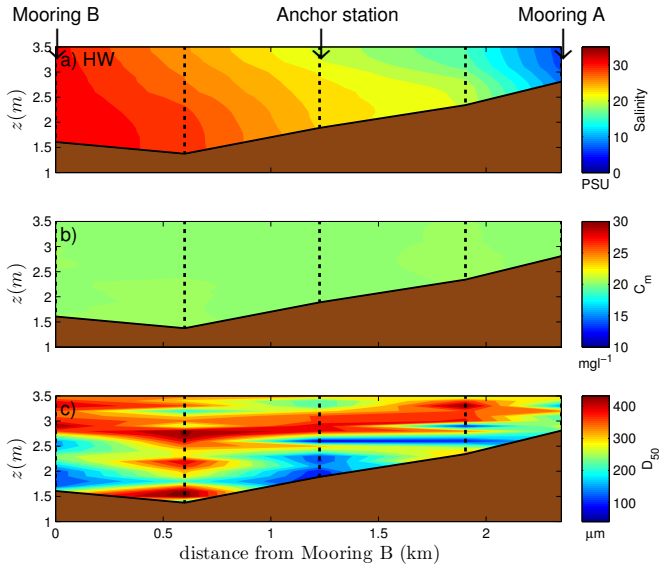

Figure 4.32: Spatial survey between Mooring A and B of Salinity and SPM characteristics of a spring tide at high water in March 2011. a) Salinity profiles. b) Profiles of mass concentration (C_m) and c) Profiles of D_{50} (μm).

flood and high water, thus obtaining vertical profiles of salinity and SPM characteristics throughout the RETZ. Figure 4.31 shows vertical profiles of salinity, C_m and D_{50} during the flood of a spring tide in March. Salinity profiles give an indication of the salinity gradient and extent of the marine influence. At this point in the flood Mooring B and the Anchor station were influenced by the marine intrusion, however Mooring A remained in freshwater (in the TIR). C_m exhibited a relatively constant concentration, whilst larger particles were observed at the surface and near the bed between Mooring B and the RETZ Anchor station. At Mooring A smaller particles were observed. As mentioned previously a change in particle size independent of C_m indicates the presence of flocculation processes. At high water the salt water intrusion was fully developed, Mooring B was in a totally marine environment with regards to salinity, and evidence of stratification was found (Figure 4.32). Again C_m remained relatively unchanged whilst D_{50} increased, however at high water the rise in D_{50} was evident throughout the RETZ. This complies with the time series LISST-100 data shown earlier in the Chapter in which both Mooring A and B exhibit a peak in D_{50} at high water during spring tides.

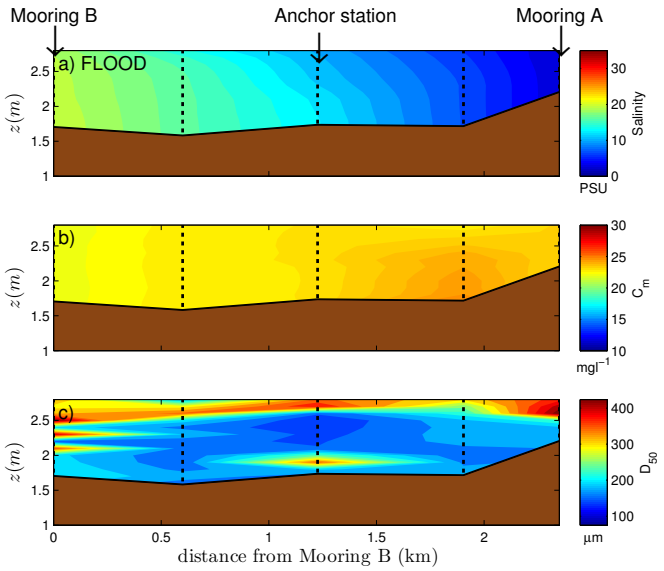

Figure 4.33: Spatial survey between Mooring A and B of Salinity and SPM characteristics during the flood of a spring tide in July 2011. a) Salinity profiles. b) Profiles of mass concentration (C_m) (mgl^{-1}) and c) Profiles of D_{50} (μm).

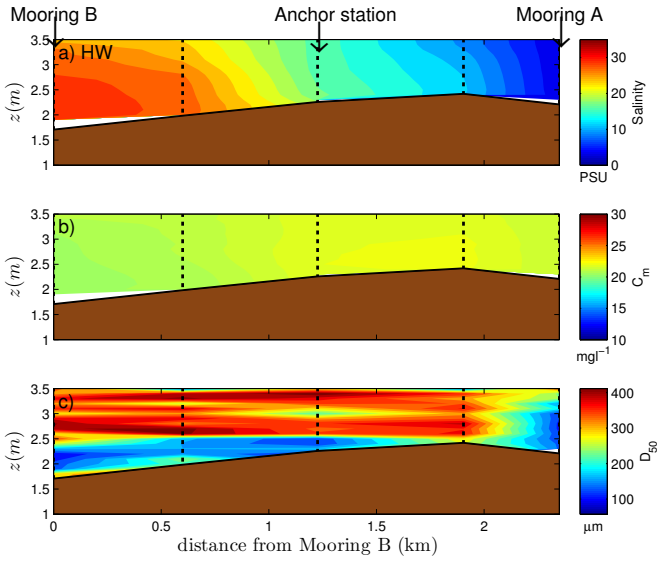

Figure 4.34: Spatial survey between Mooring A and B of Salinity and SPM characteristics of a spring tide at high water in July 2011. a) Salinity profiles. b) Profiles of mass concentration (C_m) (mgl^{-1}) and c) Profiles of D_{50} (μm).

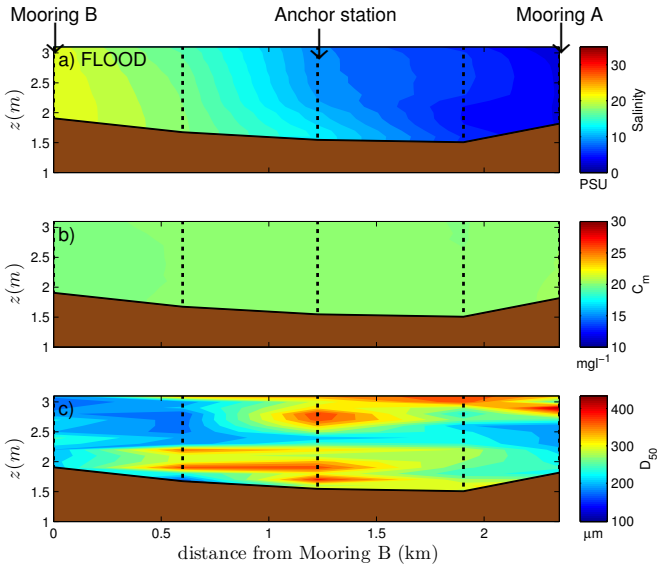

Figure 4.35: Spatial survey between Mooring A and B of Salinity and SPM characteristics during the flood of a spring tide in November 2011. a) Salinity profiles. b) Profiles of mass concentration (C_m) and c) Profiles of D_{50} (μm).

July

Moving onto profiling data collected in July, Figure 4.33 portrays the onset of the flood phase of the tide, salinities at Mooring B were below 20. Figure 4.33b indicates C_m did not vary notably throughout the RETZ with the exception of a slight increase at the bed around the intermediate profile between Mooring A and the Anchor station, which coincided with small particles, characteristic of a resuspension event. Throughout the RETZ elevated values of D_{50} were reported close to the surface (Figure 4.33c). As C_m did not increase at this time flocculation may be inferred. Figure 4.34 indicates a subtle longitudinal gradient in C_m occurred at high water, increasing towards Mooring A. In addition to this D_{50} notably increased throughout the RETZ with the exception of Mooring A. Due to the observed gradient in C_m advection of larger particles of marine origin may have occurred, possibly in conjunction with flocculation.

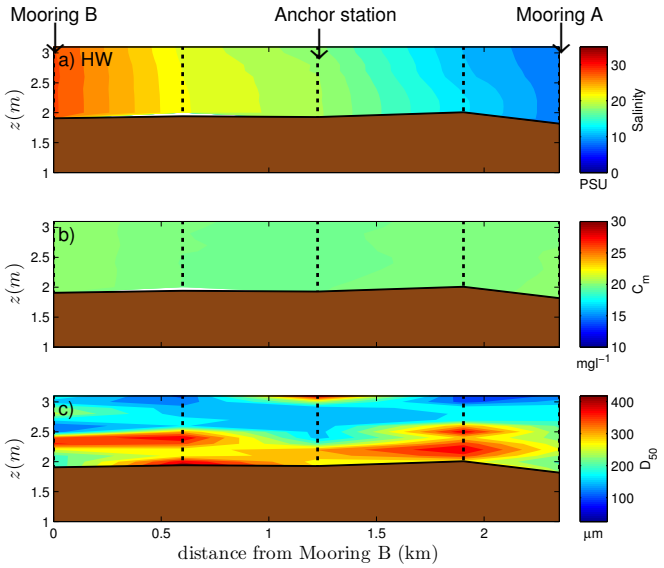

Figure 4.36: Spatial survey between Mooring A and B of Salinity and SPM characteristics of a spring tide at high water in November 2011. a) Salinity profiles. b) Profiles of mass concentration (C_m) and c) Profiles of D_{50} (μm).

November

In November spatial surveys for the RETZ show D_{50} increased throughout the water column between Mooring A and Mooring B at the beginning of the flood (Figure 4.35c). Interestingly, smaller particles were reported near to the bed at Mooring A and Mooring B at this time, which corresponds with the LISST-100 time series data collected at Mooring A and B in November. As C_m again remains relatively unchanged the rise in D_{50} could be explained by flocculation processes.

Finally at high water the concentration of larger particles remained largely confined between Mooring A and B (Figure 4.36c). The rise in D_{50} did not correspond with a change in C_m (Figure 4.36b) thus leading to an inference of flocculation again determining particle size at high water. Furthermore the population was observed closer to the bed at high water, therefore deposition of SPM may have been induced.

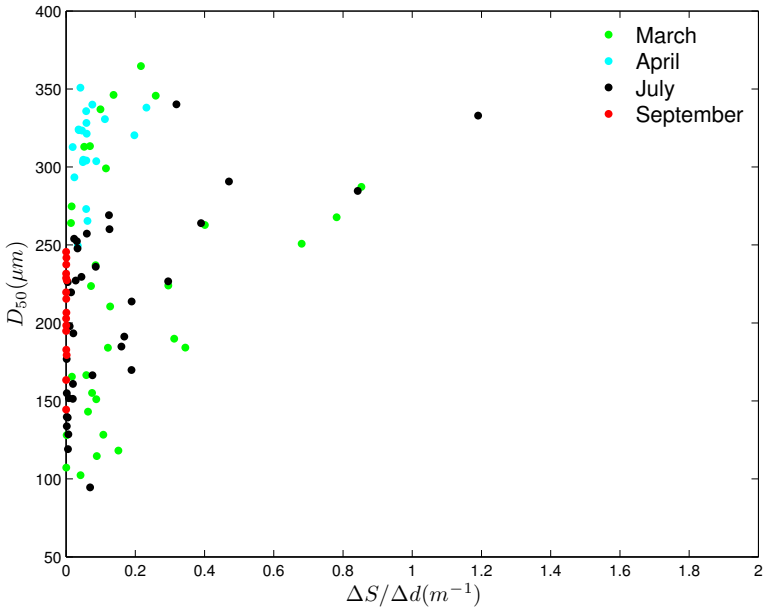

Figure 4.37: Particle size (D_{50}) as a function of the salinity gradient for profiling data collected from the RETZ anchor station in March, April, July, September and November.

Schlieren effects on LISST-100 particle size measurements in the RETZ

As discussed in Chapter 3 schlieren effects can give rise to an over-estimation of particle size by the LISST-100 when deployed in an environment with large density gradients (Styles, 2006; Mikkelsen et al, 2008). The estuarine environment experiences steep fluctuating density gradients therefore schlieren effects must be considered.

Figure 4.37 examines the relationship between the salinity gradient ($\Delta S/\Delta d$) and median particle size (D_{50}) for profiling LISST-100 and CTD data throughout all field campaigns. If schlieren was affecting the D_{50} measurements from the LISST-100 then a negative correlation would be seen between particle size and the salinity gradient. Figure 4.37 indicates this is not the case, in fact the largest particles are distributed towards the smaller salinity gradients. Therefore, it can be assumed schlieren effects were not causing a bias in the particle size distributions from the LISST-100 in this study.

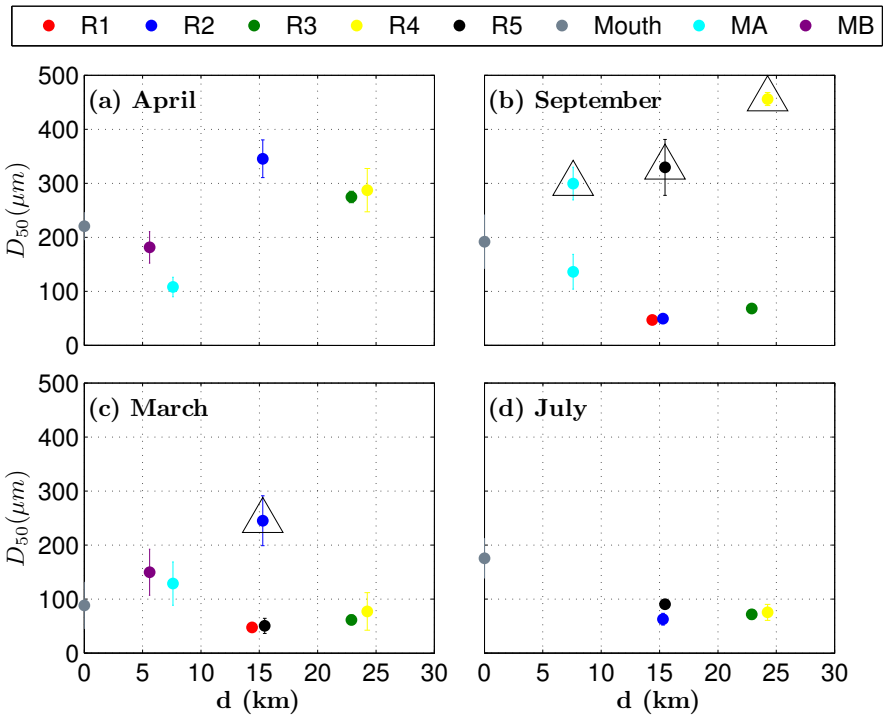

Figure 4.38: Seasonal variation in comparison between tidally averaged $(D_{50})(\mu m)$ at the estuary mouth with the 5 main tributaries of the Dyfi estuary. (a) April 2010, (b) September 2010, (c) March 2011 and (d) July 2011. R is the River station. MA is Mooring A. MB is Mooring B. d is the distance from the mouth of the estuary in km.

4.2.3 Particle size distributions from catchment to coast

This section compares particle size observations of the five main tributaries of the river Dyfi with particle size measurements obtained in the RETZ and at the mouth of the estuary. Figure 4.38 compares spot measurements of D_{50} from the tributaries introduced in Figure 3.10 in Chapter 3 with measurements at the mouth of the estuary and measurements made at low water for both Moorings A and B.

In April (Figure 4.38(a)) the depth averaged value of D_{50} over a tidal cycle at the mouth of the estuary was smaller than the size of particles in the tributaries. The average D_{50} of particles sampled in the tributaries was $302\mu m$ which is $118\mu m$ bigger than the D_{50} reported at the mouth. Furthermore, D_{50} values at Moorings A and B were also smaller

than D_{50} measured in the tributaries. The opposite was true in July, the D_{50} of the particles entering the river Dyfi were $100\mu m$ on average smaller than D_{50} observed at the mouth. As mentioned previously mooring data was not successfully obtained in July. In March with the exception of an anomalous result at River Station 2 (highlighted by a black), D_{50} in the tributaries was also smaller that at the mouth by an average of $28\mu m$. The standard error however shown in Figure 4.38 suggests this is not a significant result. Moreover D_{50} was reported as larger at Mooring A and B than the tributaries including the associated standard errors. This could indicate the RETZ was acting as a trap for larger particles in March.

The results from September present three significantly larger D_{50} values at river Stations 4 and 5 and at Mooring A, indicated by black triangles on Figure 4.38b. The D_{50} was notably higher at these stations, the measurements made at these sites were undertaken after the major river event on year day 257, which may have introduced larger particles to the system through inundation of parts of the flood plain typically above the high water mark. Considering just the D_{50} values acquired before the river event, on average D_{50} was smaller in the rivers by $136\mu m$ compared to the mouth of the estuary and Mooring A.

4.3 Discussion

This chapter presents data describing the hydrodynamic and SPM characteristics throughout the Dyfi system over varying temporal and spatial scales. Data from Moorings A and B allowed the investigation of near-bed hydrodynamic and sediment characteristics over tidal, lunar and seasonal time scales. Spatial surveys carried out at high water on a seasonal time frame allowed the comparison of vertical water column characteristics throughout the estuary at slack water. Anchor station data provides information of the temporal evolution of SPM and hydrodynamic characteristics at a position between Moorings A and B between the flood and ebb phase of the tide. Furthermore, spatial surveys between moorings A and B give rise to SPM characteristics and salinity

structure vertically throughout the water column and horizontally throughout the RETZ during the flood and at high water. Particle size data from tributaries encompassing the drainage pattern of Dyfi system are discussed and compared to the mouth of the estuary on a seasonal scale.

Firstly, considering the observations section 4.2.1, notable seasonal variations in Q were shown, data collected in March, April and November displays baseline levels of river flow rates having ranged from $10 - 30m^3s^{-1}$. Conversely in September during the river flood event Q exceeded $600m^3s^{-1}$. A strong tidal and spring-neap modulation in h was observed for all mooring data with the exception of September. Figure 4.3a shows the dampening effect a river event causes to h. Predominantly winds were blowing to the north east throughout the field campaigns with the exception of November in which winds travelling in a southerly direction prevailed (Figure 4.4d).

Moving on to the hydrodynamics of the study site, comparisons of u and ϵ at both mooring positions for each field campaign were made. Overall u and ϵ were greater at Mooring B mooring compared to Mooring A for all campaigns. In addition to this flood dominance in u occurred for all field campaigns with the exception of the river event in September, which will be discussed in a later Chapter. The fastest tidal currents were observed in April at Mooring B, maximum values of u_h on the flood during spring tides reached $1.2ms^{-1}$ with an associated tidal range of $2.0m$ (Figure 4.23b). Figure 4.25b shows the minimum values of spring tide flooding u_h as $0.75ms^{-1}$ in November with an associated tidal range of $2.1m$. Furthermore, characteristic of the Dyfi estuary, consistently observed was the strong asymmetry of the tide. The ebb was up to 2.5 times longer than the flood for all field campaigns.

In all cases a minimum in ϵ occurred during high water throughout the water column. In March and April at a time of prevailing winds travelling in a north easterly direction ϵ_h displayed a peak during the ebb which does not appear to be correlated with u_h, (Figures 4.9, 4.11 and 4.7); peaks corresponded with τ_{wind} and θ_{wind} by either the process of breaking waves or shear created between the wind and the surface of the water column.

u_{bed} and ϵ_{bed} show a stronger correspondence than u_h and ϵ_h, so near-bed tidal currents dominate dissipation rates at the bed, whereas at the surface the wind becomes influential (Figure 4.5). In November the opposite case was true, winds travelling to the south dominated and the maximum values of ϵ_h occurred during the flood (Figures 4.13 and 4.15). The maximum values of ϵ_h corresponded with the maximum opposing τ_w. As seen in March, ϵ_{bed} in November did not appear to be affected by τ_w or wind direction, it was u_{bed} that dominated ϵ_{bed} near to the bed (Figure 4.15).

Profiles of salinity and temperature from the mouth of the estuary to the TIR around high water show the water column structure. Vertical homogeneity was presented with respect to salinity and temperature from the mouth of the estuary to the TIR and temporally over the seasonal scale. Spatial surveys in the RETZ however observed some stratification with respect to salinity during the flood (Figures 4.31; 4.33; 4.35;). Profiles from July and September showed the warmest temperatures and the greatest range between the temperature ($3.2°C$ and $3.4°C$) of the river compared to the coastal ocean (Figures 4.18 and 4.29). The coldest temperatures of the water column occurred during March, presenting the least difference in temperature between the two water masses (Figure 4.16). Vertical homogeneity of temperature and salinity indicates the estuary was well mixed, due to the combination of shallow water and strong tidal currents.

The time series of LISST 100X data from the mooring deployments allows the comparison of near-bed suspended sediment characteristics within the estuary and between the measurement campaigns. At Mooring A similar SPM patterns were observed in March and April. During neap tides corresponding peaks in C_v and D_{50} coincided with peak flood current speeds. During spring tides however, a peak in C_v and D_{50} were both observed at high water and C_v showed another maximum at low water. At Mooring B the signals in SPM were more complex. In March and April, C_v presented a largely semi-diurnal signal coinciding with low and high water. In March D_{50} also followed the same semi-diurnal trend whereas in April spikes in D_{50} remained diurnal in frequency, occurring at high water. C_m displayed two significant peaks in March at Mooring B above $40mgl^{-1}$, which occurred at the same time as a minimum in C_v and a peak of

$400\mu m$ in D_{50}. A rise in concentration and a fall in volume in conjunction with particle size growing suggests advection or resuspension of larger particles and not flocculation (Figure 4.21c and d).

The SPM characteristics at Mooring A and B in November were anomalous when compared to March and April. An ebb dominance in SPM concentrations was reported despite the flood dominance in tidal currents. Concentration and size of sediments remained positively correlated, however the peaks occurred during the ebb phase of the tide. A peak was first reported at Mooring A after maximum ebb current speeds occurred and a second peak was shown at Mooring B further on in the ebb phase of the tide. A subsidiary peak in C_v was presented during maximum ebb currents at Mooring B. Conversely, at both Mooring A and B C_v,C_m and D_{50} displayed minimum values during the flood phase of the tide. This time series data can then be complemented by the spatial surveys conducted between Mooring A and B during the flood and at high water during a spring tide. Figure 4.35 indicates larger particles were introduced to the RETZ during the flood however they were not present in the mooring data as the moorings were deployed close to the bed. Furthermore Figure 4.36 shows further floc growth occurred at high water between Mooring A and B; if this flocculation signal remained trapped in the RETZ between the two moorings through deposition that would explain the absence of the signals in D_{50} at the mooring stations.

The spatial surveys carried out in March and April indicate a rise in C_m and D_{50} around Mooring A at high water which corresponds with Mooring A data (Figure 4.27 and 4.26). Moreover, Anchor station data collected during a spring tide in April complements the time series data from Moorings A and B during that period. Figure 4.30 shows the rise in D_{50} observed at high and low water, which did not correlate to a change in C_m therefore flocculation is assumed. The extent of floc growth at high water was greater than at low water, this could be due to increased salinity enhancing flocculation. The spatial surveys conducted in the RETZ during a spring tide in March also corresponded to the time series data collected at Mooring A and B, again presenting evidence to suggest flocculation was occurring at high water (Figure 4.32). In September and July elevated D_{50}

values spatially coincided with increased Chl_a which could suggest biologically enhanced flocculation was occurring in these areas (Figure 4.29 and 4.28).

Figure 4.38 showing river surveys indicates D_{50} was smaller in the tributaries compared to D_{50} at the mouth of the estuary and in the RETZ in March and July. The same was true for September with the exception of measurements made after the major river event on year day 257. This notable difference between D_{50} in the river pre and post river event indicates the river introduced larger particles in to the system which would not usually have occurred in suspension; due to increased run off from surrounding agricultural land. In April the converse was true, D_{50} was larger in the rivers compared to the mouth of the estuary and the RETZ under normal river conditions, although the standard error on this particular set of data were large compared to the values themselves. Moreover, Figure 4.38 presents spot measurements, therefore further sampling of these tributaries would be necessary to draw further interpretation on the comparison of particle size in the river with the mouth of the estuary and the RETZ.

4.4 Summary Points

- Mooring A and Mooring B locations present flood dominant tidal currents and asymmetric tides. The ebb was a minimum of 2.5 times longer than the flood phase of the tide.
- Spatial surveys show vertical homogeneity with respect to temperature and salinity from the mouth of the estuary to the TIR at high water. Spatial surveys concentrated in the RETZ report evidence of stratification with respect to salinity during the flood.
- Near-bed TKE dissipation values were well correlated with near-bed tidal currents. Poor correlations were reported between depth averaged values of dissipation and tidal current speeds. Wind stress and direction played an influential role in determining TKE dissipation values higher in the water column.

- Near-bed volume concentration and median particle size were well correlated overall, presenting strong diurnal and semi-diurnal signals at Mooring A and Mooring B, supporting evidence was also shown in the spatial survey data.
- Temporal anchor station survey data showed flocculation at high water and low water, advection of smaller particles during the flood and de-flocculation of larger particles coinciding with maximum ebb currents during a spring tide in April.
- Spatial surveys between in the RETZ provided evidence to suggest flocculation during the flood and more extensively at high water in March and November.
- On the whole, median particle size at the mouth was greater than median particle size measured at the river stations. However, during a river event the median particle size at river stations rose notably as larger particles were liberated from the freshly inundated parts of the flood plain.
- Finally, Schileren effects were negated due to the poor correlation between salinity gradient and particle size shown in Figure 4.37.

Chapter 5

Turbulence Control of Floc Size on a Tidal Scale

5.1 Introduction

This Chapter examines the relationship between turbulence and particle size on a tidal scale. Turbulence has been identified as playing a major role in determining particle size in the estuarine environment (Winterwerp, 2002; Fugate and Friedrichs, 2003; Winterwerp et al, 2006; Braithwaite et al, 2012). Understanding the controls of particle size on small temporal scales is important as size is directly to linked settling velocity (W_s). W_s governs the transport fate of suspended particles, determining whether they are deposited on the bed or transported throughout the estuary (Fugate and Friedrichs, 2003; Jackson et al, 1997). This is in turn important for the transport of biogeochemical components associated with SPM throughout the estuarine environment and the potential transfer to the coastal ocean.

The potential mechanisms for SPM transport are limited to resuspension, advection and flocculation/de-flocculation as discussed in Chapter 2. This Chapter aims to identify these mechanisms occurring in the RETZ and to assess their effects on particle size. Turbulence has the ability to enhance flocculation of particles in suspension by increasing collision rates; however, a critical shear stress is eventually reached which de-flocculates

particles (Dyer, 1989). It is also important to note the role of salinity in the estuarine environment in enhancing flocculation; in the presence of salt water, particles become less negatively charged and van der Waal forces of attraction cause clay particles to collide and remain attached.

Initially, particle size distributions (PSDs) are examined in differing tidal phases, followed by the direct comparison of D_{50} with turbulence and tidal currents. The relationship of effective density and D_{50} is explored in order to investigate particle characteristics further. An empirical model is then utilised to explore the significant controls on D_{50} on a tidal scale. Finally, the relationship between the Kolmogorov Microscale and particle size is considered.

5.2 Observations

Observations presented in this chapter include data from both Mooring A and Mooring B collected in March 2011, April 2010 and November 2011. Mooring data from September, collected at a time of an extreme river event will be considered in Chapter 6. LISST-100 data provide information on particle size (D) and volume concentration C_v. ADV and ADCP data are utilised to calculate current speeds u_{bed} and u_h, TKE dissipation rates ϵ_{bed} and ϵ_h, turbulence parameter G_{bed} and G_h and Kolmogorov microscale $\mu_{k_{bed}}$ and μ_{k_h}. This chapter aims to consider variations in floc size over tidal and lunar scales in conjunction with the local turbulence regime.

5.3 Results

5.3.1 Particle size distribution (PSD)

The particle size distribution (PSD) of both mooring sites throughout March, April and November are presented. The PSD is examined in conjunction with h and u_h. Investigating the full spectrum of particle size classes from $2.5 - 500\mu m$ provides a more

in depth understanding of floc size evolution than solely referring to D_{50}. It is then possible to ascertain how floc size changes according to the phase of the tide, the strength of ambient current speeds, and TKE dissipation rates in both regions of the estuary.

March

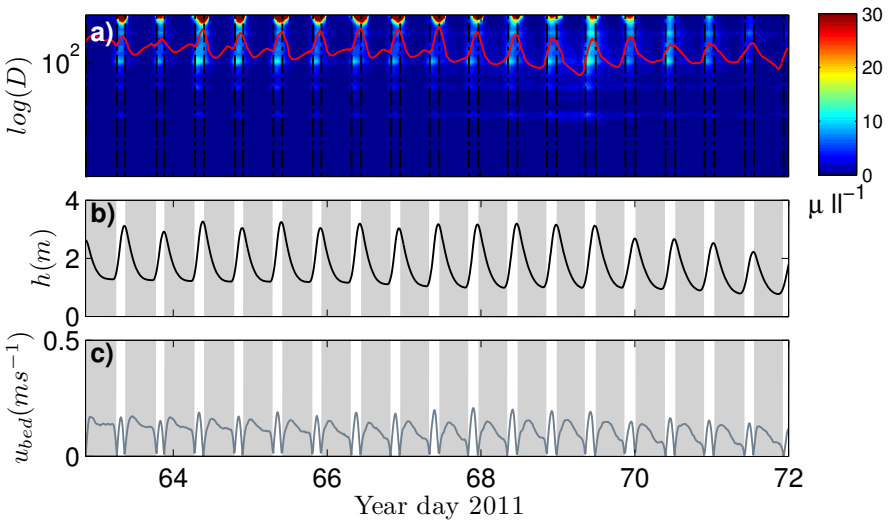

Figure 5.1: LISST-100 observations from Mooring A in March 2011 . (a) C_v distribution of particle size spectra (D). Red line is D_{50}. (b) h (m) and (c) u_{bed} (ms^{-1}). Grey shaded areas represent the ebb phase of the tide.

Figure 5.1 shows the LISST-100 and ADCP data for the whole sampling period at Mooring A in March. A repeating tidally modulated signal in both PSD and D_{50} was observed. Furthermore, a distinct difference between spring and neap tides PSDs was reported. Figure 5.2 examines a spring and neap tidal cycle in further detail; during spring tides the occurrence of large particles centred on $396\mu m$ corresponded with high water. A group of particles centred on $108\mu m$ were observed around low water and the early onset of the flooding tide. Less variation in particle size was reported for neap tides. The population of particles observed at low water on spring tides was still present. Conversely, at high water larger particles were not observed.

Figure 5.3 considers the particle size spectra for both spring and neap cases at periods of

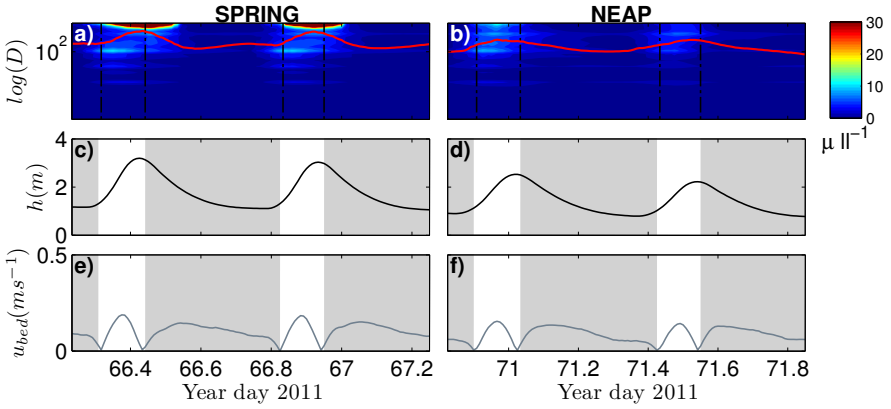

Figure 5.2: Spring and neap tidal cycles from Mooring A in March 2011. (a) and (b)C_v distribution of particle size spectra (D). Red line is D_{50}. (c) and (d) h (m) and (e) & (f) u_{bed} (ms^{-1}) for spring and neap tides respectively. Grey shaded areas represent the ebb phase of the tide.

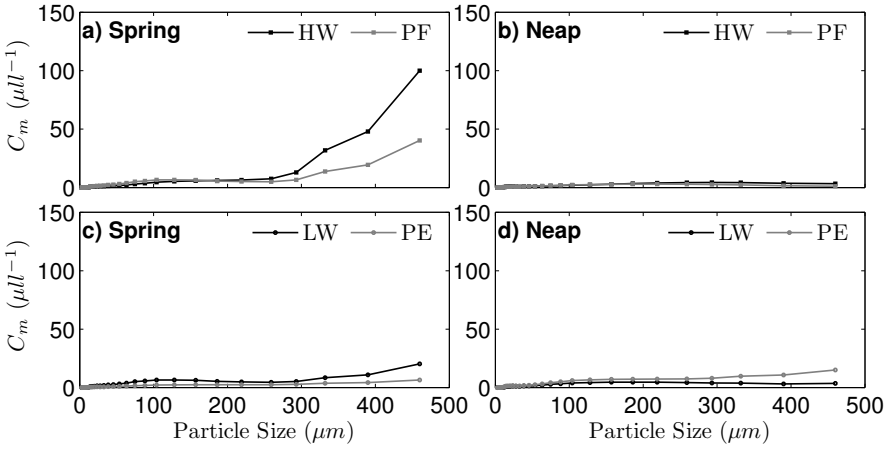

Figure 5.3: Particle size spectra for 1 tidal cycle comparing periods of high current speeds with slack water or low current speeds at Mooring A in March 2011. (a) and (b) Black line represents high water and grey line peak flood phase of the tide for a neap and spring tide respectively. (c) and (d) Black line represents low water and the grey line peak ebb phase of the tide for a neap and spring tides respectively.

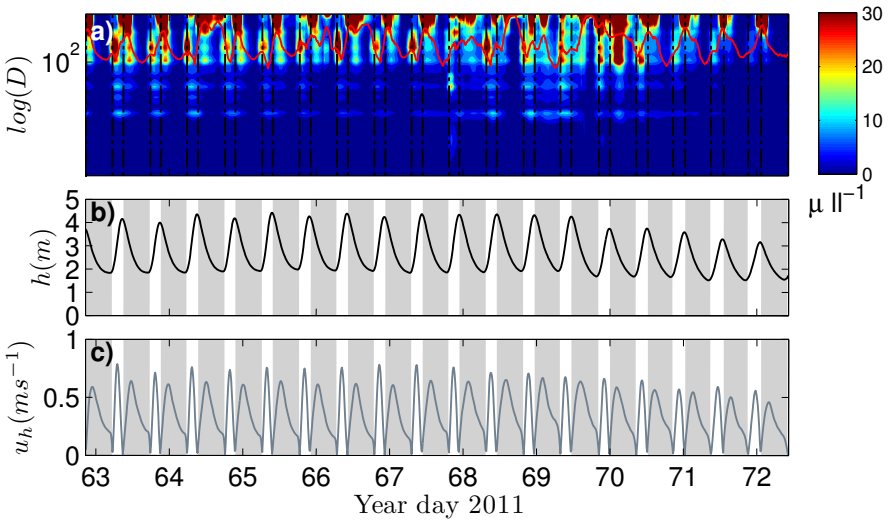

Figure 5.4: LISST-100 observations from Mooring B in March 2011 . (a) C_v distribution of particle size spectra (D). Red line is D_{50}. (b) h (m) and (c) u_h (ms^{-1}). Grey shaded areas represent the ebb phase of the tide.

low and high turbulent conditions. At high water during the spring tide, the maximum C_v of the largest particle size classes were observed. During periods of peak tidal current speeds and low water, C_v values were up to three times lower (Figure 5.3). Figure 5.3b displays the PSDs for the neap tide, in which the signal of high C_v values of particles greater than $300\mu m$ were not observed at high water. The PSDs do not vary significantly between the tidal phases in the neap case.

Figure 5.4 displays more complicated PSD and D_{50} patterns over tidal and lunar time scales for the data from Mooring B in March 2011. The rise in concentration of particles above $200\mu m$ did however correlate well with less turbulent conditions around high and low water. The spring to neap modulation was less pronounced in Mooring B compared to Mooring A.

Examining the PSD in more detail over a spring and neap tidal cycle indicates two distinct populations of particle sizes formed. One population size centred on $175\mu m$ which occurred at low water and the other centred on $375\mu m$ at high water (Figure 5.5). The same signal in PSD was recorded during spring and neap tides, although the

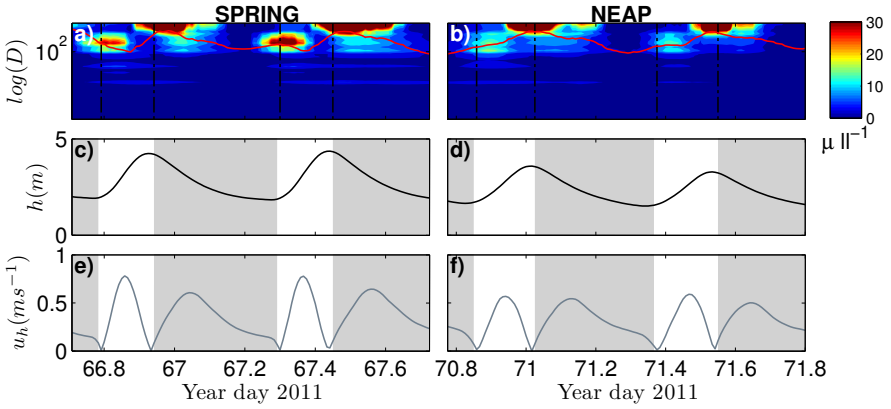

Figure 5.5: Spring and neap tidal cycles from Mooring B in March 2011. (a) and (b)C_v distribution of particle size spectra (D). Red line is D_{50}. (c) and (d) h (m) and (e) and (f) u_h (ms^{-1}) for spring and neap tides respectively. Grey shaded areas represent the ebb phase of the tide.

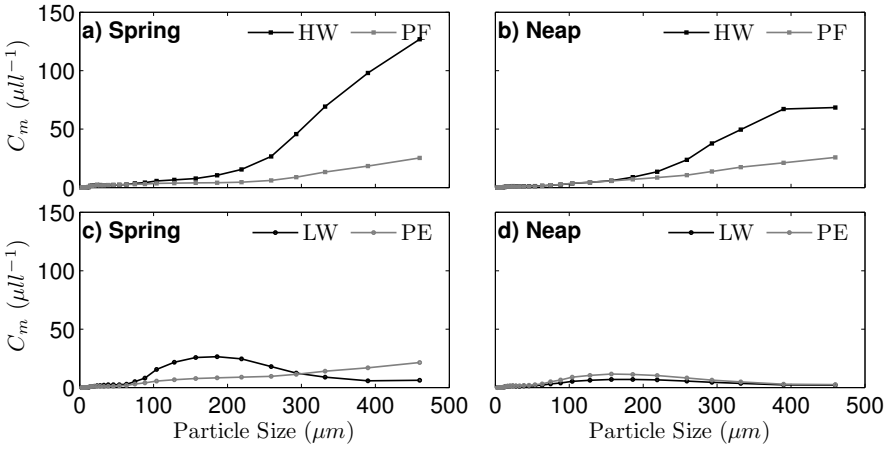

Figure 5.6: Particle size spectra for 1 tidal cycle comparing periods of high current speeds with slack water or low current speeds at Mooring B in March 2011. (a) and (b) Black line represents high water and grey line peak flood phase of the tide for a neap and spring tide respectively. (c) and (d) Black line represents low water and the grey line peak ebb phase of the tide for a neap and spring tides respectively.

Table 5.1: Summary of median particle diameter (D_{50}) and mass concentration (C_m) evolution on a tidal scale for Mooring A and B during spring and neap tides for data collected in March 2011. HW = high water, PE = peak ebb, LW = low water and PF = peak flood.

Spring				
	HW	**PE**	**LW**	**PF**
	$C_m(D_{50})$	$C_m(D_{50})$	$C_m(D_{50})$	$C_m(D_{50})$
Mooring A	18(264)	18(110)	19(124)	19(202)
Mooring B	21(226)	21(173)	24(139)	22(136)
Neap				
	HW	**PE**	**LW**	**PF**
	$C_m(D_{50})$	$C_m(D_{50})$	$C_m(D_{50})$	$C_m(D_{50})$
Mooring A	18(67)	18(68)	18(75)	18(75)
Mooring B	19(287)	19(212)	18(134)	19(206)

concentrations at low water were lower during the neap tide example.

Considering the particle size spectra in both the spring and neap case infers the large particles (greater than $300\mu m$) formed in conjunction with higher values of C_v, under less turbulent conditions at high water (Figure 5.6), however the magnitude was greater during spring tides. At low water, particles from $100 - 200\mu m$ were observed in both spring and neap cases, again greater C_v values were recorded for spring tides. During peak ebb tidal current speeds this signal is not observed. The neap tide presented similar PSDs to the spring tide with the exception of the period of maximum ebb tidal currents which exhibited a signal of particles ranging from $100 - 200\mu m$.

To summarise the March PSD data, on spring tides at both Moorings A and B the maximum C_v of a population of particles with an average size of $390\mu m$ was observed at high water (Figure 5.3a and 5.6a). This evidence is further consolidated by the rise in D_{50} reported at both Mooring locations, shown in Table 5.1. At Mooring B a smaller population of a similar C_v was reported at low water, this signal was not as pronounced at the Mooring A. The neap tide examples differ notably between the two sampling locations. At Mooring B the PSD was observed as seen on spring tides, however the C_v

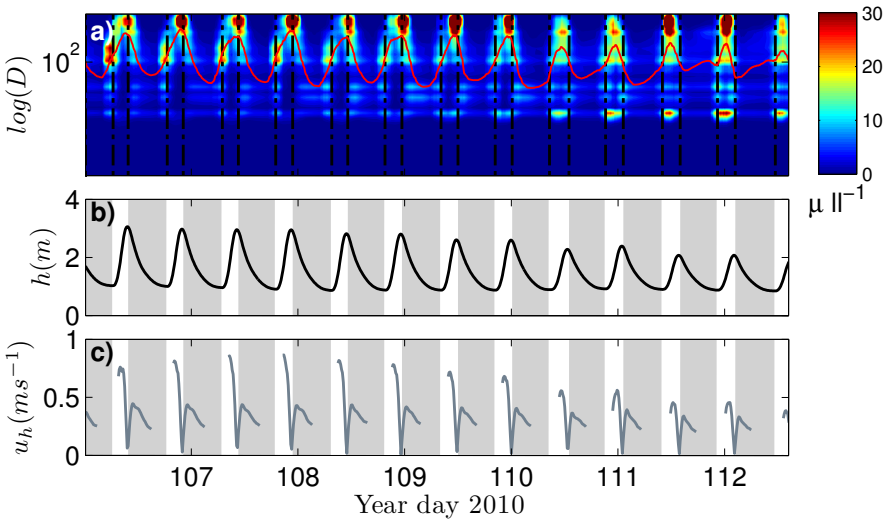

Figure 5.7: LISST-100 observations from Mooring A in April 2010 . (a) C_v distribution of particle size spectra (D). Red line is D_{50}. Black dashed lines indicate high and low water. (b) h (m) and (c) u_h (ms^{-1}). Grey shaded areas represent the ebb phase of the tide.

of particles was lower (Figure 5.6b). Conversely, Figure 5.3b suggests during neap tides at Mooring A, low C_v values were observed compared to Mooring B. The maximum C_v value was observed around low water continuing in to the flooding phase of the tide. This is shown via the D_{50} values in the summary Table 5.1.

April

Figure 5.7 shows the full time series of LISST-100 and ADCP data recorded at Mooring A in April. The PSD in Figure 5.7a suggests a strong repetitive signal in particle size over tidal and lunar time scales. Peak spring tide occurred on year day 108 and progressed into neap tides at year day 111 which exhibited the smallest current speeds and tidal range. A distinct spring to neap signal in PSD is evident. Smaller values of D_{50} occurred during neap tides than on spring tides. The PSD indicates two different size classes occurred during neap tides, which were not present during spring tides. This could explain the reduction of D_{50} during neap tides discussed in the previous results Chapter 4.

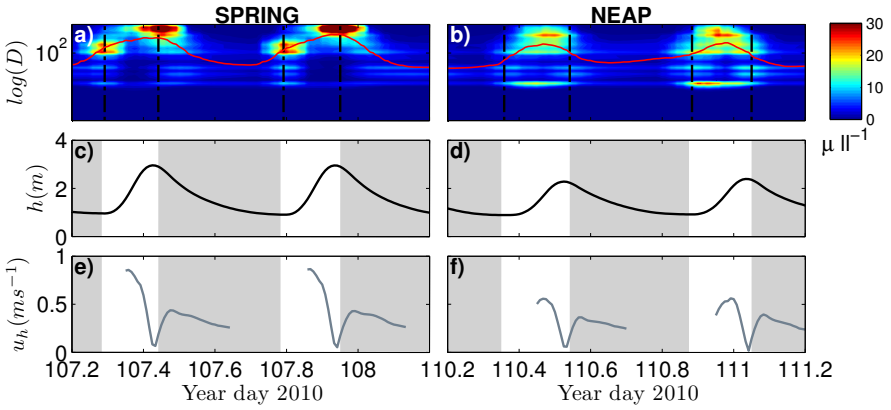

Figure 5.8: Spring and neap tidal cycles from Mooring A in April 2010. (a) and (b) C_v distribution of particle size spectra (D). Red line is D_{50}. Black dashed lines indicate high and low water. (c) and (d) h (m) and (e) and (f) u_h (ms^{-1}). Grey shaded areas represent the ebb phase of the tide.

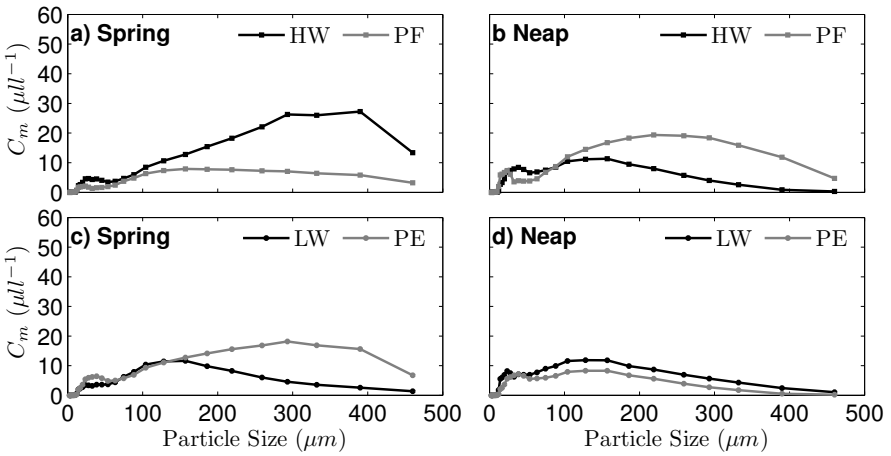

Figure 5.9: Particle size spectra for 1 tidal cycle comparing periods of high current speeds with slack water or low current speeds at Mooring A in April 2010. (a) and (b) Black line represents high water and grey line peak flood phase of the tide for a neap and spring tides respectively. (c) and (d) Black line represents low water and the grey line peak ebb phase of the tide for a neap and spring tides respectively.

In order to examine the modulation of PSD over a lunar scale, Figure 5.8 examines a spring and a neap tide in further detail. Figure 5.8a shows a population of larger particles centred on $375\mu m$ formed at high water during a period of low turbulent conditions on a spring tide. The population of particles forming around low water were consistently smaller (centred on $158\mu m$) than the population observed at high water. In the case of the neap tides Figure 5.8b indicates an entirely different PSD pattern. The largest population occurred during peak flood tidal currents along with a population of smaller particles centred on $19\mu m$.

Figure 5.9 investigates the difference in PSD in accordance with the level of turbulent kinetic energy exerted on the particles in suspension for a spring and neap tidal cycle. The population of large particles which occurred at high water during spring tides is shown in Figure 5.9a; C_v peaked between 300 and $500\mu m$. Conversely, Figure 5.9a also shows the larger particles found at high water were not observed as flood currents reached a maximum. Moreover the population of particles centred on $158\mu m$ was observed in Figure 5.9c at low water. The opposite is true for the neap tide, the highest C_v values were associated with particles around $250\mu m$ during the peak flood phase (Figure 5.9b); at high water the concentration of larger particles declined. Considering the neap tide example further, Figure 5.9d suggests the PSD for low water and peak ebb tidal currents were almost identical, in which both periods presented a maximum C_v value between 100 and $200\mu m$.

Moving onto the PSD from Mooring B in April 2010; Figure 5.10 also presents a strongly repeating pattern in the PSD, however the pattern was more complicated in this case. The population of smaller particles, centred on $19\mu m$ was observed at Mooring A from year day $110-112$, and also featured at Mooring B during neap tides (Figure 5.10a). u_h was larger at Mooring B than Mooring A, most notably during the ebb. Over 8 days, on average the maximum ebb current speeds at Mooring B were $0.32ms^{-1}$ faster than at Mooring A. The maximum difference occurred during spring tides ($0.4ms^{-1}$) and the minimum during neap tides ($0.14ms^{-1}$). In addition to this, the peak values of u_h were achieved on average 147 minutes later during the tidal phase at Mooring B than Mooring

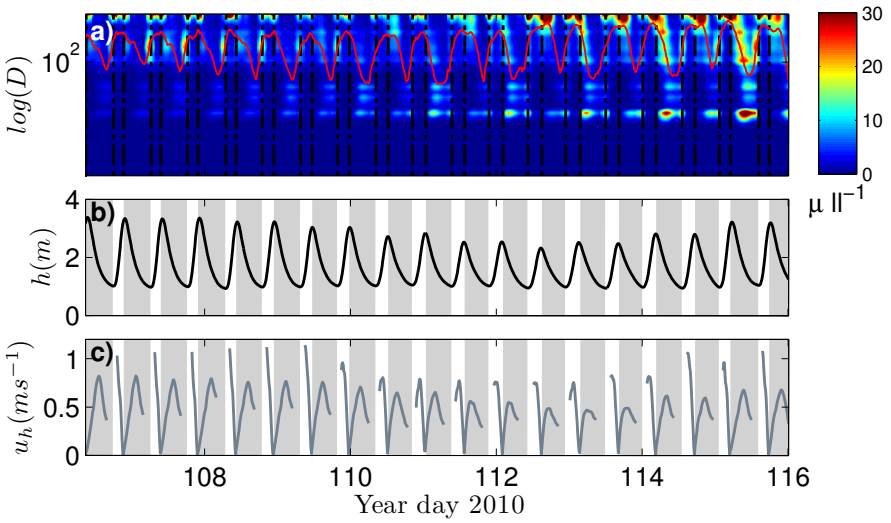

Figure 5.10: LISST-100 observations from Mooring B in April 2010 . (a) C_v distribution of particle size spectra (D). Red line is D_{50}. Black dashed lines indicate high and low water. (b) h (m) and (c) u_h (ms^{-1}). Grey shaded areas represent the ebb phase of the tide.

A for the duration of the sampling period.

During the spring tide shown in Figure 5.11a the largest particles were found at high and low water. At low water two definitive groups of larger particles were observed, one centred on $174\mu m$ and the other centred on $375\mu m$. During the flood the smaller of the two populations was not present. During neap tides a similar signal in PSD is described in Figure 5.11b with the exception of a population of small particles centred on $19\mu m$ occurring around low water and after high water, which coincided with the maximum ebb current speeds. The population of particles centred on $174\mu m$ detected in the water column around low water on spring tides was not as prevalent during neap tides, as shown in Figure 5.11b.

Figure 5.12 examines the difference in high and low turbulent conditions on PSD in further detail; the size spectrum at Mooring B was dissimilar to the spectrum presented from Mooring A, primarily as the maximum C_v was observed in the largest size classes, which could infer the size spectrum exceeded $500\mu m$ at this location. During the spring

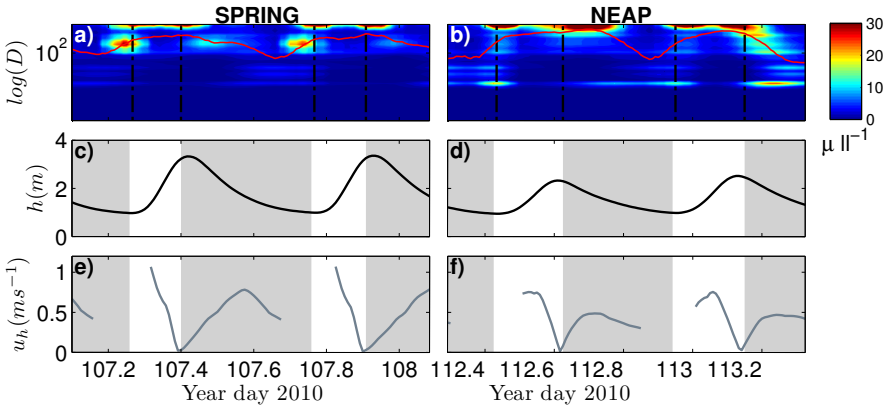

Figure 5.11: Spring and neap tidal cycles from Mooring B in April 2010. (a) and (b)C_v distribution of particle size spectra (D) and D_{50} in red (c) and (d) h (m) and (e) and (f)u_h (ms^{-1}) for spring and neap tides respectively. Grey shaded areas represent the ebb phase of the tide.

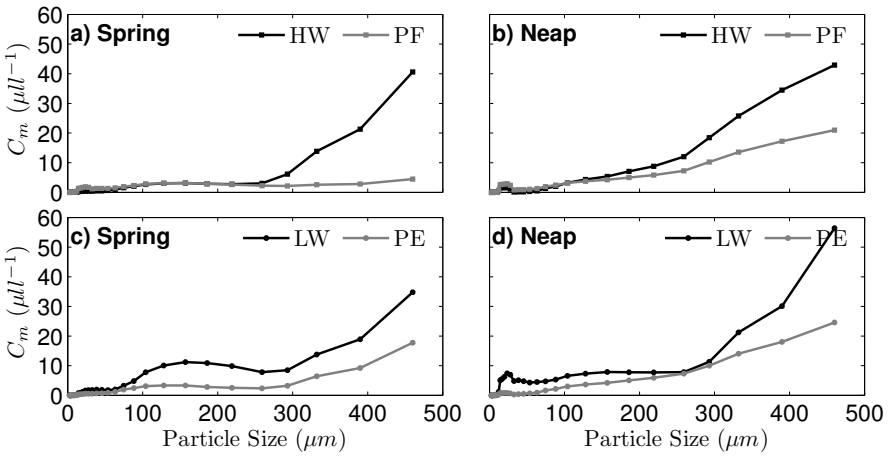

Figure 5.12: Particle size spectra for 1 tidal cycle comparing periods of high current speeds with slack water or low current speeds at Mooring B in April 2010. (a) and (b) Black line represents high water and grey line peak flood phase of the tide for a neap and spring tides respectively. (c) and (d) Black line represents low water and the grey line peak ebb phase of the tide for a neap and spring tides respectively.

Table 5.2: Summary of median particle diameter (D_{50}) and mass concentration (C_m) evolution on a tidal scale for Mooring A and B during spring and neap tides for data collected in April 2010. HW = high water, PE = peak ebb, LW = low water and PF = peak flood.

Spring				
	HW	**PE**	**LW**	**PF**
	$C_m(D_{50})$	$C_m(D_{50})$	$C_m(D_{50})$	$C_m(D_{50})$
Mooring A	15(266)	15(210)	16(112)	15(189)
Mooring B	16(262)	16(135)	17(193)	17(210)
Neap				
	HW	**PE**	**LW**	**PF**
	$C_m(D_{50})$	$C_m(D_{50})$	$C_m(D_{50})$	$C_m(D_{50})$
Mooring A	15(100)	15(80)	18(91)	18(158)
Mooring B	16(345)	17(294)	18(164)	16(312)

tide example the maximum C_v occurred at $460\mu m$ at high water, whereas during peak flood conditions the population of larger particles was not observed. Figure 5.12b presents the size spectrum for low water and peak ebb current stages of the spring tide. Both phases indicated similar spectra, the population of particles centred on $175\mu m$ seen in Figure 5.11a were observed and the greatest C_v corresponded with the largest particle size classes (greater than $300\mu m$). Figure 5.12b shows the size spectra for the periods of high water and peak flood tidal currents for a neap tide. Interestingly the spectra were similar, however there was a higher C_v of the largest size class which occurred during high water. At the time of low water and peak ebb tidal currents the largest concentration of particles were found again in the upper size classes (greater than $300\mu m$).

In summary, there are similarities to be draw between the PSDs seen at Mooring B and the Mooring A in April, however it is important to note the signals are more complicated at Mooring B. Markable differences were evident between spring and neap tides with respect to PSDs. During spring tides, maximum volumes of the largest size classes were reported at high water, at both Mooring A and B, this is reflected in maximum values of D_{50} shown in the summary Table 5.2. At low water a smaller population of particles were

observed, centred on $175\mu m$ at both sampling locations, however at Mooring B larger particles (greater than $300\mu m$) were also observed (Figure 5.12a). This explains the higher D_{50} shown in Table 5.2 for Mooring B at low water. During peak flood currents at both Mooring locations D_{50} increased compared to low water (Table 5.2).

For the neap tide case the PSDs observed at each location differ, at Mooring A the maximum C_v of the largest particle size classes corresponded with the flood phase of the tide rather than the more quiescent periods characteristic of high and low water. Further evidence of this is shown in Table 5.2, maximum D_{50} was observed during peak flood, Table 5.2 also indicates D_{50} was elevated during peak flood current speeds at Mooring B. At Mooring B during neap tides a signal of larger particles coincided with high and low water (Figure 5.12b), which is again conveyed by the D_{50} values in Table 5.2. The signal at high water persisted into the ebb phase of the tide, giving rise to elevated D_{50} values during maximum ebb current speeds.

November

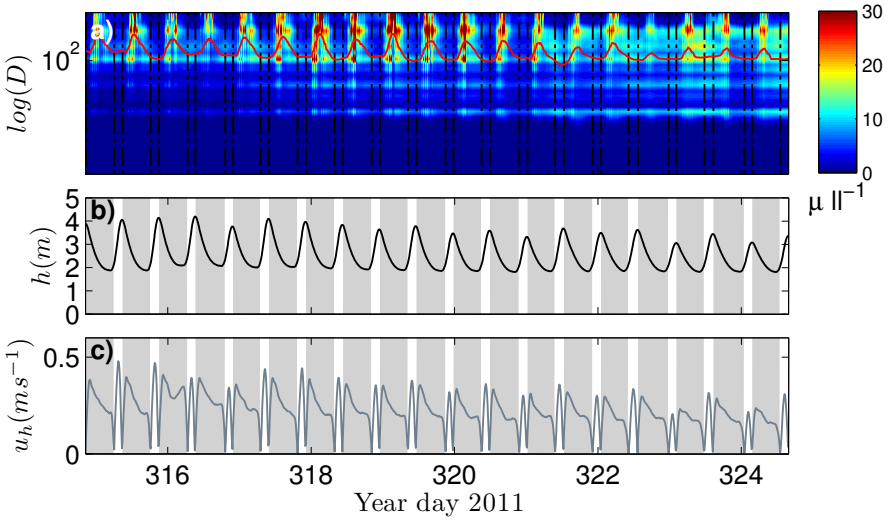

Figure 5.13: LISST-100 observations from Mooring A in November 2011 . (a) C_v distribution of particle size spectra (D). Red line is D_{50}. (b) h (m) and (c) $u_h(ms^{-1})$. Grey shaded areas represent the ebb phase of the tide.

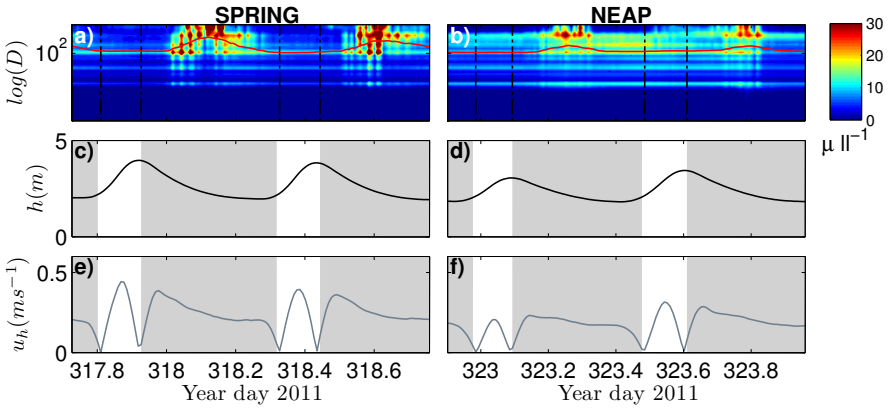

Figure 5.14: Spring and neap tidal cycles from Mooring A in November 2011. (a) and (b)C_v distribution of particle size spectra (D). Red line is D_{50}. (c) and (d) h (m) and (e) and (f) $u_h(ms^{-1})$ for spring and neap tides respectively. Grey shaded areas represent the ebb phase of the tide.

Moving onto data collected in November 2011. Primarily investigating the data collected from Mooring A; Figure 5.13 presents a strongly repeating pattern in PSD and D_{50} on a tidal and lunar time scale. It is important to note that current speeds during this period were relatively low compared with previous field campaigns. On closer inspection of this data set, Figure 5.14 suggests a different PSD pattern occurred at Mooring A compared to data collected in March and April.

Two distinct periods of elevated C_v of particles above $200\mu m$ were observed during each tidal cycle. This signal occurred during the ebb in both spring and neap cases, with the neap case having exhibited lower concentrations (Figure 5.14b). Interestingly the main signal occurred after peak ebb current speeds; therefore it is not obvious from the D_{50} data alone how SPM was entering the estuary. The LISST-100 measurements acquired by the Moorings A and B were point measurements obtained $0.3m$ from the bed. A point measurement would not represent the entire vertical profile of the water column, therefore SPM could have occurred higher in the water column. As the majority of larger particles were observed during the ebb, after peak currents speeds, the signal did not correlate with quiescent conditions as seen in March and April at Mooring A, thus the particle size distribution did not reflect this.

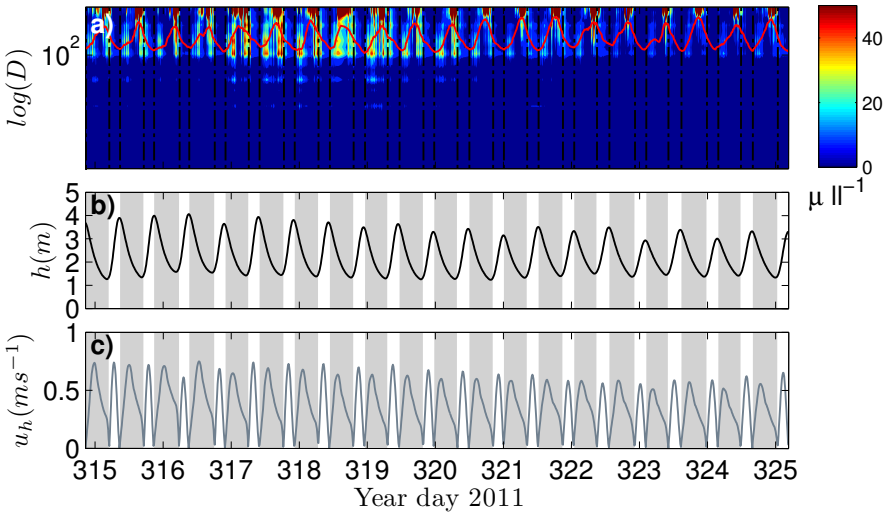

Figure 5.15: LISST-100 observations from Mooring B in November 2011 . (a) C_v distribution of particle size spectra (D). Red line is D_{50}. (b) h (m) and (c) $u_h(ms^{-1})$. Grey shaded areas represent the ebb phase of the tide.

Returning focus back to Mooring B, Figure 5.15 exhibits the PSD and D_{50} time series data. Higher values of u_h were reported at Mooring B compared to Mooring A and the PSD signals were more complex as seen in the March and April data.

During spring tides a semi-diurnal signal was observed. Figure 5.16a reports C_v increased for $200\mu m$ particles during peak ebb current speeds and another population of particles centred in $300\mu m$ before and during low water. As u_h increased during the flood a rise in C_v of larger particles was observed. During neap tides a similar pattern in PSD was found, however the concentrations were lower (Figure 5.16b).

Figure 5.17 presents regression analysis of G_h with D_{50} and C_v and u_h for the period of maximum ebb current speeds during a tidal cycle. G is a turbulence parameter typically employed in flocculation models (Winterwerp, 1998; Braithwaite et al, 2012), it is caluculated as follows:

$$G = \sqrt{\frac{\epsilon}{\nu}} \tag{5.1}$$

Where ν denotes the kinematic viscosity of water ($10^6 m^2 s^{-1}$) and ϵ is the TKE dissipation

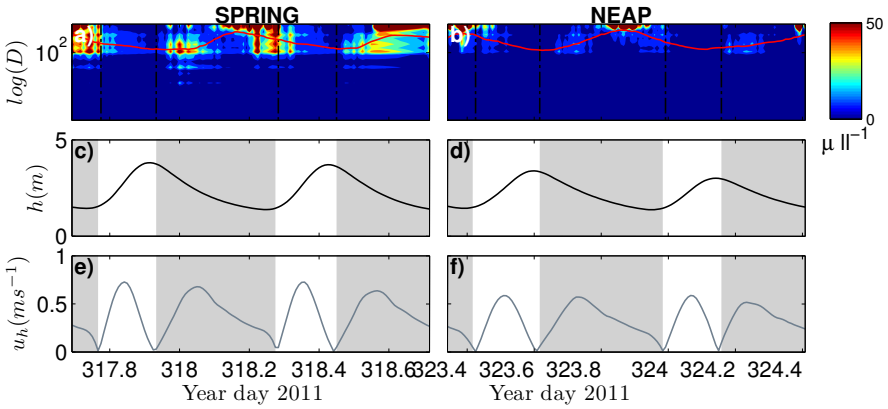

Figure 5.16: Spring and neap tidal cycles from Mooring B in November 2011. (a) and (b)C_v distribution of particle size spectra (D). Red line is D_{50}. (c) and (d) h (m) and (e) and (f)$u_h(ms^{-1})$ for spring and neap tides respectively. Grey shaded areas represent the ebb phase of the tide.

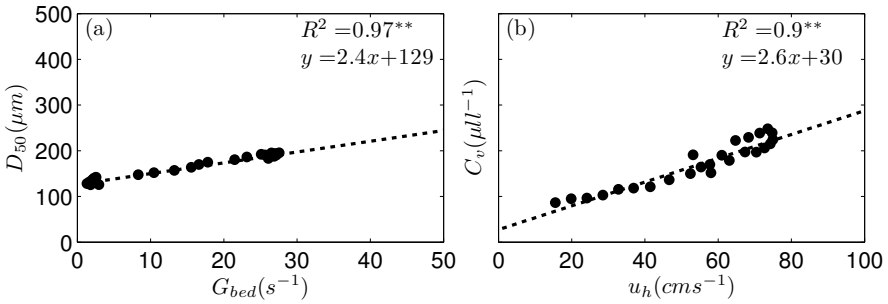

Figure 5.17: SPM characteristics and hydrodynamic properties of the water column in Mooring B during peak ebb current speeds in November 2011. (a) Relationship between D_{50} and G_h. (b) Relationship between C_v and u_h.

Table 5.3: Summary of median particle diameter (D_{50}) and mass concentration (C_m) evolution on a tidal scale for Mooring A and B during spring and neap tides for data collected in November 2011. HW = high water, PE = peak ebb, LW = low water and PF = peak flood.

Spring				
	HW	**PE**	**LW**	**PF**
	$C_m(D_{50})$	$C_m(D_{50})$	$C_m(D_{50})$	$C_m(D_{50})$
Mooring A	17(135)	18(130)	18(130)	18(134)
Mooring B	16(135)	16(280)	17(262)	17(193)
Neap				
	HW	**PE**	**LW**	**PF**
	$C_m(D_{50})$	$C_m(D_{50})$	$C_m(D_{50})$	$C_m(D_{50})$
Mooring A	19(103)	19(102)	19(105)	19(105)
Mooring B	16(198)	17(245)	18(215)	16(187)

rate (Wkg^{-1}), G thus represents the turbulent shear in the flow (Winterwerp, 1998). Figure 5.17a indicates a significant relationship between D_{50} and turbulent conditions represented by G, therefore floc size increased with larger values of G during this phase of the tidal cycle. Furthermore 5.17b infers a significant positive correlation between C_v and u_h during maximum ebb current speeds. This indicates C_v increased linearly with current speeds at this time.

In summary, the PSD at Mooring A displayed one major peak in C_v of particles above $200\mu m$ during both spring and neap tides after peak ebb current speeds occurred, although smaller concentrations were observed during neap tides. D_{50} values in Table 5.3 do not support this evidence as the largest particles were observed after peak ebb currents were reached. Table 5.3 indicates a background size class of $130\mu m$ during spring tides and $100\mu m$ during neap tides at Mooring A. Mooring B data reports two major peaks in C_v; one of $200\mu m$ particles coinciding with maximum u_h during the ebb and the other of particles above $200\mu m$ which occurred at the end of the ebb after the peak current speeds at Mooring A. The same PSD pattern was reported for spring and neap tides at Mooring B, neap tides displayed lower C_v values as seen at Mooring A. Table 5.3

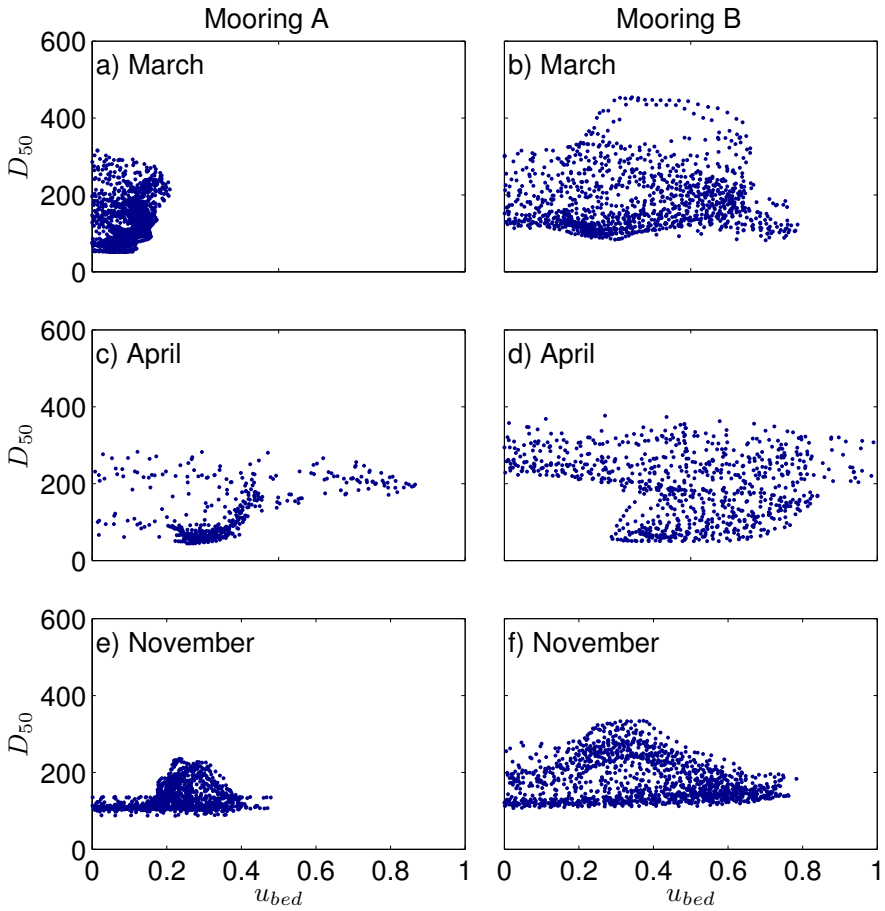

Figure 5.18: Comparison of correlations between median particle size (D_{50}) and current speed close to the bed (u_{bed}) for Mooring A and B in March, April and November. u_{bed} obtained from an ADV at Mooring A in March.

indicates the largest D_{50} values occurred during maximum ebb current speeds for both spring and neap tides at Mooring B, furthermore the overall D_{50} was larger at Mooring B than at Mooring A.

5.3.2 Interactions between D_{50} and turbulence conditions

Investigating time series of PSDs in conjunction with u_h and h has provided an understanding of particle size evolution on a tidal scale in the RETZ. The effects of turbulence on these PSDs must now be considered. As seen in Chapter 4 the relationship between

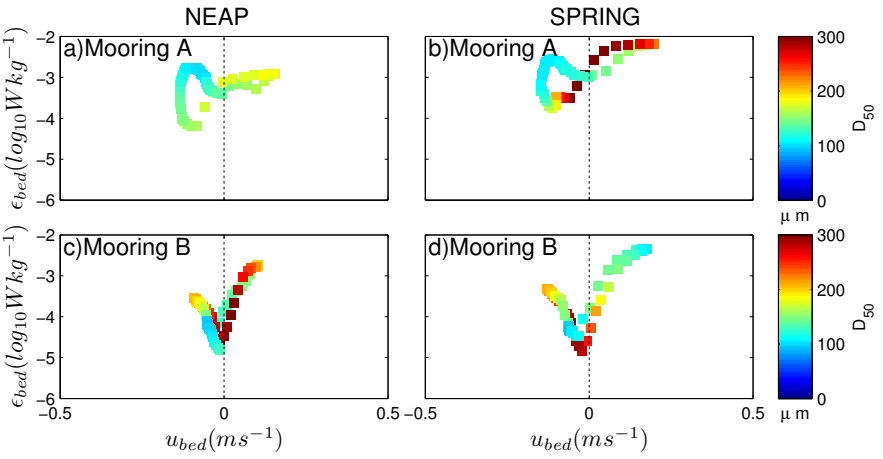

Figure 5.19: Evolution of D_{50} on a tidal scale as a function of ϵ_{bed} and u_{bed} in March 2011. (a) Neap tidal cycle in Mooring A. (b) Spring tidal cycle in Mooring A. (c) Neap tidal cycle in Mooring B and (d) Spring tidal cycle in Mooring B. Positive velocities denote the flood and negative the ebb.

current speed and TKE dissipation rates can be complex, therefore the correlation between the hydrodynamic characteristics and particle properties may also not be linear. For example Figure 5.18 shows D_{50} was not strongly correlated to current speeds close to the bed (u_{bed}) for data collected in March, April and November. It is important to note u_{bed} at Mooring A was obtained from an ADV $0.3m$ from the bed, whereas u_{bed} measurements from ADCPs were calculated from averaging the two data bins closest to the bed, therefore u_{bed} values from an ADV would be expected to be lower.

In order to examine the complex involvement of turbulent parameters in the evolution of particle size; D_{50}, u_h and ϵ_h are compared on a tidal scale. In doing so the contribution of current speed and TKE dissipation can be considered in conjunction with modulations in D_{50}. Moreover, concentrating on individual tidal cycles allows lunar modulations to be examined.

March

Starting with Mooring A, Figure 5.19a indicates the largest particles (above $200\mu m$) occurred during the flood and around high water during neap tides. At low water particles around $100\mu m$ were observed and the particle size increased throughout the flood. At the onset of the ebb, particle size decreased to a minimum corresponding with maximum ϵ_{bed}. It is interesting to note u_{bed} and ϵ_{bed} were not well correlated during the ebb for both spring and neap tides at the Mooring A. Moving onto the spring tide example at Mooring A (Figure 5.19b), a similar pattern of D_{50} tidal evolution was observed, however the maximum D_{50} at high water was higher (above $300\mu m$).

Figures 5.19c and d describe the evolution of D_{50} throughout a neap and spring tidal cycle respectively at Mooring B. The relationship between u_{bed} and ϵ_{bed} was stronger at Mooring B, again the maximum D_{50} coincided with high water for both spring and neap cases reaching $300\mu m$, moreover, D_{50} values of around $100\mu m$ were observed at low water. As the flooding tidal currents decreased towards high water D_{50} increased, at maximum ϵ_{bed} on the flood D_{50} reached a minimum. During the ebb D_{50} decreased from the maximum at high water even once ϵ_{bed} and u_{bed} began to fall after peak ebb current speeds.

April

Figure 5.20 examines the relationship between D_{50}, u_h and ϵ_h for both mooring locations in April for a spring and a neap tide. At Mooring A the maximum D_{50} corresponded with maximum u_h and ϵ_h on the flood during the neap tide, during the ebb D_{50} remained less than $50\mu m$. Conversely, Figure 5.20b describes a spring tide example at Mooring A which reported a decline in D_{50} as u_h and ϵ_h increased during the flood and the ebb. The maximum D_{50} then coincided with a period of low turbulent activity at high water.

At Mooring B the maximum D_{50} occurred at high water and into the flood for both spring and neap tides (Figure 5.20c and d). Furthermore, during the ebb ϵ_h increased

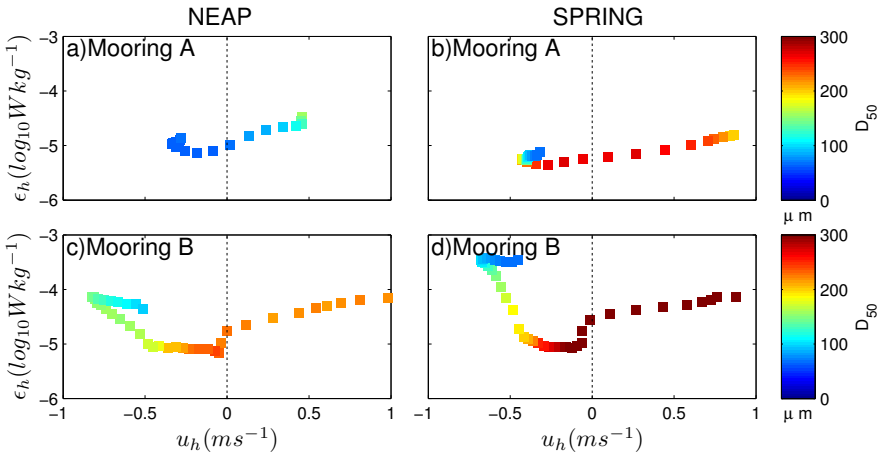

Figure 5.20: Evolution of particle size on a tidal scale as a function of ϵ_h and u_h in April 2011. (a) Neap tidal cycle in Mooring A. (b) Spring tidal cycle in Mooring A. (c) Neap tidal cycle in Mooring B and (d) Spring tidal cycle in Mooring B. Positive velocities denote the flood and negative the ebb.

an order of magnitude higher than the flood, at the same time D_{50} decreased, reaching a minimum at the end of the ebb (Figure 5.20c and d).

November

Finally addressing data collected in November, Figure 5.21 portrays data collected at Mooring A and B during neap and spring tides. Overall u_{bed} reported in November was comparable to values observed in March. However ϵ_{bed} and u_{bed} did not appear to be related to D_{50} in the same manner as seen in April and March.

At Mooring A during a neap tide example, D_{50} was around $100\mu m$ at low water, throughout the flood D_{50} decreased to a minimum of $75\mu m$ at high water (Figure 5.21a). During the ebb on the same tide, D_{50} presented a peak of $190\mu m$ after maximum ϵ_{bed} and u_{bed}. Again for Mooring A but on a spring tide, Figure 5.21b presented the same pattern in D_{50} however the peak in D_{50} was higher (approximately $250\mu m$) and persisted for longer period.

At Mooring B, a similar D_{50} tidal signal was presented in Figures 5.21c and d for a neap

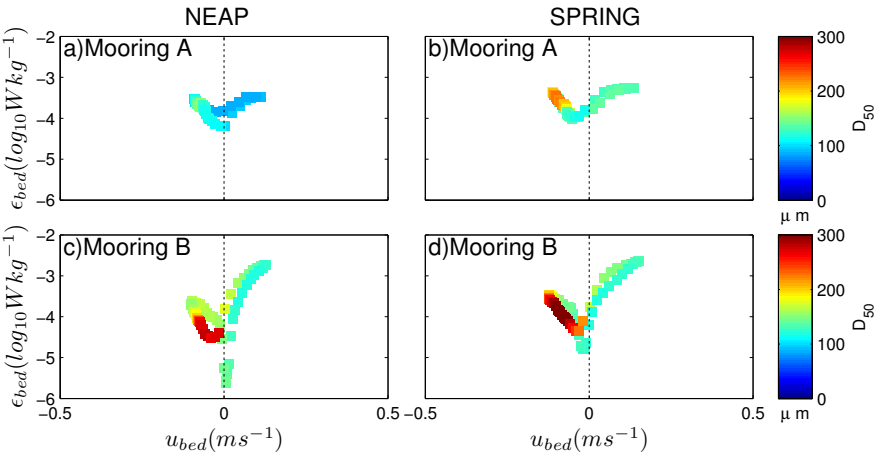

Figure 5.21: Evolution of D_{50} on a tidal scale as a function of ϵ_{bed} and u_{bed} in November 2011. (a) Neap tidal cycle in Mooring A. (b) Spring tidal cycle in Mooring A. (c) Neap tidal cycle in Mooring B and (d) Spring tidal cycle in Mooring B. Positive velocities denote the flood and negative the ebb.

and spring case. During the flood in both the neap and spring tides D_{50} decreased from the size of particles at low water to a minimum at high water. During the ebb particle size increased and a marked incline of D_{50} was observed after maximum ϵ_{bed} and u_{bed} as seen at Mooring A. The main differences between the spring and neap case at Mooring B with regards to D_{50} were the onset of the peak in D_{50}, the magnitude of the peak and the period of maximum D_{50}.

5.3.3 Relationship between D_{50} and effective density (ρ_e)

Floc density is an important factor in determining the effects of local turbulent conditions on particle size. The density of a particle plays a major roll in determining the settling velocity of a particle and thus its fate; whether it will be deposited at the bed or remain in suspension, and in the estuarine case potentially transported to the coastal ocean. Effective density (ρ_e) values were calculated by the following equation.

$$\rho_e = \frac{C_m}{C_v} \tag{5.2}$$

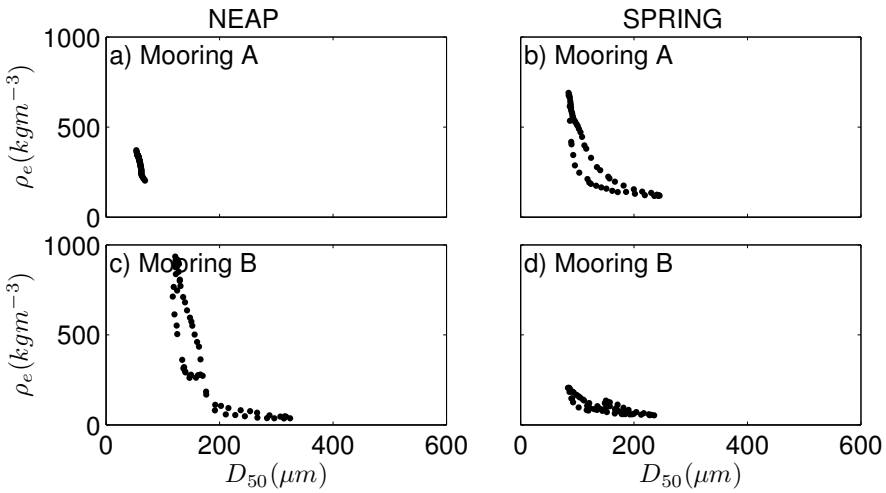

Figure 5.22: Comparison of median particle size (D_{50}) as a function of effective density (ρ_e) for Mooring A and B during spring and neap tides in March 2011.

Effective density, in this case refers to the density of a floc in suspension. In Equation 5.2 C_m represents mass concentration obtained from calibrated measurements of beam attenuation from the LISST-100 and C_v represents volume concentration; values obtained directly from the LISST-100.

This section addresses the relationship between floc density and floc size, comparing Mooring A and B data for spring and neap tidal cycles for the three field campaigns discussed above. Firstly, the correlation between size and density is considered, followed by an introduction of current velocity modulations in addition to size and density, comparing both Mooring locations for spring and neap cases.

March

Overall, in March Figure 5.22 shows D_{50} and ρ_e were inversely correlated at both locations, for spring and neap tides, therefore as floc size increased the effective density of flocs decreased. The smallest and the largest densities were observed at Mooring B. Furthermore, the relationship was not linear and the minimum effective density values were limited by the density of water.

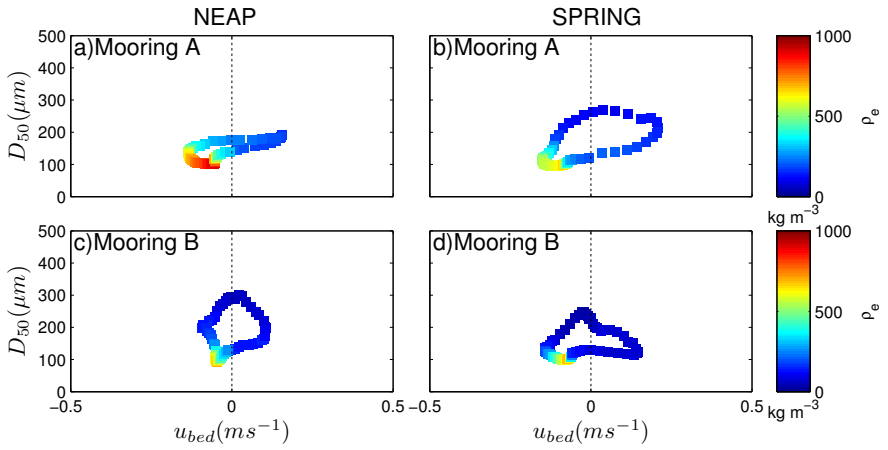

Figure 5.23: Relationship between D_{50} and ρ_e over (a) & (c) spring and (b) & (d) neap tidal cycles during March in Mooring A and Mooring B respectively.

Continuing now to incorporate the affects of current velocity, Figure 5.23a indicates high density particles around $100\mu m$ occurred during the ebb on a neap tide at the Mooring A. Moreover, during the flood the lowest densities were recorded at peak flow when D_{50} was at a maximum. A similar relationship between D_{50} and density was observed during a spring tide in Figure 5.23b, however the maximum D_{50} was higher and corresponded to a lower density.

At Mooring B the highest densities also corresponded with a D_{50} of approximately $100\mu m$ in both spring and neap cases. In the neap tide case as D_{50} increased ρ_e decreased throughout the tidal cycle (Figure 5.23c). The same was true for the ebb phase of the spring tide, however during the flood ρ_e remained low regardless of D_{50}.

April

In April, an inverse relationship was observed between floc size and density during spring and neap tides at both sampling locations (Figure 5.24). The correlation was not as strong at Mooring B during spring tides, however on the whole the largest flocs corresponded with the smallest densities and vice versa.

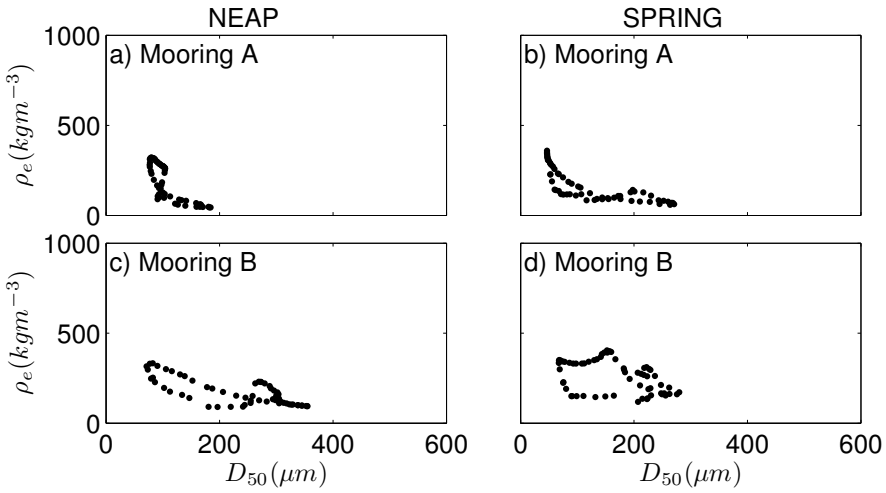

Figure 5.24: Comparison of median particle size (D_{50}) as a function of effective density (ρ_e) for Mooring A and B during spring and neap tides in April 2010.

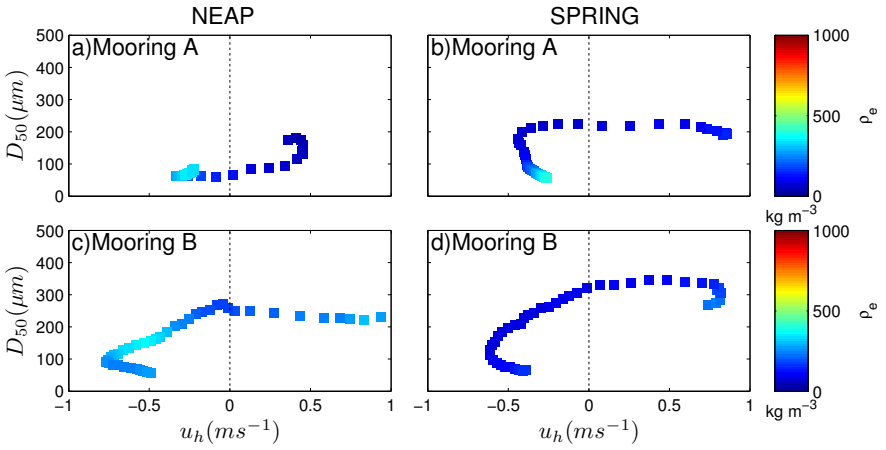

Figure 5.25: Relationship between D_{50} and ρ_e over (a) & (c) spring and (b) & (d) neap tidal cycles during April in Mooring A and Mooring B respectively.

Figure 5.25 presents D_{50} as a function of ρ_e and u_h for data from Mooring A and B during April, comparing spring and neap tides. During the neap tide example at Mooring A, the maximum D_{50} coincided with the overall minimum in ρ_e, conversely the most dense flocs occurred at peak ebb current velocities (Figure 5.25a). During the spring tide at Mooring A as seen during the neap tide, the maximum density corresponded with the smallest D_{50} values and vice versa. The main difference between spring and neap tide examples at Mooring A was the relationship between D_{50} and u_{bed}.

Figures 5.25c and d describe the same relationships for Mooring B . In the neap tide example the largest D_{50} values corresponded with the lowest densities at high water. As the ebb velocities increased towards peak flow, D_{50} decreased and before peak flow is reached a section of higher density particles were observed. During the flood D_{50} showed a slight decline in size which corresponded with a rise in density. Considering the spring tide case, overall the densities of particles were low compared to the neap tide with the exception of peak flow during the flood and towards the end of the ebb when density increased (Figure 5.25d)

November

As mentioned in the previous section, the PSD observed in November at both sampling locations differed to PSD results obtained from data collected in March and April. However, the floc properties appear to be similar; for example Figure 5.26 portrays the inverse relationship between floc size and density observed in March and April. Moreover, the maximum D_{50} values were observed during spring tides.

Considering now, floc properties; size and density in conjunction with the velocity field, Figure 5.27a shows the maximum D_{50} corresponded with the lowest density flocs during the neap tide example at Mooring A. Although, it is important to note the maximum D_{50} coincided with maximum velocities during the ebb. On a spring tide at Mooring A the same relationship was observed however the range of size and density was larger.

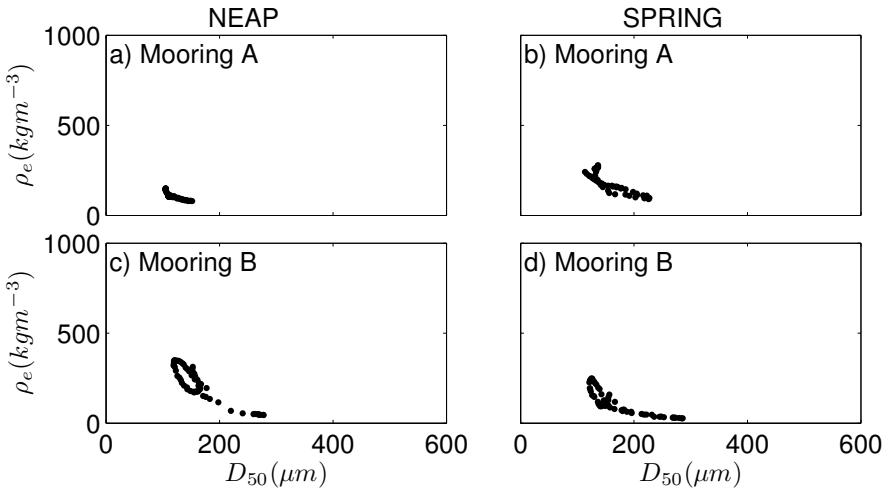

Figure 5.26: Comparison of median particle size (D_{50}) as a function of effective density (ρ_e) for Mooring A and B during spring and neap tides in November 2011.

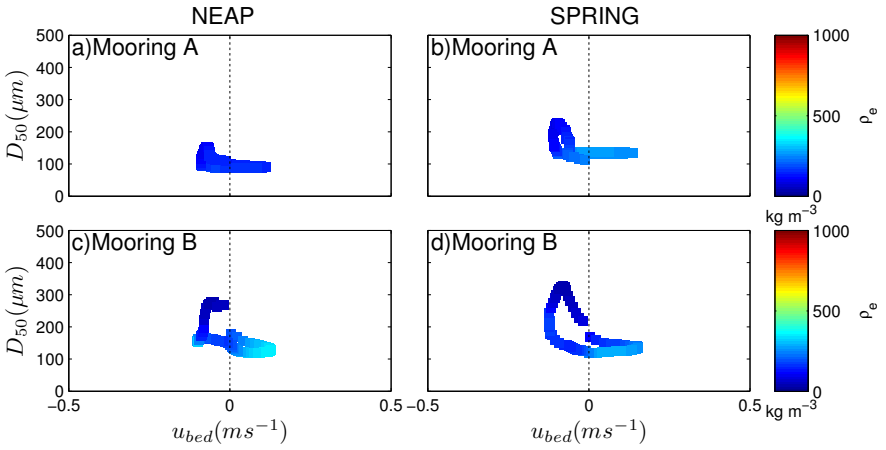

Figure 5.27: Relationship between D_{50} and ρ_e over (a) & (c) spring and (b) & (d) neap tidal cycles during November in Mooring A and Mooring B respectively.

Moving on to Mooring B, Figure 5.27d suggests the same relationship again with a broader range of particle size and densities. Finally the neap tide example at Mooring B indicates as seen above an inverse relationship between D_{50} and ρ_e, furthermore the most dense particles are recorded at this time during the peak flow on the flood phase of the tide which corresponds with the smallest D_{50} in the tidal cycle.

5.3.4 Empirical derivation of D_{50}

Predicting particle size in an estuarine environment can be challenging due to the multitude of factors driving the evolution of particle size. In this section, observational data from March and April are utilised to determine the key drivers in controlling particle size at Mooring A and B on a tidal scale. The empirical derivation of D_{50} is calculated via a method introduced by Braithwaite et al (2012), through the multiple regression of observed values of D_{50} on a quantitative value of advection into the estuary and a disaggregation term described in the equations below. Data from November were not analysed with this method as the PSDs indicated a different regime with respect to SPM characteristics, that would not be predicted by multiple regression analysis as the major peak in D_{50} did not correlate with either a period of high or low current speeds as seen in March and April. This relatively simple method has the potential to provide insight into the physical processes governing particle size. The effects of three disaggregation terms are compared:

$$D_{50u} = \alpha_D h + \beta_D u_{bed} + \lambda_D \tag{5.3}$$

$$D_{50G} = \alpha_D h + \beta_D G_{bed} + \lambda_D \tag{5.4}$$

$$D_{50\mu_k} = \alpha_D h + \beta_D \mu_{k_{bed}} + \lambda_D \tag{5.5}$$

h presents an advective term, utilised as a proxy for tidal displacement and therefore accounts for salinity affects, for example when h is high seawater enters the estuary and thus tidal displacement increases. α_D therefore represents the longitudinal gradient of particle size from the mouth of the estuary to the TIR. The turbulence parameter or current speed represents the disaggregating forces applied to particles in suspension,

therefore β_D represents a particle break up term. In addition, turbulence parameters and current speeds can also represent resuspension events. Values for turbulence parameters and current speed were taken close to the bed, in March those values were obtained from an ADV, $0.3m$ from the bed. For April when ADV instruments were not deployed, an average of the two bins closest to the bed from the ADCP profile was used. Finally the third constant (λ_D) indicates the mean size of particles over the total regression period. Examining model outputs on a tidal scale gives rise to a clearer understanding of the ability of the model.

March

Table 5.4: Results from the application of Equation 5.5 to data collected in Mooring A during March per tidal cycle. The values in brackets indicate standard error. Column 3 shows the R^2 values for a linear regression between h and D_{50}. Column 6 shows the R^2 value for the multiple regression. Highlighted rows are plotted in the following figure. N denotes neap tides and S denotes spring tides.

Tide	$\alpha_D(\mu m m^{-1})$	R^2	$\beta_D(\mu m(m/s)^{-1})$	$\lambda_D(\mu m)$	R^2
1	21.5(4.4)	0.28	-0.29(4.4)	206.3(9)	0.45
2	17.8(3.6)	0.28	-0.22(3.6)	197.4(6.7)	0.44
3	53.9(4.5)	0.65	-0.4(4.5)	219.9(9.9)	0.76
4	50.4(5)	0.62	-0.25(5)	194.3(10)	0.67
5	63.5(3.5)	0.8	-0.28(3.5)	194.6(7.1)	0.86
6	60.9(4)	0.73	-0.35(4)	209.1(7.9)	0.82
7	71.9(3.6)	0.81	-0.32(3.6)	207.8(6.6)	0.87
8	70.9(4.5)	0.77	-0.28(4.5)	200.1(8.5)	0.81
9S	**88(2.9)**	**0.87**	**-0.39(2.9)**	**199.3(5.2)**	**0.94**
10	70.1(3.7)	0.84	-0.17(3.7)	162.9(6.8)	0.86
11	66.9(3.7)	0.84	-0.15(3.7)	151(7.1)	0.85
12	59.5(5)	0.71	0.011(5)	121.7(9.5)	0.71
13	47.5(3.7)	0.74	-0.063(3.7)	136.9(6.8)	0.74
14	46.2(6.9)	0.44	-0.097(6.9)	144.8(11)	0.45
15	44.7(2.8)	0.81	-0.058(2.8)	137.8(4.1)	0.82
16	43.7(3.2)	0.75	-0.097(3.2)	142.9(4.4)	0.77
17N	**65.8(2.8)**	**0.91**	**-0.064(2.8)**	**134(3.6)**	**0.91**
18	59.8(5.1)	0.67	-0.1(5.1)	108.4(5.5)	0.69
19	18.5(2)	0.49	-0.093(2)	68.01(1.7)	0.6
20	4.1(0.36)	0.53	-0.029(0.36)	54.74(0.28)	0.73

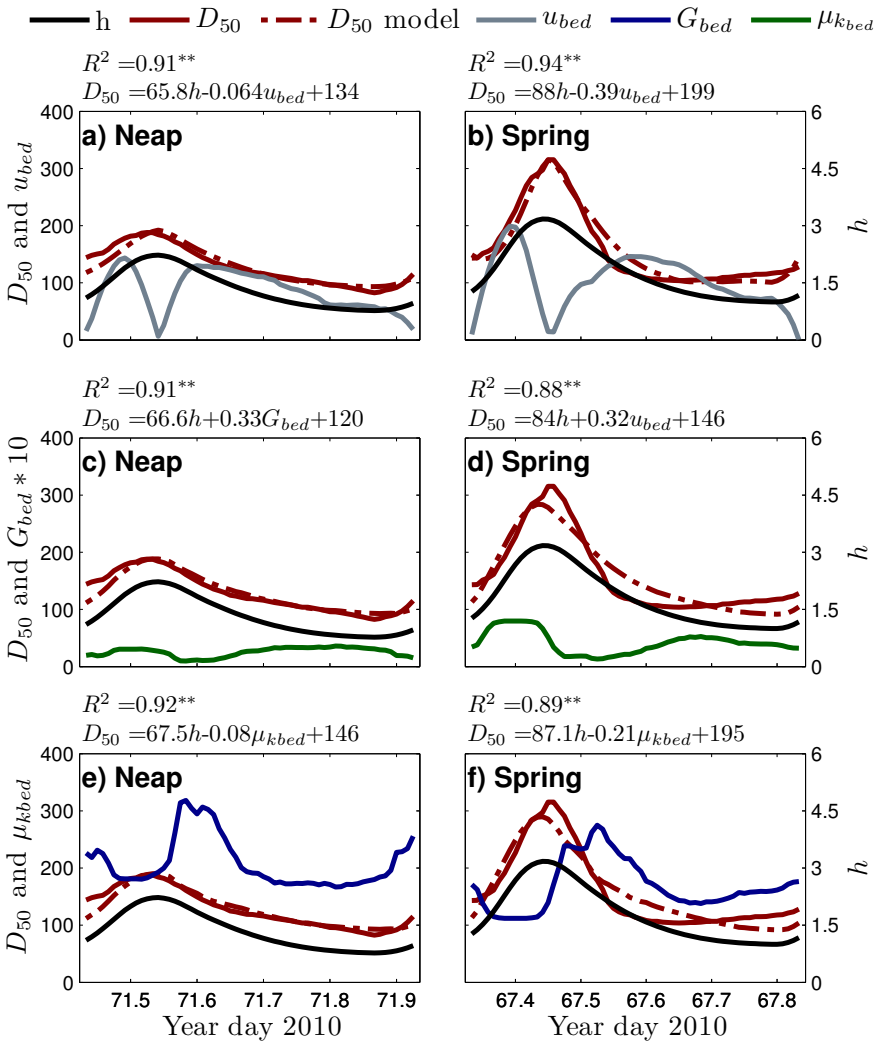

Figure 5.28: Empirically calculated D_{50} over neap and spring tidal cycles in Mooring A during March. Red line represents observed D_{50}, dashed red line represents the model D_{50}, black line represents surface height, grey lines represent $u_{bed}(mms^{-1})$, dark blue lines represent G_{bed} and dark green are $\mu_{k_{bed}}$.

In March good agreement was shown between modelled and observed D_{50} values at Mooring A for both spring and neap tides (Figure 5.28). Interestingly, negative values for β_D were associated with u_{bed} in both spring and neap tide examples, showing an increase in u_{bed} resulted in a decline in D_{50}. This relationship is evident in Figures 5.28a and b when comparing D_{50} and h, however both β_D values were less than $1\mu(m/s)^{-1}$. β_D values associated with G_{bed} were positive, as shown in Figure 5.28 and also less than $1\mu(m/s)^{-1}$, this suggests G_{bed} and D_{50} were positively correlated, this could infer enhanced turbulence resuspended larger particles, or the turbulence could have been too weak to affect D_{50} significantly. β_D constants associated with $\mu_{k_{bed}}$ at Mooring A in March are negative, inferring an inverse correlation with D_{50}. The spring and neap examples in Figures 5.28e and f display D_{50} clearly out of phase with $\mu_{k_{bed}}$.

Table 5.4, as discussed above suggests an inverse relationship between D_{50} and u_{bed} throughout the lunar cycle as β_D remains negative. It is important to note however the associated standard error relative to the value of the constant. In addition to this Table 5.4 displays positive α_D values which again infers a positive longitudinal gradient of particle size which increased from the mouth of the estuary to the TIR. Furthermore, column three in Table 5.4 describes the contribution of h alone in predicting D_{50}, which indicates the contribution of current speeds are relatively small in comparison, however the contribution is shown to vary throughout the lunar cycle, presenting the highest contribution during neap tides.

At Mooring B a significant agreement of modelled and observed D_{50} values were found (Figure 5.29). In addition, Figure 5.29 infers a stronger agreement during neap tides compared to spring tides. During spring tides the flood phase of the tide was least well described, additionally observed values of D_{50} appear to have been less in phase with h than neap tides. Figures 5.29a and b describe an inverse relationship between D_{50} and u_{bed} for both spring and neap cases, this was reflected in the comparatively large negative β_D values. β_D values associated with G_{bed} were also negative but smaller, indicating a weaker inverse correlation with D_{50}. β_D constants associated with $\mu_{k_{bed}}$ at Mooring B in March were positive, inferring a positive correlation with D_{50}. The spring example,

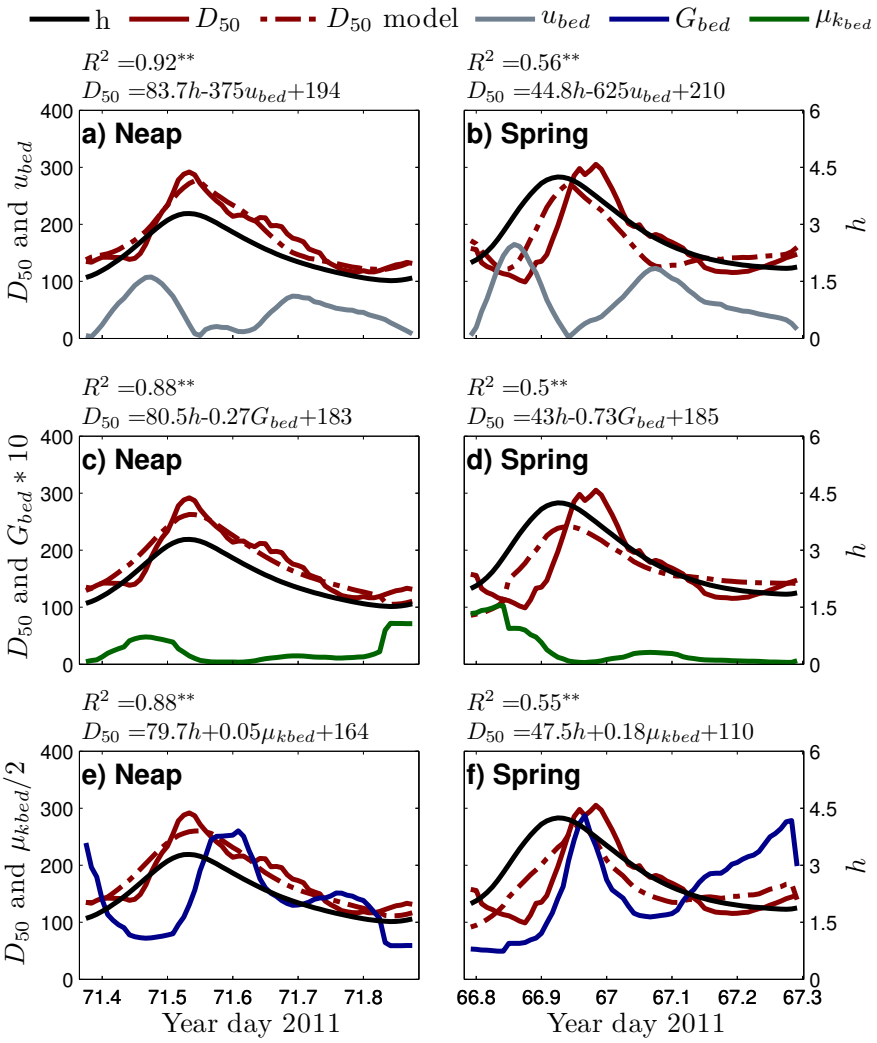

Figure 5.29: Empirically calculated D_{50} over neap and spring tidal cycles in Mooring B during March. Red line represents observed D_{50}, dashed red line represents the model D_{50}, black line represents surface height, grey lines represent $u_{bed}(mms^{-1})$, dark blue lines represent G_{bed} and dark green are $\mu_{k_{bed}}$.

Table 5.5: Results from the application of Equation 5.5 to data collected in Mooring B during March per tidal cycle. The values in brackets indicate standard error. Column 3 shows the R^2 values for a linear regression between h and D_{50}. Column 6 shows the R^2 value for the multiple regression.

Tide	$\alpha_D(\mu m m^{-1})$	R^2	$\beta_D(\mu m (m/s)^{-1})$	$\lambda_D(\mu m)$	R^2
1	42.1(3.6)	0.67	-371.8(3.6)	176.2(5.9)	0.78
2	53.8(3.7)	0.72	-499.5(3.7)	191.9(5.7)	0.84
3	-40.9(14)	0.15	109.7(14)	248.3(23)	0.16
4	31.1(4.1)	0.36	-695.5(4.1)	200.4(6.5)	0.72
5	18.5(5.7)	0.14	-589.8(5.7)	192.1(9.4)	0.39
6	-0.611(6.6)	0.00	-124.3(6.6)	210.5(11)	0.02
7	-16(10)	0.03	-803.8(10)	305.1(18)	0.20
8S	**44.8(6.2)**	**0.36**	**-625.5(6.2)**	**210.4(10)**	**0.56**
9	53.3(6.7)	0.50	-288.4(6.7)	188.8(12)	0.54
10	8.6(3.2)	0.09	341.3(3.2)	149.9(6.3)	0.34
11	-74(16)	0.25	858.6(16)	190.5(30)	0.32
12	29.4(5)	0.39	370(5)	121.4(8.5)	0.50
13	-104(12)	0.56	679.6(12)	215.5(22)	0.60
14	13.4(8.8)	0.04	150.2(8.8)	231.1(13)	0.05
15	73.8(4.1)	0.85	31.78(4.1)	161.9(6.8)	0.85
16	88.6(3.4)	0.91	-247.5(3.4)	191.3(5.1)	0.92
17N	**83.7(3.3)**	**0.87**	**-375.1(3.3)**	**193.9(3.7)**	**0.92**
18	105(3.7)	0.84	-758.1(3.7)	202.8(3.6)	0.93

Figure 5.28f displays D_{50} in phase with $\mu_{k_{bed}}$, thus consolidating this point.

Considering results for each individual tidal cycle presented in Table 5.5, predominantly positive values of α_D again suggesting particle size increased towards the TIR relative to the mouth. Moreover, any negative α_D values were associated with relatively large standard errors therefore the regression could not be considered further. Mostly negative β_D values were observed indicating particle size was reduced as u_{bed} increases. When positive values of β_D were reported they were associated with a low R^2 value or a change in the direction of the particle size gradient. It can therefore be assumed these were atypical relationships between particle size and u_{bed}. Furthermore, during tidal cycles $11-15$ large and positive β_D values were observed which corresponded to a period of enhanced observed D_{50}, coinciding with maximum flows discussed in Chapter 4. Finally, as seen at Mooring A, the contribution of h in predicting observed D_{50} values was consistently

higher than u_{bed} at Mooring B.

April

April data from Mooring A are now to be considered. Figure 5.30 presents the empirical model results for a spring and neap tides for each disaggregation or resuspension factor. Low water and the onset of the flood were not well described due to the absence of ADCP data at that time. R^2 values indicate the model was most successful on spring tides. As discussed in section 5.3.1 maximum D_{50} occurred during peak flood current speeds in April at Mooring A on neap tides which does not fit with the disaggregation hypothesis, this may explain the weaker fit in the neap tide case. Although, resuspension of larger particles would give rise to large positive β_D values, furthermore at this time the contribution of h to the overall R^2 values was small compared to the contribution of β_D (Table 5.6). Figure 5.30c displays a negative β_D value for G during the neap tide, inferring a rise in G results in a decline in D_{50}. This is not the case during the spring tide, however the β_D values were low compared to the α_D. Figures 5.30e and f present small but negative β_D values for $\mu_{k_{bed}}$, therefore as $\mu_{k_{bed}}$ increased D_{50} decreases. A common feature of all regressions shown in Figure 5.30 was a large positive α_D value which indicates D_{50} was positively correlated with the advection of salt water.

Table 5.6 includes values for α_D,β_D and λ_D along with the associated R^2 values for the model output solely using h to describe changes in D_{50}, and using h combined with u_{bed} as the disaggregation parameter for each individual tidal cycle. For all cases except tidal cycle 12 α_D constants were positive, which insinuates a positive longitudinal gradient of particle size towards the TIR from the mouth. As β_D was positive D_{50} increased as u_{bed} increased and vice versa, as seen in March data this can represent resuspension of larger particles. It is important again to note the relative contribution of h compared to u_{bed} in Table 5.6. During spring tides, h explained the majority of the variation in D_{50}, however during neap tides this changed and u_{bed} accounted for more of the variability relative to h. However it is also important to highlight the overall R^2 values decreased during neap

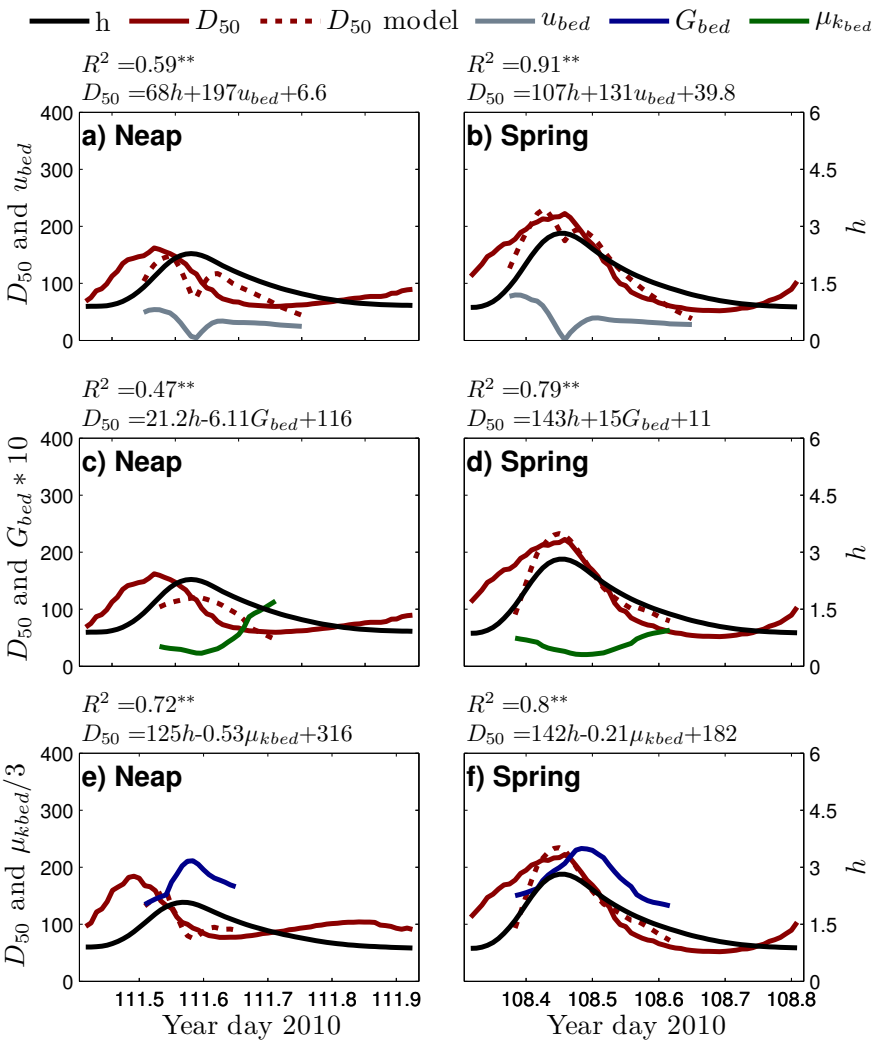

Figure 5.30: Empirically calculated D_{50} over neap and spring tidal cycles in Mooring A during April. Red line represents observed D_{50}, dashed red line represents the model D_{50}, black line represents surface height, grey lines represent $u_{bed}(mms^{-1})$, dark blue lines represent G_{bed} and dark green are $\mu_{k_{bed}}$.

Table 5.6: Results from the application of equation 5.5 to data collected in Mooring A during April per tidal cycle. The values in brackets indicate standard error. Column 3 shows the R^2 values for a linear regression between h and D_{50}. Column 6 shows the R^2 value for the multiple regression.

Tide	$\alpha_D(\mu m m^{-1})$	R^2	$\beta_D(\mu m(m/s)^{-1})$	$\lambda_D(\mu m)$	R^2
1	99.3(6.2)	0.66	144.4(6.2)	55.85(8.9)	0.9
2	132(7)	0.69	137(7)	52.14(9.7)	0.92
3	103(5)	0.61	125.8(5)	51.92(6.8)	0.94
4	138(5.9)	0.70	121.7(5.9)	45.64(8.1)	0.95
5S	**107(6.4)**	**0.59**	**131.3(6.4)**	**39.77(8.4)**	**0.91**
6	125(8.8)	0.53	167.5(8.8)	20.17(12)	0.88
7	125(14)	0.44	189.1(14)	5.384(17)	0.76
8	124(15)	0.40	237.1(15)	-15.02(18)	0.75
9N	**68.1(14)**	**0.11**	**196.6(14)**	**6.641(15)**	**0.59**
10	39.8(16)	0.05	238.8(16)	-2.506(19)	0.47
11	16.8(18)	0.00	218.1(18)	39.21(17)	0.40
12	-8.41(17)	0.08	261.1(17)	21.08(17)	0.53

tides.

Figure 5.31 compares the observed and modelled D_{50} results from Mooring B. The model showed good agreement with observed values of D_{50} for both spring and neap tides (all R^2 values were above 0.65), overall spring tides display a stronger fit as seen in at Mooring A, u_{bed} and G_{bed} were both associated with positive β_D values throughout the lunar cycle, therefore D_{50} increased as the disaggregation parameters increased. Moreover, negative values of β_D less than $1\mu m(m/s)^{-1}$ were associated with $\mu_{k_{bed}}$, suggesting D_{50} was inversely related to $\mu_{k_{bed}}$. α_D remained positive as seen at Mooring A, thus suggesting a positive gradient of D_{50} extending from the mouth up to the TIR.

Table 5.7 displays the regression constants for each tidal cycle using u_{bed} as the disaggregation or resuspension parameter. As seen at Mooring A, positive values for both α_D and β_D prevailed, again indicating particles increased in size with distance from the mouth, and D_{50} increased as u_{bed} increased. As discussed previously a positive β_D value does not coincide with the disaggregation hypothesis however positive values could indicate resuspension of larger particles. Column three in Table 5.7 shows the R^2 contribution of

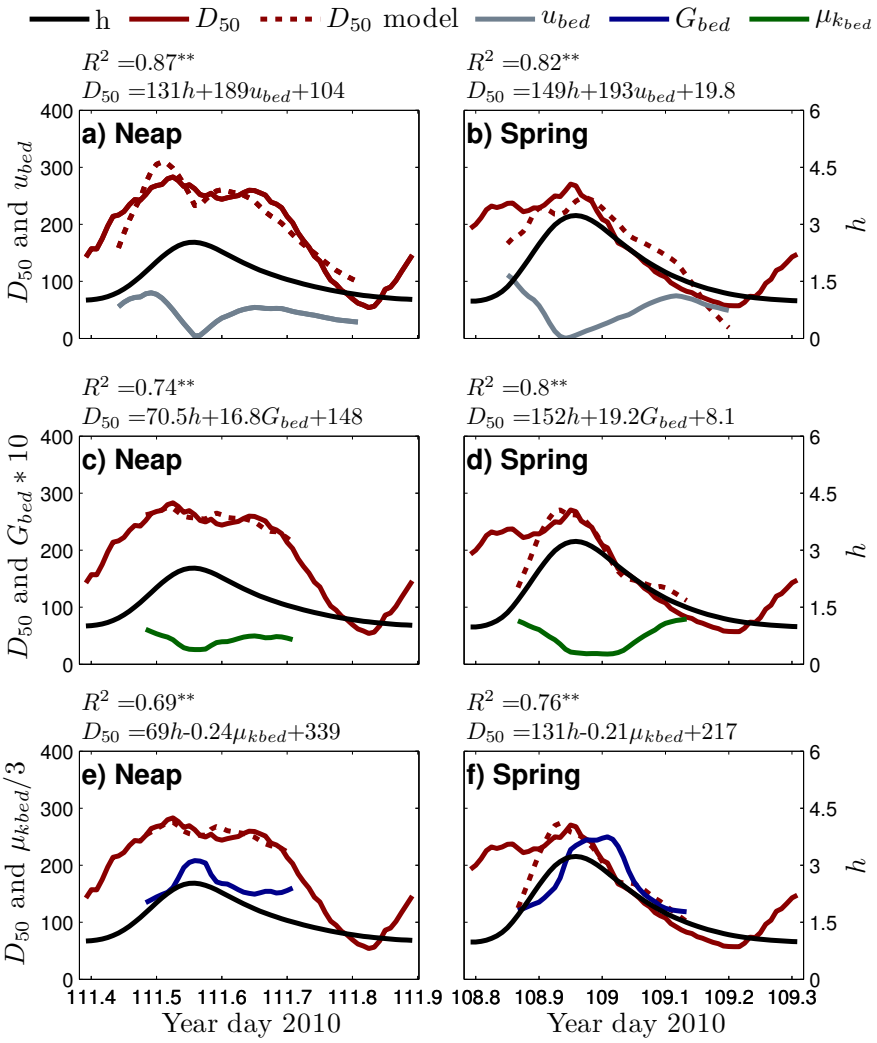

Figure 5.31: Empirically calculated D_{50} over neap and spring tidal cycles in Mooring B during April. Red line represents observed D_{50}, dashed red line represents the model D_{50}, black line represents surface height, grey lines represent $u_{bed}(mms^{-1})$, dark blue lines represent G_{bed} and dark green are $\mu_{k_{bed}}$.

Table 5.7: Results from the application of equation 5.5 to data collected in Mooring B during April per tidal cycle. The values in brackets indicate standard error. Column 3 shows the R^2 values for a linear regression between h and D_{50}. Column 6 shows the R^2 value for the multiple regression.

Tide	$\alpha_D(\mu m m^{-1})$	R^2	$\beta_D(\mu m(m/s)^{-1})$	$\lambda_D(\mu m)$	R^2
1	87.1(6.5)	0.3	106.8(6.5)	94.37(11)	0.85
2	94.7(10)	0.35	153.4(10)	83.67(17)	0.7
3	105(9.3)	0.4	157.1(9.3)	74.73(16)	0.79
4	130(14)	0.49	169.6(14)	45.14(24)	0.83
5	135(11)	0.23	277.4(11)	0.3653(19)	0.79
6S	**149(13)**	**0.39**	**193(13)**	**19.8(20)**	**0.82**
7	116(4.8)	0.54	133(4.8)	63.4(7.2)	0.94
8	138(13)	0.4	172.8(13)	31.49(20)	0.72
9	126(5.6)	0.66	165.5(5.6)	79.84(7.8)	0.92
10	114(19)	0.29	126.8(19)	55.4(30)	0.44
11N	**131(8.2)**	**0.64**	**189.4(8.2)**	**104.3(10)**	**0.87**
12	174(19)	0.34	198.8(19)	19.21(23)	0.69
13	161(19)	0.56	142(19)	174(19)	0.65
14	226(25)	0.36	307.7(25)	-0.5607(30)	0.67
15	214(12)	0.66	209.4(12)	99.13(13)	0.89
16	224(18)	0.52	314.9(18)	6.653(24)	0.79
17	175(12)	0.55	211.5(12)	111.5(14)	0.85
18	194(22)	0.35	303.5(22)	23.75(34)	0.66

h without u_{bed}, which indicates h was overall more influential on D_{50} than u_{bed} however the impact of u_{bed} was by no means negligible.

5.3.5 Effects of Kolmogorov microscale on floc size

Previous literature has noted particle size is limited by the Kolomogorov microscale (Braithwaite et al, 2012). As the Kolmogorov microscale increases particles are able to grow, however if it begins to decrease particles are torn apart due to the reduction in the eddie length scale associated with a decline in the Kolmogorov microscale. In addition to this Braithwaite et al (2012) have suggested particles in suspension require time to react to the ambient turbulent conditions thus giving rise to a phase lag between μ_k and D_{50}. With this evidence in mind the relationship between the Kolmogorov microscale

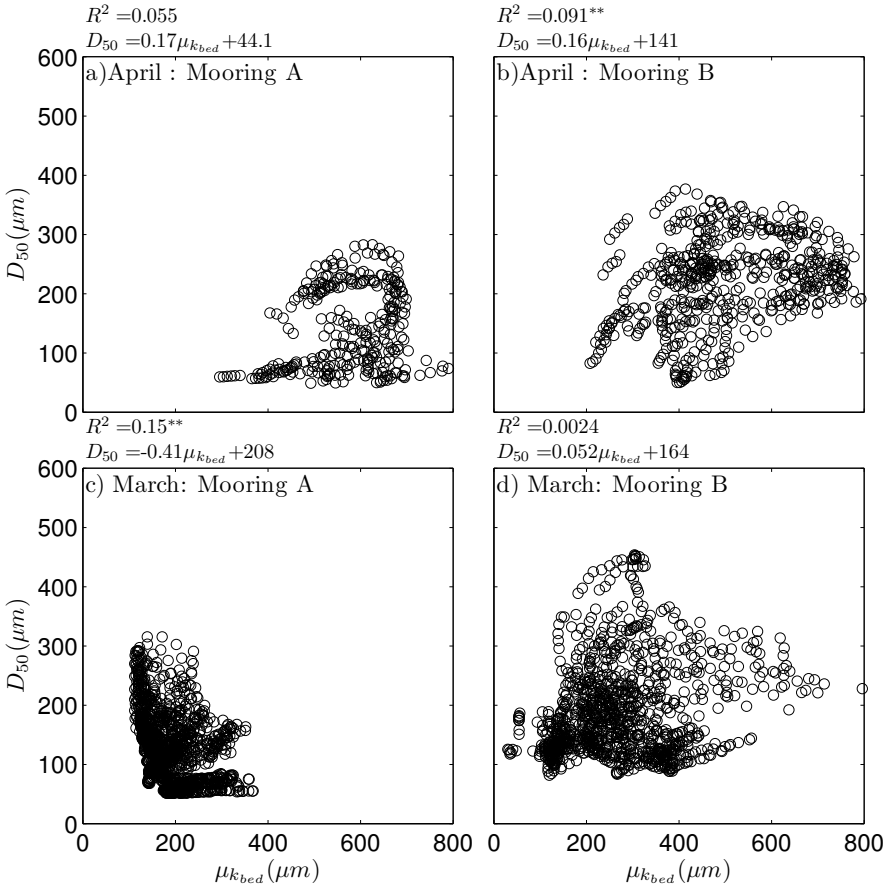

Figure 5.32: Comparing the relationship between $\mu_{k_{bed}}$ and D_{50} April and March.

and particle size is examined for data collected during March and April at Moorings A and B.

Figure 5.32a indicates a weak relationship between $\mu_{k_{bed}}$ and D_{50} for April and March data sets at both Moorings A and B. A stronger relationship was observed at Mooring A in March, presenting an R^2 value of 0.15^{**}, this relationship is weak but statistically significant due to the larger number of degrees of freedom (as discussed in Chapter 3). In addition Mooring B during April represents a weak but statistically significant correlation. Conversely when an individual tidal cycle is considered the relationship is enhanced. To investigate this further, over the time scale of one tidal cycle $\mu_{k_{bed}}$ is correlated with D_{10},D_{50} and D_{90}.

March

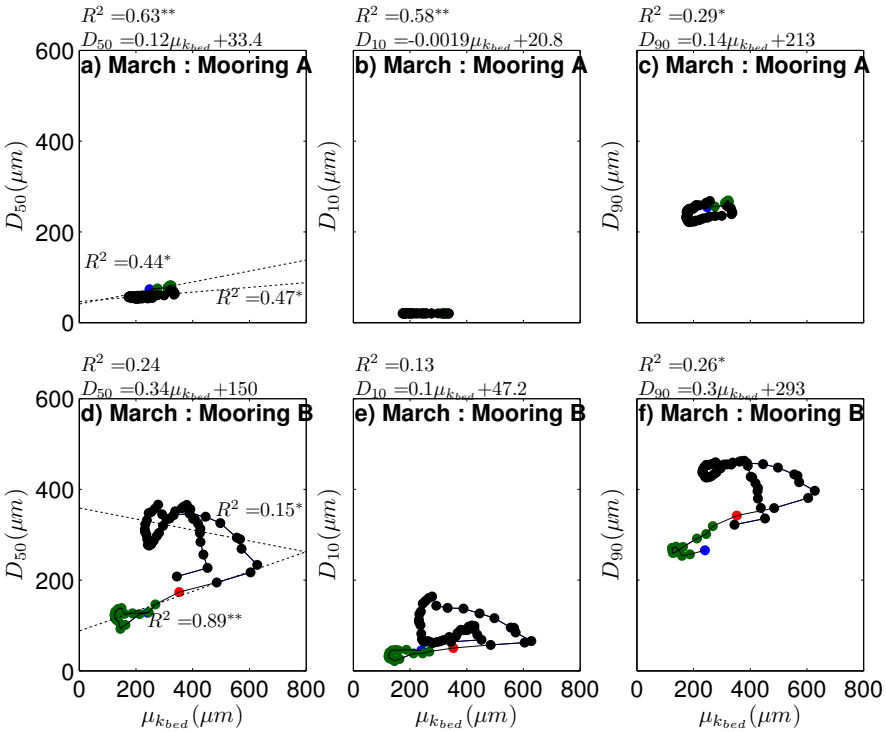

Figure 5.33: Relationship between $\mu_{k_{bed}}$ and particle size (D_{50}, D_{10} and D_{90}) at Mooring A and Mooring B over 1 tidal cycle during March. Black markers = ebb phase of tide, green markers = flood phase of tide, red = High water and blue = low water.

Data collected at Mooring A in March displays significant positive correlations of particle size with $\mu_{k_{bed}}$ (Figures 5.33a,b and c). The range of particle size and $\mu_{k_{bed}}$ throughout a tidal cycle was markedly smaller at Mooring A compared to Mooring B, making the correlation between $\mu_{k_{bed}}$ and D_{50} difficult to test. Lower R^2 values were observed at Mooring B compared to the Mooring A, the increased variability was contributed to mainly by the latter part of the ebb phase (black markers), which denote enhanced fluvial influence (Figures 5.33d,e and f). Moreover, a wider range of particle size and $\mu_{k_{bed}}$ was reported at Mooring B. Considering Figure 5.33 further, the relationship between D_{50} and $\mu_{k_{bed}}$ appears to present differing correlations with regards to the tidal phase and thus the influence of terrestrially derived particles. Two regression lines have been added to Figures 5.33a and d to highlight the two different signals comparing periods of enhanced

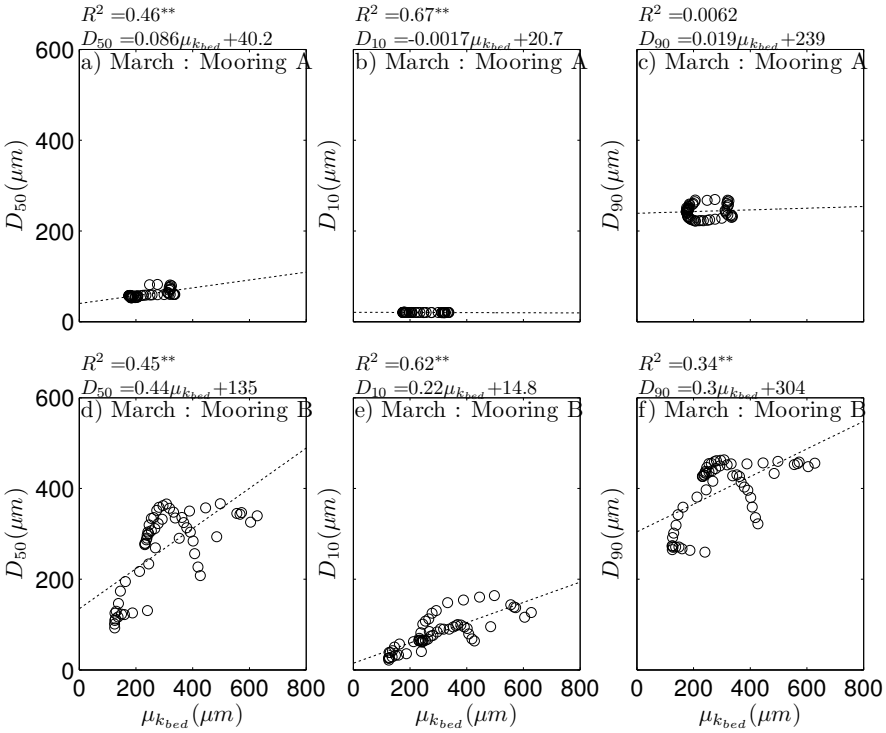

Figure 5.34: Relationship between $\mu_{k_{bed}}$ and particle size (D_{50}, D_{10} and D_{90}) at Mooring A and Mooring B over 1 tidal cycle during March with a phase lag of 60 minutes applied.

fluvial influence with periods of enhanced marine influence.

Phase lags were also applied to the March data set, Figure 5.34 indicates the correlation between $\mu_{k_{bed}}$ and D_{50} was not enhanced for Mooring A data. Conversely, at Mooring B, R^2 values increased by an average of 0.3. The correlation was improved mainly due to the higher particle sizes reported on the ebb corresponding with the larger $\mu_{k_{bed}}$ values after the application of the phase lag.

April

Figures 5.35a to f present one tidal cycle tide, comparing D_{10},D_{50} and D_{90} with $\mu_{k_{bed}}$ for Mooring A and B during April. Firstly considering Mooring A, significant positive correlations were observed between $\mu_{k_{bed}}$ and particle size. The strongest correlation was

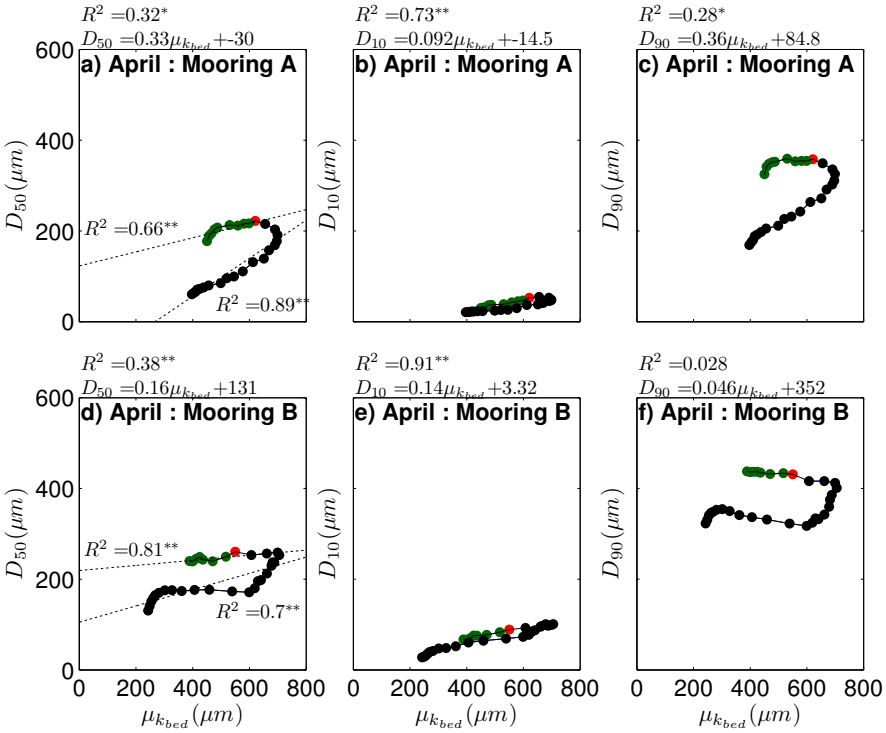

Figure 5.35: Relationship between $\mu_{k_{bed}}$ and particle size (D_{50}, D_{10} and D_{90}) in Mooring A and Mooring B over 1 tidal cycle during April. Black markers = ebb phase of tide, green markers = flood phase of tide and red = High water.

with D_{10}, however the range of particle size was small in this case. In the case of D_{50} and D_{90} the particle size on the flood (green markers) was higher at the same $\mu_{k_{bed}}$ value on the ebb, resulting in a weaker correlation than D_{10}.

Figures 5.35d,e and f display the same relationships for Mooring B. As seen at Mooring A, D_{10} displays the highest R^2 value compared to D_{50} and D_{90}. At Mooring B a wider range of $\mu_{k_{bed}}$ values were observed and larger particles were reported on the flood compared to the ebb. Additionally, as discussed in previous chapters, ADCP mooring data collected in April was not complete throughout the tidal cycle due to the blanking range, which could have had implications to the correlations on a tidal scale. Again, considering the tidal phases discreetly, the marine and terrestrially dominant phases of the tide appear to present separate correlations, as shown by enhanced R^2 values in Figures 5.35a and d compared to R^2 values taking the whole tidal cycle into account. Overall D_{50} values

were lower during the ebb at both mooring locations, indicating the transport of particles with different properties by the river into the RETZ. Phase lags ranging from $12 - 72$ minutes were applied to the data sets in order to examine the relationships further. The phase lags allowed the comparison of particle size data with previous $\mu_{k_{bed}}$ values, thereby correcting for the possibility of particles taking time to react to the local turbulence. The addition of a phase lag did not enhance the relationship, in fact the correlation weakened.

Another floc property that could affect the relationship between size and the ambient turbulent conditions is the yield strength of the floc. For example a floc with a higher yield strength could with stand higher turbulence before de-flocculation occurs. If the floc strength of SPM entering the RETZ via advection of the tide or by fluvial SPM transport then significant variability should be expected when interrogating the relationship between $\mu_{k_{bed}}$ and D_{50}.

Parker et al (1972) introduced the concept of floc strength (C_f) acting as a coefficient, modulating the relationship between $\mu_{k_{bed}}$ and D_{50}, also employed by Jago et al (2007) as shown by the Equation 5.6:

$$D_{50} = C_f \epsilon^{-\lambda} \tag{5.6}$$

Where λ is equal to 1 when D_{50} is bigger than μ_k and 0.5 when μ_k is bigger than D_{50}. Rearranging Equation 5.6 enables the calculation of floc strength coefficient (C_f).

Results for individual tidal phases are shown in Table 5.8 for both Mooring locations in March and April. Addressing floc strength in March first, Table 5.8 indicates flocs were weakest during the ebb and at low water at Mooring A, however floc strength appears relatively constant at Mooring B, with the exception of high water slack when floc strength is at a minimum. Overall, floc strength is higher at Mooring A compared to Mooring B in March, thus indicating particles of a terrestrial origin has a higher floc strength. Although, the strongest flocs were observed during the flood at Mooring A. Moving on to the floc strength values in April, Table 5.8 shows particles observed on the ebb, at a period of enhanced fluvial influence were consistently weaker than

Table 5.8: Comparison of averaged values of floc strength parameter C_f over tidal phases for March and April Moorings A and B.

	FLOOD	**HW**	**EBB**	**LW**
March				
Mooring A	4.7	4.4	3.6	3.9
Mooring B	0.6	0.5	0.8	0.7
April				
Mooring A	0.7	0.4	0.3	-
Mooring B	1.5	0.8	0.9	-

particles observed during the flood. Furthermore, floc strength was weaker at Mooring A compared to Mooring B, this is the converse of the relationship observed in March. An interpretation of this data could be that during April marine particles introduced to the estuary were stronger, perhaps due to the presence of biological agents enhancing flocculation processes.

5.4 Discussion

This Chapter examined the evolution of particle size throughout a tidal cycle in conjunction with ambient hydrodynamic and turbulence parameters. Initially the PSDs were discussed, followed by the relationship between D_{50} and ϵ as a function of u. Correlations between D_{50} and particle density were also conducted. An empirical model was utilised to better understand and quantify the relative contributions of turbulence parameters in governing particle size on a tidal scale. Finally, the Kolmogorov microscale was considered as a limiting factor on particle size.

Firstly, considering the PSDs, at Mooring A during spring tides in April, a rise in particle size of two distinct populations centred on 108 and 396μm) were seen at low water and high water respectively (Figure 5.8). The same was true in March however the C_v of particles at low water was lower (Figure 5.2). An explanation for two distinct signals at high and low water could be advection of marine particles into the estuary

during the flood; however an advection signal should also appear on the ebb as the advected particles are transported towards the mouth of the estuary. But the population of particles observed at low water was not the same size as the population seen at high water, therefore unless the original advected particles were partially de-flocculated to produce a smaller population size, it is not likely to have been an advection signal. An alternative explanation is that flocculation of smaller particles occurred at low and high water. For example, marine particles were introduced to the estuary during the flood, and at high water slack, current velocities fall to zero and local turbulent conditions reach a minimum, so particles we able to flocculate and settle out of suspension. At Mooring A, during low water current velocities did not reach zero due to the influence of the river flow rates. In the absence of marine influence, terrestrially derived particles dominated, flocculation of such particles then form the smaller population, which is advected by the river.

During neap tides at Mooring A in April a different PSD was observed (Figure 5.8b). A peak in C_v of particles encompassing the size range of both size populations observed during spring tides occurred during the flood with the maximum corresponding with the fastest current speeds, furthermore simultaneously a population of smaller particles centred on $19\mu m$ was observed. This change in PSD on neap tides compared to the PSD observed during spring tides was unlikely to be a resuspension signal as current speeds were too low. It is more likely that lower values of u provided conditions conducive for flocculation before high water. During neap tides the marine influence was lessened therefore lower C_v was expected and the flocculation signal was then limited by the availability of material in suspension to flocculate. In March a similar signal was observed at Mooring A on neap tides, although the C_v was considerably lower (less than $15\mu l l^{-1}$), therefore flocculation signals were not as obvious.

Moving now to Mooring B, in March and April PSDs during spring tides were similar to the PSDs discussed for Mooring A, however marine influence was greater at Mooring B which enhanced flocculation. As shown in Figures 5.11a and 5.5a larger particle sizes peaked at high and low water as seen at Mooring A, however on the whole C_v was higher

at Mooring B. During spring tides the maximum floc sizes were reported at high water due to flocculation as seen at Mooring A, at the onset of the ebb particle size decreased due to either or a combination of de-flocculation and preferential settling of larger particles. At low water the river dominates SPM contribution to the estuary, which introduces a smaller population of particles for flocculation. Following low water the onset of the flood introduced larger marine particles by either resuspension or advection and the process continues. This cycle of processes largely explains the evolution of flocs size in March and April at Mooring B during spring tides. During neap tides the evolution of floc size was similar however overall C_v values were lower due to the reduction of marine influence.

Contrary to the PSDs seen in March and April, November data presented a primary signal in C_v of larger particles during the ebb (Figures 5.14 and 5.16). At Mooring A the maximum D_{50} and C_v were observed during ebb after peak current speeds were achieved. The PSD was the same during spring and neap tides at this location, however higher values of C_v were reported during spring tides. At Mooring B two peaks in C_v of larger particles were recorded, the first coincided with maximum ebb current speeds and the second with the later part of the ebb and the onset of low water, after the signal observed at Mooring A. Mooring data alone represented the near bed SPM characteristics, spatial surveys of the water column between Mooring A and B throughout the flood and high water provided evidence of flocculation higher in the water column. With this evidence in mind it appears a flocculation signal persisted after high water in the RETZ, lower current speeds observed in November than in March and April did not de-flocculate particles during the ebb, in fact the flocculation signal was enhanced throughout the ebb near to the bed as flocs began to settle out. The rise in C_v and D_{50} which coincided with peak ebb velocities at Mooring B could be due to resuspension of flocs which recently settled after high water, therefore lower current speeds would be required to do so. This resuspension signal was not observed at Mooring A as the material was not available.

In addition to considering the size and concentration of flocs in conjunction with hydrodynamic conditions to conclude flocculation processes are occurring, the fractal model introduced by Kranenburg (1994) can be applied to the data. The fractal model infers

a unique relationship between particle size and the number of particles that a given floc can be composed of. The particles that flocculate to form flocs are referred to as primary particles. Kranenburg (1994) presented the following equation to describe the fractal nature of flocs.

$$C_m = \rho_s C_v (\frac{D_p}{D_{50}})^{3-nf} \tag{5.7}$$

ρ_s is the sediment density, D_p is the diameter of the primary particle and nf represents the fractal dimension which determines the scale at which flocculation is predicted. Assuming a fractal dimension of 2, as suggested by Kranenburg (1994) for flocs in suspension, the relationship can be simplified to show.

$$C_m = (\frac{C_v}{D_{50}})^{3-nf} \tag{5.8}$$

Equation 5.8 can be applied to observational data to test whether values for size and concentrations of mass and volume are related in accordance with the fractal model.

Figure 5.36 shows the fractal model relationship applied to data collected at Moorings A and B for all field campaigns. The strong and significant correlations shown in Figure 5.36 for all field campaigns provides evidence to support hypothesises of flocculation occurring in the RETZ as data clearly follows the fractal model. If this relationship was poor it could not be concluded that flocs interact in a coherent fashion through flocculation. It is important to note Figure 5.36c representing data collected at Mooring A in September does not include data post dating the major river event. At this time the system was out of equilibrium with regards to SPM size and concentrations which will be discussed further in Chapter 6.

PSD analysis has only considered the phase of the tidal cycle, Figures 5.20 to 5.21 consider how D_{50} was related to TKE dissipation and current speed. Firstly, bivariate analysis of D_{50} and current speed for the whole sampling periods did not give rise to statistically significant relationships, therefore analysis was focused on a tidal scale to

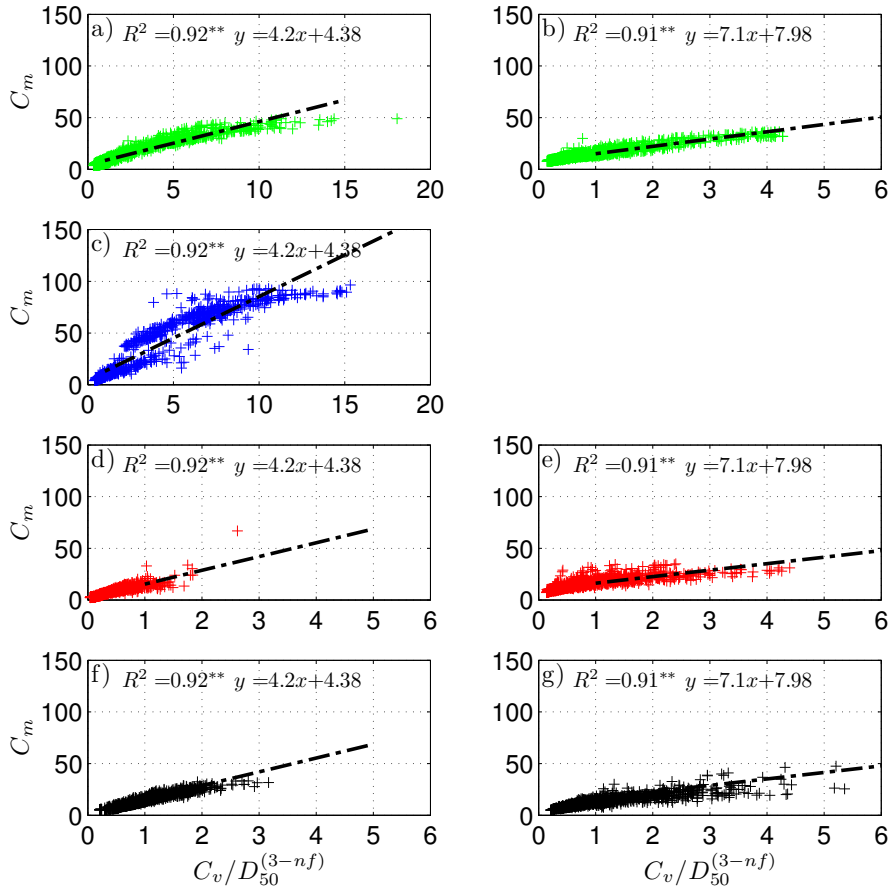

Figure 5.36: Seasonal comparison of Winterwerp's fractal model hypothesis for Moorings A and B. Green markers represent data collected in April, Blue markers denote data collected in September, excluding data after the major river event, Red markers show data collected in March and Black markers denote data collected in November. a,c,d and f represent Mooring A. b, e and g represent Mooring B.

eliminate some of the variability introduced by analysing longer time periods. During neap tides at Mooring A in March and April a positive correlation between ϵ_h, u_h and D_{50} was apparent as the largest particles occurred around peak flood current speeds, this could have been due to resuspension of larger particles, however as current speeds were lower during neap tides it is more likely to have been floculation occurring before high water, furthermore profiling data from Chapter 4 support this concept.

During spring tides overall, D_{50} decreased as ϵ_h and u_h increased (Figures 5.20 and 5.19) and vice versa. This infers de-flocculation of particles during more turbulent conditions such as maximum current speeds, and flocculation giving rise to the largest particles observed when turbulent conditions were low at high and low water. As previously discussed the relationship between current speed and TKE dissipation has not always been observed to be linear. Moreover, the maxima in ϵ_{bed} during the ebb in both spring and neap cases of Figures 5.19a and b coincides with the smallest D_{50} but not the maximum values of u_{bed}.

Spring and neap data for Mooring B in March and April largely show the smallest D_{50} corresponding with the highest levels of ϵ_h and vice versa, although D_{50} does not show much variation throughout the flood phase of the tide, indicating a poor correlation between ϵ_h, u_h and D_{50} during this phase. These observations provide further evidence to suggest flocculation occurred at high water and de-flocculation during periods of enhanced TKE dissipation.

Observations from November showed D_{50} enhanced during the ebb, without coinciding with either highly turbulent or quiescent periods for both mooring locations, therefore the flocs were not reacting directly to local turbulent conditions. However, at Mooring B a minor peak in D_{50} was observed coinciding with a peak in TKE dissipation and current speed during the ebb, as discussed above this could be due to resuspension of recently flocculated particles.

Section 5.3.3 examined the relationship between effective density and D_{50} (Figures 5.22,

5.24 and 5.26), for both mooring locations, which provided evidence to suggest lower densities were consistently associated with bigger particles and vice versa. As flocs form their density relative to their size and the primary particles reduces due to interstitial water pockets combined between primary particles and the potential organic component. Therefore, lower densities observed at a time of large flocs forming strongly suggests flocculation was occurring in the RETZ. Furthermore effective density decreasing as mass concentration remains unchanged infers de-flocculation, liberating primary particles with lower associated densities.

The main focus of this Chapter revolves around the interaction between particle size and turbulence parameters, the effects of salinity on particle size is however well documented in the literature (Fugate and Friedrichs, 2003; Manning and Dyer, 1999). The empirical model utilised in this Chapter assesses the contribution of salt water intrusion and turbulence parameters in governing particle size over a tidal scale.

Starting with Mooring A, in March modelled D_{50} compares well with observed values (Figure 5.28) for both spring and neap cases. Disaggregation or resuspension parameter u_{bed} was associated with a small but negative β_D indicating an inverse relationship however β_D values associated with G_{bed} were positive and negative ones associated with $\mu_{k_{bed}}$, therefore once again it appears the advection of salt water was the prominent factor in the Mooring A. In April, Figure 5.30 also indicates significant relationships for all three regressions for spring and neap tides at Mooring A, although it is interesting to note, stronger correlations were shown during spring tides than on neaps. This could be due to the maximum D_{50} corresponding with peak flooding currents and thus out of phase with the salt water intrusion (represented by h). During spring tides the peak in D_{50} corresponds with high water, a period of low turbulence and current speeds which infers an inverse relationship however, positive β_D are shown in case, thus suggesting the dominant factor to be the advection of salt water into the estuary.

Mooring B, Figure 5.31 shows the model output was well correlated to the observed D_{50} values in April in both spring and neap cases. Positive β_D components were displayed,

again suggesting the importance of tidal height and the advection of salt water over the turbulence regime in governing particle size at this time. In contrast, β_D values were negative for both u_{bed} and G_{bed} where positive components are shown for $\mu_{k_{bed}}$ (Figure 5.29). This indicates disaggregating parameters such as current speed and turbulence parameters contributed to the variation of D_{50} on a tidal scale however, the overall conclusions suggest the phase of the tide and therefore advection of salt water and marine influence play a major role in regulating D_{50} throughout Mooring B in April 2010 and March 2011.

In order to assess the relationship between turbulence parameters and D_{50} further μ_k was compared to D_{50}, if the Kolmogorov microscale was acting as an upper limit for particle growth then a positive correlation should be apparent. As seen in the Figures describing the empirical model output a positive correlation between μ_k and particle size was not obvious. Figure 5.32 presents poor correlation for all data sets when the full length of mooring data was considered. When individual tidal cycles are identified the correlations improve (Figures 5.33 and 5.35) and interesting trends between floc properties from marine origins compared to terrestrially derived particles emerge. Due to the inverse relationship shown between particle size with u_{bed} and G_{bed} at Mooring B in March (Figure 5.29) the relationship between particle size and μ_k was expected to be significant.

Figures 5.33d, e and f presented statistically significant but relatively poor correlation, however with a phase lag of 60 minutes applied to the data the correlation was notably enhanced. In summary if particle size presents a positive correlation with μ_k then a phase lag can enhance the relationship as a correspondence between eddy size and particle size growth is already established, the phase lag aligns particles with the turbulence data more likely to be acting upon it. However, as seen in the empirical modelling results the turbulence parameter μ_k was not always deemed the sole parameter governing particle size. For example, at Mooring A the influence of terrigenous sediments was higher, it appears these particles do not follow the Kolmogorov equilibrium between size and turbulence; this could be due to their floc strength or the fact that these particles require

longer to react to a new turbulence regime, different from the river. This could also explain the variability in the relationship between the Kolmogorov microscale and D_{50} during the ebb at Mooring B also. Another potential explanation for a lack of correlation between D_{50} and the Kolmogorov microscale could be the ambient turbulence conditions were not sufficient enough to affect particle size. For example studies by Jago et al (2006) and Braithwaite et al (2012) reported relationships between turbulence and particle size, however these studies were undertaken in tidally energetic environments such as the Irish Sea and the Menai Strait respectively. For example Jago et al (2006) reported maximum values of TKE dissipation of $log_{10}\epsilon = -0.5 W kg^{-1}$, whereas maximum values in the Dyfi reached $log_{10}\epsilon = -2 W kg^{-1}$.

Considering the potential impacts of floc strength on the relationship between $\mu_{k_{bed}}$ and D_{50} further, Figure 5.37 explores three mechanisms in which $\mu_{k_{bed}}$ relates to floc size. Green arrows denote the relationship between $\mu_{k_{bed}}$ and D_{50} during the ebb (and

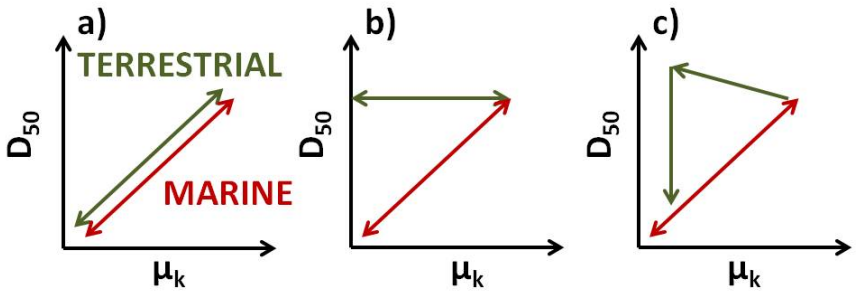

Figure 5.37: Schematic diagram comparing the relationship between the Kolmogorov microscale and D_{50} for marine and terrestrially derived flocs.

including low water, i.e. periods of fluvial influence) and red arrows the flood (and including high water, i.e. periods of marine influence). In the case of schematic a, particle size throughout the tidal phase relates to the turbulence regime, larger particles occur as the turbulent eddy length scale increases. This is true of a system in which floc strength and general composition remains constant, a more closed system than the estuarine environment. Secondly, schematic b shows a system in which particles on the flood relate to the turbulence regime, whereas during the ebb; when terrestrially derived particles are

introduced to the system, these newly introduced particles are unaffected by the ambient turbulence conditions. This could be due to the newly introduced particles exhibiting a high floc strength, or simply the particles have not yet reacted to the turbulence thus leading to a phase lag relationship. Finally, schematic c again explores the possibility of particles introduced during the ebb not adhering to the commonly accepted $\mu_{k_{bed}}$ and D_{50} relationship, furthermore this schematic identifies the signal observed at Mooring B in March. Once again, particles introduced to the RETZ during the flood were scaled in size by the ambient turbulence regime, however at the onset of the ebb, which coincided with enhanced values of floc strength, particle size continued to increase as the turbulent eddy length scales decreased. This could be due to flocs with a higher floc strength not only withstanding higher turbulence conditions, but elevated turbulence in the early ebb actually enhancing flocculation. This enhancement reaches a critical point at which D_{50} decreases dramatically, most likely due to a critical shear stress having been reached that even stronger flocs cannot resist and de-flocculation occurs. Following this fall in D_{50}, the normal equilibrium between particle size and turbulence is restored, coinciding with the onset of the flood.

5.5 Summary Points

- PSD data suggests flocculation signals occur at high and low water during spring tides. At high water flocs are most likely to be composed of primary particles of marine origin, whereas at low water both mooring locations are dominated by the river and therefore terrigenous sediments.
- The main difference between the PSD at Mooring B compared to Mooring A is bigger particles are found at Mooring B, due to enhanced availability of SPM of marine origin to flocculate.
- An inverse relationship between particle size and effective density is established. Larger particles report the lowest densities, which is indicative of flocculated particle characteristics, providing further evidence for the flocculation argument.

- D_{50}, C_m and C_v follow the fractal model presented by Kranenburg (1994), providing yet further evidence to suggest flocculation is occurring.

- The empirical model suggests the relationship between D_{50} and tidal height, representing the advection salt water, is much more significant than the correlation with turbulence parameters or tidal currents.

- Estuarine sediment dynamics in November presented an ebb dominance in suspended sediment transport and a flood dominance in tidal currents. Evidence from spatial surveys in the RETZ shows a flocculation signal formed during the flood and at high water relatively high in the water column. During the ebb this flocculation signal settled as it was advected out of the estuary as observed at Moorings A and B. Furthermore, evidence of a resuspension signal at Mooring B during peak ebb currents was also observed when recently flocculated material was liberated from the bed.

- A positive correlation between the Kolmogorov Microscale and D_{50} is only observed during March at Mooring B during the flood. The influence of the river at Mooring A and during the ebb at Mooring B breaks down the relationship between the Kolmogorov microscale and particle size, this has been linked to floc strength. When a positive relationship occurs, a phase lag of 60 minutes is found to enhance the relationship. The effects of turbulence parameters can require a time lag in order to align with the reaction of the D_{50} measurement acted upon.

Chapter 6

Seasonal Variation in Hydrodynamic and SPM Characteristics

6.1 Introduction

This Chapter aims to provide context for tidal and lunar variations in SPM and hydrodynamic characteristic interactions considered in previous Chapters. SPM and hydrodynamic characteristics vary on a seasonal scale in the estuarine environment which can have a significant impact on the transfer of terrestrial material to the coastal oceans. It is therefore imperative to gain a sound understanding of the transfer of SPM throughout the RETZ on a seasonal scale. In the previous Chapter, variations in SPM characteristics such as particle size have been investigated on a tidal scale for spring and neap cases. Here temporal and spatial scales are broadened to encompass differing seasonal conditions and assess the estuary system as a whole.

Superimposed on seasonal variations are extreme flood events. Extreme flood events such as river flooding can significantly affect the local SPM and hydrodynamic conditions in the estuarine environment, this can in turn impact the transfer of biogeochemical components associated with SPM throughout the estuarine system (Dyer, 1989; North et al, 2004).

6.2 Observations

Observations for this Chapter include March 2011 and April 2010 mooring data, representing Winter and Spring type conditions respectively. Tidally averaged SPM and hydrodynamic properties are examined as a function of tidal range. A point flux of coarse and fine particles is calculated and compared as a time series and the net tidal flux for both Moorings A and B. Despite being so close on the annual calender these months are assumed to represent different seasons as shown by the meteorological conditions presented in Chapter 4. In addition data from the mooring deployed in September 2010 during the extreme flood event are examined. The PSD throughout two flood events will be considered in conjunction with wind stress, TKE dissipation and tidal currents. Moreover tidally averaged SPM characteristics are presented to allow the comparison of broader trends. Finally, suspended sediment fluxes are calculated for this period and the net effect of a flood event on sediment transport is considered.

6.3 Results

6.3.1 Comparison of seasonal tidally averaged estuarine hydrodynamic properties

Primarily a comparison of tidally averaged hydrodynamic and turbulence properties for Moorings A and B in March and April are presented, including absolute maximum current speeds per tidal cycle (U_T), tidally averaged turbulence parameter (G_T) and tidally averaged Kolmogorov microscale (μ_{k_T}). Each parameter is displayed as a function of the tidal range (h_T).

March

A significant positive correlation is observed between U_T and h_T at both Mooring A and B in March (Figures 6.1a and d). At Mooring B, a steeper gradient was reported in

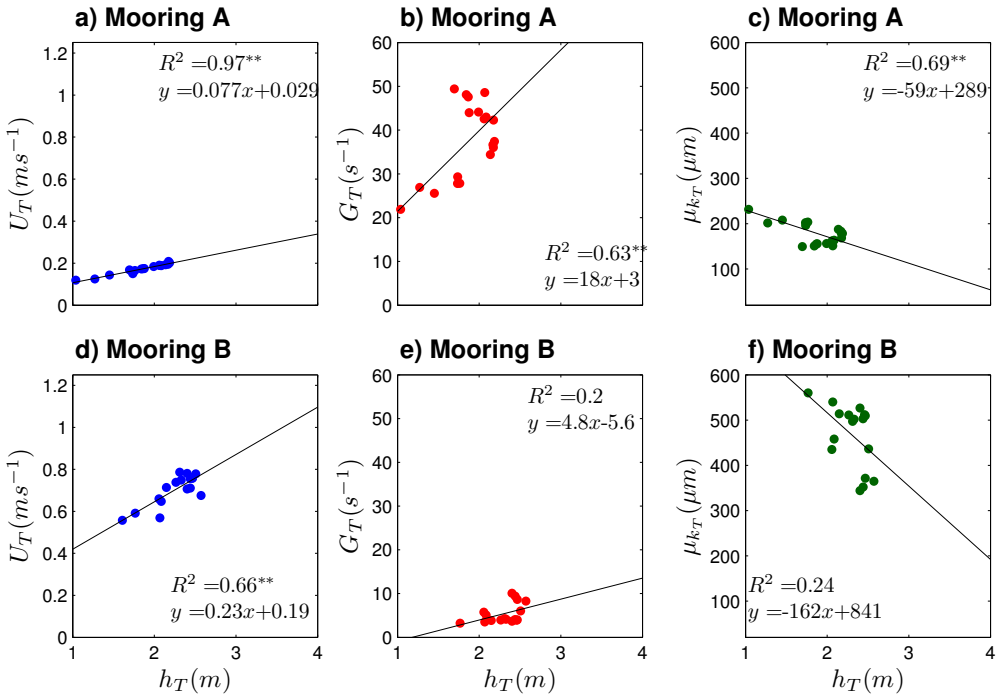

Figure 6.1: Tidally averaged hydrodynamic properties at Moorings A and B in March 2011. (a),(b) and (c) represent data. h_T = tidal range in (m). Using adcp data for RETZ.

Figure 6.1 which regressed tidal range against maximum current sppeds. This indicates that for any given tidal range value (h_T) a higher maximum current speed (U_T) value was observed at Mooring B than at Moorings A . This relationship at the Moorings A may be affected by the lower U_T recorded as current data was acquired close to the bed from the ADV in this case. Statistically significant relationships were observed in March between G_T and h_T at Mooring A(Figure 6.1b), although at Mooring B the relationship was weaker and not significant. Finally, negative relationships between μ_{k_T} and h_T at both mooring locations were observed, again only the relationship at Mooring A was statistically significant. In summary, hydrodynamic parameters, current speed, turbulence parameter G and the Kolmogorov microscale showed significant correlation to tidal range at Mooring A in March, whereas only current speed displayed a significant correlation to tidal range at Mooring B.

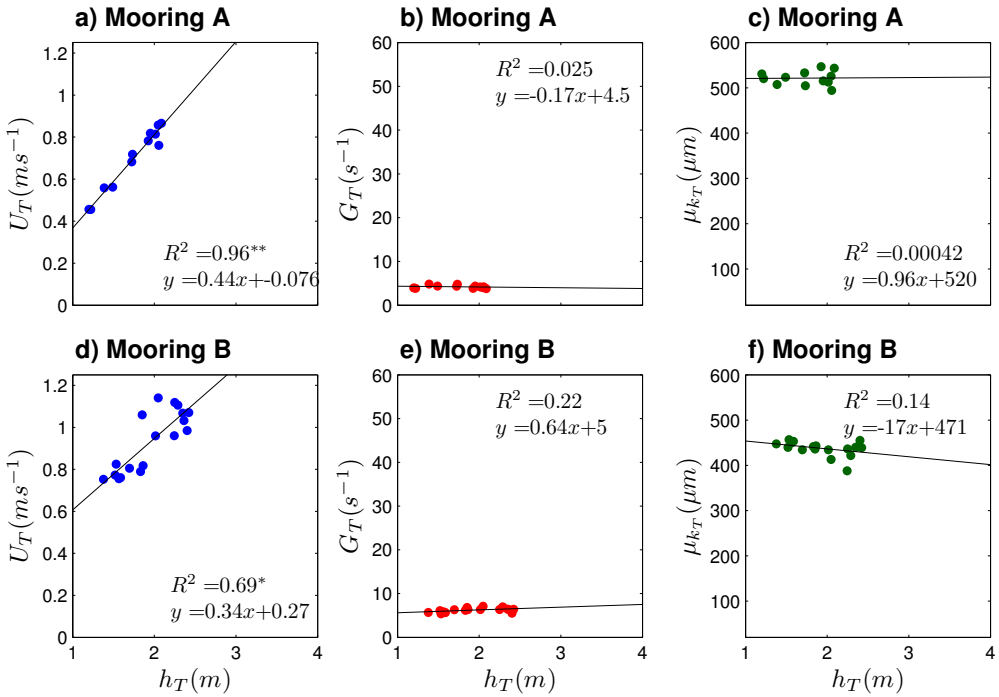

Figure 6.2: Comparison of tidally averaged hydrodynamic properties at Moorings A and B in April 2010. h_T = tidal range in (m).

April

Figure 6.2 indicates a significant positive correlation between U_h and h_T at both Moorings A and B. Since spring tides were associated with the fastest current speeds and neap tides with the lowest. Moving on to G_T, Figure 6.2b reports a weak relationship with h_T for Mooring A data, suggesting G_T was not significantly related to h_T at this time ($R^2 = 0.025$). Furthermore, Mooring B presented a statistically insignificant relationship also (Figure 6.2e), inferring G_T was unrelated to h_T at both mooring locations. In addition to a poor correlation with G_T, h_T did not represent a significant correlation with μ_{k_T} at Mooring A or B either (Figure 6.2c and f). In summary, a significant correlation between maximum current speeds and tidal range was found at both moorings, however neither turbulence parameters G_T or μ_{k_T} showed a significant correlation with tidal range.

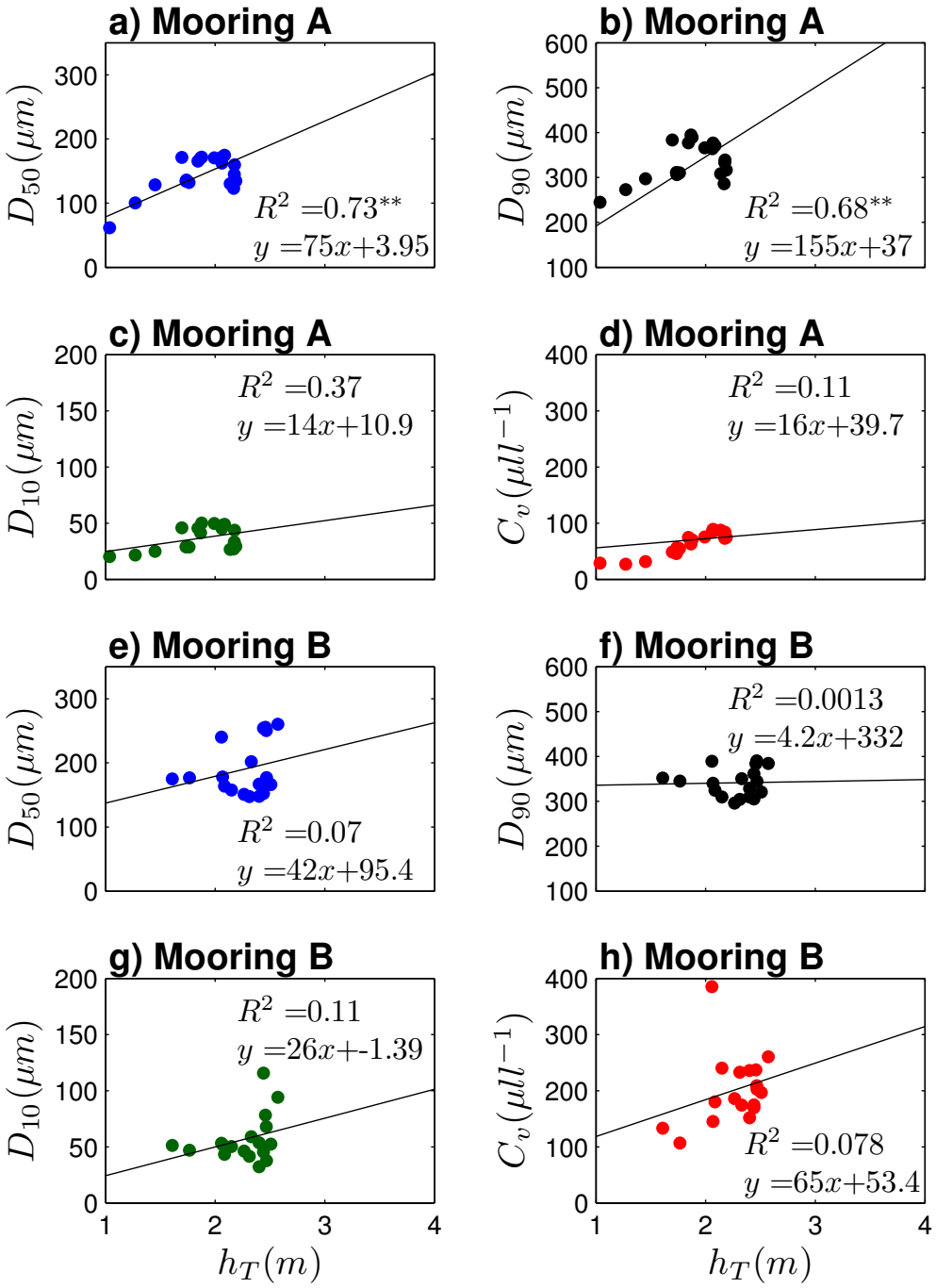

Figure 6.3: Comparison of tidally averaged SPM properties at Moorings A and B in March 2011. h_T = tidal range in (m).

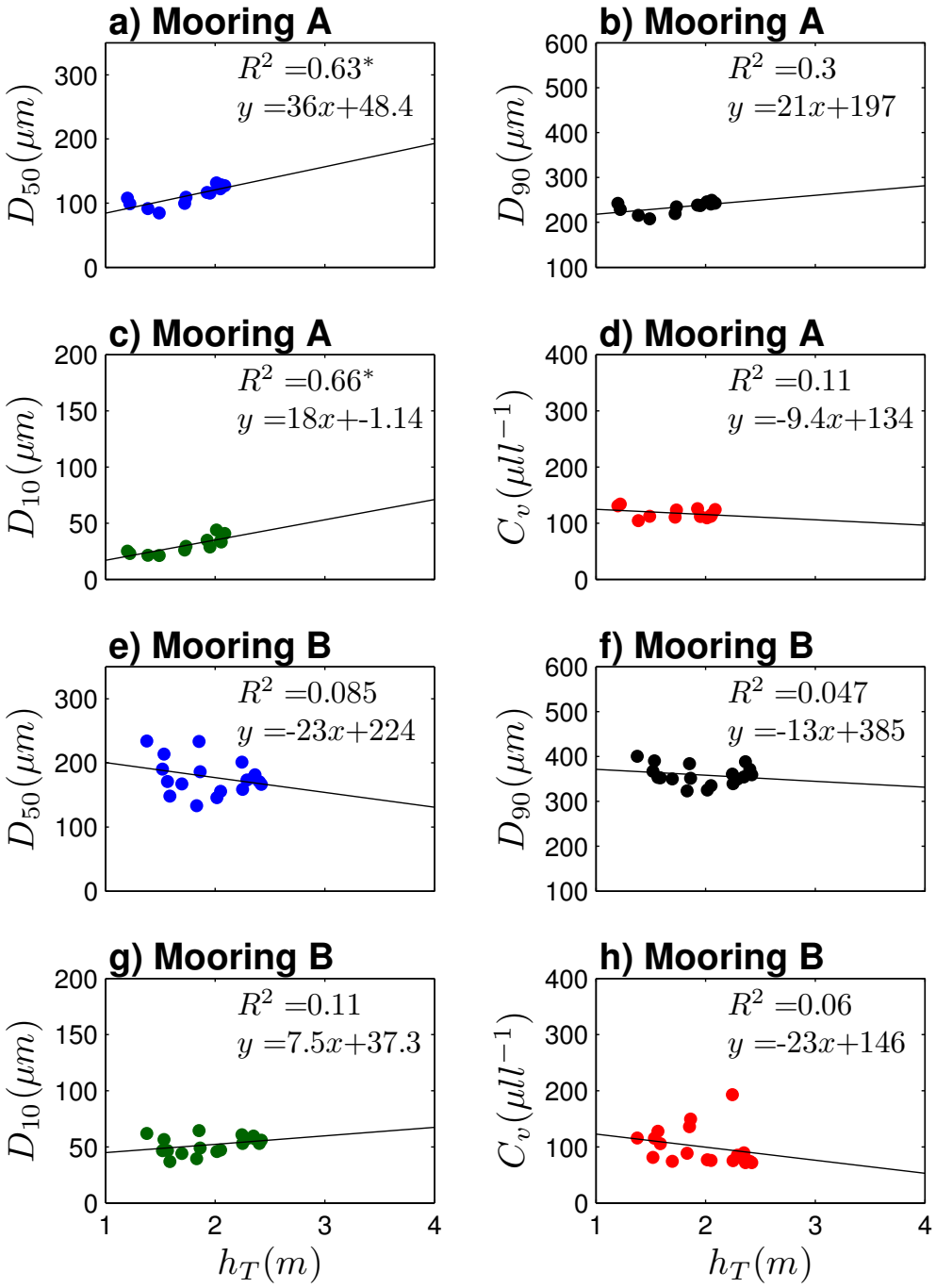

Figure 6.4: Comparison of tidally averaged SPM properties at Moorings A and B in April 2010. h_T = tidal range in (m).

6.3.2 Comparison of seasonal tidally averaged estuarine suspended particulate matter properties

March

Tidally averaged SPM characteristics are now considered as a function of h_T. SPM characteristics displayed are D_{10}, D_{50}, D_{90} and C_v. Mooring A data suggests a positive significant relationship between D_{50}, D_{90} and h_T (Figure 6.3a and b). D_{10} and C_v do not present a significant correlation with h_T. Correlations at Mooring B are weak and do not suggest a significant relationship between h_T, particle size or volume concentration during March.

April

Figure 6.4 indicates particle size across all three percentiles increased with h_T during April at Mooring A, however only D_{50} and D_{10} presented significant correlations. C_v again presented an insignificant correlation with tidal range. As seen in the previous section, stronger correlations were observed at Mooring A than at Mooring B. Figures 6.4e to g indicate particle size across the three percentiles were not significantly correlated to h_T. Finally an insignificant relationship between C_v and tidal range was also shown by Figure 6.4h. In summary the most significant relationships found were between D_{50} and tidal range at Mooring A, overall correlations with tidal range and SPM characteristics at Mooring B were insignificant.

6.3.3 Seasonal variation in estuarine suspended sediment transport

Suspended sediment fluxes were calculated for both mooring locations in March and April, comparing the transport of fine and coarse particles. The suspended sediment flux (F_{bed}) represents a point measurement of sediment transport through a unit of area over time. The difference in u_{bed} from the ADCP and ADV instruments respectively suggests the assumption of uniform vertical current speeds to be unlikely, therefore the flux is

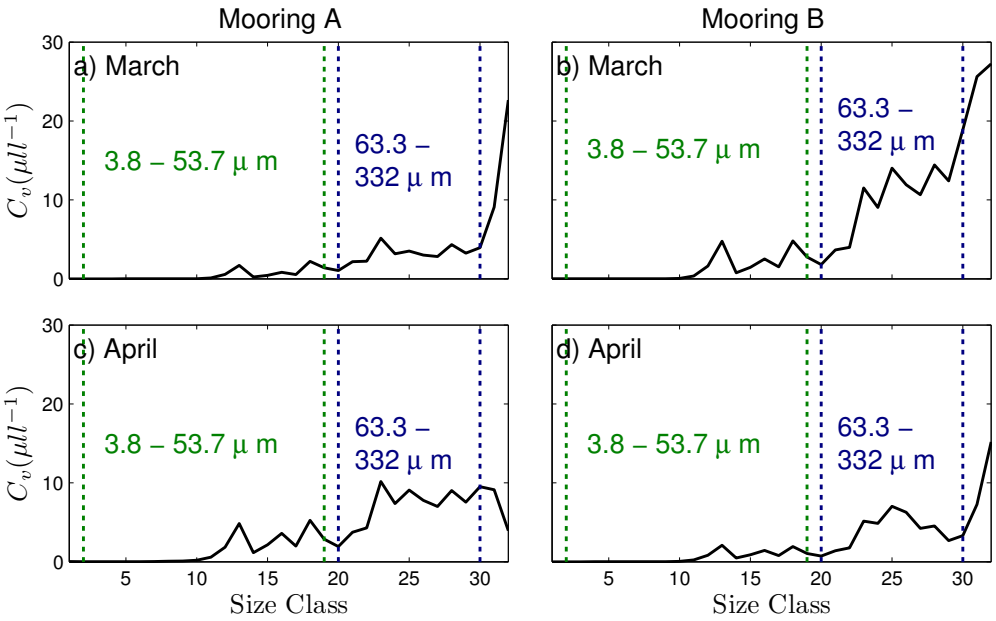

Figure 6.5: Analysis of bimodal particle size distributions in March and April.

not extrapolated to cover the cross-section of the channel. It is also important to note due to the asymmetric shape of the channel in which Mooring B was located, horizontal current speeds were not expected to be homogeneous either. The point measurement of the suspended sediment flux at the bed was calculated via Equation 6.1 below.

$$F_{bed} = C_v.u_{bed} \tag{6.1}$$

Equation 6.1 describes the suspended sediment flux calculation using data from both the ADV and ADCP instruments. C_v represents the volume concentration of a given size class. Due to the difference in behaviour of particles relative to their size, the PSD is examined once again in order to represent the transfer flux of suspended sediment according to size at each mooring location.

Figure 6.5 indicates a largely bimodal distribution in the PSD for each mooring location in March and April. The green section denotes the fine particle size range and the blue the coarse particle size range. The data was truncated; the first two and the last two size classes were not included due to the limitations of the LISST-100 at maximum and minimum ranges discussed in Chapter 3.

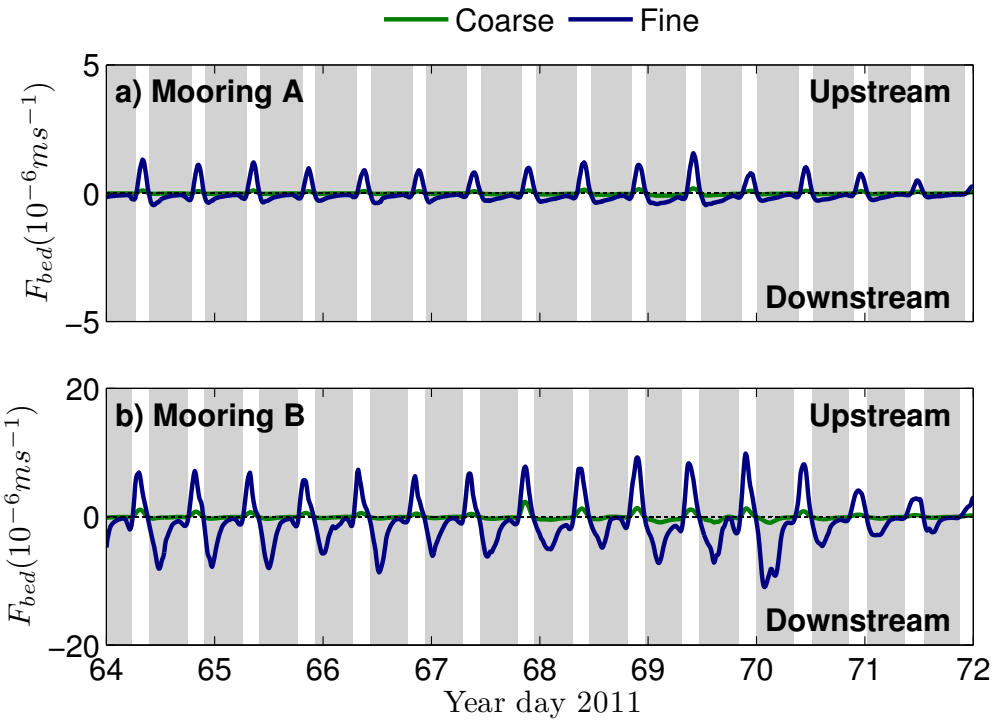

Figure 6.6: Comparison of Suspended sediment flux of coarse and fine particle sizes at Moorings A and B in March 2011.

March

The bimodal distribution was used to calculate a fine and coarse suspended sediment flux shown as a time series in Figure 6.6. The fluxes observed at Mooring A in March were smaller than observed values at Mooring B, this was partly due to using ADCP data in the flux calculation (note $y-axis$ scale in Figure 6.6a). The coarse particle flux was greater than the fine particle flux at both mooring locations (Figure 6.6), which was expected as the bimodal split of the size classes was inherently biased towards coarser particle (Figure 6.5). At Mooring A the fine particles flux was in fact close to zero throughout the sampling period, coarse particles showed a dominant flux of particles landwards during the flood. Furthermore, at Mooring B the export of coarse particles dominated the transport flux which was much greater than observed values at Mooring A and the spring to neap modulation of transport was evident (Figure 6.8).

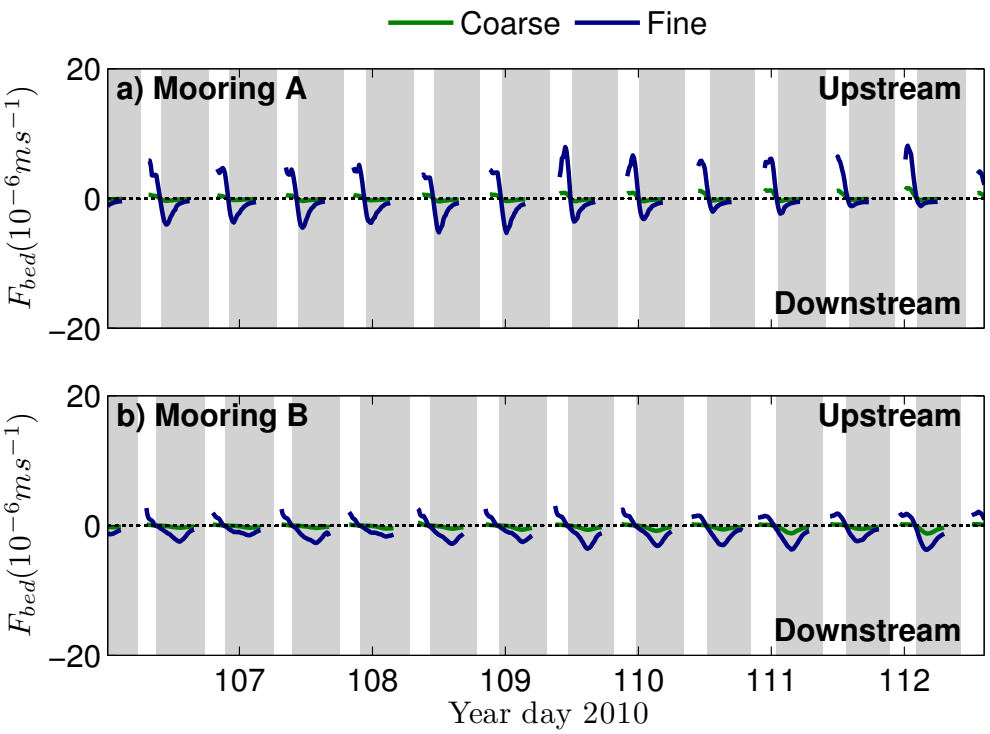

Figure 6.7: Comparison of Suspended sediment flux of coarse and fine particle sizes at Moorings A and B in April 2010.

April

In April coarse particles also dominated at Mooring A, the fine particle flux was predominantly in a landwards direction, which increased as tidal range decreased. During neap tides coarse particles are also imported into the estuary at the Moorings A (Figure 6.7a). Conversely at the Mooring B the flux of both size classes is predominantly towards the mouth, suggesting fine and coarse particles were exported past this site. As seen at Mooring A the transport of coarse particles is greater than fine particles. Figure 6.7b also indicates the overall flux of suspended sediment is lower at the Mooring B compared to Mooring A.

After considering the time series of suspended sediment flux throughout the sampling periods at both mooring locations for March and April, the net tidal flux is now consid-

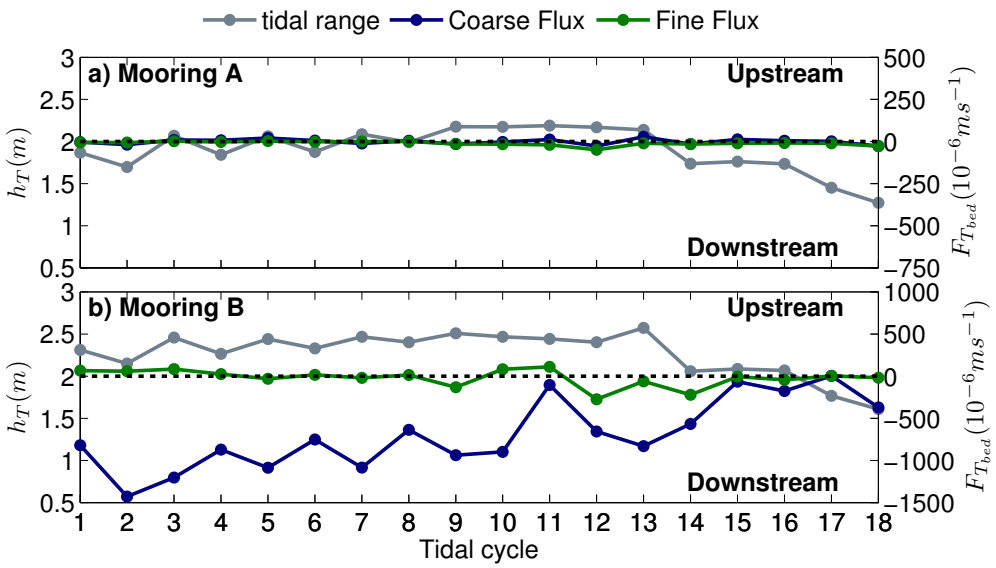

Figure 6.8: Tidally averaged suspended sediment flux of fine and coarse particles at Moorings A and B in March 2011. ADV used to calculate $F_{T_{bed}}$ at Mooring A.

ered. The net tidal flux is simply the sum of the flux over a tidal cycle which indicates the net direction of sediment transport per tidal cycle.

March

The net tidal flux of suspended sediment was notably low at Mooring A in March, namely due to the lower values of u_{bed} from the ADV. The net flux of both coarse and fine particles remained close to zero, suggesting the transfer of suspended sediments was in equilibrium at this location within the estuary in March. The net tidal flux of fine particles at Mooring B was also close to equilibrium in March. On the other hand, a maximum net flux of coarse particles occurred in March and April for the first 14 tidal cycles. Towards the end of the sampling period, when h_T decreased the net flux also declined (Figure 6.6b).

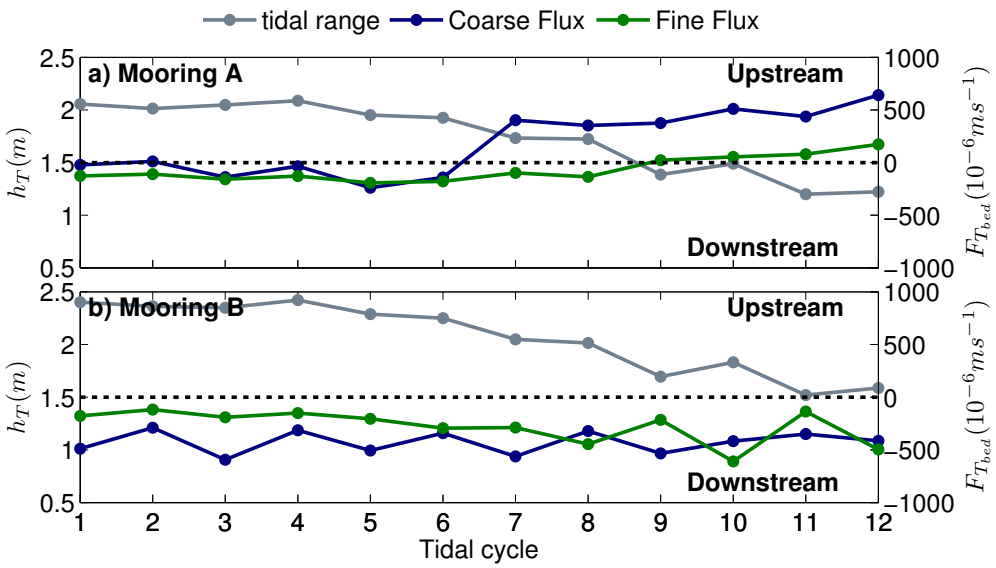

Figure 6.9: Tidally averaged suspended sediment flux of fine and coarse particles at Mooring A and B in April 2010.

April

Figure 6.9 presents the net tidal flux of coarse and fine particle with tidal range for mooring data collected in April. At Mooring A, the net transport of coarse particles transfers from exporting to importing particles as h_T decreased towards 1.7 m at neap tides. Fine particles showed the same trend, however F_{T_h} values were considerably lower. At Mooring B, fine and coarse particles net fluxes were towards the mouth of the estuary throughout the sampling period. The export of coarse particles was greater than the fine and appeared to increase as h_T decreased (Figure 6.9b). The net total suspended sediment flux of fine and coarse particles throughout the whole sampling periods in March and April are compared in Table 6.1.

Summary

Table 6.1 suggests Mooring B acted as an exporter of coarse particles in both March and April however, the export value was an order of magnitude higher in March. Conversely,

the export of fine particles was an order of magnitude higher in April. In April at Mooring A the net transport of coarse particles over the sampling period was positive, whereas the net transport of fine particle was towards the mouth. However, it is important to note data missing from ADCP measurements in April could bias the results of the net SPM flux. For example as neap tides progressed, the period at which the ADCP blanking range was greater than the water level increased, thus leading to a bias towards the flood phase of the tide. In March an overall net export of fine and coarse particles was observed at the Moorings A, the magnitude of which was not possible to compare due to the use of ADV measurements for u_{bed}. In summary data collected in April cannot be used meaningfully to calculate a net tidal flux due to gaps in the data set, but March flux calculations suggest the RETZ was acting as a net exporter of suspended sediments.

Table 6.1: Net suspended sediment flux ($10^{-6} ms^{-1}$) of coarse and fine particles for sampling periods in March and April.

Month	Mooring	Fine	Coarse
March	TIR	-594	-519
	RETZ	-354	-15085
April	TIR	-789	2153
	RETZ	-3328	-5131

6.3.4 Effects of river flood events on estuarine hydrodynamic and SPM characteristics

The role of turbulence parameters in governing particle size has been examined over varying time scales including; seasonal, lunar and tidal. It is well known extreme river flood events can dramatically affect estuarine sediment dynamics and thus the size and fate of suspended sediment. This section therefore aims to examine the effects of river flooding on SPM and hydrodynamics characteristics and interactions to ultimately assess the impacts on suspended sediment transport.

Figure 6.10 gives an overview of the SPM and hydrodynamics conditions during the river event in September 2010. Two river flood events took place during the sampling period

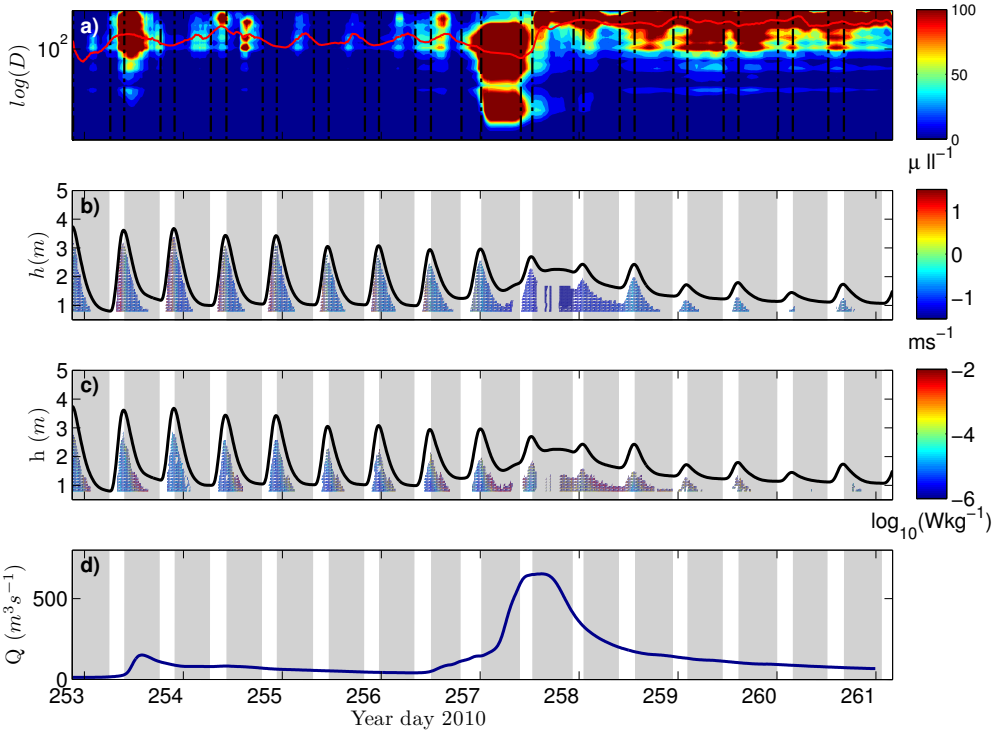

Figure 6.10: Particle size spectra and hydrodynamic properties of Mooring A during a river event in September 2010. a) C_v of particle size (D) distributions, D_{50} in red. b) Contour of u. c) Contour of ϵ. d) River discharge (Q).

during year days 253 and 257. The major river event which occurred on year day 257 presented flow rates over three times greater than the previous minor river event and over 30 times greater than the annual average river flow rate for the Dyfi.

The PSD observed in September was notably different to PSDs reported in March, April and November data sets. The maximum C_v of the largest size classes were over three times greater than previous data sets. During the minor flood event an enhanced C_v of particles larger than $200\mu m$ were observed. In between the two river flood events, C_v dropped with the exception of the flood and following ebb tides of year day 254. As Q increased on year day 256 and 257, C_v increased dramatically across a broad range of particle size classes (Figure 6.10a). Moreover, a sustained C_v ($100\mu l l^{-1}$) of particles larger than $200\mu m$ was reported after the major river event. Figures 6.10b and c suggest the major river event notably modified the tidal variation in u and ϵ; in fact post-

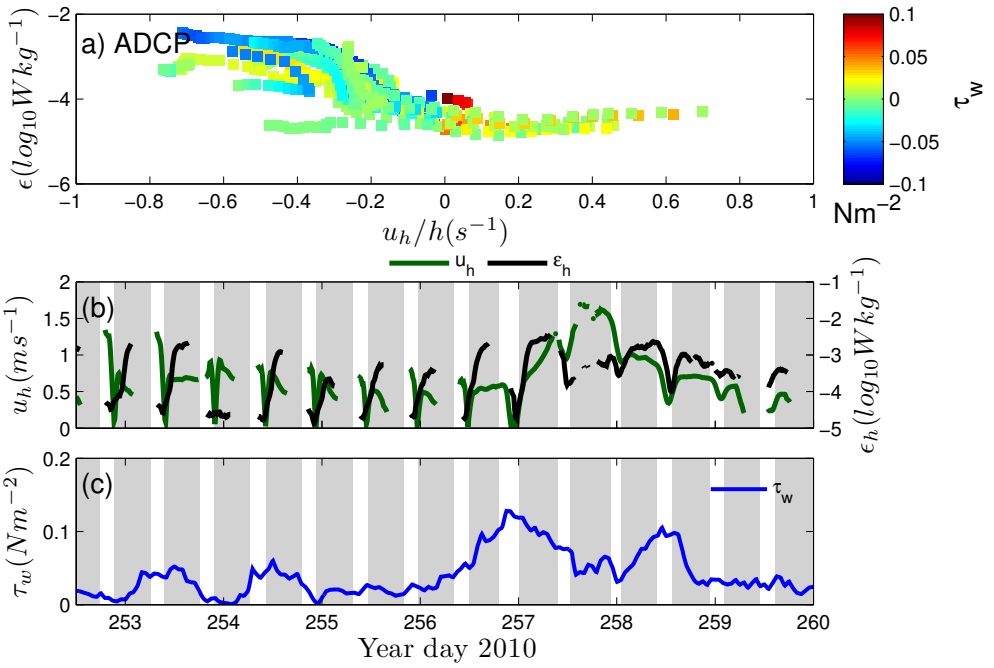

Figure 6.11: Relationship between hydrodynamic parameters u_h and ϵ_h with τ_w. a) ϵ_h as a function of u_h/h and τ_w. b) Time series of ϵ_h and u_h. c) Time series of τ_w.

major river event u remained negative (i.e. downstream) up to and including year day 261, suggesting the flooding tide was not penetrating the TIR. The highest levels of ϵ were recorded during the major river event, furthermore on a tidal scale the maximum ϵ occurred during the ebb due to the combined effects of the river and tidal currents (Figure 6.10d).

As discussed in Chapter 4, ϵ_h can be related to θ_{wind} and τ_{wind} in addition to tidal currents. Winds travelling in a North Easterly direction dominated during this sampling period especially at the time of the river flood events as these winds are associated with low pressures and increased rainfall. Figure 6.11 indicates the maximum values of ϵ_h corresponded with the ebb phase of the tide when the wind and current direction opposed each other (blue markers on Figure 6.11a). Furthermore, Figure 6.11c shows the wind stress (τ_w) was enhanced in accordance with the onset of the river event, as the river event progressed τ_w decreased and the maximum ϵ_h occurred at the end of year

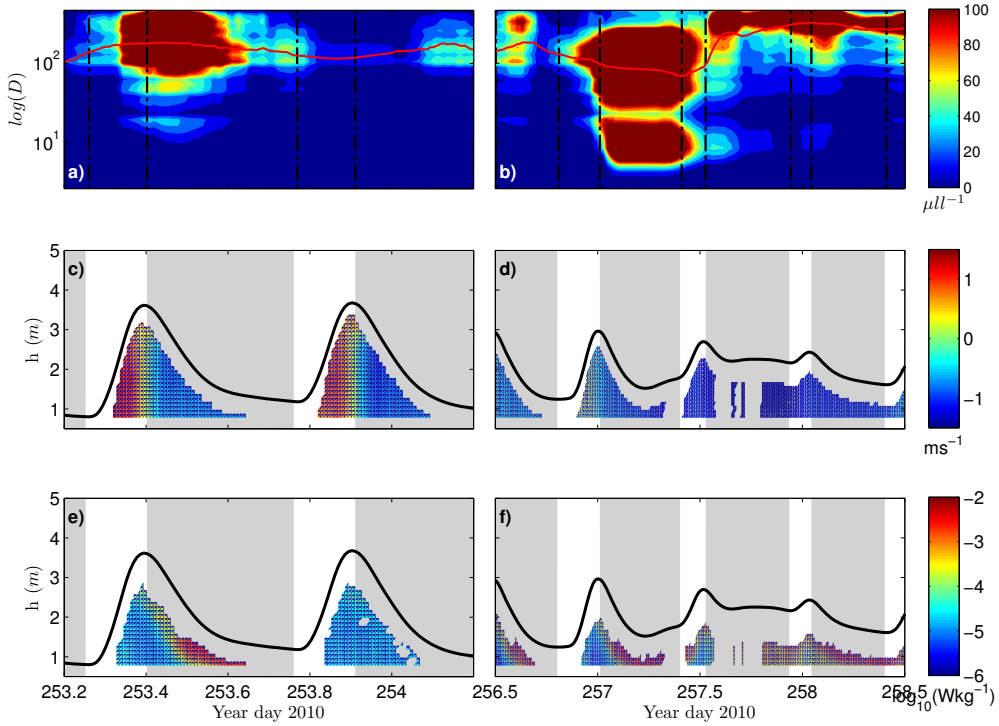

Figure 6.12: Comparison of particle size spectra and hydrodynamic properties in the TIR during minor and major flooding events. a),c) and e) represent the PSD, (u) and (ϵ) profiles during the minor flood event. b), d) and f) represent the major river event.

day 257.

In order to assess the affects of hydrodynamic parameters such as u and ϵ on the PSD under river flood conditions the two river flood events are considered in further detail (Figure 6.12). During the minor river event the most prominent signal in the PSD was the population of particles greater than $200\mu m$ which persisted for one tide. A decline in C_v of these particles corresponded with the maximum ϵ recorded during the ebb when current speeds were approximately $0.5ms^{-1}$. At the time of the major river event C_v increased dramatically throughout the particle size classes, the ϵ was at a maximum at this time and the flood tidal currents were undermined by the flow of the river, which resulted in sustained negative velocities. The PSD proceeded to change after approximately one tidal cycle, presenting a sustained concentration of particles greater than $200\mu m$ despite the sustained values of ϵ recorded throughout year day 257 and 258.

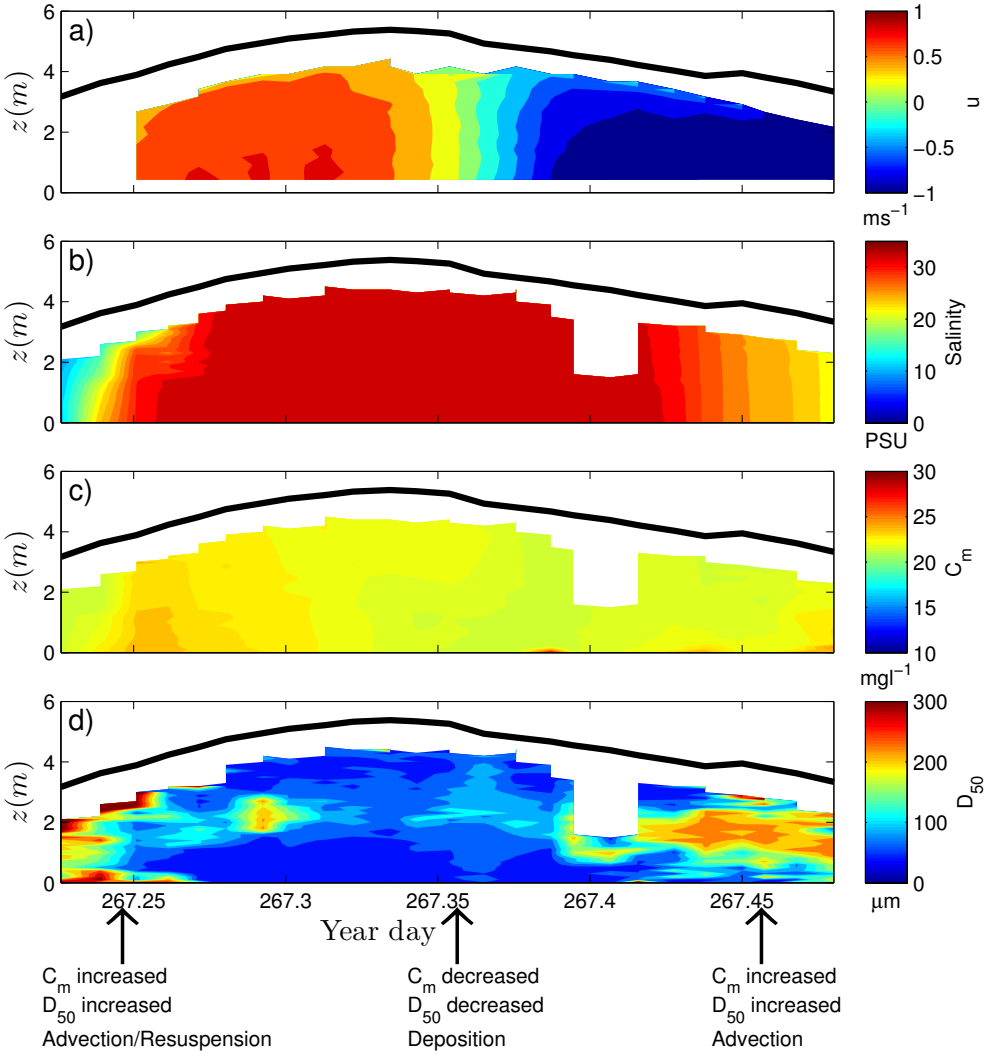

Figure 6.13: Vertical profiling data at the mouth of the estuary post-river event in September 2010. a) Current velocity u. b) Salinity. c) Mass concentration C_m. d) Median particle size (D_{50})

An Anchor station survey was conducted at the mouth of the estuary performing vertical profiles with the LISST-100 and CTD throughout a tidal cycle post-river event. This survey allowed the interrogation of SPM and hydrodynamic properties at the mouth to compare to the RETZ, in order see if the effects of a river event can be observed even at the mouth. Figure 6.13 shows a rise in C_m and D_{50} occurred during the flood. This could be either advection of larger particles or resuspension. At high water the C_m and D_{50} decreased most likely due to deposition. Following high water slack as the current direction reversed the elevated signal of larger particles observed at Mooring A post-river event was observed at the mouth during the ebb and into low water. After discussing the variations in estuarine SPM characteristics under river event conditions it is now necessary to consider how the transfer flux of suspended sediments were affected at this location under such conditions. Figure 6.14 presents a time series of the coarse and fine suspended sediment flux in the context of h, u_h and D_{50}. h and u_h which indicates the dampening of the tidal signal at this mooring during the major flood event, furthermore neap tides approach the period of the major river event thereby accentuating the strength of the river in modifying the tidal signal. The most prominent signal in D_{50} during the sampling period is the sustained increase above $200\mu m$ for days after the major river event which coincided with a drop in effective density, however it is important to note tidal modulations in D_{50} were still present in between flood events and as a background signal, similar to the signals observed in March and April. There was an obvious export signal of both fine and coarse particle during the flood events, the coarse flux was notably larger than the fine as observed in March and April (Figure 6.15d). Outside of the river event periods of transfer of both coarse and fine particles was to be close to zero.

Moreover, it is imperative to mention the maximum flux of suspended sediment was an order of magnitude higher in September than in March and April. Figure 6.15 displays the net tidal flux of coarse and fine particles over the sampling period. Coarse particles were exported during tidal cycle three when fine particles remained close to equilibrium at the time of the minor event. In between the river flood events the system returned to equilibrium, however during the major river event a considerable net export of both

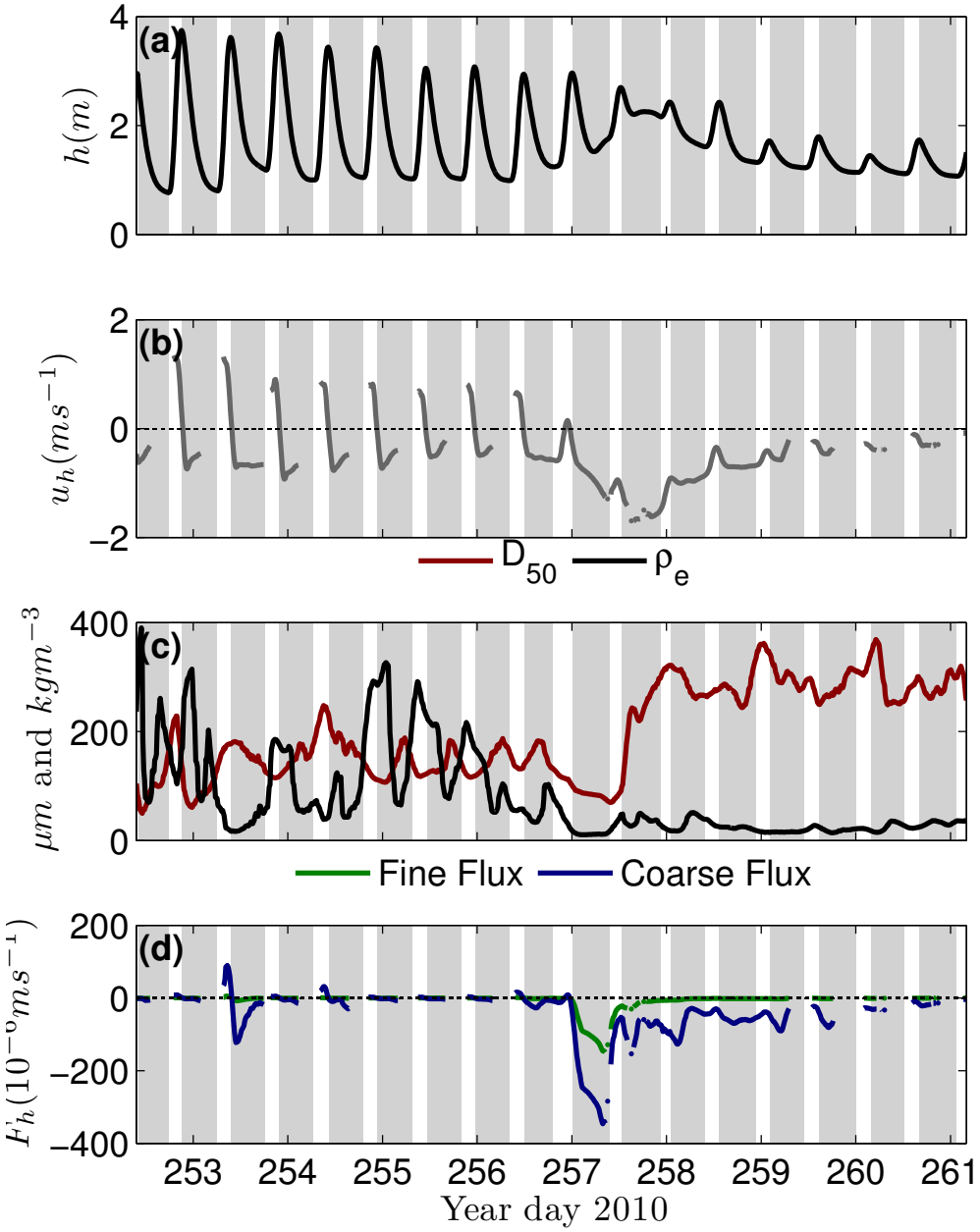

Figure 6.14: Suspended sediment flux of fine and coarse particles at Mooring A in September 2010. a) h. b) u_h. c) D_{50} in red and ρ_e in black. d) Blue line denotes coarse particle flux and the green line represents the fine particle flux.

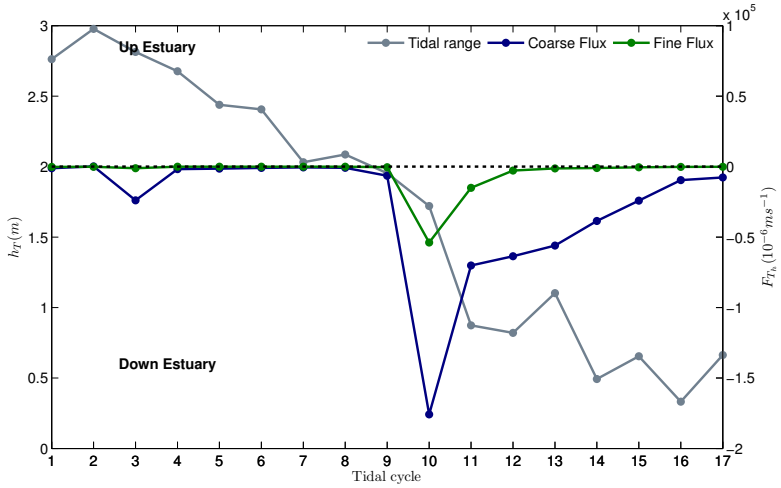

Figure 6.15: Tidally averaged suspended sediment flux of fine and coarse particles at Mooring A in September 2010.

Table 6.2: Net suspended sediment flux ($10^{-6}ms^{-1}$) of fine and coarse particle sizes for the sampling period in September 2010.

Fine	Coarse
-77023	-482610

fine and coarse particles was observed. As seen in all flux calculations the coarse flux was greater than the fine. The net coarse particle flux reached maxima at tidal cycle 10, declined dramatically during the two following tidal cycles and proceeded to display a steady decline and returned close to equilibrium after seven tidal cycles.

Finally, Table 6.2 presents the net flux of coarse and fine particles throughout the whole sampling period. This data indicates the export of both fine and coarse particles throughout this period was an order of magnitude higher than the maximum export of coarse particles observed at the Mooring B during March under normal river conditions.

6.4 Discussion

This Chapter aimed to identify the affects of differing seasonal conditions on estuarine hydrodynamic and SPM characteristics, including the transfer flux of suspended sediments in and out of the estuary during of periods of extreme river flood events.

Tidally averaged hydrodynamic data indicates U_T was significantly correlated with h_T throughout March and April, inferring as one would expect, spring tides were associated with the fastest tidal currents (Figures 6.1 and 6.2). Atypically, turbulence parameter G_T did not present the same correlation throughout March and April, suggesting tidal currents were not always the dominant factor governing the production of turbulence in the estuary. As discussed in Chapter 4 wind has been identified as an influential force affecting TKE dissipation rates, causing the breakdown of the linear relationship between tidal currents and TKE dissipation. The only significant correlation of G_T with h_T occurred during March at Mooring A; whereas at Mooring B no significant relationships were found between either G_T or μ_{k_T} and h_T (Figure 6.1). This could be due to the more sheltered position of Mooring A compared to Mooring B, dampening the affects of wind stress on TKE dissipation. During April the tidally averaged turbulence parameters conveyed insignificant correlations with tidal range at both mooring locations (Figure 6.2), however at this time the magnitude and direction of the prevailing winds were such that the influence of the wind was greater than in March.

Moving onto size and volume concentration, Figures 6.4 and 6.3 show that at Mooring A for both March and April, D_{50} increased linearly with h_T, presenting a significant relationship. This evidence indicates at this location, bigger particles were associated with higher current speeds and increased advection of marine material, regardless of seasonal conditions. Moreover, in March at Mooring A this also indicated that larger particles were associated with larger values of G_T as measurements were made using an ADV close to the bed . The differing results reflect how different the Mooring B environment was; including bathymetry, advection of salt water and mixing, current speeds and tur-

bulence. The bathymetry of Mooring A was strongly channelised whereas the Mooring B location was not; giving rise to significant differences in the import and export of suspended sediments and thus the size and C_v presented. Furthermore, as this location presented an overall more dynamic environment, this could have led to the superimposition of various suspended sediment transport mechanisms such as advection, resuspension and flocculation/de-flocculation. Superimposition of multiple mechanisms of control can create difficult combinations of signals in particle size behaviour to interpret.

Considering the data collected during the river event, D_{50} increased significantly during both major and minor flood events, after the major event, however D_{50} remained elevated for multiple days without displaying tidal modulation. Furthermore, during the major river event the tidal variation in u_h and h were dampened by the river and values of ϵ_h were at the maximum for the sampling period (Figure 6.10). Strong winds travelling to the North East prevailed throughout the sampling period (Figure 4.3), especially throughout the river flood events and they are commonly associated with enhanced precipitation. Figure 6.11 suggests North easterly winds opposed the direction of current flow during the ebb giving rise to the maximum in ϵ_h, moreover the strength of the wind in the form of τ_w was identified. This evidence suggests breaking waves and or shear stress from wind acting upon the surface of the water column affected the production of turbulent energy in addition to tidal currents at this time. In turn the rise in ϵ_h observed during the ebb may affect the behaviour of sediments in suspension through a combination of resuspension and de-flocculation.

Profiling data from the anchor station at the mouth of the estuary after the major river event indicated advection or resuspension of larger particles during the flood, a reduction of concentration and size at high water and a signal of larger particles advecting to the mouth during the ebb and low water. The particle characteristics at the mouth align with the characteristics observed at Mooring A (larger less dense particles), inferring the affects of the river event were observed longitudinally throughout the estuary.

Moving on to the suspended sediment transfer flux calculations, it is clear the transport of

coarse particles was greater than the fine particle flux throughout all seasonal conditions presented, including the river flood event. This is due to the bimodal split determined in Figure 6.5 and also the limited C_v of particles in the smaller size classes as one might expect in a estuary dominated by cohesive sediments. Between the two seasonal conditions represented by March and April, the largest flux was recorded at Mooring B in March, however it was in the same order of magnitude as fluxes reported in April. The flux calculated in March at Mooring A was the smallest recorded, this is most likely due to using ADV measurements rather than ADCP measurements in the flux calculation.

The net tidal flux calculations provided valuable information on the net movement of the two particle size classes over a tidal cycle. In March at Mooring A, the flux was considerably smaller than other net fluxes, which has been previously discussed. Figure 6.8a indicates the system was close to equilibrium and did not present a lunar variation in the net tidal flux as seen in April. At Mooring A in March, the PSD varied from the observed semi-diurnal pattern of particle size increasing around high and low water, a lone flocculation signal at high water was observed however, during neap tides the C_v was reported as significantly lower, thus not presenting notable flocculation signals (Figure 5.8). This may have resulted in less deposition of suspended sediments and thus reduce the net transfer flux of suspended sediments into the estuary.

At Mooring B a net export of fine and coarse particles was observed during March (Figures 6.8). The highest flux of sediments was of coarse particles in March at Mooring B, therefore coarse particles were not depositing at this location. These particles could have been deposited further downstream or even transported to the coastal ocean at the mouth of the estuary depending on the extent of the advection. Understanding the extent of coarse particles exportation is crucial as coarser particles can present a high organic composition relevant to the transport of carbon and contaminants throughout the estuarine environment (Ittekkot, 1988; Arndt et al, 2009). Although it is not clear from this data how far the particles were advected, evidence suggests the particles were not depositing at Mooring B in March.

Finally, the flood event flux data set displays a minor and a major river event, demonstrating the effects on PSD and suspended sediment fluxes at Moorings A (Figures 6.10 and 6.14). After a minor event C_v of particles greater than $200\mu m$ increased notably inferring the river event introduced larger particles of a terrestrial origin, after this initial river event particle size decreased at a time of enhanced ϵ_h (Figure 6.12) which may have presented the energy required to de-flocculate larger particles, on the other hand these particles may have been transported further downstream under such conditions. After the major river event increased C_v values across the whole size spectra were presented which could have been a mixture of resuspension and introduction of terrestrially derived sediments liberated from surrounding marsh and agricultural land. After the initial surge of particles across the particle size spectra a population of particles greater than $200\mu m$ persisted for days after the river event despite the high observed values of ϵ_h. This could be explained by particles of a higher yield strength entering the estuary during an extreme river event (Droppo, 2001).

Moving onto the export of suspended sediments at this time, the minor river event resulted in a net export of both fine and coarse particles during the tidal cycle in question (Figure 6.15) which was followed by a return to equilibrium. Conversely, the major river event resulted in a net tidal export of coarse and fine particles for days after the event. It may not be surprising to observe a net export of sediments during a river event, however it is important to understand the effects of river flood events on the net transfer of estuarine sediments as climate models predict the frequency of extreme flood events to rise in the near future (IPCC, 2013). From the current data set it could be suggested that river flood events increase the export of suspended sediments at the TIR seawards, thus increasing the transfer of the biogeochemical components associated with the exported particles. Depending on the severity of the river flood event the export the enhanced levels of sediment transport can be sustained for multiple days after the event. This could potentially seriously implicate the transport of pathogens and contaminants in estuaries as they have the potential to become highly concentrated in the ETM.

6.5 Summary Points

- U_T and h_T were significantly positively correlated throughout all seasonal conditions however, G_T was not always significantly correlated with h_T. This evidence again suggests tidal currents are not the sole factor determining the production of turbulent kinetic energy in this estuarine environment.

- At Mooring A under both seasonal conditions D_{50} increased linearly with h_T, indicating D_{50} was elevated due to enhanced marine influence and faster tidal currents.

- Mooring B represents a more complex environment with regards to hydrodynamics and SPM characteristics, therefore the signals apparent at the Moorings A were not observed; its location was more vulnerable to wind influence enhancing TKE dissipation during the ebb independent of the tidal current. The complication in the SPM characteristics may be due to the superimposition of mechanisms such as resuspension, advection and flocculation/de-flocculation.

- During river flood events suspended particles presented a sustained rise in size independent tidal modulations; evidence suggests larger particles of a higher yield strength were introduced to the estuary during the river flood events.

- Characteristics of larger particles liberated from the flood plains during the river event were observed at the mouth of the estuary after the flood event.

- In March the RETZ (Both Mooring A and B) acted as a net exporter of mainly coarse particles under normal river conditions.

- River flood events resulted in the export of fine and coarse particles an order of magnitude higher than observed under normal river flow conditions, thus affecting the transport of biogeochemical components associated with suspended sediments. Evidence suggests the magnitude of a river event dictates the period and magnitude of SPM export after the river event occurs.

Chapter 7

Synthesis and Conclusions

The aim of this study was to develop our understanding of interactions between floc properties and physical processes occurring throughout the RETZ, including variations in transfer flux of SPM, on tidal and lunar scales, along with low frequency seasonal modulations in climatic conditions such as river flood events.

In order to achieve this aim *in situ* high resolution observational data sets were collected from the Dyfi estuary. Five extensive field work campaigns were undertaken to ascertain how hydrodynamic forcings in the RETZ affect the size and concentration of SPM over seasonal, lunar and tidal temporal scales. Furthermore the four main tributaries of the river Dyfi and the mouth of the estuary were sampled.

Chapter 4 identified the main trends in hydrodynamic and SPM characteristics of the estuary; analysis in Chapter 5 then focused on the relationship between floc size and the hydrodynamic regime of the RETZ on a tidal scale, concentrating specifically on the role of turbulence. Chapter 6 broadened the temporal scale to identify seasonal modulations in SPM characteristics and therefore the role of the RETZ in transporting SPM. The impacts of extreme river events were also addressed including floc properties and SPM fluxes during elevated river flow.

Tidal scale variations

One of the first hydrodynamic characteristics of the estuary identified was the asymmetric nature of the tidal wave, giving rise to a shorter flood phase with faster current speeds and a longer ebb with relatively slower current speeds. The estuary was well-mixed with respect to salinity and temperature, though the spatial surveys in the RETZ showed some stratification during the flood phase of the tide.

Chapter 4 examined the relationship between current speed and TKE dissipation on tidal scales. Measurements close to the bed (u_{bed} and ϵ_{bed}) showed a stronger correlation than observations averaged over the whole depth of the water column (u_h and ϵ_h). The first hypothesis in Chapter 2 states:

Hypothesis 1: *TKE dissipation near to the bed is determined by the local velocity field which in a macrotidal estuary is governed by tidal forcing.*

Evidence suggests this is true close to the bed where TKE dissipation is dominated by tidal currents interacting with the bed, identified by measurements of u_{bed} and ϵ_{bed} from ADV instruments $0.3m$ above the bed. However, under certain circumstances outlined in Chapter 5 wind stress becomes important. Peaks in ϵ_h correlated with the magnitude of wind stress, and in certain instances, the direction of the wind. For example if the wind direction opposes the direction of the tide, waves can be created which enhance TKE dissipation at the surface of the water column. It is proposed that wind direction and magnitude can play an influential role in governing TKE dissipation at the surface of the water column in the RETZ in addition to tidal currents.

Diurnal and semi-diurnal modulations of SPM properties were observed throughout the RETZ in March, April and September. In March and April peaks in D_{50} largely correlated with periods of low turbulent conditions during high and low water, whereas the maximum D_{50} values in November occurred during the ebb. Furthermore, spatial surveys throughout the RETZ provided evidence to suggest flocculation was prevalent

during the flood and at high water (Figures 4.31,4.32,4.35 and 4.36).

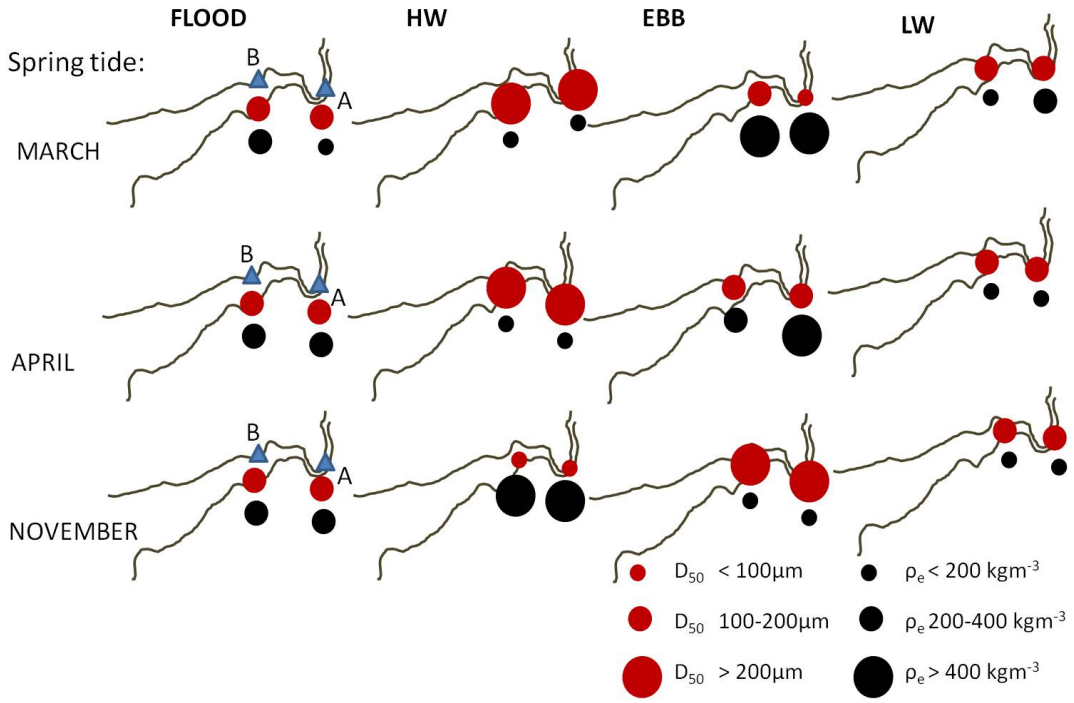

Figure 7.1: Schematic of floc size and effective density evolution in the RETZ during a spring tide for March, April and November.

Figure 7.1 presents a schematic of the evolution of floc properties (D_{50} and ρ_e) observed on a tidal scale. In March, during a spring tide, less dense particles ranging in size from $100 - 200\mu m$ occurred in the RETZ (at both Moorings A and B) during the flood (Figure 7.1). At high water floc size increased and effective density decreased, inferring flocculation. Following high water floc size decreased and effective density increased; this could be due to resuspension of smaller flocs, de-flocculation of macro-flocs or preferential settling of larger flocs. At low water flocs in the size range of $100-200\mu m$ with a relatively low effective density occurred due to either advection of terrigenous SPM or flocculation of material previously trapped in the RETZ. However, during high water, ebb and low water observations of C_m remained constant, which rules out resuspension or advection, therefore flocculation and de-flocculation must have been occurring.

Lunar scale variations

Variation in SPM properties and general hydrodynamic parameters were observed. The tidal scale described in the previous section outlined the spring tide case. Figure 7.2 addresses the evolution of particle properties during a neap tide. Larger flocs with the lowest effective densities occurred during the flood on neap tides. During neap tides, tidal range and thus marine influence decreases along with current speeds; if strong tidal currents associated with elevated values of TKE dissipation limit flocculation, lower current speeds could allow flocculation to occur before high water. Another possible explanation could be the resuspension of flocs deposited at the bed during a previous tide; this is unlikely though as current speeds were markedly lower during neap tides. Following high water, floc size decreased during the ebb and at low water and effective density increased which is more similar to the spring tide case.

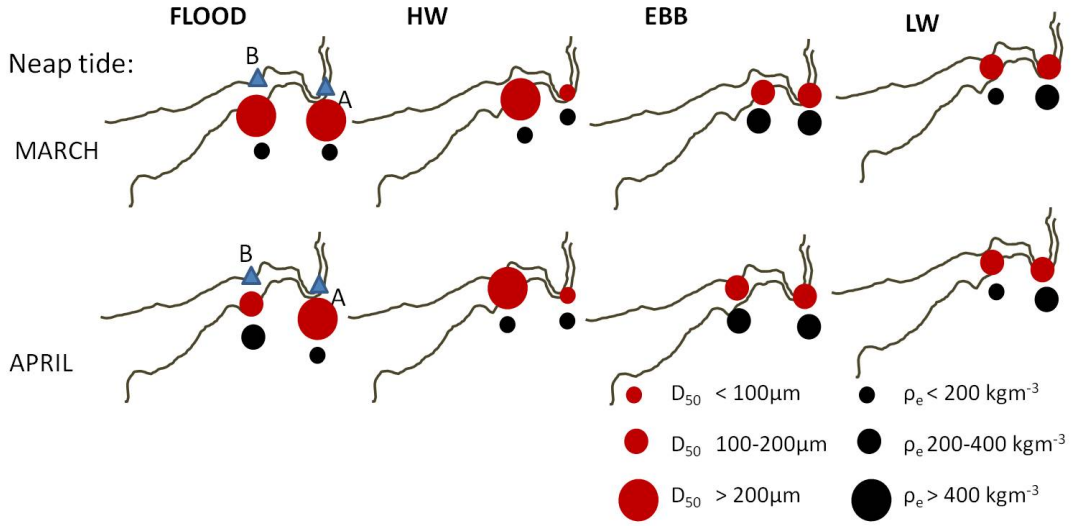

Figure 7.2: Schematic of floc size and effective density evolution in the RETZ during a neap tide for March and April.

Seasonal scale variation

During April the evolution of floc size and effective density was essentially the same as in March during spring tides, with the exception of larger flocs reported at Mooring A and less dense flocs at Mooring B during the ebb (Figure 7.1). Particle size distributions shown in Chapter 5 indicated flocculation at high water and low water during spring tides in March and April. Furthermore, two populations of larger floc sizes were identified, representing terrigenous and marine origins. Particle sizes above $200\mu m$ were observed at high water and between $100 - 200\mu m$ at low water. At high water the influence of the river as a fluvial source of SPM is at a minimum, whereas the marine influence is highest. The reverse is true at low water as the river dominates the RETZ.

In November a different trend in floc size and effective density was observed. Figure 7.1 shows floc size increased in the RETZ with an associated fall in effective density during the ebb, rather than at low or high water. Spatial surveys conducted in the RETZ showed larger flocs in the RETZ during the flood and at high water, this was not observed by Moorings A and B as the signals were higher in the water column. During the ebb flocs have had chance to settle throughout the water column, therefore the signals were observed at the Moorings during the ebb only. These signals still differ from observations made in March and April, this could be due to settling velocities. In November the settling velocities could have been slower than in March and April, therefore the flocs formed at high water did not settle to the bed, so were not observed by the LISST-100 at that time. Following high water the flocs began to settle out; at the same time they were advected seawards during the ebb, thus explaining the signal of large flocs with low densities observed successively at Mooring A followed by Mooring B during the ebb. In March and April, de-flocculation was observed during the ebb, giving rise to smaller, more dense particles; this is not the case in November due to slower current speeds and thus less turbulent conditions.

Overall, larger flocs were observed at Mooring B compared to Mooring A according to data presented in Chapter 5. This could be due to the availability of material being

more abundant in the upper estuary than the TIR, furthermore the marine influence was shown to correlate with larger particles by empirical model analysis (Chapter 5, Subsection 5.3.4). Moreover, hydrodynamic data from Mooring B indicates a more dynamic environment than Mooring A, with higher overall current speeds and TKE dissipation values. Chapter 6 examined tidally averaged values of SPM and hydrodynamic characteristics, which highlighted the more complex signals in SPM data from Mooring B due to the superimposition of advection, resupension and flocculation processes. Finally, Mooring B was situated in a location more vulnerable to the affects of wind stress than Mooring A, further complicating the relationship between SPM and the hydrodynamics.

Implications of extreme river events on floc properties and hydrodynamics

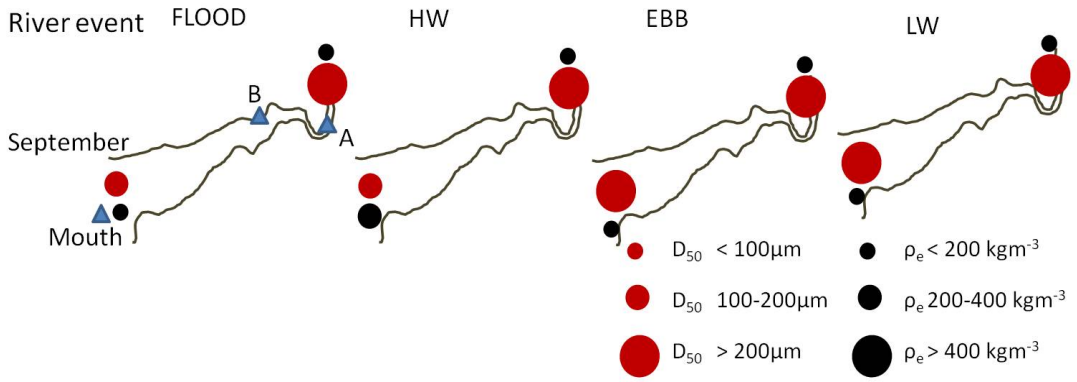

Figure 7.3: Schematic comparison of floc size and effective density at the mouth of the estuary with the TIR on a tidal scale during a river event.

Figure 7.3 compares floc size and effective density in the TIR with the mouth of the estuary after a major river event. Floc size and effective densities remained large and low, respectively, throughout the tidal cycle after the river event. This infers that larger particles were introduced to the RETZ through the process of the river event inundating the adjacent flood plains composed of mudflats and liberating larger particles. The fate of these larger particles can be considered through SPM flux calculations. These calculations address the second hypothesis stated in Chapter 2.

Hypothesis 2: *Under normal conditions the RETZ acts as a sediment trap due to the ETM, under conditions of elevated river flow the RETZ acts as a net exporter for SPM.*

After a period of enhanced river flow rates the estuary was shown to act as a net exporter of SPM at the TIR. In March the RETZ acted as an overall net exporter of SPM, although the magnitude of export was an order of magnitude higher during the river event. This could have serious implications for the overall long term balance of sedimentation in the estuary. Through the export of elevated concentrations of SPM,the transfer of the biogeochemical components including pathogens and contaminants associated with the exported particles could be enhanced, thus implicating carbon pathways and potential contaminant dispersal between the river catchments, RETZ and the coastal ocean. Moreover, predictions of increased storm events in the near future suggested by IPCC (2013) indicate river events will become more common, thus enhancing SPM export further and accentuating the impacts to biogeochemical pathways in the estuarine environment.

SPM data from the estuary mouth shows that during the flood and at high water floc size remained relatively small, therefore the flocs of marine origin were smaller than the flocs observed at the TIR. At the onset of the ebb and during low water Figure 7.3 indicates that floc size increased, due to the advection of larger particles observed at the TIR. Hypothesis 3 explores the potential of river events in determining particle size longitudinally throughout the estuary, including the mouth, thus governing the size of particles exported to the coastal ocean.

Hypothesis 3: *The size of terrestrially derived SPM entering from the river dictates the size of flocs throughout the estuary during river events.*

Figure 7.3 suggests flocs with similar properties (size and effective density) as flocs observed in the TIR during the high river flows were advected through the RETZ to the mouth of the estuary. Profiling data shown in Chapter 6 showed these flocs advecting past the anchor station at the mouth during the ebb. Furthermore, Figure 4.38 from Chapter 4 indicates the size of terrestrial SPM influences floc size observed in the RETZ

at low water during major river flood events. Therefore, this hypothesis can be accepted.

Turbulence control of floc size

Finally, the role of turbulence control on floc size in the RETZ must be considered, the last hypothesis stated:

Hypothesis 4: *Floc size in the RETZ is governed by local turbulent conditions, the Kolomogorov microscale represents the upper limit for floc growth, modulated on a tidal temporal scale.*

Data presented in Chapter 5 shows overall there was a strong correlation between the turbulence parameters and floc size, however the Kolomogorov length scale did not act as the sole limiting factor on floc growth. During periods of marine influence (during the flood, high water and early onset of the ebb), most notably at Mooring B, an enhanced relationship was identified between floc size and the Kolmogorov microscale. Moreover, during periods at which the influence of the river was high (during the mid and late ebb and low water at Mooring B or the entire tidal cycle at Mooring A in the TIR), the relationship breaks down. This could be due to the following reasons; flocs of a terrigenous origin could have a higher floc strength than marine derived flocs. This would lead to a situation in which a relationship between turbulence is observed when marine influence dominates and no relationship as the fluvial regime becomes most dominant. This scenario was not observed, however the particles observed as the fluvial regime dominated presented a different correlation to the turbulence regime in the RETZ than the particles introduced during marine dominance.

In March at Mooring B the correlation was reversed during fluvial dominance compared to the marine case; particles continued to grow as turbulence increased. This relationship corresponded to higher floc strength coefficients observed in the fluvial case compared to the particles of marine origin. In April, a different relationship was observed again; particles of marine and terrestrial origins both scaled in size with turbulence, however the

terrestrial particles were consistently lower. Weaker floc strength coefficients of terrestrially derived particles were observed, explaining the different correlations. In summary, it is the particle properties (i.e. floc strength) that govern the relationship between SPM and local turbulence; SPM sources give rise to variations in particle properties thus altering the way in which particles scale with local turbulence conditions.

Further work

The extensive data sets explored in this study have drawn interesting and varied conclusions regarding SPM estuarine dynamics including; modulations in SPM properties on varying temporal and spatial scales, the transport of SPM under enhanced river flow conditions, the relationship between TKE dissipation and tidal currents, and the interactions between the Kolmogorov microscale and floc size throughout the RETZ. However, turbulence control of SPM properties remains a highly complex mechanism, further work is required in this area to test conclusions drawn and continue to interrogate the questions which arose from the data, namely through extended observations. Primarily, field campaigns seasonally spaced more evenly would provide more meaningful seasonal conclusions, profiling above mooring locations throughout a tidal cycle, endeavouring to minimise gaps in data around low water, would eliminate the possibility of missing signals in SPM higher in the water column. Moving the mooring representing the TIR conditions further upstream and extending spatial surveys above the TIR into the river, could provide a better understanding of the terrestrially derived SPM properties before their interaction with the marine environment.

In order to improve the accuracy of SPM flux calculations at the mooring positions, profiling above the moorings and laterally across the estuary could provide data to calculate the flux for the cross sections of the channel, rather than a point flux. Point measurement fluxes, such as the calculations shown in Chapter 6 could misrepresent net SPM fluxes if the vertical distribution was not uniform, therefore a cross-sectional flux of SPM would be more satisfactory. This could be undertaken at spring and neap tides over a

seasonal time scale. With enhanced SPM flux estimates, identifying the biogeochemical components of flocs could provide a means of quantifying the impacts of river events on the export pathways of biogeochemical components. Further sampling of tributaries is necessary, spot measurements are not necessarily a true representation of SPM properties at these sites.

The suggestions for further work outlined above, remain centred on the Dyfi estuary, however it would be interesting to apply the sampling regime utilised in this study on an estuarine environment with a larger tidal range to test whether a more energetic regime results in stronger evidence of turbulence control on floc size. Furthermore, the sampling regime should be transferred to a microtidal location in order to investigate the potential of a critical stress at which flocculation begins. Finally, there is significant potential to use the data sets collected to validate existing flocculation models (Winterwerp, 1998; Pejrup and Mikkelsen, 2010; Braithwaite et al, 2012) and improve predictions through the modification of flocculation/de-flocculation parameters.

References

Agrawal Y, Pottsmith H (2000) Instruments for particle size and settling velocity observations in sediment transport. Marine Geology 168(1-4):89–114

Agrawal YC, Pottsmith HC (1994) Laser diffraction particle sizing in STRESS. Continental Shelf Research 14(10):1101–1121

Agrawal YC, Whitmire A, Mikkelsen Oa, Pottsmith HC (2008) Light scattering by random shaped particles and consequences on measuring suspended sediments by laser diffraction. Journal of Geophysical Research 113(C4):C04,023, DOI 10.1029/2007JC004403

Alldrege AL, Gotschalk C, Passow U, Riebesell U (1995) Mass aggregation of diatom blooms : Insights from a mesocosm study. Deep Sea Research II 42(1):9–27

Allen G, Salomon J, Bassoullet P, Du Penhoat Y, Grandpre C (1980) Effects of tides on mixing and suspended sediment transport in macrotidal estuaries. Sedimentary Geology 26:69–90

Arfi R, Guiral D, Bouvy M (1993) Wind Induced Resuspension in a Shallow Tropical Lagoon. Estuarine, Coastal and Shelf Science 36:587–604

Arndt S, Regnier P, Vanderborght JP (2009) Seasonally-resolved nutrient export fluxes and filtering capacities in a macrotidal estuary. Journal of Marine Systems 78(1):42–58, DOI 10.1016/j.jmarsys.2009.02.008

Baker ET, Lavelle JW (1984) The effect of particle size on the light attenuation coefficient of natural suspensions. Journal of Geophysical Research 89:8197–8203

Bale AJ, Morris AW (1987) In Situ Measurement of Particle Size in Estuarine Waters. Estuarine, Coastal and Shelf Science 24:253–263

Bartz R, Zaneveld JV, McCave I, Hess F, Nowell A (1985) ROST and BEAST : Devices for in-situ measurement of particle settling velocity. Marine Geology 66:381–395

Bohlen W (1987) Time variability of suspended material concentration in estuaries. In: Proceedings of the 1987 National conference on hydraulic engineering., American Society of Chemical engineering., New York, pp 219–224

Bolanos R, Moate B, Souze A (2009) Measuring suspended sediment and its wave and turbulence forcing in the Dee estuary. Coastal Dynamics

Bowers DG, Al-Barakati A (1997) Tidal Rectification on Drying Estuarine Sandbanks. Estuaries 20(3):559–568

Braithwaite KM, Bowers DG, Nimmo Smith WaM, Graham GW (2012) Controls on floc growth in an energetic tidal channel. Journal of Geophysical Research 117(C2):C02,024, DOI 10.1029/2011JC007094

Brown JM (2007) Coastal area modelling: Sand transport and morphological change. PhD thesis, Bangor University

Brown JM, Davies AG (2009) Methods for medium-term prediction of the net sediment transport by waves and currents in complex coastal regions. Continental Shelf Research 29(11-12):1502–1514

Bunt J, Larcombe P, Jago CF (1999) Quantifying the response of optical backscatter devices and transmissometers to variations in suspended particulate matter. Continental Shelf Research 19(9):1199–1220

Burban Py, Xu Yj, Mcneil JOE, Lick W (1990) Settling Speeds of Flocs in Fresh Water and Seawater. Journal of Geophysical Research 95(10):18,213–18,220

Burton D, Althaus M, Millward G, Morris A, Statham P, Tappin A, Turner A (1993) Processes influencing the fate of trace metals in the North Sea. Philosophical Transactions of the Royal Society 342:557–568

Cameron W, Pritchard D (1963) Estuaries. In: Hill M (ed) The Sea, volume 2 edn, Wiley, New York, pp 306–324

Camp T, Stein P (1943) Velocity gradients and internal work in fluid motion. Journal of the Boston Society of civil Engineers 30:219–237

Chen S, Eisma D (1995) Fractal geometry of in situ flocs in the estuarine and coastal environments. Netherlands Journal of Sea Research 32(2):173–182

Colling A, Park D, Phillips J, Rothery D, Wright J, Brown J (1989) Waves, tides and shallow-water processes. Butterworth-Heinemann

Crombie S (2000) Laboratory characterisation of settling velocities for Brisbane river mud flocs. Phd, University of Queensland

Davies EJ (2013) Scattering properties of suspended particles. PhD thesis, University of Plymouth

Davies J (1964) A morphogenetic approach to worl shorelines. Zeitschrift fur Geomorphologie 8:127–142

Dewey K, Crawford, W R, Dewey RK, Crawford WR (1988) Bottom stress estimates from vertical dissipation rate profiles on the continental shelf. American Meterological Society 18:1167–1177

Droppo IG (2001) Rethinking what constitutes suspended sediment. Hydrological Processes 15(9):1551–1564, DOI 10.1002/hyp.228

Dyer K (1974) The salt balance in stratified estuaries. Estuarine and Coastal Marine Science 2(3):273–281, DOI 10.1016/0302-3524(74)90017-6

Dyer K (1989) Sediment processes in estuaries: future research requirements. Journal of Geophysical Research 94(C10):14,327–14,339

Dyer K (1997) Estuaries a Physical Introduction, second edi edn. John Wiley and Sons

Dyer K, Manning A (1999) Observation of the size, settling velocity and effective density of flocs, and their fractal dimensions. Journal of Sea Research 41(1-2):87–95, DOI 10.1016/S1385-1101(98)00036-7

Eisma D (1986) Flocculation and de-flocculation of suspended matter in estuaries. Netherlands Journal of Sea Research 20:183–199

Eisma D, Kalf J (1996) In situ particle (floc) size measurements with the NIOZ in situ camera system. Journal of Sea Research 36:49–53

Ellis K, Bowers D, Jones S (2004) A study of the temporal variability in particle size in a high-energy regime. Estuarine, Coastal and Shelf Science 61(2):311–315, DOI 10.1016/j.ecss.2004.06.001

Feddersen F, Williams aJ (2007) Direct Estimation of the Reynolds Stress Vertical Structure in the Nearshore. Journal of Atmospheric and Oceanic Technology 24(1):102–116, DOI 10.1175/JTECH1953.1

Fugate DC, Friedrichs CT (2002) Determining concentration and fall velocity of estuarine particle populations using ADV, OBS and LISST. Continental Shelf Research 22(11-13):1867–1886

Fugate DC, Friedrichs CT (2003) Controls on suspended aggregate size in partially mixed estuaries. Estuarine, Coastal and Shelf Science 58(2):389–404, DOI 10.1016/S0272-7714(03)00107-0

Gabrielson J, Lukatelich R (1985) Wind-related Resuspension of Sediments in the Peel-Harvey Estuarine System. Estuarine, Coastal and Shelf Science 20:135–145

Gargett AE (1999) Velcro Measurement of Turbulence Kinetic Energy Dissipation Rate. Journal of Atmospheric and Oceanic Technology pp 1973–1993

Haynes J, Dobson M (1969) Physiography, Foraminifera and Sedimentation in the Dyfi Estuary (Wales). Journal of Geology 6:217–255

Hill PS, Syvitski JP, Cowan EA, Powell RD (1998) In situ observations of floc settling velocities in Glacier Bay , Alaska. Marine Geology 145:85–94

Holm-Hansen O, Riemann B (1978) Chlorophyll a determination: Improvemnets in methodology. Oikos 30:438–447

IPCC (2013) Climate Change 2013: The Physical Science Basis. Group I to the Fifth Assessment Report of the Intergovernmental Panel on Climate Change

Ittekkot V (1988) Global trends in the nature of organic matter in river suspensions. Nature 332:436–438

Ives K (1978) Rate theories. In: The Scientific Basis of Flocculation, Sijthoff and Noordhoff Interna- tional, Alphen aan den Rijn, Netherlands, pp 37–61

Jackson Ga, Maffione R, Costello, D K, Alldrege, A L, Logan, B E, Dam, Hans G (1997) Particle size spectra between 1um and 1cm at Monterey Bay determined using mulitple instruments. Deep-Sea Research I 44(11):1739–1767

Jago C, Bull C (2000) Quantification of errors in transmissometer-derived concentration of suspended particulate matter in the coastal zone: implications for flux determinations. Marine Geology 169(3-4):273–286

Jago C, Jones S (1998) Observation and modelling of the dynamics of benthic fluff resuspended from a sandy bed in the southern North Sea. Continental Shelf Research 18:1255–1282

Jago C, Jones S (2002) Diagnostic criteria for reconstruction of tidal continental shelf regimes: changing the paradigm. Marine Geology 191(3-4):95–117, DOI 10.1016/S0025-3227(02)00527-3

Jago C, Jones S, Sykes P, Rippeth T (2006) Temporal variation of suspended particulate matter and turbulence in a high energy, tide-stirred, coastal sea: Relative contributions of resuspension and disaggregation. Continental Shelf Research 26(17-18):2019–2028, DOI 10.1016/j.csr.2006.07.009

Jago C, Kennaway G, Novarino G, Jones S (2007) Size and settling velocity of suspended flocs during a Phaeocystis bloom in the tidally stirred Irish Sea, NW European shelf. Marine Ecology Progress Series 345:51–62

Jago CF, Bale A, Green MO, Howarth M, Jones S, Mccave IN, Millward G, Morris AW, Rowden A, Williams J, Hydes D, Turner A, Huntley D, Van Leussen W (1993) Resuspension Processes and Seston Dynamics, Southern North Sea. Philosophical Transactions of The Royal Society A 343(1669):475–491

Jarvis J (1970) A Physical Investigation of tidal phenomena in the Dovey estuary with particular reference to channel development and sediment movement. PhD thesis, Aberystwyth University

Jones D, Wills MS (1956) The attenuation of light in sea and estuarine waters in relation to the concentration of suspended solid matter. Journal of the Marine Biological Association of the United Kingdom (35):431–444

Jones NL, Monismith SG (2008) The Influence of Whitecapping Waves on the Vertical Structure of Turbulence in a Shallow Estuarine Embayment. Journal of Physical Oceanography 38(7):1563–1580, DOI 10.1175/2007JPO3766.1

Jones S, Jago C, Prandle D, Flatt D (1994) Suspended Sediment Dynamics: Measurement and modelling in the Dover Strait. In: Mixing and Transport in the Environment, chap 10, pp 183–201

Jones S, Jago C, Bale A, Chapman D, Howland R, Jackson J (1998) Aggregation and resuspension of suspended particulate matter at a seasonally stratified site in the southern North Sea: physical and biological controls. Continental Shelf Research 18:1283–1309

Karp-boss L, Azevedo L, Boss E (2007) LISST-100 measurements of phytoplankton size distribution : evaluation of the effects of cell shape. Limnology and Oceanography: Methods 5:396–406

Kolmogorov AN (1941) The local structure of turbulence in incompressible viscous fluid for very large Reynolds numbers. Dokl Akad Nauk SSSR 30(4):299–303

Kranck K (1973) Flocculation of suspended sediment in the sea. Nature 246:348–350

Kranenburg C (1994) The Fractal Structure of Cohesive Sediment Aggregates. Estuarine, Coastal and Shelf Science 39(5):451–460, DOI 10.1006/ecss.1994.1075

Kraus N, Lohrmann A, Ramon C (1994) New Acoustic Meter for Measuring 3D Laboratory Flows. Journal of Hydraulic Engineering 120(3):406–412

Krivtsov V, Goldspink C, Sigee D, Bellinger E (2001) Expansion of the model 'Rostherne' for fish and zooplankton: role of top-down effects in modifying the prevailing pattern of ecosystem functioning. Ecological Modelling 138(1-3):153–171, DOI 10.1016/S0304-3800(00)00400-2

Krivtsov V, Gascoigne J, Jones S (2008) Harmonic analysis of suspended particulate matter in the Menai Strait (UK). Ecological Modelling 212(1-2):53–67, DOI 10.1016/j.ecolmodel.2007.10.039

Krivtsov V, Howarth M, Jones S (2009) Characterising observed patterns of suspended particulate matter and relationships with oceanographic and meteorological variables: Studies in Liverpool Bay. Environmental Modelling & Software 24(6):677–685, DOI 10.1016/j.envsoft.2008.09.012

Lane A, Prandle D, Harrison A, Jones P, Jarvis C (1997) Measuring Fluxes in Tidal Estuaries: Sensitivity to Instrumentation and Associated Data Analyses. Estuarine, Coastal and Shelf Science 45(4):433–451, DOI 10.1006/ecss.1996.0220

Large WG, Pond S (1981) Open Ocean Momentum Flux Measurements in Moderate to Strong Winds. Journal of Physical Oceanography 11:324–336

van der Lee E, Bowers D, Kyte E (2009) Remote sensing of temporal and spatial patterns of suspended particle size in the Irish Sea in relation to the Kolmogorov microscale. Continental Shelf Research 29(9):1213–1225, DOI 10.1016/j.csr.2009.01.016

Lick W, Huang H, Jepsen R (1993) Flocculation of Fine-Grained Sediments Due to Differential Settling. Journal of Geophysical Research 98(6):10,279–10,288

Liss S, Droppo I, Leppard G, Milligan T (2004) Flocculation in natural and engineered environmental systems. CRC Press, Florida

Lunau M, Lemke A, Dellwig O, Simon M (2006) Physical and biogeochemical controls of microaggregate dynamics in a tidally affected coastal ecosystem. Limnology and Oceanography 51(2):847–859, DOI 10.4319/lo.2006.51.2.0847

Maggi F (2005) Flocculation dynamics of cohesive sediment. PhD thesis, Delft University of Technology

Maggi F, Manning A, Winterwerp J (2006) Image separation and geometric characterisation of mud flocs. Journal of Hydrology 326(1-4):325–348, DOI 10.1016/j.jhydrol.2005.11.005

Manning A, Dyer K (1999) A laboratory examination of floc characteristics with regard to turbulent shearing. Marine Geology 160(1-2):147–170, DOI 10.1016/S0025-3227(99)00013-4

Manning A, Friend P, Prowse N, Amos C (2007) Estuarine mud flocculation properties determined using an annular mini-flume and the LabSFLOC system. Continental Shelf Research 27(8):1080–1095, DOI 10.1016/j.csr.2006.04.011

McCave I (1984) Size spectra and aggregation of suspended particles in the deep ocean. Deep Sea Research Part A Oceanographic Research Papers 31(4):329–352, DOI 10.1016/0198-0149(84)90088-8

Mehta AJ, Partheniades E (1975) An Investigation Of The Depositional Properties Of Flocculated Fine Sediments. Journal of Hydraulic Research 13(4):361–381

Mikes D, Verney R, Lafite R, Belorgey M (2004) Controlling factors in estuarine flocculation processes: experimental results with material from the Seine Estuary, northwestern France. Journal of Coastal Research 41:82–89

Mikkelsen Oa, Hill PS, Milligan TG (2006) Single-grain, microfloc and macrofloc volume variations observed with a LISST-100 and a digital floc camera. Journal of Sea Research 55(2):87–102, DOI 10.1016/j.seares.2005.09.003

Mikkelsen OA, Milligan TG, Hill PS, Chant RJ, Jago CF, Jones SE (2008) The influence of schlieren on in situ optical measurements used for particle characterization. Limnology and Oceanography: Methods 6:133–143

Miller KS, Rochwarger MM (1972) A covariance approach to spectral moment estimation. IEEE Trans Inform Theory 18:588–596

Moody JA, Butman B, Bothner MH (1987) Near-bottom suspended matter concentration on the Continental Shelf during storms: estimates based on in situ observations of light transmission and a particle size dependent transmissometer calibration. Continental Shelf Research 7(6):609–628

Nikora V, Aberle J, Green M (2004) Sediment Flocs: Settling Velocity, Flocculation Factor, and Optical Backscatter. Journal of Hydraulic Engineering (October):1043–1047, DOI 10.1061/(ASCE)0733-9429(2004)130

North EW, Chao SY, Sanford LP, Hood RR (2004) The influence of wind and river pulses on an estuarine turbidity maximum: Numerical studies and field observations in Chesapeake Bay. Estuaries 27(1):132–146, DOI 10.1007/BF02803567

Officer C (1981) Physical dynamics of estuarine suspended sediments. Marine Geology 40:1–14

Parker D, Kaufman W, Jenkins D (1972) Floc breakup in turbulent flocculation processes. J Sanit Eng Div Proc Am Soc Civ Eng 98:79–99

Patchineelam SM, Kjerfve B (2004) Suspended sediment variability on seasonal and tidal time scales in the Winyah Bay estuary, South Carolina, USA. Estuarine, Coastal and Shelf Science 59(2):307–318, DOI 10.1016/j.ecss.2003.09.011

Pejrup M, Mikkelsen OA (2010) Factors controlling the field settling velocity of cohesive sediment in estuaries. Estuarine, Coastal and Shelf Science 87(2):177–185

Pond S, Pickard G (1978) Introductory Dynamic Oceanography. Pergamon Press

Prandle D, Lane A, Manning AJ (2005) Estuaries are not so unique. Geophysical Research Letters 32(23):L23,614

Reynolds O (1883) An experimental investigation of the circumstances which determine whether the motion of water shall be direct or sinuous, and of the law of resistance in parallel channels. Philosophical Transactions of The Royal Society A 174:935–982

Reynolds O (1895) On the dynamical theory of in compressible viscous fluids and the determination of the criterion. Philosophical Transactions of The Royal Society London 186:123–164

Richardson L (1922) Weather prediction by Numerical Process. Cambridge University Press, Cambridge

Robins PE (2013) Development of a morphodynamic model of the Dyfi Estuary to inform future management decisions: Model update and further validation. Tech. rep., CCW Contract Science Report No. 1033

Sanford LP (1994) Wave-Forced Resuspension of Upper Chesapeake Bay Muds. Estuaries 17(1):148, DOI 10.2307/1352564

Sanford LP, Suttles SE, Halka JP (2001) Reconsidering the Physics of the Chesapeake Bay Estuarine Turbidity Maximum. Estuaries 24(5):655–669

Sauvageot H (1992) Radar Meterology. In: Radar Meterology, Artech House Books, p 384

Sequoia Scientific (2012) LISST-100X Particle Size Analyzer User Manual Version 4.65. Tech. rep.

Shi Z (1991) Tidal bedding and tidal cyclicities within the intertidal sediments of a microtidal estuary, Dyfi River Estuary, west Wales, U.K. Sedimentary Geology 73(1-2):43–58

Shi Z, Lambb HF, Collinb RL (1995) Geomorphic change of saltmarsh tidal creek networks in the Dyfi Estuary , Wales. Marine Geology 128:73–83

Simpson J, Bowers D (1981) Models of stratification and frontal movement in shelf seas. Deep-Sea Research 28A(7):727–738

Smith CN, Stewart T, McDonald P (2003) Results from an intensive measurement programme for suspended particulate matter in a region of the Irish Sea between Anglesey and the Isle of Man. Continental Shelf Research 23(10):1005–1018, DOI 10.1016/S0278-4343(03)00058-X

Smoluchowski M (1917) Versuch einer mathematischen Theorie der Koagulationskinetik kolloiderLösnngen. Zeitschrift für Physikalische Chemie 92:129–138

Smyth WD, Moum JN (2001) 3D TURBULENCE. DOI 10.1006/rwos.2001.0134

Sokal R, Rohlf F (1995) Biometry, third edit edn. Freeman

Soloviev A, Lukas R (2003) Observation of wave-enhanced turbulence in the near-surface layer of the ocean during TOGA COARE. Deep Sea Research Part I: Oceanographic Research Papers 50(3):371–395, DOI 10.1016/S0967-0637(03)00004-9

Son M, Hsu TJ (2008) Flocculation model of cohesive sediment using variable fractal dimension. Environmental Fluid Mechanics 8(1):55–71, DOI 10.1007/s10652-007-9050-7

Stramski D, Boss E, Bogucki D, Voss KJ (2004) The role of seawater constituents in light backscattering in the ocean. Progress in Oceanography 61(1):27–56, DOI 10.1016/j.pocean.2004.07.001

Styles R (2006) Laboratory evaluation of the LISST in a stratified fluid. Marine Geology 227(1-2):151–162, DOI 10.1016/j.margeo.2005.11.011

Taylor GI (1935) Statistical Theory of Turbulence. Proceedings of the Royal Society of London A: Mathematical, Physical and Engineering Sciences 151:421–444, DOI 10.1098/rspa.1935.0158

Terray E, Donelan, M A, Agrawal YC, Drennan, W M, Kahma, K K, Williams A, Hwang, P A, Kitaigorodskii, S A (1995) Estimates of Kinetic Energy Dissipation under Breaking Waves. Journal of Physical Oceanography 26:792–807

Thurston W (2009) Turbulence as a mediator of processes in a macrotidal estuary. PhD thesis, University of Leeds

Traykovski P, Latter RJ, Irish JD (1999) A laboratory evaluation of the laser in situ scattering and transmissometery instrument using natural sediments. Marine Geology 159(1-4):355–367

Traykovski P, Geyer W, Irish J, Lynch J (2000) The role of wave-induced density-driven fluid mud flows for cross-shelf transport on the Eel River continental shelf. Continental Shelf Research 20(16):2113–2140, DOI 10.1016/S0278-4343(00)00071-6

Uncles R, Stephens J (1989) Distributions of suspended sediment at high water in a macrotidal estuary. Journal of Geophysical Research 94(C10):14,395–14,405

Uncles R, Stephens J, Law D (2006) Turbidity maximum in the macrotidal, highly turbid Humber Estuary, UK: Flocs, fluid mud, stationary suspensions and tidal bores. Estuarine, Coastal and Shelf Science 67(1-2):30–52, DOI 10.1016/j.ecss.2005.10.013

Van Leussen W, Cornelisse J (1993) The role of large aggregates in estuarine fine-grained sediment dynamics. Nearshore and Estuarine Cohesive Sediment Transport, Coastal Estuarine Studies 42:75–91, DOI 10.1029/CE042p0075

Velegrakis A, Gao S, Lafite R, Dupont J, Huault M, Nash L, Collins M (1997) Resuspension and advection processes affecting suspended particulate matter concentrations in the central English Channel. Journal of Sea Research 38(1-2):17–34, DOI 10.1016/S1385-1101(97)00041-5

Verney R, Lafite R, Brun-Cottan JC (2009) Flocculation Potential of Estuarine Particles: The Importance of Environmental Factors and of the Spatial and Seasonal Variability of Suspended Particulate Matter. Estuaries and Coasts 32(4):678–693, DOI 10.1007/s12237-009-9160-1

Voulgaris G, Trowbridge J (1998) Evaluation of the Acoustic Doppler Velocimeter (ADV) for Turbulence Measurements. Journal of Atmospheric and Oceanic Technology 15:272–289

Weeks A, Simpson J, Bowers D (1993) The relationship between concentrations of suspended particulate material and tidal processes in the Irish Sea. Continental Shelf Research 13(12):1325–1334

Weir D, McManus J (1987) The role of wind in generating turbidity maxima in the Tay Estuary. Continental Shelf Research 7(11-12):1315–1318, DOI 10.1016/0278-4343(87)90035-5

Wiles PJ, Rippeth TP, Simpson JH, Hendricks PJ (2006) A novel technique for measuring the rate of turbulent dissipation in the marine environment. Geophysical Research Letters 33(21):L21,608

Winterwerp J, Manning A, Martens C, de Mulder T, Vanlede J (2006) A heuristic formula for turbulence-induced flocculation of cohesive sediment. Estuarine, Coastal and Shelf Science 68(1-2):195–207, DOI 10.1016/j.ecss.2006.02.003

Winterwerp JC (1998) A simple model for turbulence induced flocculation of cohesive sediment. Journal of Hydraulic Research 36(3):309–326

Winterwerp JC (2002) On the flocculation and settling velocity of estuarine mud. Continental Shelf Research 22:1339–1360

Wolanski E, King B, Galloway D (1995) Dynamics of the Turbidity Maximum in the Fly River Estuary , Papua New Guinea. Estuarine, Coastal and Shelf Science 40:321–337

Woodruff JD, Geyer WR, Sommer CK, Driscoll NW (2001) Seasonal variation of sediment deposition in the Hudson River estuary 179:105–119

Wright LD, Boon JD, Xu JP, Kim SC (1992) The Bottom Boundary Layer of the Bay Stem Plains Environment of Lower Chesapeake Bay. Estuarine, Coastal and Shelf Science 35:17–36

Xu F, Wang DP, Riemer N (2008) Modeling flocculation processes of fine-grained particles using a size-resolved method: Comparison with published laboratory experiments. Continental Shelf Research 28(19):2668–2677, DOI 10.1016/j.csr.2008.09.001

Xu JP, Wright LD, Boon JD (1994) Estimation of bottom stress and roughness in lower Chesapeake Bay by the inertial dissipation method. Journal of Coastal Research 10(2):329–338

Young IR, Banner ML, Donelan Ma, McCormick C, Babanin AV, Melville WK, Veron F (2005) An integrated system for the study of wind-wave source terms in finite-depth water. Journal of Atmospheric and Oceanic Technology 22(7):814–831

Appendix 1

Table 1: Table of regression analysis for resuspension events for each tide during the ebb at Mooring B in November 2011.

tide	α_D	λ_D	${R^2}_D$	α_v	λ_v	${R^2}_v$
1	0.595	75.1	0.128	0.635	125	0.71
2	1.83	77.6	0.97	3.55	115	0.85
3	1.14	99.9	0.45	1.18	129	0.80
4	-0.382	143	0.0762	1.05	119	0.56
5	2.6	30	0.902	2.36	129	0.97
6	6.02	36.1	0.718	5.61	96	0.90
7	2.99	97.2	0.954	2.01	124	0.8
8	1.68	164	0.475	2.56	106	0.60
9	6.35	79.6	0.425	7.67	94.3	0.95
10	4.43	106	0.554	3.68	94.4	0.88
11	1.93	89.8	0.974	4.46	95.6	0.89
12	2.01	77.1	0.925	3.1	93.9	0.69
13	1.36	85.2	0.925	5.89	98.2	0.85
14	1.07	55.1	0.949	5.61	88.4	0.60
15	0.194	134	0.0181	9.3	86.6	0.95
16	0.533	91.4	0.137	6.16	116	0.91
17	0.357	77.7	0.126	4.82	141	0.91
18	1.17	37.3	0.499	1.8	135	0.70
19	1.2	43.6	0.966	6.12	111	0.93
20	1.14	40.7	0.422	4.14	120	0.80
21	0.881	69.6	0.524	5.23	122	0.90
22	0.782	106	0.407	3.38	111	0.833

Appendix 2

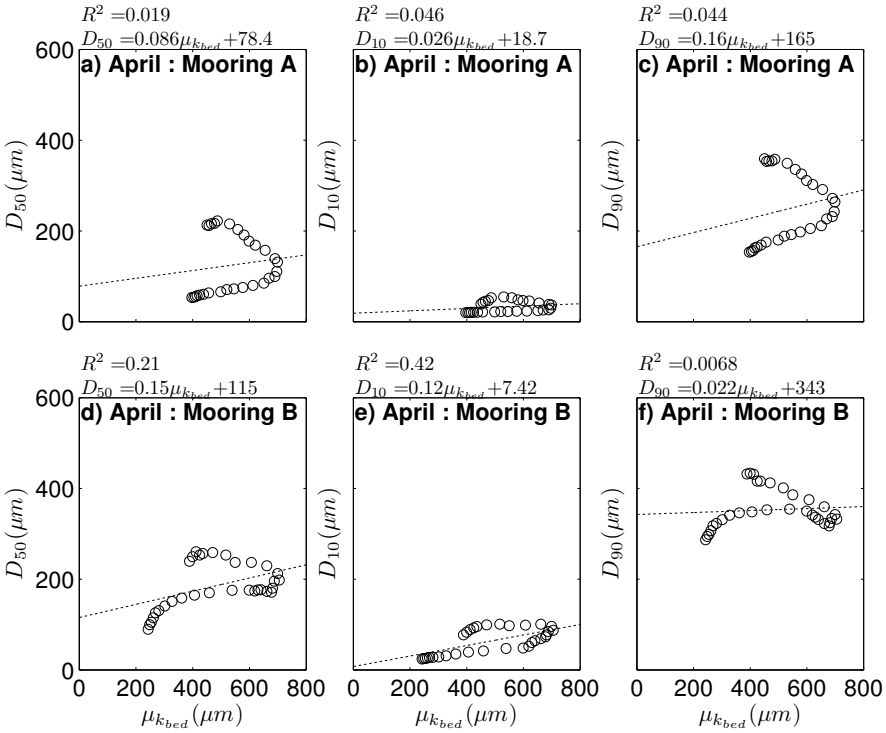

Figure 4: Relationship between $\mu_{k_{bed}}$ and particle size (D_{50}, D_{10} and D_{90}) at Mooring A and Mooring B over 1 tidal cycle during April with a phase lag of 60 minutes applied.

Appendix 3

Table 2: Results of multiple regression analysis for each tidal cycle at Mooring A in March 2011, employing G_{bed} as the disaggregation/resuspension parameter.

Tide	$\alpha_D(\mu m m^{-1})$	$\beta_D(\mu m m/s^{-1})$	$\lambda_D(\mu m)$	R^2
1	44.1(3.2)	1.55(3.2)	96.6(6.4)	0.79
2	31.3(5.6)	0.682(5.6)	138(12)	0.38
3	60.1(4.3)	1.13(4.3)	117(9.7)	0.78
4	55.7(3.7)	1.33(3.7)	102(8.3)	0.82
5	63.2(3.2)	0.925(3.2)	123(6.6)	0.88
6	60.1(3.3)	1.41(3.3)	110(8.2)	0.87
7	68.2(3.8)	0.682(3.8)	145(7.2)	0.86
8	63.1(3.6)	1.31(3.6)	113(8.4)	0.88
9	84(4.1)	0.316(4.1)	146(7.3)	0.88
10	68.2(3)	0.967(3)	110(5.9)	0.91
11	72.1(2.5)	1.15(2.5)	91.5(4.8)	0.94
12	74(3.8)	1.54(3.8)	66.4(7.3)	0.87
13	53.4(2.8)	1.07(2.8)	93.2(5.3)	0.87
14	50.7(5)	2.09(5)	74.6(9.7)	0.69
15	43.5(3)	-0.00694(3)	132(5.2)	0.81
16	40.5(3.3)	-0.137(3.3)	138(6.2)	0.75
17	66.6(2.9)	0.331(2.9)	120(4.9)	0.91
18	51.6(6.2)	-0.571(6.2)	116(9.4)	0.69
19	6.6(4)	-0.516(4)	72.8(3.6)	0.57
20	1.69(0.47)	-0.167(0.47)	56.5(0.5)	0.75
21	-10.7(1.2)	-0.094(1.2)	60.9(1.1)	0.66
22	-4.91(0.55)	-0.222(0.55)	73.1(0.69)	0.56
23	-2.29(0.62)	-0.101(0.62)	78.5(0.63)	0.26

Table 3: Results of multiple regression analysis for each tidal cycle at Mooring A in March 2011, employing $\mu_{k_{bed}}$ as the disaggregation/resuspension parameter.

Tide	$\alpha_D(\mu m m^{-1})$	$\beta_D(\mu m m/s^{-1})$	$\lambda_D(\mu m)$	R^2
1	42.1(4)	-0.558(4)	257(11)	0.67
2	27.7(5)	-0.227(5)	205(13)	0.36
3	65(4.5)	-0.596(4.5)	262(16)	0.78
4	60.3(4)	-0.639(4)	262(13)	0.81
5	67.5(3.3)	-0.42(3.3)	231(11)	0.88
6	65(3.4)	-0.698(3.4)	280(14)	0.87
7	73.1(3.8)	-0.346(3.8)	231(12)	0.86
8	68.1(3.6)	-0.682(3.6)	277(15)	0.88
9	87.1(4)	-0.211(4)	195(12)	0.89
10	72.8(2.9)	-0.373(2.9)	212(9.3)	0.92
11	76.1(2.4)	-0.399(2.4)	206(6.9)	0.94
12	75.3(4.2)	-0.395(4.2)	195(10)	0.85
13	57.2(2.9)	-0.297(2.9)	186(7.5)	0.87
14	55.5(5.6)	-0.411(5.6)	216(14)	0.65
15	44.6(3.1)	-0.0274(3.1)	138(7.4)	0.81
16	42.7(3.4)	-0.0359(3.4)	142(8.3)	0.75
17	67.5(2.8)	-0.085(2.8)	146(6.9)	0.92
18	53.7(5.8)	0.0855(5.8)	83(13)	0.68
19	1.06(3.9)	0.116(3.9)	34.7(5.6)	0.63
20	0.876(0.4)	0.0349(0.4)	45.1(0.71)	0.84
21	-9.99(1.2)	0.00424(1.2)	58.2(1.7)	0.65
22	-5.17(0.58)	0.0325(0.58)	61.2(1.4)	0.57
23	-2.13(0.63)	0.0126(0.63)	73.6(1.2)	0.23

Table 4: Results of multiple regression analysis for each tidal cycle at Mooring B in March 2011, employing G_{bed} as the disaggregation/resuspension parameter.

Tide	$\alpha_D(\mu mm^{-1})$	$\beta_D(\mu mm/s^{-1})$	$\lambda_D(\mu m)$	R^2
1	52.3(3.3)	-0.758(3.3)	166(3.7)	0.82
2	67.2(2.8)	-1.33(2.8)	186(3.2)	0.91
3	-32.4(8.8)	-3.39(8.8)	321(11)	0.62
4	39.4(4.4)	-1.61(4.4)	183(5.6)	0.67
5	24.7(5.1)	-1.36(5.1)	182(6.2)	0.51
6	2.15(6.4)	-0.112(6.4)	209(5.9)	0.095
7	-29.1(6.1)	-3.04(6.1)	330(8.2)	0.73
8	43(6.6)	-0.732(6.6)	185(7.1)	0.5
9	57.4(5.8)	-1.3(5.8)	193(7.2)	0.65
10	9.51(3.8)	-0.17(3.8)	181(5.1)	0.1
11	-64.7(15)	-3.28(15)	329(22)	0.42
12	30.7(5.4)	0.546(5.4)	136(8)	0.42
13	-95.1(11)	-3.07(11)	321(17)	0.67
14	-11(5.9)	3(5.9)	179(7.1)	0.65
15	81(3.8)	-0.854(3.8)	179(4.1)	0.89
16	95.5(3)	-1.23(3)	197(3.4)	0.95
17	80.5(4)	-0.27(4)	183(3.5)	0.88

Table 5: Results of multiple regression analysis for each tidal cycle at Mooring B in March 2011, employing $\mu_{k_{bed}}$ as the disaggregation/resuspension parameter.

Tide	$\alpha_D(\mu mm^{-1})$	$\beta_D(\mu mm/s^{-1})$	$\lambda_D(\mu m)$	R^2
1	44.4(3.3)	0.129(3.3)	111(6)	0.82
2	61.2(2.9)	0.202(2.9)	102(5.9)	0.9
3	-48.3(11)	0.375(11)	140(23)	0.44
4	29.6(4.2)	0.219(4.2)	88(8.1)	0.71
5	15.4(5.4)	0.181(5.4)	97.6(10)	0.47
6	-0.295(6.5)	0.0624(6.5)	185(12)	0.042
7	-47.6(7.8)	0.563(7.8)	109(16)	0.63
8	47.5(6.3)	0.184(6.3)	110(12)	0.55
9	54.9(6.5)	0.151(6.5)	123(16)	0.56
10	8.51(3.9)	-0.0167(3.9)	181(11)	0.088
11	-64.6(17)	0.544(17)	121(49)	0.34
12	29.1(5)	-0.208(5)	199(15)	0.49
13	-97.5(11)	0.474(11)	138(38)	0.63
14	-26.8(5)	-0.568(5)	389(11)	0.79
15	79.3(4.7)	0.0737(4.7)	142(10)	0.86
16	92.9(3.5)	0.108(3.5)	146(8.1)	0.93
17	79.7(4.1)	0.0476(4.1)	164(6.2)	0.88

Table 6: Results of multiple regression analysis for each tidal cycle at Mooring A in April 2010, employing G_{bed} as the disaggregation/resuspension parameter.

Tide	$\alpha_D(\mu mm^{-1})$	$\beta_D(\mu mm/s^{-1})$	$\lambda_D(\mu m)$	R^2
1	153(11)	29.6(11)	-30.8(28)	0.9
2	148(4)	60.3(4)	-71.2(11)	0.98
3	99.8(20)	-3.21(20)	111(36)	0.82
4	140(5.2)	41.6(5.2)	-20.8(12)	0.97
5	143(20)	15(20)	11(37)	0.79
6	169(15)	40.6(15)	-69.9(43)	0.87
7	134(56)	0.0711(56)	64.1(84)	0.55
8	168(5.5)	103(5.5)	-228(11)	0.99
9	21.2(61)	-6.11(61)	116(60)	0.47
10	130(25)	47(25)	-105(38)	0.62
11	129(22)	36.4(22)	-102(23)	0.89
12	196(70)	76.3(70)	-259(1e+002)	0.46

Table 7: Results of multiple regression analysis for each tidal cycle at Mooring A in April 2010, employing $\mu_{k_{bed}}$ as the disaggregation/resuspension parameter.

Tide	$\alpha_D(\mu mm^{-1})$	$\beta_D(\mu mm/s^{-1})$	$\lambda_D(\mu m)$	R^2
1	147(11)	-0.352(11)	270(36)	0.9
2	149(4.9)	-0.587(4.9)	452(29)	0.97
3	116(20)	-0.0464(20)	115(48)	0.82
4	139(6)	-0.385(6)	331(31)	0.96
5	142(18)	-0.209(18)	182(39)	0.8
6	163(16)	-0.331(16)	249(65)	0.85
7	197(60)	-0.279(60)	176(99)	0.57
8	166(7.9)	-0.917(7.9)	617(29)	0.97
9	-31.5(84)	0.27(84)	-21.3(52)	0.49
10	124(23)	-0.367(23)	254(45)	0.65
11	125(35)	-0.525(35)	316(35)	0.72
12	139(66)	-0.561(66)	332(85)	0.37

Table 8: Results of multiple regression analysis for each tidal cycle at Mooring B in April 2010, employing G_{bed} as the disaggregation/resuspension parameter.

Tide	$\alpha_D(\mu mm^{-1})$	$\beta_D(\mu mm/s^{-1})$	$\lambda_D(\mu m)$	R^2
1	76.4(12)	5.99(12)	113(21)	0.79
2	105(8.4)	19.4(8.4)	52.4(14)	0.84
3	23.2(18)	-3.51(18)	214(25)	0.54
4	127(15)	18.6(15)	39.3(27)	0.84
5	-4.73(21)	-5.78(21)	241(29)	0.47
6	152(17)	19.2(17)	8.06(30)	0.8
7	41.9(16)	-1.48(16)	181(19)	0.62
8	227(16)	35.2(16)	-110(27)	0.89
9	46.2(17)	0.0258(17)	197(19)	0.6
10	455(81)	100(81)	-480(1.4e+002)	0.69
11	70.5(8.3)	16.8(8.3)	148(16)	0.74
12	259(11)	12.9(11)	-25.3(10)	0.95
13	4.21(90)	8.35(90)	283(1.4e+002)	0.078
14	295(14)	16(14)	-19.5(12)	0.95
15	242(18)	56.1(18)	-38.9(32)	0.89
16	427(38)	70.3(38)	-281(57)	0.85
17	75.7(21)	11(21)	216(34)	0.35
18	59.9(45)	-7.09(45)	265(57)	0.57

Table 9: Results of multiple regression analysis for each tidal cycle at Mooring B in April 2010, employing $\mu_{k_{bed}}$ as the disaggregation/resuspension parameter.

Tide	$\alpha_D(\mu m m^{-1})$	$\beta_D(\mu m m/s^{-1})$	$\lambda_D(\mu m)$	R^2
1	76.6(11)	-0.114(11)	201(16)	0.8
2	87.6(9.8)	-0.227(9.8)	274(14)	0.73
3	75.8(27)	-0.109(27)	212(33)	0.52
4	111(13)	-0.19(13)	230(22)	0.82
5	80.4(25)	-0.148(25)	219(29)	0.42
6	131(16)	-0.208(16)	217(26)	0.76
7	105(15)	-0.181(15)	216(15)	0.74
8	194(21)	-0.352(21)	248(32)	0.78
9	93.3(16)	-0.146(16)	239(14)	0.7
10	332(61)	-0.882(61)	451(1e+002)	0.65
11	69(9.3)	-0.239(9.3)	339(21)	0.69
12	326(25)	-0.496(25)	257(21)	0.87
13	43.1(63)	-0.281(63)	444(1.1e+002)	0.12
14	342(22)	-0.554(22)	317(27)	0.9
15	229(19)	-0.693(19)	545(38)	0.87
16	333(40)	-0.674(40)	423(51)	0.76
17	84.7(21)	-0.2(21)	361(35)	0.4
18	226(54)	-0.341(54)	264(54)	0.57